JAGIELLONIAN UNIVERSITY

DOCTORAL THESIS

Studies of Critical Phenomena in Causal Dynamical Triangulations on a Torus

Author:
Dániel NÉMETH

Supervisors:
Prof. dr hab. Jerzy JURKIEWICZ
Dr. hab. Jakub GIZBERT-STUDNICKI

A thesis submitted in fulfillment of the requirements for the degree of Doctor of Philosophy

in the

Faculty of Physics, Astronomy and Applied Computer Science
Jagiellonian University

Declaration of Authorship

Ja, niżej podpisany, Dániel NÉMETH, (nr indeksu: 1159847), doktorant Wydziału Fizyki, Astronomii i Informatyki Stosowanej Uniwersytetu Jagiellońskiego oświadczam, że przedłożona przeze mnie rozprawa doktorska pt. "Studies of Critical Phenomena in Causal Dynamical Triangulations on a Torus" jest oryginalna i przedstawia wyniki badań wykonanych przeze mnie osobiście, pod kierunkiem prof. dr hab. Jerzego Jurkiewicza i dr hab. Jakuba Gizbert-Studnickiego. Pracę napisałem samodzielnie.

Oświadczam, że moja rozprawa doktorska została opracowana zgodnie z Ustawą o prawie autorskim i prawach pokrewnych z dnia 4 lutego 1994 r. (Dziennik Ustaw 1994 nr 24 poz. 83 wraz z późniejszymi zmianami).

Jestem świadomy, że niezgodność niniejszego oświadczenia z prawdą ujawniona w dowolnym czasie, niezależnie od skutków prawnych wynikających z ww. ustawy, może spowodować unieważnienie stopnia nabytego na podstawie tej rozprawy.

Kraków, ...
(data) (podpis doktoranta)

JAGIELLONIAN UNIVERSITY

Abstract

Faculty of Phyiscs, Astronomy and Applied Computer Science
Jagiellonian University

Doctor of Philosophy

Studies of Critical Phenomena in Causal Dynamical Triangulations on a Torus

by Dániel NÉMETH

This document contains my publications and results based on research done as a member of the Causal Dynamical Triangulations (CDT) group at the Jagiellonian University during my PhD studies. The field of my research was the four-dimensional CDT, which is a lattice regularization of the theory of quantum gravity, based on the formalism of Regge Calculus and Feynman path integrals. Due to mathematical complexity, analytical solutions to the model exists only in two dimensions. The four-dimensional theory is analyzed by numerical simulations. Earlier discoveries include dynamically emergent quantum de Sitter universes with emergent four-dimensional properties, scale-dependent spectral dimensions and a complex phase structure in which first- and higher-order phase transitions were shown to exist. The document describes the nature of previously not yet analyzed phase transitions, new ways to analyze triangulations and the impact of classical and dynamical (quantum) scalar fields in four-dimensional CDT with toroidal spatial topology. The main results of the dissertation are the six publications attached to the last chapter. This document is intended as an introduction to CDT and serves as a guide to the papers comprising the doctoral thesis.

JAGIELLONIAN UNIVERSITY

Abstract

Faculty of Phyiscs, Astronomy and Applied Computer Science
Jagiellonian University

Doctor of Philosophy

Studies of Critical Phenomena in Causal Dynamical Triangulations on a Torus

by Dániel NÉMETH

Niniejszy dokument zawiera moje publikacje i wyniki oparte na badaniach prowadzonych jako członek grupy Causal Dynamical Triangulations (CDT) na Uniwersytecie Jagiellońskim podczas studiów doktoranckich. Obszarem moich badań był czterowymiarowy model CDT, który stanowi sieciową regularyzację teorii kwantowej grawitacji, opartą na formalizmach rachunku Regge i całek po trajektoriach Feynmana. Ze względu na złożoność matematyczną, rozwiązania analityczne tego modelu istnieją tylko w dwóch wymiarach. Czterowymiarowa teoria jest analizowana przez symulacje numeryczne. Wcześniejsze odkrycia obejmują dynamicznie pojawiające się kwantowe wszechświaty de Sittera z emergentnymi właściwościami czterowymiarowymi, zależne od skali wymiary spektralne oraz skomplikowaną strukturę fazową, w której istnieją przejścia fazowe pierwszego i wyższego rzędu. Dokument zawiera opis natury nie analizowanych dotychczas przejść fazowych, nowych sposobów analizy triangulacji oraz wpływu klasycznych i dynamicznych (kwantowych) pól skalarnych w czterowymiarowym CDT o toroidalnej topologii przestrzennej. Głównymi wynikami rozprawy jest sześć publikacji załączonych w ostatnim rozdziale. Dokument ten ma na celu wprowadzenie do CDT i stanowi przewodnik po artykułach składających się na rozprawę doktorską.

Contents

Declaration of Authorship iii

Abstract v

Abstract vii

1 Motivation to the study of parallels, random geometry and quantum gravity 1

2 Causal Dynamical Triangulations 5
2.1 Introduction to Quantum Gravity . . . 5
2.1.1 (Non-)renormalizability of quantum gravity and the need for non-perturbative approaches . . . 5
2.1.2 Regge calculus . . . 6
2.2 Causal Dynamical Triangulations . . . 9
2.2.1 Most important previous results of CDT . . . 11

3 Numerical Simulations 15
3.1 The Numerical Setup . . . 15
3.1.1 Move-2 . . . 20
3.1.2 Move-3 . . . 20
3.1.3 Move-4 . . . 21
3.1.4 Move-5 . . . 21

4 Empty Universes 23
4.1 About criticality at phase transitions . . . 23
4.2 Order parameters and the internal structure of the configurations . . . 25
4.3 Phase transitions . . . 28
4.3.1 Finite volume scaling analysis . . . 32
4.3.2 $A \downarrow B$ phase-transition . . . 32
4.3.3 $C_b \downarrow B$ phase-transition . . . 34
4.3.4 $C \downarrow B$ phase-transition . . . 35
4.3.5 Summary . . . 36

5 Universes with matter fields 39
5.1 Scalar fields as coordinates . . . 39
5.2 Dynamical scalar fields . . . 44

6 Conclusions 47

7 Publications 51
7.1 Publications . . . 52

Acknowledgements 179

A Additional Moves **181**

B Topological relations between parameters of a CDT triangulation **185**

Bibliography **189**

List of Abbreviations

ADM	**A**rnowitt-**D**eser-**M**isner
AS	**A**symptotic **S**afety
CDT	**C**ausal **D**ynamical **T**riangulations
CFT	**C**onformal **F**ield **T**heory
EDT	**E**uclidean **D**ynamical **T**riangulations
GFT	**G**roup **F**ield **T**heory
HLG	**H**ořava–**L**ifshitz **G**ravity
IR	**I**nfra **R**ed
LCDT	**L**ocally **C**ausal **D**ynamical **T**riangulations
LQCD	**L**attice **Q**uantum **C**hrono **D**ynamics
LQG	**L**oop **Q**uantum **G**ravity
MC	**M**onte **C**arlo
NCG	**N**on-**C**ommutative **G**eometry
OP	**O**rder **P**arameter
QCD	**Q**uantum **C**hrono **D**ynamics
QFT	**Q**uantum **F**ield **T**heory
QM	**Q**uantum **M**echanics
RG	**R**enormalization **G**roup
ST	**S**tring **T**heory
UV	**U**ltra **V**iolet
UVFP	**U**ltra **V**iolet **F**ixed **P**oint

To my daughter who cannot read yet...

Chapter 1

Motivation to the study of parallels, random geometry and quantum gravity

"You must not attempt this approach to the parallels. I know this way to the very end. I have traversed this bottomless night, which extinguished all light and joy of my life. I entreat you, leave the science of parallels alone. For God's sake, please give it up. Fear it no less than the sensual passion, because it, too, may take up all your time and deprive you of your health, peace of mind and happiness in life. I thought I would sacrifice myself for the sake of truth. I was ready to become a martyr who would remove the flaw from geometry and return it purified to mankind. I accomplished monstrous, enormous labours: my creations are far better than those of others and yet I have not achieved complete satisfaction. I turned back when I saw no man can reach the bottom of this night. I turned back unconsolidated , pitying myself and all mankind. Learn from my example: I wanted to know about parallels. I remain ignorant, this has taken all the flowers of my life and all my time from me...." - **A letter of Bolyai Farkas to his son Bolyai János**

Geometry, the mathematical study of shapes, always interested humans. From the ancient Greeks till today's science various topics related to geometry are key aspects to mathematics and natural sciences. Euclid laid down five axioms, which became the foundations of mathematics. At that time, mathematics was postulated in terms of words and rarely graphics, but not equations. The postulates of Euclid [7], based on his axioms, defined geometry until the 19^{th} century. His postulates were:

- A straight line segment may be drawn from any given point to any other.
- A straight line may be extended to any finite length.
- A circle may be described with any given point as its center and any distance as its radius.
- All right angles are congruent.
- If a straight line intersects two other straight lines, and so makes the two interior angles on one side of it together less than two right angles, then the other straight lines will meet at a point if extended far enough on the side on which the angles are less than two right angles.

None dared to question the truth of these postulates as any sane person could check their truths by drawing those lines and not finding any which doesn't fit. This

was true until some questioned whether it is possible to draw triangles on various non-flat shapes such that the sum of their inner angles is different than that of $\frac{\pi}{2}$. This is exactly what Bolyai Farkas is talking about in his letter to his son. He discovered that parallels can meet sometimes, but did not manage to describe the phenomena in its entirety even though he worked on that field for his whole life. Thus he warned his son not to pursue geometry and the parallels. But his son, János had his own ideas, and years later he constructed the basics of non-Euclidean geometry. Had he listened to his father, the topic of my doctoral thesis would be probably significantly different. Bolyai pursued a non-mainstream topic of mathematics, and reached success with it. Later Riemann based his work on the work of Bolyai (and others), which was then used by Einstein when he worked out the general theory of relativity. The science of fundamental physics brings forth our knowledge of nature, if we wouldn't walk off-road in the theory space, but only follow the mainstreams, we wouldn't be able to solve the hardest problems of science.

In the beginning of the twentieth century the appearance of two theories gave us an enormous leap towards understanding nature. The paradigm shift which is related from one hand to the curving relativistic four dimensional spacetime described by general relativity (**GR**) and from the other hand to the discreteness of the nature as it is seen by quantum mechanics turned science into science-fiction in the eye of the scientifically not educated people. The math and physics, needed in order to understand it, started to be so complex and demanding, that scientific results became non-trivial. Many physical theories are validated or falsified via mathematical derivations and many cannot be accessed because of their mathematical complexity. The work presented in this thesis belongs to a similar off-road field, which is strongly related to parallels and geometry. Quantum gravity is the field where quantum mechanics and general relativity meets. Quantum mechanics is the theory which describes the smallest scales, the tiny fluctuations of matter, the rules of nature that escape every-day's experience, and gravity is the theory which describes the physics of the largest scales, the orbiting of planets and even the earliest history of the Universe. Their intersection should be the theory of quantum gravity, the theory which describes how the attraction between bodies behaves on the smallest scales, on the scales where other forces of nature dominate and bodies fall apart to their components. As we advanced in our understanding of the world and the Universe it turned out that quantum gravity could potentially explain also the largest scales and the earliest moments of history. It could tell us why do we have such a large-scale structure of galaxies that we see, could explain why visible matter constitutes only four percent of everything, could hint at whether we live in a closed or an open Universe, and foreshadow a potential cold-death at the end of times. The quantum theory of gravity has the potential to explain the nature and the structure of space-time, to resolve singularities of GR and furthermore to explain or disprove the theories regarding dark matter and dark energy.

After Einstein introduced GR many scientist tried to find the theory of quantum gravity without success. The first attempt to describe quantum gravity was a naive application of perturbative methods of QFT to GR, but it failed. The treatment of infinities by perturbative renormalization techniques, which can be used in case of the standard model physics, cannot be applied to gravity, which turned out perturbatively non-renormalizable [8]. However S. Weinberg conjectured that gravity may adhere to an Asymptotic Safety (**AS**) scenario [9, 10, 11], where using Renormalization Group Flow (**RG**) techniques one may find a *fixed point*, where there exist only a

finite number of coupling constants needed to describe the full quantum theory in a non-perturbative way. In a lattice formulation of a quantum theory fixed points are typically connected to phase transitions, and the hypothesis is that there is at least one non-trivial fixed point for gravity related to the ultraviolet (**UV**) regime, which necessarily requires the existence of a higher order phase transition. Such a phase transition can be typically recognised from the diverging correlation length and related scaling exponents.

By the end of the 20^{th} century, with the increasing available computational power, numerical algorithms became widely used. One of the most notable computer based techniques in physics is related to Lattice Quantum Chronodynamics (LQCD) [12, 13], which was developed in parallel with the physical experiments. The basic idea is to discretize the continuum theory such that the field variables are located at the vertices of a regular D-dimensional lattice (D depends on the dimensionality of the discussed model). The lattice spacing a, which is the length between two adjacent vertices of the lattice, should be sent to zero while keeping the relevant physical observables constant, in order to reach the continuum limit within the numerical simulations. Since the beginning of the development of lattice theories, many physically relevant observations were derived from numerical simulations, e.g., related to phase transitions [14], physical masses of particles [15] and many other phenomena. In contrast to the LQCD, lattice quantum gravity is special in a sense that the lattice connectivity itself encodes the geometric degrees of freedom and therefore provides information about the distinct features of gravitational physics on the quantum level. In order to create a physically relevant model of lattice quantum gravity one also has to be able to include matter fields, e.g., scalar fields or gauge fields [16, 17].

This document is a guide to a collection of articles published in the past years and constituting my doctoral thesis. All of the publications were published in peer-reviewed journals.

The structure of this document is as follows: The introduction to Causal Dynamical Triangulations (CDT), which is a non-perturbative approach in the quest of quantizing gravity, is the topic of chapter two. In chapter three, I discuss some details of numerical implementation and Monte Carlo simulation methods used to study CDT. The forth and fifth chapters discuss respectively the results of my studies obtained for empty Universes (pure gravity) and Universes with matter content (gravity coupled to scalar fields). Afterwards, all publications which constitute my thesis are briefly discussed in chapter six, together with information about my contribution to them. The published papers are attached at the very end in chapter seven in the following order:

[1] J. Ambjorn G. Czelusta et al. "The higher-order phase transition in toroidal CDT". In: J. of High Energ. Phys. 2020 (5), p. 30.
DOI: 10.1007/JHEP05(2020)030

[2] J. Ambjorn et al. "Towards an UV fixed point in CDT gravity". In: Journal of High Energy Physics 2019 (7), p. 166.
DOI: 10.1007/JHEP07(2019)166

[3] J. Ambjorn et al. "Topology induced first-order phase transitions in lattice quantum gravity". In: Journal of High Energy Physics 2022 (4), p. 103.
DOI: 10.1007/JHEP04(2022)103.

[4] J.Ambjorn et al. “Cosmic voids and filaments from quantum gravity”. In: The European Physical Journal C 81 (8 2021), p. 708.
DOI: 10.1140/epjc/s10052-021-09468-z

[5] J. Ambjorn et al. “Matter-Driven Change of Spacetime Topology”. In: Phys. Rev. Lett. 127 (16 Oct. 2021), p. 161301.
DOI: 10.1103/PhysRevLett.127161301

[6] J. Ambjorn et al. “Scalar fields in causal dynamical triangulations”. In: Classical and Quantum Gravity 38 (19 Sept. 2021), p. 195030.
DOI: 10.1088/1361-6382/ac2135

Chapter 2

Causal Dynamical Triangulations

2.1 Introduction to Quantum Gravity

"The beauty and clearness of the dynamical theory, which asserts heat and light to be modes of motion, is at present obscured by two clouds..." - **Lord Kelvin**

Lord Kelvin wrongly predicted the end of physics in the late nineteenth century. The two clouds mentioned were the problem of heat and radiation, more precisely the theorised material which fills everything called "ether" and the black body radiation. When we mention modern physics, we refer to the time when the solutions to these two "clouds" were presented in the form of special relativity and quantum mechanics. The start of the twentieth century brought us an explosion of physical theories, as special relativity led to general relativity, which is extensively studied today in relation to astrophysical and cosmological models or technologies, such as GPS tracking devices. In the same time, quantum mechanics evolved into quantum field theory, and later our technological advancements led to the ability to measure properties of particles. The standard model of particle physics is one of the greatest achievements in physics, as it gives an explanation to the fundamental nature of matter. The biggest problem of modern physics is that the theory of matter and the theory of gravity cannot be matched into a unified framework together. Many physicist tried in the past hundred years to describe the theory of quantum gravity, which led to many different research projects, such as Loop Quantum Gravity (LQG), String Theory (ST), Causal Sets (CS), Group Field Theory (GFT), Non-Commutative Geometry (NCG), Canonical Quantum Gravity (CQG), Hořava–Lifshitz Gravity (HLG), Asymptotic Safety (AS), Euclidean Dynamical Triangulations (EDT), Causal Dynamical Triangulations (CDT) and many other approaches.

2.1.1 (Non-)renormalizability of quantum gravity and the need for non-perturbative approaches

Merging the quantum theory with gravity is not a trivial task. Quantum field theory (QFT) predicts fluctuations of fields, and according to GR and Einstein's field equations, where there is energy density, there is curvature. These fluctuations can at very high energies produce such a large energy density in a small volume that the naive application of Einstein's equations would predict the appearance of black holes[18, 19]. The problems with UV-completion of quantum gravity become apparent in the perturbative expansion of a QFT based on GR. Such a formulation is perturbatively non-renormalizable [20], which means, that the naive application of the perturbation

theory would result in infinitely many parameters and coupling constants appearing in the theory, that cannot be eliminated via renormalization thus yielding the theory to be un-predictive.

It is well known, that the couplings appearing in QFTs are scale dependent, this scale dependence is referred to as "running of the couplings". In the case of the full theory, where one integrates from zero to infinite momenta (or alternatively zero distances) many models exhibit infinite divergences, the solution to which is provided by some cutoff Λ introduced to the high energy regime. Up to this cutoff the theory is predictive, and the aim is to remove the cutoff and avoid the appearance of infinities. The UV completeness of a QFT is provided by the existence of fixed points of the renormalization group flow in the coupling constant space: as the energy scale changes, the running coupling constants approach some fixed point value. The microscopic theory is defined in such fixed points, thus finding them is a crucial part of any theory based on QFT language. Let g be a coupling constant of a given theory, then the so-called "beta function" $\beta(g)$ will define the scale dependence, or running of the coupling. The fixed points are defined by zeros of $\beta(g)$, which can result in a free or an interactive theory. The free theory is achieved when the zero of the beta function corresponds to zero values of the couplings, which is called "asymptotic freedom" and such a fixed point is called trivial or Gaussian. If instead zeros of the beta function are achieved for a finite number of non-zero couplings, it is called "asymptotic safety", where one has non-trivial fixed points corresponding to an interactive theory [21]. A fixed point corresponding to high energy, or short scale, is called the "ultraviolet" (UV) fixed point, while the "infrared " (IR) fixed point will correspond to the low energy, or large scale theory.

A QFT description of GR means, that one treats the metric tensor $g_{\mu\nu}$ as the field of gravitation and defines an action in terms of geometric invariants obtained from the metric tensor, such as, e.g., $R, R^2, R_{\mu\nu}R^{\mu\nu}$, etc. The most important couplings in case of gravity are the Newton's coupling G, and the cosmological constant Λ. The theory of gravity is perturbatively non-renormalizable, as applying perturbation theory in every order one has to introduce infinitely many counter-terms and the corresponding new couplings, which renders the theory to be non-predictive. Nevertheless, according to the "asymptotic safety" conjecture, formulated by Steven Weinberg [9], most of the (potentially infinitely many) couplings appearing in such a theory become irrelevant at the non-trivial UV fixed point, and there will be only a finite number of relevant couplings rendering the theory non-perturbatively renormalizable, i.e., UV-complete and predictive to arbitrarily large energy scale. Therefore a non-perturbative description of quantum gravity is needed which can be done with the help of numerical simulations. The non-perturbative approach discussed in this thesis is called Causal Dynamical Triangulations (CDT) and it is based on Regge calculus and Feynman path integral formulation.

2.1.2 Regge calculus

Before jumping into the description of CDT, it is necessary to discuss the mathematical formulation that led to it. This formulation was introduced by Regge, and is called Regge calculus [22]. The aim of Regge was to approximate space-times, which are solutions to the Einstein field equations, via piecewise-flat manifolds.[1]

[1] Often the name *piecewise-linear manifold* instead of *piecewise-flat manifold* is used.

The approximation is done with the help of internally flat triangular building blocks (simplices) glued together in a non-trivial way, hence the name "triangulation". The simplices in a 2-dimensional triangulation are triangles, in 3-dimensions are tetrahedra and in 4-dimensions are pentachora. All simplices in a triangulation are glued to each other via their $(d \downarrow 1)$ dimensional faces (links for $d = 2$, triangles for $d = 3$ and tetrahedra for $d = 4$). These $(d \downarrow 1)$ dimensional sub-simplices are also connected via "hinges", also called "bones", which are $(d \downarrow 2)$ dimensional objects. The hinges play a crucial role, as curvature can be defined there locally. The curvature is related to the angular difference (deficit angle) at a given bone. Let's imagine a triangulation consisting of n equilateral triangles glued together along edges (links) around a single point (vertex). If $n = 6$ then one can place it on a flat 2-dimensional surface . If $n = 5$ then one can place it only if it is cut along one edge, and it will be visible that a triangle is "missing". The angle associated to the missing (or for $n > 6$ extra) triangles is the deficit angle.

Let us consider the simplest (nontrivial) case of a three-dimensional Riemannian manifold which is well approximated by a fine triangulation. Following the approach of Regge [23], the discretized curvature is obtained by considering parallel transport of a vector around a bone. Many simplices (in this case tetrahedra) touch each other at the bone forming a bundle p. One can associate the number of simplices in the bundle with bone density ρ at p, which is equal to the number of simplices divided by a unit area. The deficit angle (ϵ_p) associated with the bone is a measure of a dihedral angle:

$$\epsilon_p = 2\pi \downarrow \sum_n \theta_n, \tag{2.1}$$

θ_n being the dihedral angle of the n-th simplex at the bone. One can alternatively define $\epsilon = \frac{1}{N}\epsilon_p$, which is the deficit angle of the bone smeared on its simplices. Now, let's take a loop a with area Σ around the bundle and parallel transport a vector $\vec{A}$ around the loop. If n_Σ is a unit vector orthogonal to Σ, then one can define:

$$\vec{\Sigma} = \Sigma n_\Sigma, \tag{2.2}$$

which is an area vector associated with the loop. Parallel transporting a vector around the bundle will rotate $\vec{A}$ by an angle σ due to the process of the parallel transport. One can associate a vector of length σ to the rotation, and let this vector be parallel to the bone, so it will be defined by:

$$\vec{\sigma} = \sigma n, \tag{2.3}$$

where n is the unit vector parallel to the bone. Rotating $\vec{A}$ by an angle σ will produce the vector $\vec{A}' = \vec{A} + \delta\vec{A}$. The infinitesimal change $\delta\vec{A}$ will be equal to the product $\delta\vec{A} = \vec{\sigma} \times \vec{A}$. The rotation angle σ is proportional to the number of simplices (N) visited by the loop a circumventing the bone p, thus :

$$\sigma = N\epsilon, \tag{2.4}$$

where N can be expressed in terms of the bone density ρ, the oriented area vector Σ and the unit vector parallel to the bone n:

$$N = \rho\, n \cdot \vec{\Sigma}. \tag{2.5}$$

Putting all the expressions together the infinitesimal change $\delta\vec{A}$ is given by:

$$\delta\vec{A} = \rho\epsilon(n\vec{\Sigma}) \cdot (n \times \vec{A}). \tag{2.6}$$

Using coordinate (vector component) notation:

$$\delta A_\mu = \rho\epsilon(n^\nu \Sigma_\nu)(\varepsilon_{\mu\alpha\beta} n^\alpha A^\beta), \tag{2.7}$$

where: $\varepsilon_{\mu\alpha\beta}$ is the Levi-Civita symbol. Now, one can express the n and $\vec{\Sigma}$ vectors in the dual space, i.e., the space of two-forms:

$$n_\nu = \frac{1}{2}\varepsilon_{\nu\rho\sigma} n^{\rho\sigma}, \tag{2.8}$$

and

$$\Sigma_\nu = \frac{1}{2}\varepsilon_{\nu\alpha\beta}\Sigma^{\alpha\beta}. \tag{2.9}$$

Using the fact that $n^{\nu\lambda} = \downarrow n^{\lambda\nu}$, the infinitesimal change $\delta\vec{A}$ can be now written as:

$$\delta A_\mu = \frac{1}{4}\rho\epsilon(\varepsilon_{\nu\rho\sigma} n^{\rho\sigma}\frac{1}{2}\varepsilon^{\nu\alpha\beta}\Sigma_{\alpha\beta})(2n_{\gamma\mu})A^\gamma = \frac{1}{2}(\rho\epsilon n_{\alpha\beta} n_{\gamma\mu})\Sigma^{\alpha\beta}A^\gamma. \tag{2.10}$$

Using the continuous counterpart of the same equation with the help of the Riemann tensor one can write:

$$\delta A_\mu = \frac{1}{2}R^\gamma{}_{\mu\alpha\beta}\Sigma^{\alpha\beta}A_\gamma. \tag{2.11}$$

Comparing the the two equations one can recognise the discretized Riemann curvature tensor. The Ricci tensor can be then defined by index contraction:

$$R^\alpha{}_{\mu\alpha\nu} = R_{\mu\nu} = \rho\epsilon(\delta_{\mu\nu} \downarrow\ n_\mu n_\nu), \tag{2.12}$$

where we switched back to the unit vector n. And with further index contraction one can get the Ricci scalar:

$$R = R^\alpha{}_\alpha = \rho\epsilon(\delta^\alpha{}_\alpha \downarrow\ n^\alpha n_\alpha) = 2\rho\epsilon, \tag{2.13}$$

which gives a direct connection between curvature of continuous Riemannian manifolds and their discretized approximations. The above formula can be generalized to more dimensions as well as to pseudo-Riemannian manifolds.

Using Regge calculus, the Regge action S_R, i.e., the gravitational action for a piecewise-flat triangulation, can be formulated. The starting point of this is the Einstein-Hilbert action:

$$\frac{1}{16\pi G}\int d^d x\sqrt{\downarrow g}(R \downarrow\ 2\Lambda), \tag{2.14}$$

where G is the Newton's constant, R is the scalar curvature and Λ is the cosmological constant. Writing the curvature in terms of Regge calculus one gets the form:

$$\frac{1}{16\pi G}\int d^d x\sqrt{\downarrow g}R = \frac{1}{8\pi G}\int d^d x\sqrt{\downarrow g}\rho\epsilon = \kappa\sum_{n_{(d\downarrow 2)}} k_n\epsilon_n, \tag{2.15}$$

where $\kappa = (8\pi G)^{\downarrow 1}$ is the (inverse) bare gravitational constant, k_n denotes the volume of the $(d \downarrow\ 2)$-dimensional hinge, ϵ_n is the deficit angle associated with the

hinge and the summation is over $(d \downarrow 2)$-dimensional simplices, denoted by $n_{(d\downarrow 2)}$. The term including cosmological constant reads:

$$\frac{1}{16\pi G}\int d^d x\sqrt{\downarrow g}(\downarrow 2\Lambda) = \frac{\downarrow 2\Lambda}{16\pi G}\int d^d x\sqrt{\downarrow g} = \lambda\sum_{n_d} V_{n_d}, \tag{2.16}$$

where $\lambda = \downarrow \Lambda\kappa$ is the bare cosmological constant, V_{n_d} is the volume of the d-dimensional simplices building up the triangulation and the summation is over d-dimensional simplices. This leads to the full Regge action:

$$S_R = \kappa\sum_{n_{(d\downarrow 2)}} k_n\epsilon_n + \lambda\sum_{n_d} V_n, \tag{2.17}$$

which holds in any dimension. One should note that the Regge form of the gravitational action (2.17) is not expressed in terms of the metric tensor, but in terms of numbers of simplices and sub-simplices. Expressing the Regge action for a particular triangulation can lead to a complicated form, however applying certain constraints one can simplify the expressions.

2.2 Causal Dynamical Triangulations

"The more success the quantum theory has, the sillier it looks. How nonphysicists would scoff if they were able to follow the odd course of developments!" - **Albert Einstein**

Following the ideas of Weinberg and assuming the existence of an UV fixed point for gravity the properties of quantum gravity can be analyzed using non-perturbative methods. As fixed points were found in other QFT based theories, such as Quantum Chronodynamics (QCD) [24], theorists turned towards lattice formulations (e.g. Lattice Quantum Chronodynamics (LQCD)). The simplest lattice theory of GR is called Dynamical Triangulations (DT). In DT, one can use the Regge action straight away. The spacetime is constructed by gluing d-dimensional simplicial building-blocks: triangles, tetrahedra and pentachora. The triangulation does not play a role in the physics of the model, as it serves for the purpose of regularization, providing a UV cutoff related to lattice spacing a, which should be removed in the continuum limit, if it exists. A huge difference of the DT approach from other techniques based on the Regge calculus, such as Quantum Regge Calculus [25] or some versions of LQG [26], is that the edge length (a) of all the simplices is kept fixed and thus piecewise-flat manifolds are constructed from identical equilateral simplices. Transforming the metric signature with the Wick rotation one gets an Euclidean description which allows to study the (regularized) path integral of quantum gravity using statistical methods. In the DT there is no difference between space and time, however CDT twists the picture via the introduction of a foliation and thus the notion of time is restored as the causal evolution of the leafs of the foliation. The decomposition of the four-dimensional space-time into space and time is similar to that of the Arnowitt-Deser-Misner (ADM) formalism [27]. Thus, the 4-dimensional space-time is assumed to be globally hyperbolic and each $(d \downarrow 1)$-dimensional hypersurface ("leaf" of the foliation) has the same fixed topology. The word "causal" in the name of CDT refers to the time-slicing of the triangulation, as opposed to usual DT, and "dynamical" points at the difference between CDT and traditional lattice approaches, as in CDT the lattice connectivity is not fixed and it encodes the gravitational degrees of freedom. For example, in LQCD there is a fixed and regular

lattice, on which the theory is defined, but in CDT the different lattice configurations correspond to the different trajectories (histories) in the gravitational path integral. Therefore a single configuration (single trajectory) is non-physical, and one has to compute a suitable average over an ensemble of such configurations.

In a d-dimensional CDT triangulation, by construction, every (sub-)simplex lies in a d-dimensional *slab* (part of the triangulation) between lattice (discrete) time t and $t+1$. Different types of simplicial building blocks (simplices) $s_{\alpha\beta}$ can be defined through indicating the number α of their vertices in t and the number β of vertices in $t+1$. In 2 dimensions there are two types of building blocks, i.e., triangles: s_{21} and s_{12}. In 3 dimensions there are three different types of building blocks , i.e., tetrahedra: s_{22}, s_{31} and the mirror reflection s_{13}. Finally, in 4 dimensions there are 4 types of such simplices: s_{41} with its mirror-reflection s_{14} and s_{32} with its mirror-reflection s_{23}. Due to this construction and the symmetry of the action, as we will see, CDT exhibits a time reflection symmetry as well. Thanks to a small number of different categories of simplices appearing in the four-dimensional CDT and due to topological constraints of the triangulated manifolds, see Appendix B, the Regge action (2.17), which governs the dynamics of the model, can be expressed in terms of these 4-dimensional simplices and vertices in a triangulation $\mathcal{T}$ [28]:

$$S_R = \downarrow (\kappa_0 + 6\Delta)N_0 + \kappa_4(N_{41} + N_{32}) + \Delta N_{41}, \tag{2.18}$$

where $N_0 = \sum s_{10}$ is the total number of vertices, while $N_{41} = \sum(s_{41} + s_{14})$ and $N_{32} = \sum(s_{32} + s_{23})$ are the total numbers of the the various types of simplices in the triangulation $\mathcal{T}$. The three bare coupling constants are κ_0, the bare inverse Newton constant, κ_4, the bare cosmological constant, and Δ, related to the asymmetry between lengths of space-like and time-like links in the lattice. From now on we will refer to N_0, N_{41} and N_{32} as *global numbers*.

The path integral of quantum gravity is formally defined as:

$$\mathcal{Z}_{QG} = \int D[g_{\mu\nu}]e^{iS_{EH}[g_{\mu\nu}]} \rightarrow^{reg} \rightarrow \sum_{\mathcal{T}} \frac{1}{C_{\mathcal{T}}} e^{iS_R[\mathcal{T}]} = \mathcal{Z}_a, \tag{2.19}$$

where D is the measure term, which enables one to integrate over geometries, i.e., diffeomorphism invariant equivalence classes of smooth metrics $g_{\mu\nu}$, and S_{EH} is the Einstein - Hilbert action. After the lattice regularization ($\rightarrow^{reg}$) the path integral is replaced by a sum over all possible triangulations with a measure $1/C_{\mathcal{T}}$, the size of the automorphism group of $\mathcal{T}$. The index a in $\mathcal{Z}_a$ refers to the lattice regulator, which is the edge length of the simplices and S_R is the Regge action (2.18), which is the lattice-regularized version of the Einstein-Hilbert action. The distinction of space and time introduced by the foliation is also present in the edge lengths, as the time-like edge lengths a_t and the space-like edge lengths a_s are not necessarily the same, which gives rise to a degree of freedom, called the asymmetry parameter α, where $\downarrow \alpha a_t^2 = a_s^2$ in the Lorentzian setting. The aim of CDT is to define the gravitational path integral, or at least approximate it as close as it gets. All possible triangulations $\mathcal{T}$ include only such triangulations which respect the foliation structure and some additional topological constraints. To be able to treat the model with methods of statistical physics a Wick rotation has to be applied to the partition function to change the metrics from Lorentzian to Euclidean signature. Due to the imposed global foliation the "Euclideanization" of the path integral via the Wick rotation is well defined, and is related to the analytic continuation of the Regge action to negative values of

α in the lower half of the complex α plane. Performing it one turns the path integral into the partition function:

$$\mathcal{Z}_R = \sum_{\mathcal{T}} \frac{1}{C_{\mathcal{T}}} e^{\downarrow S_R[\mathcal{T}]}, \tag{2.20}$$

where, for a simpler notation, we kept the same symbol S_R for the (now) Euclidean Regge action. The Wick rotation allows for the application of statistical physics methods on the model, for example one can compute the expectation values of observables as:

$$\langle \mathcal{O} \rangle = \frac{1}{\mathcal{Z}} \sum_{\mathcal{T}} \frac{1}{C_{\mathcal{T}}} \mathcal{O} e^{\downarrow S_R[\mathcal{T}]}. \tag{2.21}$$

One of the benefits of the Wick rotation is that the model became suitable for numerical Monte Carlo (MC) simulations, where the partition function can be approximated by an ensemble of configurations generated in such simulations. The past twenty years of numerical studies of the 4-dimensional CDT model led to many interesting and important results.

2.2.1 Most important previous results of CDT

CDT was formulated in the beginning of the 21st century and became recognized by the quantum gravity community in the following years. The introduction of the foliation to the triangulation allowed for the addition of the asymmetry parameter between space and time, which was promoted to a new coupling constant Δ in the action (2.18). This particular change had a huge impact on the properties of the CDT model, compared to DT, as due to the enforced causality constraint the ensemble of triangulations present in the partition function (defined by eq. (2.20)) became significantly reduced. In the same time the third coupling constant (Δ) allowed for an extended view on the phase-diagram of simplical quantum gravity. There were only two phases in DT, one phase where a link of the generic triangulation gathered a significant number of simplices around itself, and its end vertices experienced a huge coordination number[2],comparable to the system size, thus the name "collapsed phase". The generic geometries of the other phase could be described by the, so-called, branched polymers [29], hence the name "branched polymer phase". The analogues of these phases [30] are present in CDT[3], however the topological restriction related to the foliation resulted in the appearance of two new phases [31, 32, 33]. This became apparent when new observables were used related to the newly introduced time-foliation. The number of spatial tetrahedra at a given CDT foliation leaf (with integer lattice time t) can be computed and it is, by definition, proportional to the spatial three-volume at t, which defines the, so-called, volume profile $V_3(t)$, shown in Fig. 2.1.

Apart from a "collapsed" volume profile of phase B (where all three-volume is concentrated in one spatial "slice", i.e., the 3-dimensional foliation leaf of integer t), and the heavily fluctuating volume profile of the "branched polymer" phase A (independent number of tetrahedra in each spatial slice) there are new phases where the volume profiles averaged over MC configurations follow a particular smooth function. The most interesting new phase is phase C ,where, in the case of the fixed

[2]The coordination number of a vertex is defined as the number of four-simplices which share the vertex.

[3]Phase B is the collapsed phase and phase A is the branched polymer phase

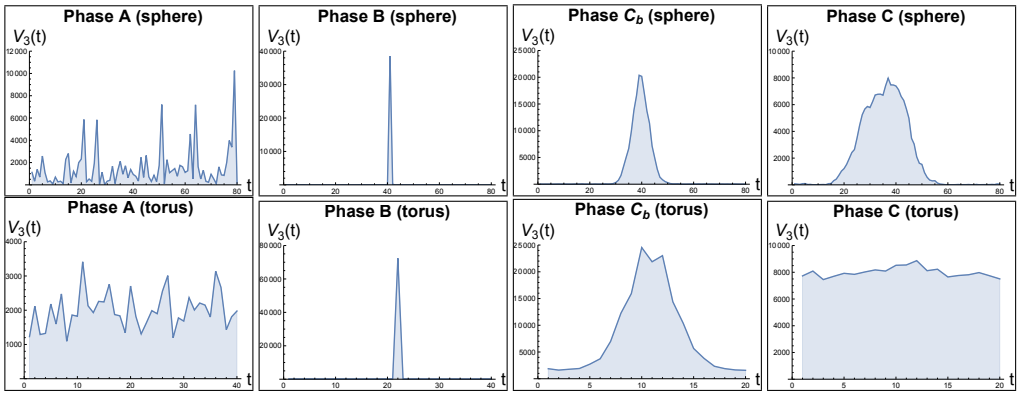

FIGURE 2.1: Spatial volume profiles of generic CDT configurations in different phases. Top: Spherical CDT: A, B, C_b, C; Bottom: Toroidal CDT: A, B, C_b, C, respectively.

spherical topology of spatial slices, the resulting average volume profile behaves as $cos^3(t)$, which corresponds to the (Euclidean) de Sitter solution of GR [34]. Therefore phase C is also called the de Sitter or the semi-classical phase and it is related to the IR limit of quantum gravity. The fourth phase, which is called the bifurcation phase (C_b), exhibits a smooth volume profile in case of large-enough fixed total volumes (lattice sizes). The volume profile in phase C_b is similar to the volume profile in phase C measured for the spherical spatial topology, however it scales in a non-canonical way when the lattice volume is increased. Furthermore, in phase C_b every second spatial slice of integer lattice time coordinate contains a vertex with macroscopically large coordination number, similar to "high-order" vertices encountered in phase B.

By analyzing fluctuations of the spatial volume it was possible to derive an effective action[35] of CDT parametrized by the spatial volume, or alternatively by the scale factor. The effective action in the de Sitter phase (C) [36] turned out to be consistent with the Hartle-Hawking minisuperspace model [37, 38, 39]. This result is non-trivial, as in the case of CDT the scale factor is obtained after "integrating out" all other geometric degrees of freedom present in the lattice, while in the minisuperspace model, where spacetime isotropy and homogeneity is put in by hand, the scale factor is the only degree of freedom. Therefore, this feature of CDT is fully emergent. One could also show that the notion of effective dimension of spacetime first measured in case of 2D CDT[40] and also in the case of Locally Causal Dynamical Triangulations (LCDT) [41] was extended to higher dimensions. In the case of 4-dim CDT in phase C it was measured to be consistent with the topological dimension four. This was not so obvious as the effective dimension measured in other phases of CDT (and earlier in DT) was different than four[42]. Both the, so-called, Hausdorff dimension [43], related to the scaling of an area and volume and the spectral dimension [44], defined by a heat kernel of the Laplace operator, were measured. Additionally, the spectral dimension was shown to exhibit a non-trivial scale dependence changing from four in large scales (comparable to the configurations size) to approximately two in short scales and also in the presence of matter fields[45] it can deviate from the classical values. The above phenomenon of "dimensional reduction" was also confirmed in many other approaches to quantum gravity (e.g., in ST [46], NCG [47], HLG [48], AS [49, 50, 51] and LQG [52]).

Most of the phase transitions present in the CDT model with spherical spatial topology were analyzed, and the $A \downarrow C$ phase transition was found to be first-order [53, 54, 30], while the $B \downarrow C_b$ and the $C \downarrow C_b$ turned out to be continuous [54, 32]. The existence of higher order (continuous) phase transitions is an important results in view of the perspective existence of the UV fixed point of quantum gravity[4], however the first study of the RG trajectories in CDT [55, 56] did not show a convincing evidence for the existence of the UV fixed point. One of the issues was that a part of the phase-diagram was out of reach due to computational difficulties, thus the analysis of some phase transitions was not possible. Also at that time the available computational power was significantly smaller than presently. With the help of modern technology much larger system sizes can be analyzed nowadays within available computational resources.

Most of the results presented above were obtained for the CDT model with fixed spherical topology of the spatial slices. As the spatial topology choice is one of the free parameters of the model, in the past few years the main focus of the 4-dimensional CDT research was on models with toroidal spatial topology. It was found that the phase-diagram is almost invariant under the change of the topology, as all observed phases were present in both cases [57]. A huge difference between the spherical and the toroidal case is visible in the volume-profile of phase C, see Fig. 2.1, and it is related to the potential term appearing in the effective action of CDT, which is different in the two cases [35]. In the spherical case the potential term can be interpreted as coming from GR and it is consistent with the minisuperspace model, which also contains such a potential term for the scale factor. However, in the case of the toroidal CDT, one does not have a classical analogue of the measured potential, thus it can be interpreted as a quantum correction. Using the spatial topology of a three-torus allowed for an introduction of many new methods of analysing the lattice-regularized quantum geometries, as it will be presented in Chapter 5. It was also possible to investigate the region of the phase-diagram which was thought to be not available in the spherical CDT, see Chapter 4.

In this thesis we will present results related to the toroidal CDT: the study of the remaining phase transitions, including critical phenomena at the phase-transition lines. Then we will also discuss how to add scalar fields to the model of CDT, and either use them as semi-classical maps defining a coordinate system on the geometry, or couple them to the geometry and analyse the effects of their back-reaction. But first, let us turn our attention to the numerical implementation of the CDT model, which is the topic of the next chapter.

[4] As explained in Chapter 4, such a fixed point should appear as a higher order transition point in CDT.

Chapter 3

Numerical Simulations

3.1 The Numerical Setup

"The student should not lose any opportunity of exercising himself in numerical calculation and particularly in the use of logarithmic tables. His power of applying mathematics to questions of practical utility is in direct proportion to the facility which he possesses in computation." - ***Augustus De Morgan***

In the case of the four-dimensional CDT there is no analytical solution, however certain numerical methods provide useful tools in the quest to find out more about the nature of the model. One of those tools is a Monte Carlo (MC) simulation [58]. In a MC simulation one attempts to numerically approximate the path integral or rather, in the Euclidean formulation, the partition function of eq. (2.20), and estimate expectation values or correlators of various observables based on a sample of independent configurations generated with a probability proportional to the Boltzmann weight: $\exp(\downarrow S)$. There are various algorithms enabling to realize this goal. In this discussion we will present the Metropolis Algorithm, as this is the one that is used in the case of four-dimensional CDT. One starts from any initial state of the model (in the CDT case any allowed triangulation with a given fixed topology[1]), and applies a set of local changes (moves) transforming state A to B. In order to ensure that the probability of generating a state converges to the required equilibrium probability $\propto \exp(\downarrow S)$, the probability of performing the move has to satisfy the detailed balance condition:

$$\mathcal{P}(A)\mathcal{W}(A \to B) = \mathcal{P}(B)\mathcal{W}(B \to A), \tag{3.1}$$

where $\mathcal{P} \propto e^{\downarrow S}$ is the probability distribution of a state and $\mathcal{W}$ is the transition probability from one state to another. Additionally, the moves have to be selected in such a way, that all possible states can be reached with a finite number of performed moves, in other words, the configuration space should be closed with respect to the selected moves. This condition provides ergodicity, which is crucial to ensure a meaningful statistics. In the Metropolis algorithm the transition probability $\mathcal{W}$ is chosen to be

$$\mathcal{W}(A \to B) = min\{1, e^{\downarrow \Delta S}\}, \tag{3.2}$$

[1] In practice one usually uses an initial configuration which is easy to be constructed "by hand".

where $\Delta S = S(B) \downarrow S(A)$ is the change of the action by the move.[2] As already mentioned, after the so-called *thermalization* period, the probability distribution of configurations generated by the Metropolis algorithm reaches an equilibrium defined by the partition function (the action S). This is the point, when one can start collecting a sample of configurations, which has to be large enough to ensure good statistics of the measured observables.

CDT is perfectly suitable for numerical simulations due to its relatively simple construction. The foliated space-times (MC states) are constructed by gluing the four-dimensional simplicial building blocks, presented in Fig. 3.1, to each other, fulfilling some global and local constraints (discussed later in detail).

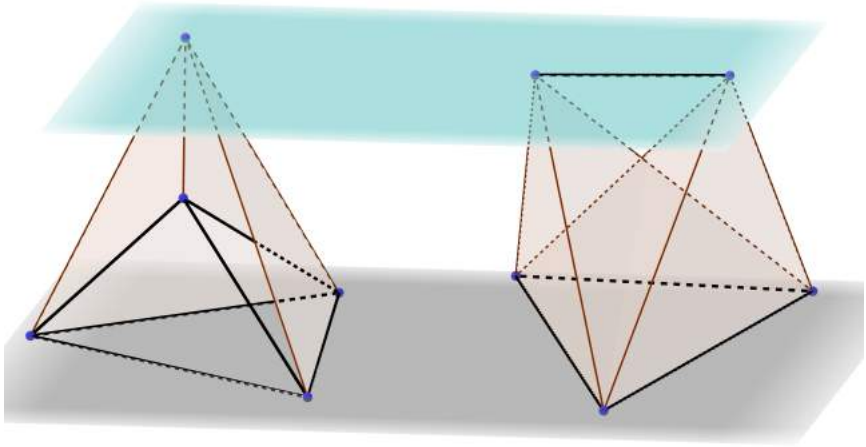

FIGURE 3.1: Two building blocks of the triangulation. The left simplex is s_{41} and the right one is s_{32}. The other two types, s_{14} and s_{23}, are mirrored-symmetric versions of them.

Due to the nature of the triangulation every simplex has exactly five neighbors, thus the local neighborhood of a hinge (i.e. a triangle in the four-dimensional CDT) can be simply discussed. The MC moves used in CDT are based on the so-called Pachner (or Alexander) moves [59], modified in such a way that, as shown later, the foliation structure with fixed topology of each spatial slice is conserved. Within our simulation code we keep track of the vertices forming the 4-simplices and adjacency relations between the simplices. This information is enough to reconstruct the whole triangulation. Nevertheless, in order to optimize and speed up the code, we also keep track of some additional information, e.g., some specific types of subsimplices or their coordination numbers.[3] When we perform a measurement we usually have to calculate observables from the actual adjacency relations or other data that we store. As Fig. 3.1 shows, the graphical representation of simplices on a 2-dimensional figure is difficult. Due to this reason, we will present the idea of the moves of 4-dimensional CDT by showing how they impact the triangulation at the $t + \frac{1}{2}$ plane. Technically the $t + \frac{1}{2}$ plane describes the connectivity structure of

[2] In the case of CDT the transition probability $\mathcal{W}$ depends also on a "geometric" factor related to the number of possible locations in a triangulation where the move and its inverse can be performed.

[3] The coordination number measures how many 4-dimensional simplices meet at a given vertex, link or triangle.

the triangulation in a *slab*, defined by all simplices between spatial slices at (integer) lattice time t and $t+1$. This treatment simplifies the discussion as it reduces the dimensionality of the problem by one, because on the $t+\frac{1}{2}$ plane a slab of the 4-dimensional triangulation is mapped to a 3-dimensional graph decorated by colors. The construction of the building-blocks of this 3- dimensional graph is analogous to the method used in [60] in the case of three-dimensional CDT. Specifically, the color or, with other words, the type of the links (solid black/grey or dashed) is important, as only links of the same type can be connected. When referring to the links of such a graph, the words "color" or "type" will be used interchangeably.

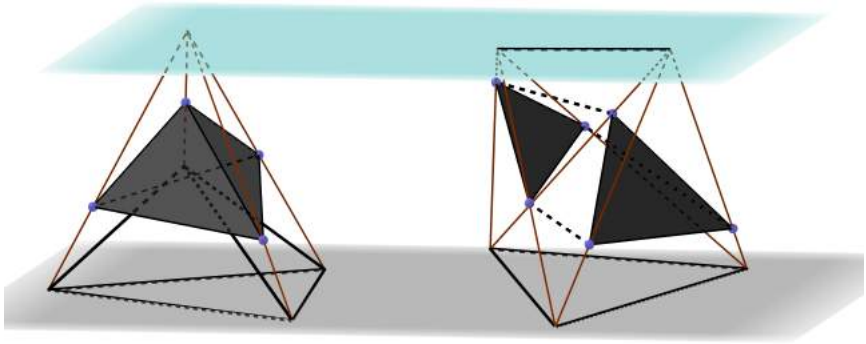

FIGURE 3.2: The figure shows the representations of s_{41} (left) and s_{32} (right) simplices in the $t+\frac{1}{2}$ plane. The simplex s_{41} is a single colored tetrahedron, s_{32} is a bi-colored prism with two triangular and three rectangular faces. The other two types of simplices s_{14} and s_{23} are mirror-reflections.

In the $t+\frac{1}{2}$ plane, instead of the 4-simplices, we now have 3-dimensional objects: tetrahedra and prisms, see Fig. 3.2. In order to distinguish between the s_{41} and the s_{14} simplices we attribute colors to the tetraedra, such that a tetrahedron belonging to the s_{41} simplex will have all black (triangular) faces, and all triangles of a tetrahedron belonging to the s_{14} simplex will be grey. Even though each 4-simplex has formally 5 neighbors, the tetrahedra have only four, which means that (for better clarity of the graphs) we omit the neighbors belonging to the previous/next slab. The prisms with black / grey triangular faces and transparent rectangular sides represent the s_{32}/s_{23} simplices, respectively. Due to the topological constraints imposed on the CDT triangulations (the fixed spatial topology must be preserved in all layers interpolating between the spatial slices at t and $t+1$) the discretized geometry of the $t+\frac{1}{2}$ layer must be also connected in a specific way, meaning that a black triangle can be glued only to a black triangle, a grey triangle to a grey triangle, and a transparent rectangle to a transparent rectangle. It reflects the fact that the s_{41} simplex can be adjacent only to s_{41} or s_{32} simplices[4], the s_{32} simplex can be adjacent only to s_{41}, s_{32} or s_{23} simplices, etc.

In order to simplify notation we will represent the black / grey tetrahedra by the black / grey dots, and the prisms by the blue / red dots, such that a blue dot

[4]Here we disregard the connections to the s_{14} simplices of the previous slab.

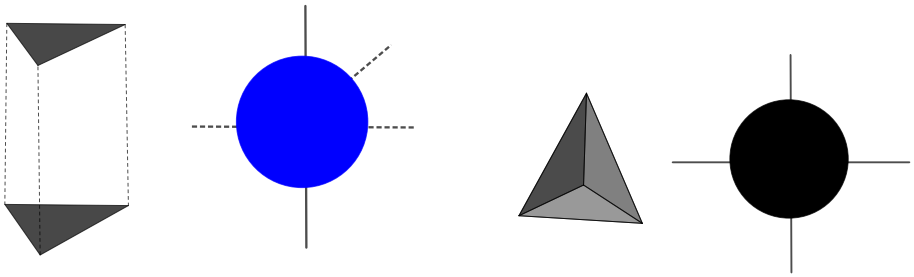

FIGURE 3.3: The figure presents the 3-dimensional elements of the $t + 1/2$ plane. The prism with triangular bases and rectangular sides (left panel) comes from a s_{32} simplex. In the graphical representation it will be a blue dot with two solid black and three dashed legs. The tetrahedron (right panel) comes from a s_{41} simplex. In the graphical representation it will be a black dot with four solid black legs (connections to neighboring slabs are omitted). Similarly, one has a red dot with two solid grey and three dashed legs, and a grey dot with four solid grey legs, coming from the mirror-reflected s_{23} and s_{14} simplices, respectively, which are not shown in the plot.

represents a prism with two black triangles (and three transparent rectangles) and a red dot is a prism with two grey triangles (and also three transparent rectangles). In the 4-dimensional context the black / grey dots will correspond to the s_{41} / s_{14} simplices in the slab, and the blue / red dots will correspond to the s_{32} / s_{23} simplices, respectively. The dots will be connected by "legs" of various type, representing the different type of connections (through colored triangles or rectangles) in the $t + \frac{1}{2}$ plane. Thus a solid black / grey leg will represent a black / grey triangle, and the dashed leg will be a transparent rectangle, see Fig. 3.3. In order to preserve the topological restrictions, only the legs of the same color / type can be connected. All possible connections between colored dots are presented in Fig 3.4 (up to mirror-reflections). As, by definition, the manifold-constraints of the original triangulation

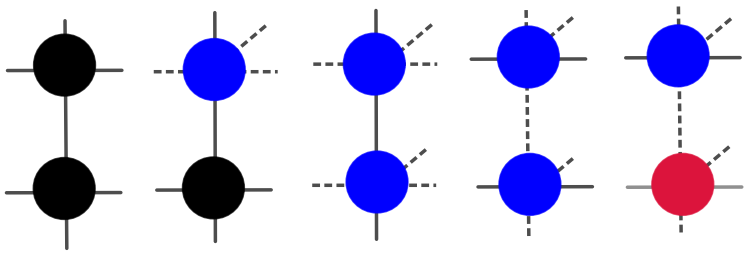

FIGURE 3.4: The figure presents possible connections between various objects of the $t + \frac{1}{2}$ plane. Black dots (tetrahedra) can be connected to each other and to blue dots (prisms) via solid black legs (triangles). Similarly, blue dots can be connected to black and blue dots via solid black legs, but they can be also connected to blue and red dots via dashed legs (rectangles). The red dots have two solid grey legs, which can be connected to other red or grey dots, which are not shown in the figure.

are not violated, and the description of the triangulation in the $t + \frac{1}{2}$ plane is still a manifold (a three-dimensional one), it is in one-to-one correspondence with the

transition tensor of the triangulation from slice t to $t+1$. An example (part of the) $t+\frac{1}{2}$ slice of a CDT triangulation and the corresponding graph with colored dots and various types of legs is presented in Fig. 3.5.

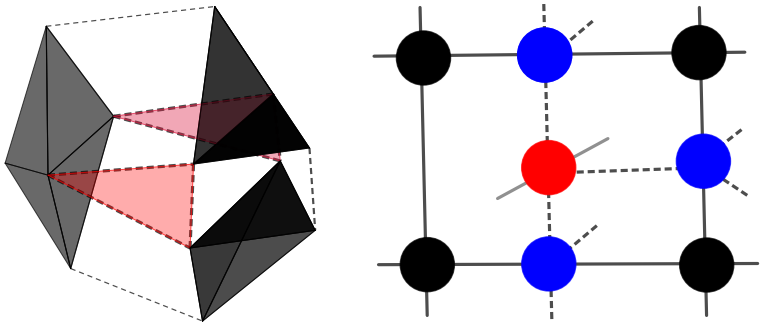

FIGURE 3.5: An example of a possible connection between four s_{41}, three s_{32} and one s_{23} simplices in the $t+\frac{1}{2}$ plane (left panel) and the corresponding graphical representation (right panel). A solid black loop in the graphical representation is a spatial link in the CDT triangulation. I deleted here a sentence with "red triangles" - you did not introduce such triangles in the description - it becomes a mess

One should note that if, in the original CDT triangulation, two s_{41} simplices are connected to the same vertex at $t+1$ then these simplices correspond necessarily to two adjacent tetrahedra in the $t+\frac{1}{2}$ plane, or in the graphical representation two black dots connected by a solid black line. The same is of course true for the mirror-reflected s_{14} simplices and thus the grey dots connected by a solid grey line. Additionally, using the graphical representation one can recognise the links of the original CDT triangulation as closed loops in the colored dot graphs. Closed solid loops are spatial links (black on slice t and grey on slice $t+1$), while closed dashed loops are time-like links of the original triangulation. Then, the coordination number of a link in the original triangulation is related to the number of dots along that loop. Another important feature of this graphical representation is, that the vertices of the original triangulation are represented as 3-dimensional objects defined by the surrounding colored dots and closed loops. As it was already mentioned, the above graphical representation contains only elements of the $t+\frac{1}{2}$ plane of a slab, therefore the true coordination number of spatial links will actually also depend on a similar graph in the adjacent slab.

As the CDT moves are local, i.e., they change only the interior of a small region in a CDT triangulation, the connection to the outside region of the triangulation is preserved, which, in the graphical representation, manifests itself by the fact that the type and number of external legs remain unchanged when the move is performed.

Now, we are ready to discuss the moves with the graphical representation defined above. In the following discussion, if only black or black-and-blue dots are shown, then recoloring black to grey and blue to red will lead to the mirror-reflected version of the move.

3.1.1 Move-2

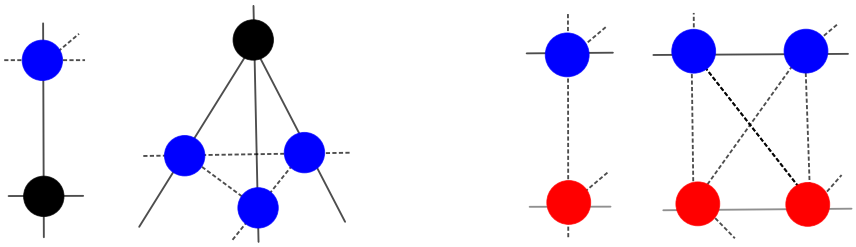

FIGURE 3.6: Move-2: version-1 (left) and version-2 (right). In the CDT triangulation it replaces a (tetrahedral) interface between 4-simplices with a link, creating additional three 4-simplices.

"Move-2" is a move that changes the interface between two (black-blue or blue-red) dots and increases the number of dots by two. It exists in two versions. Version one can be done between a black and a blue dot. The move removes two dots and replaces it by four, see Fig. 3.6. After the move, the black dot will be connected to the external leg, which was earlier connected to the blue dot, and, in the same time, all of the original black dot's external legs will become external legs of the three new blue dots. These blue dots are also connected via dashed legs. The second version of the move can be done between a blue and a red dot. The move replaces the dashed line between the original blue and red dots by four dashed lines between the blue and red dots. These new blue and red dots are connected to the external dashed legs of the original configuration.

3.1.2 Move-3

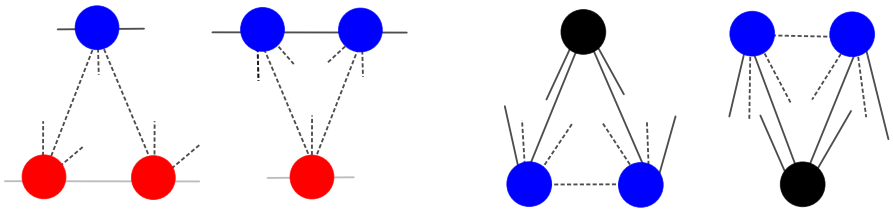

FIGURE 3.7: Move-3: version 1 (left) and version 2 (right). In the CDT triangulation it replaces the triangular interface with a dual one.

The next move is "move-3", shown in Fig. 3.7, which is an analogue of the "flip" move used in the two-dimensional CDT. It also comes in two versions. In version one it replaces one blue and two red dots with one red and two blue dots, which corresponds to replacing an s_{12} triangle with an s_{21} in the CDT triangulation. The second version removes two adjacent blue dots connected with the black dot and places them to the other side, i.e. connects them to two external legs of the original black dot. At the same time the black dot gets connected to the two external legs originally connected to blue dots. The move does not change any of the global numbers in the triangulation.

3.1.3 Move-4

The "move-4" is one of the simplest ones, and is shown in Fig. 3.8. Move-4 and its inverse are effectively a special case of a "split-merge" move. It removes a black dot and replaces it by a fully connected set of four black dots. The four dots are also connected to the external legs of the original configuration, one by one.

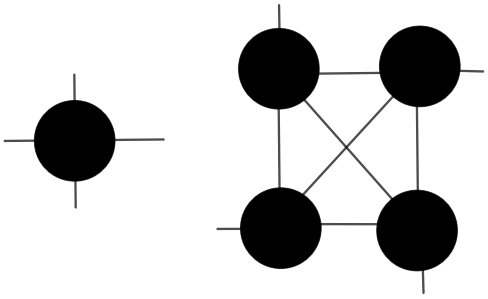

FIGURE 3.8: Move-4 replaces a black dot with four fully connected black dots, connecting each of them to the external link of the original configuration. In the CDT triangulation it adds a vertex inside an s_{41} simplex, replacing the simplex with four new s_{41} simplices.

As every solid loop in the graphical representation corresponds to a spatial link, and as it is visible in the right panel of the Fig. 3.8 there are four such solid loops, thus in the real triangulation four new spatial links are created. As all the four black dots are adjacent to each other, it can happen only if they share a vertex, thus the move creates a vertex in the original triangulation, this vertex has coordination number four.[5]

3.1.4 Move-5

The last move is "move-5", shown in Fig. 3.9.

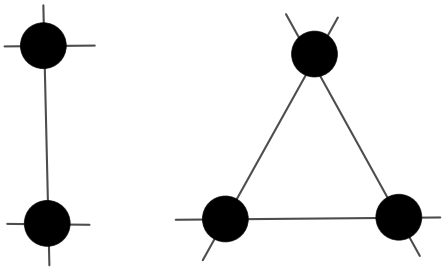

FIGURE 3.9: Move-5 replaces two adjacent black dots with three black dots. In the CDT triangulation it creates a spatial link with coordination number three. The link is signaled by a solid black loop in the graphical representation.

The move takes two adjacent black dots (tetrahedra) and replaces the triangular-interface formed by the three common vertices with a link that connects the remaining two vertices. The move creates a link with coordination number three[6], signaled by the solid black loop connecting the three black dots on the right panel in Fig. 3.9.

[5] In fact, the coordination number is eight, as there are additional s_{14} simplices in the previous slab.
[6] In fact, the coordination number is six, as there are additional s_{14} simplices in the previous slab.

The inverse move requires a link with coordination number three.

One should also note, that in the CDT code we use the full four-dimensional triangulation. In the graphical representation it could be achieved by adding a single solid external leg to each black / grey dot. This way each black (grey) dot of the $t + \frac{1}{2}$ plane would be connected to a grey (black) dot of the previous (next) slab, defined by the plane at $t + \frac{1}{2} \downarrow 1$ ($t + \frac{1}{2} + 1$). Move-4 and move-5 are the only moves which are affected by the neighboring slabs, and the connected grey / black dots of the adjacent slabs would behave exactly the same way as the black / grey dots behave in the above graphical representation description.

So far we discussed the moves which are currently used in the MC simulations of the four-dimensional CDT. In principle one could try to define some new moves, but doing so is a hard task as they must be efficient numerically and their required components (a vertex/link/triangle with a given coordination number) must be easy to be tracked during the simulations, e.g., a vertex with a given coordination number is easy to track, but it is not the case for more complex structures. In appendix A we discuss some proposals of new moves with the help of the graphical representation defined above.

Chapter 4

Empty Universes

This chapter gives a brief summary of the following articles: [1, 2, 3] which are presented as publications in the last chapter.

4.1 About criticality at phase transitions

"My memory for figures, otherwise tolerably accurate, always lets me down when I am counting beer glasses" - **Ludwig Boltzmann**

Transitions between phases can typically be described by simple models. The general idea is that one has to find some (macroscopic) properties of a given physical system that characterize the phases, and track their changes by varying the coupling constants of a given theory. For finite size systems, as the ones observed in numerical MC simulations, one cannot observe true phase transitions but only pseudo phase transitions, i.e. cross-overs, as finite size systems have finite thermodynamic potentials and also all derivatives of such potentials are finite. Anyway, one can observe that order parameters, related to some derivatives of the thermodynamic potential, become more and more singular with increasing system size (lattice volume), and by taking the volume to infinity one encounters a true phase transition. There are several phase transitions that exhibit similar behavior and can be characterized the same way, thus they will belong to the same universality class. Phase transitions belonging to the same universality class will show the same type of finite volume scaling properties. It manifests itself by universal values of scaling exponents, which can be used to measure the order of a phase transition. The notion of an order of a phase transition was introduced by Ehrenfest, who characterized phase transitions using derivatives of thermodynamic potentials (e.g. free energy, entropy, chemical potential... etc). If the n^{th} order derivative diverges at the transition point then one has an n^{th} order phase transition. This picture was refined by Landau by introducing the notion of local order parameters (OP) (in the context of the Ising model), and Ginzburg [61] improved Landau's theory by adding fluctuations to the model. Since then the classification of phase transitions shifted towards distinguishing between two types of phase transitions: first-order, which has a divergent first-order derivative of the thermodynamic potential, and higher-order (also called continuous), where the second- or higher-order derivative diverges. Furthermore, in the above classification, there is a relation between the order of a transition and the correlation length. For a first-order transition one typically has finite correlation lengths, while divergent correlation length signals a continuous phase transition.

In the lattice approach, as those discussed in the thesis, finding a phase transition where the correlation length diverges is crucial as only then can the lattice spacing be taken to zero to reach the continuum limit, while keeping the physical quantities fixed. One should also note, that recent models of solid state physics revealed, that the Landau-Ginzburg characterization can also fail, when a phase cannot be characterized by a local order parameter, but rather by long-range entanglement, called topological order [62]. If the nature itself exhibits such phenomena where the traditional description of phase transitions fails then we cannot take it for granted that such a description works for a model of quantum gravity. Nevertheless, in this chapter we will stick to the Landau approach. As we will later see, most CDT transitions falls in this category, however some of them show atypical features having relation to phase transitions involving the topology of the underlying manifold.

We will present the idea of critical exponents by taking an example of the Ising model [63]. The Ising model is one of the simplest lattice models of spin chains with nearest-neighbor interactions. In one dimension it is literally a chain of spins, in two dimensions the spins are placed in vertices of a regular lattice. The Hamiltonian of the model is:

$$\mathcal{H}_I = \downarrow J \sum_{i \leftrightarrow j} \sigma_i \sigma_j, \tag{4.1}$$

where J is a coupling constant, $\sigma_i = \pm 1$ is a spin and the sum is over nearest neighbors in the lattice. Including an external magnetic field h one may write the partition function including the magnetization ($M = \sum_i \sigma_i$) as

$$\mathcal{Z}(T,h) = \sum_{\{\sigma_i\}} e^{\downarrow \beta(\mathcal{H}_I \downarrow hM)}, \tag{4.2}$$

where $\beta = \frac{1}{k_b T}$ is the inverse temperature and the sum is over all possible spin configurations. An example order parameter is $\mathcal{M}$, the average magnetization:

$$\langle \mathcal{M} \rangle = \frac{\partial \mathcal{Z}}{\partial(\beta h)} = \frac{1}{\mathcal{Z}} \sum_{\{\sigma_i\}} M e^{\downarrow \beta(\mathcal{H}_I \downarrow hM)}. \tag{4.3}$$

The susceptibility (χ) is the first-order derivative of the magnetization:

$$\chi(T,h) = \frac{1}{V} \frac{\partial \langle \mathcal{M} \rangle}{\partial h}, \tag{4.4}$$

where V is the volume of the system. The relation which follows from this is then:

$$\frac{V\chi}{\beta} = \langle \mathcal{M}^2 \rangle \downarrow \langle \mathcal{M} \rangle^2, \tag{4.5}$$

so the susceptibility χ is related to the magnetization variance. Taking the continuum limit, i.e., the lattice spacing $a \to 0$ and the lattice size $N \to \infty$ such that the physical volume $V = a^d N$ (where d is the dimension of the system) remains constant, one can compute a two-point correlation function, where the susceptibility will depend on the spatial distance of two points in the following way

$$k_b T \chi = \frac{1}{V} \int dx \int dx' [\langle m(x) m(x') \rangle \downarrow \langle m(x) \rangle \langle m(x') \rangle] = \int dx \langle m(x) m(0) \rangle_c, \tag{4.6}$$

where $\langle m(x)m(0)\rangle_c$ denotes the connected correlator G_c, which typically decays exponentially with some characteristic correlation length ξ. In case of $|x| < \xi$ the susceptibility will behave as:

$$k_B T\chi < g\xi^d, \tag{4.7}$$

where g is a constant, yielding the correlation length divergent in case of the divergent susceptibility. The correlation function can be measured with respect to the change of the temperature yielding

$$\xi(T, H = 0) \propto |T \downarrow T_{crit}|^{\downarrow \nu}, \tag{4.8}$$

which means that the correlation length scales with the critical exponent ν as T approaches the critical temperature T_{crit}.

In the lattice MC measurements, the largest available correlation length is controlled by the lattice size N, i.e., $\xi(N) \sim V^{1/d} = aN^{1/d}$. Using equation (4.8) it follows that the (pseudo-) critical temperature, or in the general the (pseudo-) critical coupling constant, which triggers the phase transition, will show the following finite-size scaling dependence:

$$T^{crit}(N) = T^{crit}(\infty) + \text{const} \times N^{\downarrow \frac{1}{\gamma}}, \tag{4.9}$$

where $T^{crit}(\infty) = T^{crit}$ is the (true) critical temperature in the thermodynamical limit ($N \to \infty$), and $\gamma = \nu d$ is the critical scaling exponent. The above scaling relation was used in the studies presented in this chapter. One should note that for a higher-order transition one expects the scaling exponent $\gamma > 1$, while for a first-order transition one typically has $\gamma = 1$.

4.2 Order parameters and the internal structure of the configurations

"Einfach wie möglich aber nicht einfacher." / "Everything should be made as simple as possible, but not simpler. " - **Albert Einstein**

The idea behind Monte Carlo numerical simulations is quite simple. As discussed in the Chapter 3, one can generate a set of (almost) statistically independent configurations using a Markov chain of "moves" applied randomly with a proper transition probability, and then use it to estimate expectation values or correlators of observables, such as order parameters related to phase transitions. The Regge action of CDT, see eq. (2.18), contains a linear combination of the total number of vertices and simplices of various types, weighted by the bare coupling constants. When changing the couplings the (averaged) values of the above mentioned *global* numbers, and also other characteristics of the triangulations, change as well. Therefore, these observables can be used to define the order parameters of CDT.

In the four-dimensional pure gravity CDT model we have three coupling constants, thus we can use them to parametrize the phase-diagram. As we will see in this section, the numerical MC simulations used in CDT reveal four distinct regions (phases) in the CDT parameter space. In order to be able to perform the MC

simulations we fix the (average) lattice volume $\bar{N}_{41}$. The volume fixing means that, throughout the MC simulation, the observed lattice volume N_{41} will perform fluctuations around the fixed value $\bar{N}_{41}$, also restricting the values of related quantities, such as coordination numbers of various sub-simplices. It also corresponds to fixing the total spatial volume $\sum_t V_3(t) = \frac{1}{2}N_{41}$ (total number of spatial tetrahedra in slices with integer lattice time coordinate t). Using different values of $\bar{N}_{41}$ one is able to perform the finite volume scaling analysis, where the change in the order parameters (OPs) can be related to the change in the lattice size, as discussed in the previous section. This way one can track the approach to the thermodynamical limit. In order to enforce fluctuations of the lattice volume N_{41} around $\bar{N}_{41}$ it is also necessary to tune the bare cosmological coupling constant $\kappa_4 \to \kappa_4^c(\kappa_0, \Delta, \bar{N}_{41})$. This way one trades the κ_4 coupling for the $\bar{N}_{41}$ volume fixing. The fixing slices-off a two-dimensional hyper-surface $\kappa_4(\kappa_0, \Delta)$ from the full parameter space for fixed $\bar{N}_{41}$.

Already, before starting any deeper analysis, one can look at the freedom of the *global* numbers characterizing a CDT triangulation and appearing in the bare Regge action (2.18), i.e., N_0, N_{41} and N_{32}. A single triangulation (a path in the path integral) is itself physically not meaningful, however if some features of a given triangulation repeat in the ensemble of generic triangulations observed in a given phase, then in such a case it makes sense to discuss these features of a particular triangulation, as they will also appear in the expectation values (averages) of the measured observables. As all global numbers (N_0, N_{41} and N_{32}) are independent of each other[1], a configuration with a given fixed N_{41} can have small or high number of vertices or other (higher-dimensional) sub-simplices, which will result in a significantly different distribution of these numbers in different phases. One can also imagine that even if all global numbers N_0, N_{41} and N_{32} were constant, the local distribution of vertices and (sub-)simplices within a configuration can be not homogeneous. Even though every simplex has exactly 5 neighbors, every vertex has a different number of simplices connected to it, which gives rise to the possibility of non-trivial vertex coordination number distributions, where some vertices are shared by only a few simplices, but some other vertices will have a large coordination number.

The (ratios of) global numbers of a configuration are natural OPs as they are the simplest degrees of freedom in our geometric setup. Thus the first two OPs can be defined as:

$$\mathcal{O}_1 = \frac{N_0}{N_{41}} \quad , \quad \mathcal{O}_2 = \frac{N_{32}}{N_{41}}. \tag{4.10}$$

There are also some OPs which are not global in the sense that they are related to a local distribution of (sub-)simplices in a triangulation. For example, as we have a foliation, we can measure the distribution of vertices as a function of the lattice time coordinate $N_0(t)$. We can also measure similar distributions for the 4-simplices, but, as the above simplices are four-dimensional objects, instead of talking about fixed t we rather talk about the four-dimensional *slab* (part of the triangulation between t and $t+1$), and denote the number of 4-simplices in the slab by $N_{41}(t)$ and $N_{32}(t)$, respectively. For example, the (three-dimensional) volume profile, introduced in Chapter 2, is simply given by: $V_3(t) = \frac{1}{2}N_{41}(t)$. If the adjacent spatial slices contain similar number of tetrahedra, then $N_{41}(t)$ will be a flat function but if the volume

[1] Although there are theoretical lower and upper limits, which in itself features an unsolved mathematical problem.

profile has a non-trivial shape, then the difference between the adjacent slices will be larger. Therefore, one can define the third OP which quantifies this:

$$\mathcal{O}_3 = \frac{1}{N_{41}} \sum_t (N_{41}(t) \downarrow N_{41}(t+1))^2. \tag{4.11}$$

The shape function $\langle V_3(t) \rangle$ (the volume profile) could potentially be also used as an order parameter. For example, in the case of spherical CDT the $\langle V_3(t) \rangle \approx \cos^3(t)$ [64] and in the toroidal CDT it is $\langle V_3(t) \rangle = \bar{N}_{41}$ in the semi-classical phase (C), while it has a completely different shape in other phases. An example of a local OP is $\mathcal{O}_4$, defined by the highest vertex coordination number among the set of vertices:

$$\mathcal{O}_4 = \frac{1}{N_{41}} \operatorname*{argmax}_v (coord(v)), \tag{4.12}$$

where v is a set of all vertices in a triangulation. One can as well measure the distribution of this quantity in the lattice time t.

Additional OPs can also be useful. For example, one can measure the total number of $type_1$-type of simplices neighboring $type_2$-type of simplices in a triangulation, where $type$ refers to a general 4-simplex. The various types of these numbers are summarized in Table 4.1.

	s_{41}	s_{32}	s_{23}	s_{14}	sums to
s_{41}	A_1	C_1	0	E	$\to 5 \cdot N_{41}$
s_{32}	C_1	$B_{1a} + B_{1b}$	D	0	$\to 5 \cdot N_{32}$
s_{23}	0	D	$B_{2a} + B_{2b}$	C_2	$\to 5 \cdot N_{23}$
s_{14}	E	0	C_2	A_2	$\to 5 \cdot N_{14}$

TABLE 4.1: The table summarizes the numbers related to the adjacency relations of 4-simplices. All rows and columns sum up to the global numbers N_{41} or N_{32}.

The rows and columns of Table 4.1 denote the adjacent $type_1$ and $type_2$ simplices, e.g., A_1 is the total number of common faces (tetrahedra) between two s_{41} simplices in a given triangulation, while C_1 counts the total number of tetrahedra connecting the s_{41} and s_{32} simplices. The parameter B_1 (and B_2), which measures the self connectivity between the s_{32} (or respectively s_{23}) simplices, can additionally be split into two sub-categories, depending on the type of a connection between the sub-simplices.[2] Subscript a denotes the connectivity via a spatial tetrahedron (s_{31}) and subscript b via a time-like tetrahedron (s_{22}). Even though Table 4.1 contains in general 10 different additional parameters characterizing a CDT triangulation, one can show that only some of these parameters are independent, but surprisingly not all can be expressed via the *global* numbers. Taking also into account all different types of sub-simplices in a triangulation (e.g. vertices, space-like links, time-like links, spatial triangles, time-like triangles,..., etc.) the topological constraints of the CDT manifolds restrict the total number of independent parameters (including the elements of Table 4.1.) to 8. The derivation of the relations is presented in Appendix B.

During a Monte Carlo simulation, the topology of the triangulations, i.e., their Euler characteristic χ, is fixed and to perform a simulation one also fixes the coupling

[2] See discussion in Chapter 3.

constants Δ and κ_0, and tunes κ_4 to the critical value corresponding to a given lattice volume $\bar{N}_{41}$. There are then two independent global parameters that can change freely[3]: the total number of vertices N_0 and the total number of s_{32} plus s_{23} simplices N_{32}. Apart from the above mentioned global parameters, there are still three independent parameters left, one can choose, e.g., C_1, C_2 and D. Statistically $\langle C_1 \rangle \approx \langle C_2 \rangle$, therefore one can effectively increase the number of order parameters by two, defining:

$$\mathcal{O}_5 = \frac{C_1 + C_2}{N_{41}} = \frac{C}{N_{41}}, \tag{4.13}$$

and

$$\mathcal{O}_6 = \frac{D}{N_{41}}. \tag{4.14}$$

In next section we will show how to use the OPs to analyze the phase-diagram of the CDT model.

4.3 Phase transitions

"God does not play dice with the Universe!" - **Albert Einstein**

Albert Einstein once criticized quantum mechanics and he said: "God does not play dice with the Universe!", maybe Gods don't but we do within our numerical simulations. As it was discussed in Chapters 2 and 3, CDT aims to study the lattice regularized path integral of quantum gravity using numerical MC methods. In the simplest case one deals with triangulated empty "universes", i.e., pure gravity models, without additional matter fields. The properties of CDT emerge as a result of interplay between the bare Regge action:

$$S_R = \downarrow (\kappa_0 + 6\Delta)N_0 + \kappa_4(N_{41} + N_{32}) + \Delta N_{41}, \tag{4.15}$$

and the entropy of states, i.e., the number of triangulations with the same value of the bare action in the partition function (2.20). Due to this entropic nature there are several phases which can be visualized in the two-dimensional parameter space[4] (κ_0, Δ). As we have a two-dimensional coupling-constant space (κ_0, Δ), sometimes we will refer to the coupling constants as coordinates in the phase-diagram. The four phases of CDT are presented in Fig. 4.1.

Even though the CDT model is simple in its construction, the resulting complexity arises in the variety of possible configurations. For very large (inverse) bare gravitational coupling κ_0 one recovers phase A, which is characterised by a vanishing kinetic term in the effective action of CDT, parametrized by the spatial volume $V_3(t)$ (or alternatively by the scale factor) [36]. The internal dynamics between the simplices results in an emerging geometry with a branched-polymer structure. For low enough asymmetry parameter Δ phase B can be observed. It is characterized by the vanishing time-extent of the generic geometric configurations. All spatial tetrahedra (3$\downarrow$ volume) gather in one spatial slice, and each of the two adjacent slices features

[3] Strictly speaking, N_{41} also changes as it fluctuates around the fixed $\bar{N}_{41}$.

[4] As explained above, the third coupling constant κ_4 is tuned to $\kappa_4^c(\kappa_0, \Delta, \bar{N}_{41})$ corresponding to the fixed lattice volume $\bar{N}_{41}$ of a MC simulation.

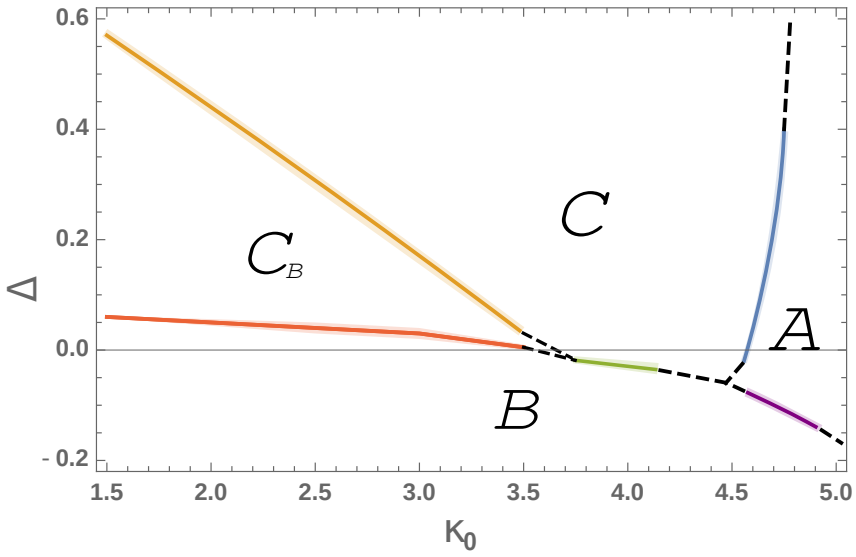

FIGURE 4.1: The phase-diagram of CDT, which shows four different phases: A (branched polymer), B (collapsed), C (de Sitter) and C_b (bifurcation).

a vertex with an almost full connectivity to the 4-simplices containing these tetrahedra. The occurrence of this phase is understandable in the context of the, so-called, balls-in-boxes model [65, 66]. The most interesting region of the phase-diagram is phase C, also called the de Sitter[5] [34] or the semi-classical phase, which can be mostly observed for positive Δ and medium range of κ_0. In the case of toroidal CDT, the spatial volume profile $V_3(t)$ of generic phase C triangulations is constant while in the case of the spherical CDT a de Sitter-like blob with the shape $V_3(t) \approx cos^3(t)$ forms. Last but not least, the remaining phase is the, so-called, bifurcation phase or shortly phase C_b. The phase is characterized by the appearance of vertices of high coordination number in every second spatial slice and the formation of a blob (different from that of phase C) in the volume profile both in the spherical and the toroidal CDT. As the de Sitter phase is physically the most interesting one, the phase transitions surrounding this region were studied the most, especially as the perspective UV fixed point of quantum gravity should lie at the border of this region. It was found, that the lattice spacing decreases with increasing κ_0 and slightly decreases with decreasing Δ [67], thus the part of the phase-diagram nearby the $C \downarrow B$ phase transition is of great interest, as the two "triple" points where the phase transition lines meet, are natural candidates to be the UVFP of the theory. Due to this it is very important to analyze the scaling exponents related to the phase transitions around the triple points. This is the reason why in this section we will present results related to the three phase transitions: $A \downarrow B$, $C \downarrow B$ and $C_b \downarrow B$. If any of them turns out to be higher-order then it will support a possibility of existence of the UVFP. However it is also known, that first-order phase transition lines may end at a higher-order point (e.g., in the phase diagram of water).

[5] Technically the name "de Sitter" should be used only for the spherical CDT case, as the toroidal CDT volume profile is constant and does not resemble any de Sitter-like solution.

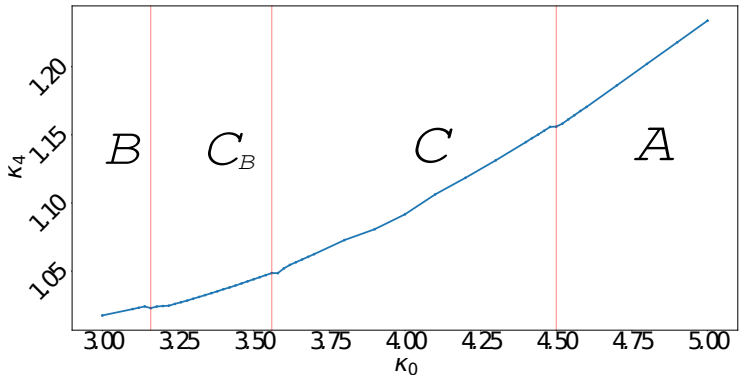

FIGURE 4.2: Values of κ_4 in the function of κ_0. Slight discontinuities in the function $\kappa_4(\kappa_0)$ signal the phase transitions, which is related to the change in entropy of the configurations on the two sides of the phase transitions. Between the vertical lines the corresponding phases are shown.

The typical way to find a phase transition is to fix one coupling constant, which will be either κ_0 or Δ in the case of 4-dimensional CDT, and then start a set of MC simulations for various values of the other coupling constant. To show the behavior of the order parameters, defined in Section, 4.2., we present Fig. 4.3 and Fig. 4.4, where the OPs were measured in CDT with toroidal spatial topology for fixed $\Delta = 0.02$, total lattice volume $\bar{N}_{41} = 160k$ and length of the (periodic) lattice time coordinate (number of spatial slices) $T = 4$. One of the parameters that strongly depend on the volume is the bare cosmological coupling constant, that have to be tuned for each $\bar{N}_{41}$, however its value also depends on the selected average volume. $\kappa_4(\kappa_0, \Delta)$ is a function of the other coupling constants, thus fixing one of it one may find how it changes in the function of the other (see Fig. 4.2).

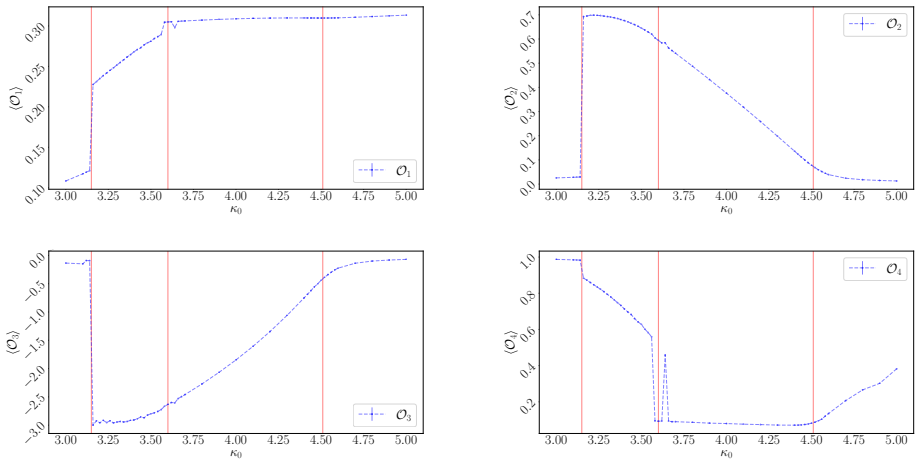

FIGURE 4.3: Example of the measured OPs from $\mathcal{O}_1$ (top left) to $\mathcal{O}4$ (bottom rigt). The most left region on the plots is phase B (collapsed), next to it is phase C_b (bifurcation), then phase C (de Sitter) and next to it phase A (branched polymer).

Red vertical lines visible in figures Fig. 4.2 - 4.3 show locations where behavior of (at least some) OPs changes, thus they signal the phase transitions. In Fig.

4.2 between the vertical red lines each corresponding phase is written. The slight discontinuities in the function $\kappa_4(\kappa_0, \Delta = fix)$ signal the locations of the phase transitions, which originates from the different entropy on the two sides.

Not every OP signals all of the phase transitions, but using different OPs one can find them. For example, $\mathcal{O}_1$, $\mathcal{O}_2$ and $\mathcal{O}_3$ distinguish seemingly three different regions, while $\mathcal{O}_4$ seems to be sensitive to all four phases. The behavior of the two new OPs, $\mathcal{O}_5$ and $\mathcal{O}_6$, is similar to $\mathcal{O}_2$, however their crossing point additionally signals the $C_b \downarrow C$ phase-transition, as presented in Fig. 4.4. This becomes apparent when one looks at the susceptibility of $(\mathcal{O}_6 \downarrow \mathcal{O}_5)$, as shown in Fig. 4.5. In the figure we plot the susceptibility $\chi(\mathcal{O}_6 \downarrow \mathcal{O}_5)$, i.e., the variance of $(\mathcal{O}_6 \downarrow \mathcal{O}_5)$, normalized by its expectation value $\langle \mathcal{O}_6 \downarrow \mathcal{O}_5 \rangle$, which shows a clear peak at the $C_b \downarrow C$ transition point. Fig. 4.4 shows the two new OPs, and their difference, which is close to zero

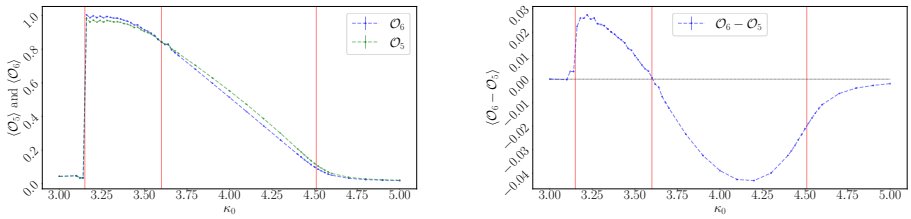

FIGURE 4.4: The new OPs $\mathcal{O}_5$ and $\mathcal{O}_6$ are shown in the left plot. Their behavior is similar to $\mathcal{O}_2$, but the crossing point additionally signals the $C_b \downarrow C$ phase-transition. The difference $\mathcal{O}_6 \downarrow \mathcal{O}_5$ is presented in the right plot, where the dashed horizontal line is at value zero.

in phase A and B, positive in phase C_b and negative in phase C, and thus is useful in recognizing all four phases of CDT. The above observations show, that it is not enough to look at one OP but rather a set of OPs should be used while analyzing phase transitions.

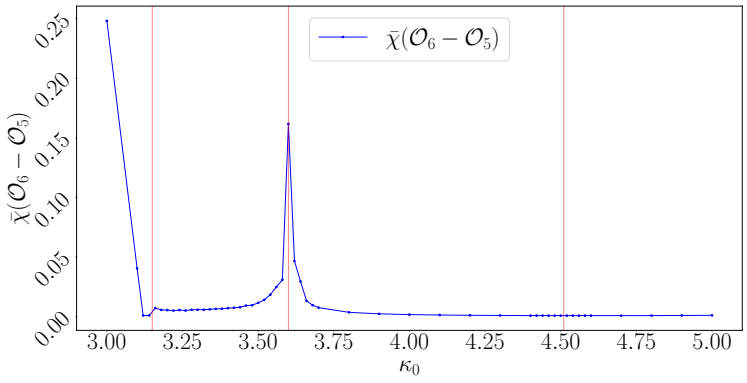

FIGURE 4.5: The figure shows the (normalized) susceptibility $\bar{\chi}(\mathcal{O}_6 \downarrow \mathcal{O}_5)/\langle \mathcal{O}_6 \downarrow \mathcal{O}_5 \rangle$. The peak of the susceptibility, i.e., the variance of $(\mathcal{O}_6 \downarrow \mathcal{O}_5)$, at the $C_b \downarrow C$ transition is a clear signal of the phase transition.

Similar plots can be drawn if one measures the OPs in the function of the coupling constant Δ for fixed κ_0, or even when choosing both (κ_0, Δ) values on some straight but not vertical nor horizontal line in the CDT phase-diagram.

4.3.1 Finite volume scaling analysis

Even though, as explained in Section 4.2., CDT phase transition signals observed for any fixed lattice volume $\bar{N}_{41}$ are not real phase transitions, as for any finite volume the free energy is finite and formally one just observes a cross-over, nevertheless using finite-size scaling analysis one can investigate the (real) phase transitions and draw conclusions about critical exponents in the thermodynamical limit. By extrapolating the scaling relations to $\bar{N}_{41} \to \infty$ one can as well find the (infinite volume) critical values of the coupling constants κ_0^∞ and Δ^∞ and of the order parameters OP^∞. Thus a typical finite-size scaling relation of a coupling $\mathcal{C}$ corresponding to the transition point will be described by a function

$$\mathcal{C}^{crit}(\bar{N}_{41}) = \mathcal{C}^\infty \downarrow \alpha \bar{N}_{41}^{\downarrow \frac{1}{\gamma}}, \tag{4.16}$$

where γ is the critical exponent, whose value may be used to distinguish between the first-order ($\gamma = 1$) and the higher-order ($\gamma > 1$) phase transition.

At the thermodynamical limit of the higher-order phase transition one can perspectively find an UVFP, however doing so in lattice simulations is not an easy task as it was shown in [55, 56]. Previous findings did not give a convincing evidence for the existence of the UVFP of CDT, however since these measurements there were many improvements both in the CDT code (making the MC simulations more efficient) and computer technology. Therefore now, using the new possibilities, one can try to re-investigate this issue in more detail.

4.3.2 $A \downarrow B$ phase-transition

This subsection is based on the publication [3].

Since the appearance of the path integral formalism of Feynman, we know that not only those paths should be taken into account which can be imagined classically but also non-classical ones too. In the formalism, for example, a point particle takes all possible paths when travelling from point A to B including also classically forbidden paths, when it tunnels through potential walls or simply goes outside of the light-cone. The contribution of most such paths however cancels out and the classical trajectory can be computed as an average of all paths. A generic triangulation of phase B is characterized by the following pattern: there is a vertex with almost maximal coordination number in a spatial slice with time coordinate $t \downarrow 1$, almost all spatial tetrahedra (3-volume) is gathered in slice t and again there is a vertex with almost maximal coordination number in slice $t + 1$. All spatial slices with the time coordinate different than t have spatial volume close to the minimal allowed cutoff. As the configurations of phase A are characteristically different, i.e., they can be characterized by branched-polymers, there is a difference in entropy of the configurations between the two phases, which results in a phase-transition between them.

The fist-order nature of the A-B transition is obvious when one looks at the finite-size scaling of the critical coupling Δ^{crit} in the function of the lattice volume $\bar{N}_{41}$ presented in Fig. 4.6. Using eq. (4.16) one can fit the critical exponent γ. The best fits resulted with critical exponent values $\gamma_{4.5} = 1.151 \pm 0.379$, $\gamma_{4.6} = 1.029 \pm 0.178$ and $\gamma_{4.8} = 1.088 \pm 0.101$ for three independent series of measurements with fixed $\kappa_0 = 4.5, 4.6$ and 4.8, respectively. All three scaling exponents are in agreement with

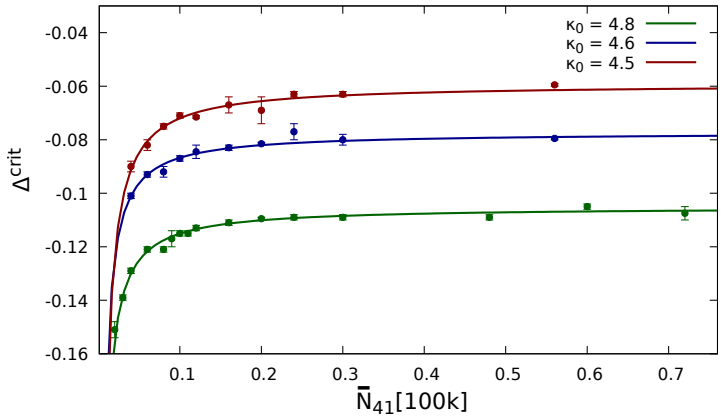

FIGURE 4.6: (Pseudo-) critical values of $\Delta^{crit}(\bar{N}_{41})$ measured for $\kappa_0 = 4.8$ (green), $\kappa_0 = 4.6$ (blue), and $\kappa_0 = 4.5$ (red) together with the fits of eq. (4.16). The solid curves were fitted with the critical exponent fixed to $\gamma = 1$ for all three data sets.

$\gamma = 1$ characteristic for the first-order transition. The same conclusion can be drawn if one looks at finite size scaling of $\mathcal{O}_2$. The fits of such scaling relations are presented in Fig. 4.7. The value of $\mathcal{O}_2$ is very small in both phases. In the infinite volume limit it approaches zero in phase B and for higher κ_0 also in phase A.

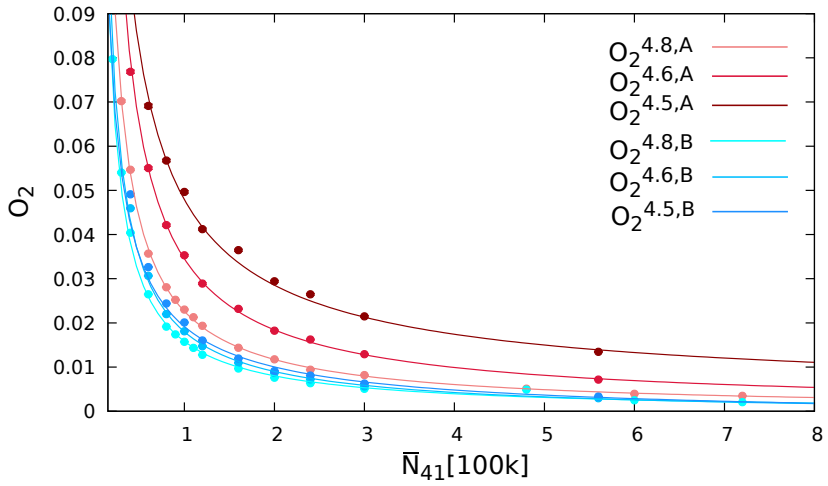

FIGURE 4.7: The running of $\mathcal{O}_2$ for $\kappa_0 = 4.8$, $\kappa_0 = 4.6$ and $\kappa_0 = 4.5$. Blue colors correspond to data measured in phase B and red in phase A closest to the phase transition point, and the darker the color the lower the corresponding κ_0 coupling, i.e., the closer to the $A\downarrow$ $B\downarrow$ C triple point. The error bars are smaller than the size of the data-points. The solid curves correspond to the fits of a relation similar to eq. (4.16) with the critical exponent fixed to be $\gamma = 1$ for all data sets.

The conclusion is that phases A and B are thought to be non-physical in the sense of an emergent semi-classical geometry. It is well explained by the fact of the decreasing connectivity between two adjacent spatial geometries, represented by the vanishing $\mathcal{O}_2$ parameter, although this phenomenon may be possibly related to the, so-called, "asymptotic silence" [68].

4.3.3 $C_b \downarrow B$ phase-transition

This subsection is based on the publication [1].

The B and C_b phases are not that different from each other, as in both phases there are vertices which connect to almost every tetrahedron on the adjacent spatial slices, and such high connectivity structure makes these phases to be effectively infinite-dimensional. Both spectral and Hausdorff dimensions differ from the topological value 4, thus these phases do not describe a four-dimensional Universe. Even though their seemingly non-physical nature the phase transition becomes important to be studied as its endpoint leads to a candidate of the UVFP of the theory, to the $B \downarrow C \downarrow C_b$ triple-point.

The volume profile of the bifurcation phase is presented in Fig. 4.8. It looks the same in the spherical and the toroidal version of CDT.

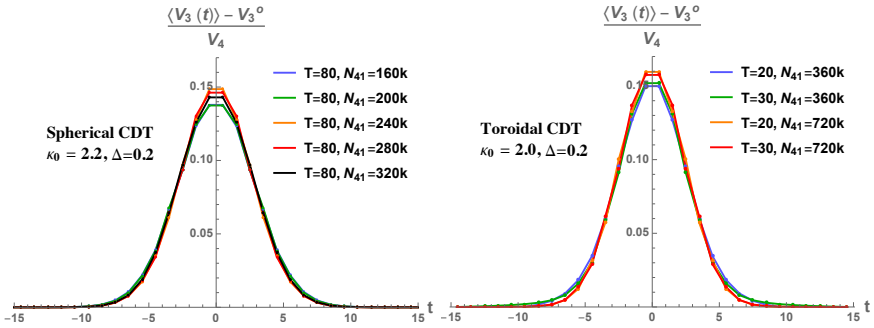

FIGURE 4.8: The (re-scaled) average spatial volume profiles $\langle V_3(t) \rangle$ observed in the bifurcation phase C_b in the spherical (left plot) and the toroidal (right plot) CDT. In both plots the spatial volume profiles were presented with respect to the centre of volume, set at $t = 0$, and shifted by a (constant V_3^0) volume measured in the *stalk* range ($|t| >\sim 10$), V_3^0 being different for each volume profile (in general V_3^0 is bigger in the toroidal CDT where discretization effects are larger). Data measured for various total $\bar{N}_{41}$ lattice volumes and different T were rescaled by $V_4 = \sum_t (\langle V_3(t) \rangle \downarrow V_3^0)$, i.e., in agreement with the Hausdorff dimension $d_H = \infty$.

The $C_b \downarrow B$ transition was analyzed for fixed $\kappa_0 = 2.0$. Starting in phase C_b and decreasing Δ close to $\Delta^{crit} \approx 0$ one finds the transition to phase B. The main difference between the two phases is the time extent of phase C_b, where the volume profile $V_3(t)$ resembles that of the spherical CDT in phase C, while in phase B it is mostly collapsed to a single spatial slice. Although, as already mentioned, there are also many similarities between the two phases, for example, the Hausdorff dimension of generic geometries is very large or even infinite in the large volume limit. Probably due to these similarities the $C_b \downarrow B$ phase transition was found to be the higher-order transition. Not only the fits to the finite size scaling relation of eq. (4.16) yielded a solution which was in disagreement with $\gamma = 1$ (as shown in Fig. 4.9) but also the order parameters showed a smooth transition between the two phases. Furthermore, the Binder cumulants tend to vanish with increasing lattice volume, which is also characteristic for a higher-order transition [69].

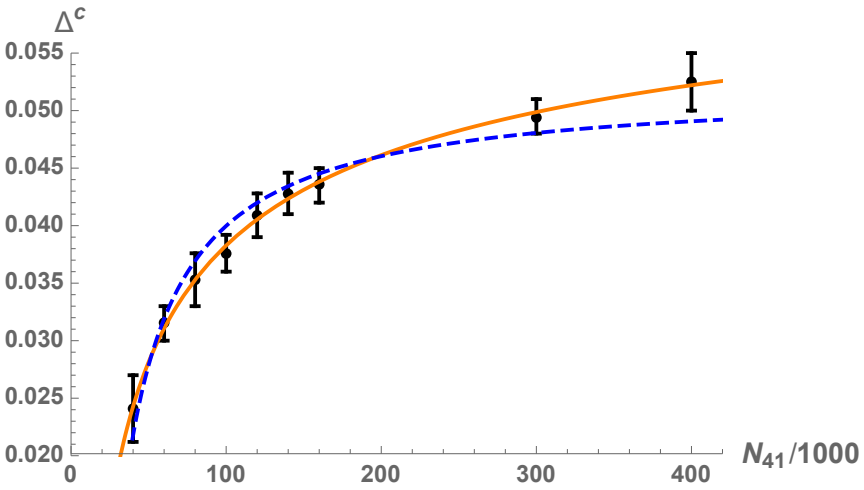

FIGURE 4.9: Lattice volume dependence of the pseudo-critical $\Delta^c(N_{41})$ values in CDT with toroidal spatial topology measured for fixed $\kappa_0 = 2.2$ together with the fit of the finite-size scaling relation (4.16) with critical exponent $\gamma = 2.51 \pm 0.03$ (orange solid line) and the same fit with a forced value of $\gamma = 1$ (blue dashed line).

Summing up, in publication [1], the $C_b \downarrow B$ transition was shown to be a higher-order phase transition in CDT with the toroidal spatial topology. This is an important result in quest for the UVFP of CDT. Due to the strong hysteresis observed in the toroidal CDT, the $C_b \downarrow C$ transition bordering the semi-classical phase was classified to be a first order transition [57].[6] The finding that the $C_b \downarrow B$ transition is higher-order provides a hope that its endpoint (i.e., the $B \downarrow C \downarrow C_b$ triple point) is also higher-order, yielding it a possible candidate for the UVFP of the theory.

4.3.4 $C \downarrow B$ phase-transition

This subsection is based on the publications [2] and [3].

Fixing the value of κ_0 in range [3.5 : 4.5] and changing Δ one can cross the $C \downarrow B$ phase transition. In the case of toroidal spatial topology the volume profile $V_3(t)$ of phase C is almost constant, and thus invariant under the translation in time, but crossing to phase B this symmetry of the generic configurations is broken to a "collapsed" volume profile. Phase C is also characterized by quite homogeneous and isotropic geometry in sufficiently large scales, but as one traverses to phase B one can immediately observe that vertices with very high coordination number appear, which breaks the above homogeneity and isotropy. As a result one observes a strong hysteresis around the phase transition line, as presented in Fig. 4.10.

In order to encounter the $C \downarrow B$ transition, instead of fixing κ_0 in range [3.5 : 4.5] and changing Δ, one can as well fix Δ in range [$\downarrow$ 0.04 : 0.00] and change κ_0. Therefore, the phase transition study, including the finite-volume scaling analysis, was performed for two different fixed κ_0 values ($\kappa_0 = 4.0$ and 4.2) and for two different fixed Δ values ($\Delta = 0$ and $\downarrow$ 0.02). The transition was determined to be the first-order phase transition, but a rather atypical one. Although the values of order parameters

[6] In contrast to this, in the spherical CDT model the $C_b \downarrow C$ transition was shown to be a higher order transition [32].

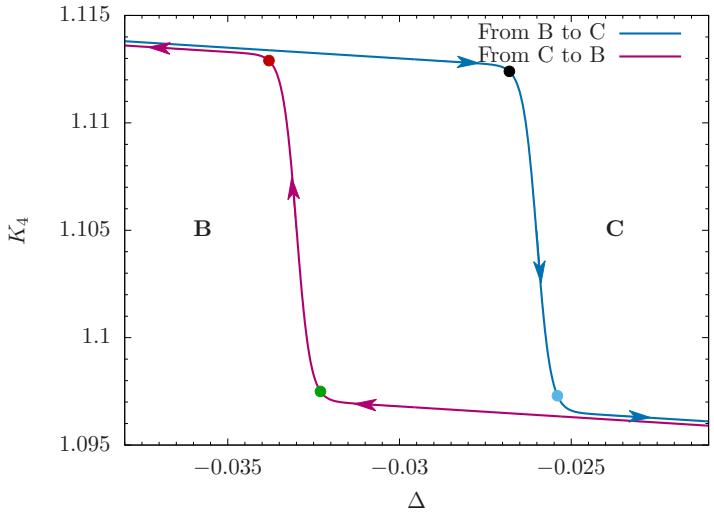

FIGURE 4.10: The plot illustrates the hysteresis measured during simulations for the lattice volume $\bar{N}_{41} = 160$k. The green and blue dots correspond to the location of the phase C side of the phase-transition, while the red and black dots correspond to the location of the phase B side of the phase-transition.

measured at both sides of the hysteresis region do not converge to a common value, which itself signals a first order transition, the size of the hysteresis region shrinks when the lattice volume $\bar{N}_{41}$ is increased, which can signal a higher-order transition in the thermodynamical limit. In order to resolve this inconsistency, in publication [2] we measured the critical exponent resulting from the scaling relation of eq. (4.16), which turned out to be $\gamma = 1.62 \pm 0.25$, suggesting a higher-order transition. Nevertheless, in publication [3] we repeated the finite-size scaling analysis using much bigger data statistics and also additional locations in the phase-diagram. We also used a slightly modified finite-size scaling relation in the form:

$$C^{crit}(\bar{N}_{41}) = C^{\infty} \downarrow \alpha(\bar{N}_{41} \downarrow c)^{\downarrow \frac{1}{\gamma}}, \tag{4.17}$$

where c is a discretization correction. We found that the critical exponents are consistent with $\gamma = 1$, see Fig. 4.11, which signals the first-order transition. We therefore concluded that the $C \downarrow B$ phase transition is a first-order transition in the case of toroidal CDT.

4.3.5 Summary

The three phase transitions discussed in this chapter were the $A \downarrow B$, $C \downarrow B$ and the $C_b \downarrow B$ transitions, out of which only the last one turned out to be a higher-order (continuous) phase transition in CDT with the toroidal spatial topology. The $A \downarrow B$ and $C \downarrow B$ phase transitions were not yet analyzed in case of the spherical CDT. What is more, the existence of the direct $C \downarrow B$ transition was not even known before the article [57] was published. The reason was that the region of the phase-diagram analyzed in detail in this thesis was at that time thought to be unreachable via MC simulations. In theory, the phase-diagram of the CDT model does not have to be the same for different spatial topologies, thus a future analysis may potentially find that the $C \downarrow B$ transition is continuous in the spherical CDT. An argument for this phase transition being continuous in the spherical CDT is related to the *effective* topology of

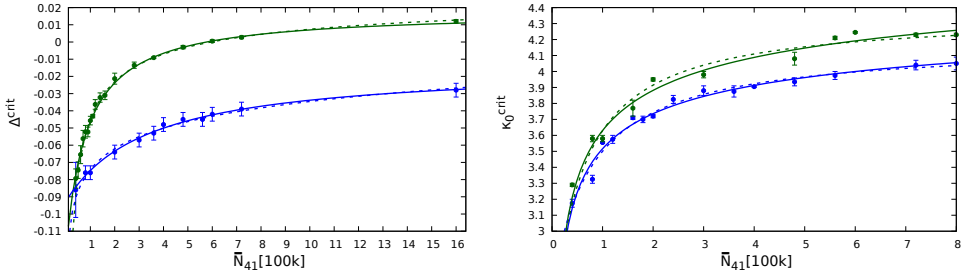

FIGURE 4.11: Finite-volume scaling of the coupling constants Δ^{crit} (left panel) and κ_0^{crit} (right panel) in the $C \downarrow B$ transition. The dashed and solid curves represent fits to eq. (4.16) and eq. (4.17), respectively. In the left panel (vertical measurements), green data-points are for fixed $\kappa_0 = 4.0$ and blue are for $\kappa_0 = 4.2$. In the right panel (horizontal measurements), green data-points are for fixed $\Delta = \downarrow 0.02$ and blue are for $\Delta = 0$.

the phases. In the case when the topology of the spatial slices is chosen to be S^3 and the time direction is compactified to S^1, which is the case in the MC simulations, the full topology of the triangulations is $S^3 \times S^1$. However, in the semi-classical phase C, the emergent (Eucledean) de Sitter-like geometry, i.e., the four-sphere, transforms the *effective* topology to S^4. To clarify the notion of the *effective* topology, let us explain that, by definition, the imposed $S^3 \times S^1$ topology of the triangulations is not changed in the MC simulations, thus the two furthest (time-like) points (poles) of the four- sphere are connected by a thin *stalk* of cutoff size, which can be treated as a lattice artifact. The *stalk* is necessary to preserve the imposed topological conditions numerically, but if only it was allowed by the MC algorithm it would completely disappear, yielding the change of topology from $S^3 \times S^1$ to S^4. It illustrates the fact that not only the space-time effective dimensionality but also the effective topology are emergent concepts on the quantum level. Thus our conjecture, formulated in [3], is the following:

phase transitions which involve a change in effective topology will be first-order transitions.

The argument is that if there are two adjacent phases separated by a phase transition, and these phases have different genera then the phase transition cannot happen smoothly resulting in the first-order transition.

In the case of CDT with toroidal spatial slices, the phase C_b has, similarly to phase C in the spherical CDT case, an effective topology S^4. At the same time, the semi-classical phase C has the toroidal effective topology T^4. As a result of the phase transition the effective topology changes, yielding the $C \downarrow B$ transition first-order. Contrary to that, as explained above, in CDT with spherical spatial slices the effective topology of the semi-classical phase is S^4, so it does not change under the phase transition, potentially making the $C \downarrow B$ transition higher-order.

So far all analysis was done in the case of empty Universes (pure gravity models). In the next chapter we will discuss how the CDT model changes in the presence of matter fields.

Chapter 5

Universes with matter fields

This chapter gives a brief summary of the following articles: [4, 5, 6].

5.1 Scalar fields as coordinates

"If people do not believe that mathematics is simple, it is only because they do not realize how complicated life is." - **Neumann János**

This section is based on the publications [4, 5].

Life (the actual physical phenomenon) is indeed complicated, much more complicated than any model designed in order to describe it. However, usually simple models are the only ones that can be solved. Also in most physical theories vacuum solutions are the simplest, easiest and first ones to be found. The same is true in GR as most of known solutions of Einstein's field equations are vacuum solutions. It is also the case of CDT, where the first twenty years of studies were dominated by pure gravity models (empty Universes) discussed above. As it was mentioned in Chapters 2 and 3, CDT is formulated in a coordinate-free way, except from the time direction where one has a natural global proper-time coordinate t, consistent with the introduced foliation. It would be therefore beneficial to introduce some notion of coordinates, making contact with other gravitational research.

The simplest extension of the CDT model is the addition of massless scalar fields. As will be shown, such scalar fields can also play role of "clocks" and "rods", enabling one to define a coordinate system in the triangulated manifold, being an analogue of the harmonic (de Donder) gauge fixing in GR. As we will discuss below, in order to apply this method of defining coordinates in CDT one also has to make a proper choice of the target space of the scalar fields. As an example, take a (smooth) Riemannian manifold $\mathcal{M}$ equipped with a metric tensor $g_{\mu\nu}$ and another Riemannian manifold $\mathcal{N}$ with a trivial flat metric $h_{\alpha\beta}$. A harmonic map $\mathcal{M} \to \mathcal{N}$ can be defined with the help of a four-component scalar field ϕ^α, with $\alpha = 1, 2, 3, 4$. In case of our setup, if $\mathcal{M}$ has a topology of the four-torus T^4, then we also choose $\mathcal{N}$ to have the same toroidal topology, and each component $\phi^\alpha(x)$ is a map $\mathcal{M} \to S^1$, which minimizes the action

$$S_M[\phi] = \frac{1}{2} \int \mathrm{d}^4x \sqrt{g(x)}\, g^{\mu\nu}(x)\, h_{\alpha\beta}(\phi^\gamma(x))\, \partial_\mu \phi^\alpha(x) \partial_\nu \phi^\beta(x). \tag{5.1}$$

Due to our choice of the trivial metric $h_{\alpha\beta}$ on $\mathcal{N}$, the four-component scalar field can be decomposed into four independent components, later denoted ϕ^x, ϕ^y, ϕ^z, and ϕ^t. Due to this, it is enough to discuss the case of a single component (let's call it ϕ). The Euler-Lagrange equations for the field resulting from eq. (5.1) give rise to the Laplace equation:

$$\Delta_x \phi(x) = 0, \quad \Delta_x = \frac{1}{\sqrt{g(x)}} \frac{\partial}{\partial x^\mu} \left(\sqrt{g(x)}\, g^{\mu\nu}(x) \right) \frac{\partial}{\partial x^\nu}, \quad \phi(x) \in S^1. \tag{5.2}$$

In the case when $\mathcal{M}$ is closed, if we chose the target space of the scalar field ϕ to be $\mathbb{R}$ then the constant zero-mode of the Laplacian would be the only solution to the equation $\Delta_x \phi(x) = 0$. If instead, as we do, one chooses a nontrivial target space of the field to be S^1 (with circumference δ) then one can obtain a nontrivial solution for the scalar field. Technically, the condition $\phi(x) \in S^1$ can be obtained by considering a scalar field with the target space $\mathbb{R}$ and identifying

$$\phi(x) \equiv \phi(x) + n\,\delta, \quad n \in \mathbb{Z}. \tag{5.3}$$

The situation of interest is when we have the toroidal manifold $\mathcal{M}$ which can be thought of as an elementary cell periodically repeating in all four directions. In such a case one can define four non-equivalent boundaries of the elementary cell, i.e. 3-dimensional connected hypersurfaces $H(\alpha), \alpha = \{x, y, z, t\}$. Let us consider the case when each component of the field $\phi^\alpha \in S^1$ winds around the circle once as we go around any non-contractible loop in $\mathcal{M}$ that crosses a boundary in direction α. In that case the field ϕ is a continuous function except when one crosses the hypersurface $H(\alpha)$, where a jump of the field with amplitude δ happens, and the Laplace equation (5.2) acquires a nontrivial boundary term leading to a non-trivial solution for the field ϕ. A corresponding function that is continuous despite the jump, will be a map

$$\phi \to \psi = \frac{\delta}{2\pi}\, e^{2\pi i \phi/\delta}, \tag{5.4}$$

which maps the scalar field ϕ to a circle in the complex plane. The interesting point is that, for a given direction α, the map ψ does not depend on the exact choice of the boundary $H(\alpha)$ of the elementary cell.[1]

In CDT we consider a discretization of the action (5.1) and the corresponding Laplace equation (5.2), where the field is localized in the center of simplices. We therefore consider a (discretized) Laplacian defined on the dual lattice, i.e., the graph whose vertices represent the 4-simplices of the original CDT triangulation, and links represent the common interfaces between the 4-simplices in the triangulation. The Laplacian on the dual lattice can be defined via the adjacency matrix A_{ij}:

$$A_{ij} = \begin{cases} 1 & \text{if (the link } i \leftrightarrow j) \in \text{dual lattice,} \\ 0 & \text{otherwise,} \end{cases} \tag{5.5}$$

where $\leftrightarrow$ refers to the adjacency relation of simplex i and j. The discrete Laplacian can be defined as:

$$L = D \downarrow A, \tag{5.6}$$

[1] Formally it depends only trivially, i.e., a continuous deformation (a "shift") of the boundary $H(\alpha)$ will only cause a shift of the phase in the complex function ψ by some constant.

where A is the adjacency matrix and D is a diagonal matrix with i-th diagonal element containing the number of neighbors of a simplex labelled i. As, in the four-dimensional CDT, each simplex in the triangulation has exactly 5 neighbors, the dual lattice of any triangulation is a five-valent graph, and therefore

$$D = 5 \cdot I, \tag{5.7}$$

with I being the identity matrix of size $N_4 \times N_4$, where N_4 is the number of all 4-simplices in the triangulation. The discretized form of the scalar field action is then given by:

$$S_M^{CDT}[\{\phi\}, \mathcal{T}] = \frac{1}{2} \sum_{i \leftrightarrow j} (\phi_i \downarrow \ \phi_j)^2 = \sum_{i,j} \phi_i L_{ij} \phi_j \equiv \phi^T L \phi, \tag{5.8}$$

where $\mathcal{T}$ underlines the impact of the triangulation on the Laplacian matrix L. The discrete analogue of the Laplace eq. (5.2) is then:

$$L\phi = 0. \tag{5.9}$$

The above equation has the same issue as before, i.e., if the target space of the field was chosen to be $\mathbb{R}$ then it would only have a trivial solution $\phi = const$. Non-trivial solutions can be found by choosing the field to take values in S^1 with circumference δ, which winds around the circle once as one goes around any non-contractible loop in the dual lattice. In order to do that one identifies:

$$\phi_i \equiv \phi_i + n \cdot \delta, \quad n \in \mathbb{Z}. \tag{5.10}$$

This can be achieved by adding a jump condition when crossing a boundary hypersurface $H(\alpha)$ in direction, α. The way of introducing such boundary hypersurfaces to CDT was proposed in [70]. As already mentioned, the exact position of the (four non-equivalent) boundaries $H(\alpha)$ in the triangulation is not important as it has only a trivial impact on our solutions, thus the boundaries are non-physical. Technically, one can define the "jump" condition by introducing the boundary jump matrix B_{ij}:

$$B_{ij} = \begin{cases} +1 & \text{if the dual link i} \to \text{j crosses the boundary } H(\alpha) \text{ in the } \textit{positive} \text{ direction,} \\ \downarrow 1 & \text{if the dual link i} \to \text{j crosses the boundary } H(\alpha) \text{ in the } \textit{negative} \text{ direction,} \\ 0 & \text{otherwise} \end{cases} \tag{5.11}$$

and defining

$$V = \frac{1}{2} \sum_{ij} B_{ij}^2 = \frac{1}{2} \sum_i |b_i|, \tag{5.12}$$

where $b_i = \sum_j B_{ij}$ is the boundary jump vector, and it measures the occasions when a tetrahedral face of a simplex i appears on the boundary. To accommodate to the jump condition we modify the discretized matter action

$$\begin{aligned} S_M^{CDT}[\{\phi\}, \mathcal{T}] = \frac{1}{2} \sum_{i \leftrightarrow j} (\phi_i \downarrow \ \phi_j \downarrow \ \delta B_{ij})^2 &= \sum_{i,j} \phi_i L_{ij} \phi_j \downarrow \ 2\delta \sum_i \phi_i b_i + \delta^2 V \\ &\equiv \phi^T L \phi \downarrow \ 2\delta \phi^T b + \delta^2 V. \end{aligned} \tag{5.13}$$

Now, the Euler-Lagrange equation for the field ϕ yields:

$$L\phi = \delta\, b, \tag{5.14}$$

so it acquires a non-trivial boundary term: $\delta\ b$. The classical solution to the scalar field distribution is formally given by

$$\phi^{classical} = \delta\ L^{\downarrow 1} b. \tag{5.15}$$

The practical problem is that the Laplacian has zero modes but, fortunately, one can find a solution in the subspace orthogonal to the zero modes. The solution strongly depends on the underlying triangulated geometry and it smoothly interpolates between the boundaries of the (toroidal) elementary cell. In the publication [4] we proposed to treat the harmonic map $\phi^{classical}$, or rather the resulting map $\psi^{classical}$, see eq. (5.4), as a coordinate in the direction α. This way one can introduce a coordinate system for every triangulation generated in the MC simulations. The coordinates can be used to visualize the differences between generic triangulations of different CDT phases. It is worth to mention that the harmonic maps (coordinates) described above have a very good property of smoothly interpolating between the 4-simplices in the geometric outgrowths, which commonly appear in the CDT triangulations forming fractal structures. Imagine such an outgrowth consisting of many simplices and linked to the rest of the triangulation by only a few simplices. Due to properties of harmonic maps all simplices in the outgrowth will have almost the same value of the field ϕ_i^α in all α-directions. Therefore the outgrowths should appear as the field condensations in the harmonic maps.

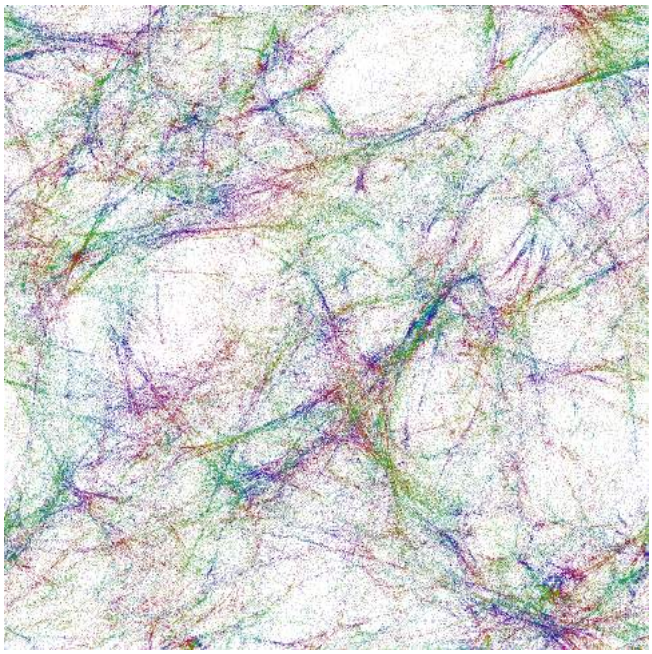

FIGURE 5.1: The 4-volume density map projected on two spatial ("x" and "y") directions measured in phase C ($\kappa_0 = 4.0, \Delta = 0.2, T = 20, \bar{N}_{41} = 720k$). Each point on the plot represents a 4-simplex having the scalar field values (coordinates) (ϕ^x, ϕ^y). The colors encode the time coordinate t of the original CDT foliation. The dense regions are geometric fractal outgrowths in the triangulation. The outgrows structure resembles cosmic voids and filaments of the real Universe.

A typical map (projected on two spatial directions: "x" and "y") measured in the semi-classical phase C of the toroidal CDT is presented in Fig. 5.1. Looking

at Fig. 5.1 it becomes apparent that the phase C generic triangulations represent a homogeneous and isotropic geometry on macroscopic scales. However, exactly as it is observed in the real Universe, there are local density fluctuations (geometric outgrows in case of CDT) showing very non-trivial voids and filaments structure. One should note that in this context this is the emerging feature of the pure quantum gravity, as the scalar fields discussed above do not have any impact (back-reaction) on the geometry, and are simply introduced for visualization purposes. Similar maps, obtained for generic triangulations of other CDT phases have completely different shapes, as discussed in publication [6].

Using the scalar fields as coordinates one can also measure the scaling of 4-volume in a triangulation by picking a (random) center and following a diffusion wave from that center and observing the growth in the volume of the diffusion shell. Looking at the scaling of the volume with radius one can measure the, so-called, Hausdorff dimension, associated with the harmonic coordinates. This was measured for the following fixed lattice volumes $\bar{N}_{41} = \{80k, 160k, 200k, 240k, 300k, 360k, 400k, 480k, 560k, 600k, 720k\}$. The 4-volume contained in a box (window) of size $\Delta\phi^x \times \Delta\phi^y \times \Delta\phi^z \times \Delta\phi^t$, denoted ΔN_{win}, normalized by the total volume N_{tot} can be used to measure the Hausdorff dimension. It was found that in phase C one obtains a universal behaviour, as presented in Fig. 5.2. The fitted Hausdorff dimension is consistent with $d_H = 4$.

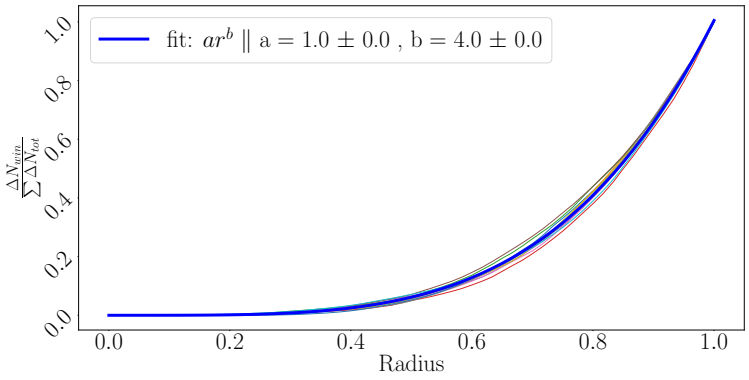

FIGURE 5.2: The figure shows the ratio of ΔN_{win} (4-volume inside the box of size $\Delta\phi^x \times \Delta\phi^y \times \Delta\phi^z \times \Delta\phi^t$) and N_{tot} (total volume) in the function of the normalized size of the box (Radius). This function was measured in measured in phase C ($\kappa_0 = 4.0, \Delta = 0.2, T = 20$). The various thin lines denotes measurements for different lattice volumes $\bar{N}_{41}$, the solid blue line is a fit of the function ar^b to their average.

5.2 Dynamical scalar fields

"The effort to understand the Universe is one of the very few things that lifts human life a little above the level of farce, and gives it some of the grace of tragedy." - **Steven Weinberg**

This section is based on the publications [5, 6].

So far the back-reaction of the matter field on the purely geometric degrees of freedom was not taken into account. Including back-reaction of quantum (later also called dynamical) scalar fields can lead to nontrivial changes of the geometry. In the results presented below, the scalar fields are massless scalar fields with the (discretized) action (5.13), minimally coupled to the geometric (Regge) action (2.18). Including such fields in the MC simulations means that not only the field values have to be generated - in the MC simulations the heat bath method [71, 72] was used - but also that the matter action will affect the probability of performing the purely geometric moves. Depending on the parameters of a simulation, either the geometric or the matter part of the action dominates, thus one can expect a phase-transition of some sort when moving in the parameter space, now also including a new coupling constant corresponding to the circumference δ of the S^1 target space (or alternatively the jump amplitude) of the scalar field.

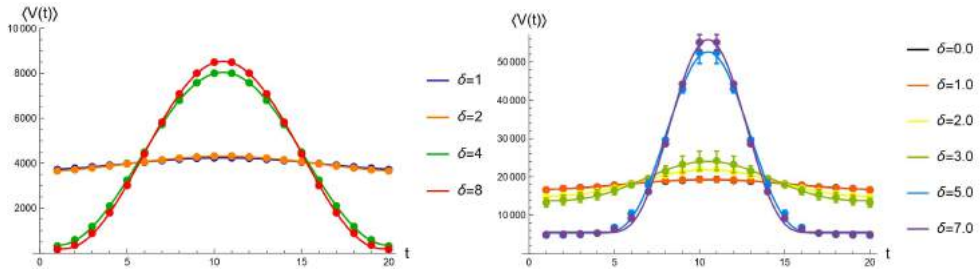

FIGURE 5.3: The volume profile in the presence of one field winding around the time direction (left) and three fields winding around the non-equivalent spatial directions (right).

The choice of the δ value is not the only additional parameter, as one can also choose the number of ϕ-fields, as well as the number and type (time- or space-like) of non-equivalent winding directions for the scalar field(s). Adding a field with $\delta = 0$ has already a visible but small effect, as it shifts some characteristics of generic triangulations appearing in the path integral, for example it lowers the ratio of N_{32}/N_{41}, and adding more fields the effect is larger. Much stronger effect is observed for large jump magnitude δ. As already discussed, if no scalar fields are added, the measured volume profile of the toroidal CDT model in the semi-classical phase C is a constant function. This is also the case of CDT coupled to the scalar fields with zero or small jump magnitude δ, but for large δ one observes a dramatic change in the volume profile, as it is shown in Fig. 5.3. In the case with one scalar field winding around the time direction, using a simple minisuperspace-like model presented in Appendix 3 of [6], one can expect to observe a "pinched" volume profile, turning the constant function into a $cos(t)$ function, as seen in the left panel of Fig. 5.3. On the other hand, as can be seen on the right panel of Fig. 5.3, the jump condition introduced only in the spatial directions will also trigger, for large-enough δ values, a kind of

"pinched" volume profile, however the reason behind it is different. In that case the fitted volume profile is given by a $cos^3(t)$ function, which corresponds to the volume profile of the (Eucledean) de Sitter sphere.

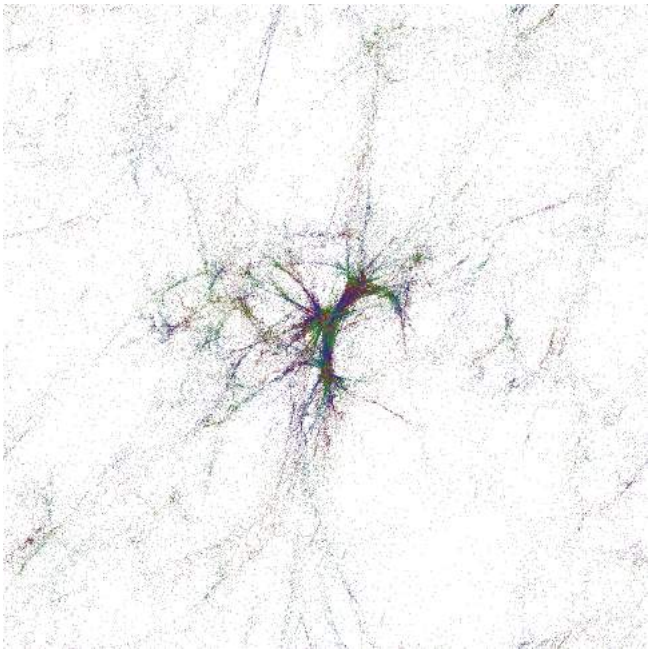

FIGURE 5.4: The 4-volume density map projected on two spatial ("x" and "y") directions measured in phase C ($\kappa_0 = 2.2\Delta = 0.6, T = 4, \bar{N}_{41} = 160k$) in the presence of 3 scalar fields winding around non-equivalent spatial directions ($\delta = 1.0$). Each point on the plot represents a 4-simplex having the scalar field values (coordinates) (ϕ^x, ϕ^y). The 4-volume is concentrated in the center of the plot, and the low-density region around it shows the "pinching" effect, leading to the effective spatial topology change.

Qualitatively, the same kind of "pinching" happens in the spatial directions, leading to the effective topology change from toroidal to spherical. By the effective topology change we mean a situation where there is still a remnant of the original CDT topology (which by definition cannot change in the MC simulations), but, due to the "pinching", the toroidal part is of cutoff size, and the dominating geometry has (almost) spherical topology. So effectively, the triangulations start to behave as if the topology of spatial slices was spherical instead of toroidal. It triggers an additional effect, also observed in the spherical CDT, leading to the non-trivial de Sitter-like volume profile of $\cos^3(t)$, i.e., it causes a "pinching" in the time direction, changing the effective topology to that of S^4. Consequently, the toroidal CDT model with scalar fields winding around spatial directions behaves effectively as the spherical CDT model.

Summarizing, the presence of the dynamical scalar fields with a non-trivial jump condition (or alternatively a nontrivial target space S^1) can trigger a phase transition, which effectively changes the topology of the CDT configurations. Fig. 5.4 shows the 4-volume density map (projected to the "x" and "y" spatial directions) of a generic triangulation in phase C in the presence of 3 scalar fields with large jump magnitude ($\delta = 1.0$) winding around 3 non-equivalent spatial directions. Most simplices are concentrated in the center of the plot and at the edge of the plot the density becomes much smaller. This is exactly the "pinching" effect, leading to a formation of a single

large geometric outgrowth, where almost all 4-volume is concentrated, and therefore changing the effective topology from the toroidal to the spherical one. The geometry looks considerably different than that of the pure gravity model, presented in Fig. 5.1, where the scalar fields were used only as maps and did not have any back-reaction impact on the underlying manifold.

Chapter 6

Conclusions

This chapter contains a summary and a description of my contribution to the publications included in Chapter 7.

In this section we will summarize the discussion presented in the previous chapters. This thesis is supposed to be a collection of publications done during my PhD studies and a guide to the presented articles together with some theoretical introduction and some additional thoughts that cannot be found elsewhere. This includes the discussion of the MC moves using a "colored dots" graph representing the discretized geometry of the $t + \frac{1}{2}$ foliation leaf, the possibility of introducing new MC moves presented in the Appendix B, the discussion of topological relations between the triangulation parameters in the Appendix A, and the results related to the Hausdorff dimension calculated from the scalar field distribution. All other figures and results were taken from the publications.

For all of the works presented in the previous chapters I performed a significant amount of numerical simulations and did a large part of the numerical data-analysis. The phase transition studies were challenging as they required simulations which lasted for several months, due to the prolonged thermalization time related to the nature of the problem. Furthermore, many measurements had to be repeated due to various technical difficulties.

In Chapter 4 (section 4.3.2) I discussed the study of the $A \downarrow B$ phase transition, presented in the publication [3]. In the case of this phase transition I was the main contributor to the study. I decided on the analysis of this particular part of the CDT phase-diagram and selected the methods and the MC simulation parameters necessary to perform the study (e.g., values of the coupling constants, values of $\bar{N}_{41}$, etc.). Data coming from the simulations was shared between the members of the CDT group and the conclusions and results were discussed on regular group meetings. Finally, I had a large contribution to editing of the text of the publication [3].

In case of the publication [1], described in Chapter 4 (section 4.3.3), my main contribution was the finding that the volume profile $V_3(t)$ of the C_b phase in the case of toroidal spatial topology contains an emergent blob, seemingly similar to that observed for the case of the spherical CDT. I collected evidence for that behavior and performed analysis to calculate the Hausdorff dimension of the observed triangulations.

After the finding that there is a direct phase transition between the B and C phases [57], the study of the $C \downarrow B$ phase transition, discussed in Chapter 4 (section 4.3.4) became one of the priorities of my PhD research. The analysis of the $C \downarrow B$

phase transition (presented in [2, 3]) was one of the most demanding works of my PhD. It required a large amount of computer simulations (several hundreds of MC runs) which had to be performed in order to achieve the published results. Each of these simulations had to be overseen one-by-one on a regular basis and then data had to be analyzed. I had also an important contribution to editing the text of the publications [2] and [3]. The findings of [2] were unclear, as signals of the phase transition were mixed and one couldn't find its order with 100% accuracy. Performing numerical simulations in additional locations in the phase diagram and increasing the statistics yielded similar result [3], however we managed to show that introducing a discretization correction to scaling relations gives the fits compatible with the scaling exponent corresponding to a first-order transition. The description of the nature of this phase transition, and as we understand it now also other CDT phase transitions, was facilitated by another study related to the scalar fields (publications [4, 5, 6]), where the notion of emergent topology became apparent. Similarly to the effective dimensionality, discussed throughout the thesis, the effective topology of the quantum universe seems to be an emergent phenomenon, and according to our conjecture, for which we seem to find evidence, whenever a phase transition occurs between phases of different effective topology then it should be a first-order transition.

All the phase transitions mentioned above were analyzed in case of empty CDT universes, which means that there were no additional matter content, only the gravitational degrees of freedom. As discussed in Chapter 5, the simplest form of a matter field which can be included in our model is a massless scalar field. For all of the scalar field related publications [4, 5, 6] I contributed by performing MC simulations, data analysis, result interpretation and co-editing the articles. Additionally, I was the corresponding author of publication [4]. The classical scalar fields, described in publications [4, 6], were used as a tool to introduce a coordinate system to the CDT triangulations. Such coordinates are a (quantum) analogue of the harmonic (de Donder) gauge fixing in GR. The massless scalar fields are harmonic maps, enabling one to visualize the non-trivial fractal structure of the underlying quantum geometries. Using the mapping, the regions of the triangulation with under- and over- 4-volume density are visible, which makes it possible to observe structures resembling cosmic voids and filaments similar to the large scale structure of the Universe. One may think of these structures, coming from the quantum fluctuations of pure gravity, as the source of initial inhomogeneities in the matter content of the early Universe, but this idea requires further studies. These maps can be measured in all CDT phases and they reveal important differences in the geometric structures of generic triangulations observed in each phase. This observation, in particular, lead to the notion of the effective topology discussed above. The back-reaction of the scalar fields was added to the simulations and discussed in publications [5, 6], where I contributed by performing the MC simulations and data analysis. Adding scalar fields with non-trivial "jump" conditions resulted in a phase transition observed for some value of the jump amplitude, see Chapter 5. In the case where the field was winding around the time direction, the phase transition led to the volume profile $V_3(t)$ consistent with a $cos(t)$ function, resulting from the minisuperspace-type approximation discussed in Appendix 3. of [6]. In the case where three scalar fields were winding around spatial directions the phase transition led to the "pinching" of the geometry in these directions and consequently to the effective spatial topology change from the toroidal to the spherical one. This in turn resulted in the de Sitter type, i.e., $cos^3(t)$, volume profile, leading to further effective topology change to that of the

four-sphere.

There is still a lot to be investigated in the CDT phase-diagram. Especially, the open question remains if there exists the UVFP of CDT. Without such a UVFP CDT can be at most treated as some effective quantum gravity model, valid only to some energy scale, but not a fundamental non-perturbatively renormalizable theory of quantum gravity. Potentially some kind of extension of the model is needed to be able to obtain such a UVFP. An extension may come from the introduction of new parameters to the bare Regge action S_R, discussed in Appendix A, although such a change should be well motivated, and some physical quantities related to the new parameters have to be found. Another extension, which may possibly yield the UVFP, can potentially come by adding various matter content. For example, adding gauge fields is currently the topic of an ongoing study, but it is at a preliminary stage and therefore it will not be discussed in this thesis.

Summing up, there is still plenty of directions which future research of CDT can follow in the quest for understanding quantum gravity. All I can say is that I am proud that, with the results presented in this thesis, I could participate in the development of the theory which has the potential to become widely accepted theory of quantum gravity.

Chapter 7

Publications

This chapter contains publications constituting the main part of the PhD thesis. The order of publications, as it was mentioned in Chapter 1., is as follows:

[1] J. Ambjorn G. Czelusta et al. "The higher-order phase transition in toroidal CDT". In: J. of High Energ. Phys. 2020 (5), p. 30.
DOI: 10.1007/JHEP05(2020)030

[2] J. Ambjorn et al. "Towards an UV fixed point in CDT gravity". In: Journal of High Energy Physics 2019 (7), p. 166.
DOI: 10.1007/JHEP07(2019)166

[3] J. Ambjorn et al. "Topology induced first-order phase transitions in lattice quantum gravity". In: Journal of High Energy Physics 2022 (4), p. 103.
DOI: 10.1007/JHEP04(2022)103.

[4] J.Ambjorn et al. "Cosmic voids and filaments from quantum gravity". In: The European Physical Journal C 81 (8 2021), p. 708.
DOI: 10.1140/epjc/s10052-021-09468-z

[5] J. Ambjorn et al. "Matter-Driven Change of Spacetime Topology". In: Phys. Rev. Lett. 127 (16 Oct. 2021), p. 161301.
DOI: 10.1103/PhysRevLett.127161301

[6] J. Ambjorn et al. "Scalar fields in causal dynamical triangulations". In: Classical and Quantum Gravity 38 (19 Sept. 2021), p. 195030.
DOI: 10.1088/1361-6382/ac2135

Pub. [1]: Discovery of a scientific result published in the paper. Performing numerical simulations, analyzing the data and discussing the results. Estimated contribution: 20%.

Pub. [2]: Conducting the main research, including the maintenance of numerical simulations, performing the analysis of the data, discussing the results, writing the initial version of the publication. Estimated contribution: 70%.

Pub. [3]: Conducting the main research, including the maintenance of numerical simulations, performing the analysis of the data, discussing the results, writing the the publication together with coauthors. Estimated contribution: 75%.

Pub. [4]: Performing numerical simulations, providing data to the collaborators, discussing the results, writing the initial version of the publication. I was the corresponding author of the paper. Estimated contribution: 20%.

Pub. [5]: Performing numerical simulations, providing data to the collaborators, doing some part of the data analysis, discussing the results. Estimated contribution: 30%.

Pub [6]: Performing numerical simulations, providing data to the collaborators, doing some part of the data analysis, discussing the results. Estimated contribution: 30%.

7.1 Publications

Published for SISSA by Springer

Received: *February 9, 2020*
Revised: *April 7, 2020*
Accepted: *April 18, 2020*
Published: *May 7, 2020*

The higher-order phase transition in toroidal CDT

J. Ambjørn,[a,b] **G. Czelusta,**[c] **J. Gizbert-Studnicki,**[c] **A. Görlich,**[c] **J. Jurkiewicz**[c] **and D. Németh**[c]

[a] *The Niels Bohr Institute, Copenhagen University, Blegdamsvej 17, DK-2100 Copenhagen Ø, Denmark*
[b] *IMAPP, Radboud University, Nijmegen, PO Box 9010, The Netherlands*
[c] *Institute of Theoretical Physics, Jagiellonian University, Łojasiewicza 11, Kraków, PL 30-348, Poland*

E-mail: ambjorn@nbi.dk, grzegorz.czelusta@doctoral.uj.edu.pl, jakub.gizbert-studnicki@uj.edu.pl, andrzej.goerlich@uj.edu.pl, jerzy.jurkiewicz@uj.edu.pl, nemeth.daniel.1992@gmail.com

Abstract: We investigate the transition between the phases B and C_b observed in four-dimensional Causal Dynamical Triangulations (CDT). We find that the critical properties of CDT with toroidal spatial topology are the same as earlier observed in spherical spatial topology where the $B - C_b$ transition was found to be higher-order. This may have important consequences for the existence of the continuum limit of CDT, describing the perspective UV limit of *quantum gravity*, which potentially can be investigated in the toroidal model.

Keywords: Lattice Models of Gravity, Lattice Quantum Field Theory, Models of Quantum Gravity, Nonperturbative Effects

ArXiv ePrint: 2002.01051

https://doi.org/10.1007/JHEP05(2020)030

JHEP05(2020)030

Contents

1 Introduction 1

2 Phase transitions in MC simulations of lattice field theories 3

3 The properties of the bifurcation phase C_b 6

4 The $B - C_b$ phase transition in the toroidal CDT 8

5 Summary and conclusions 12

JHEP05(2020)030

1 Introduction

Numerical Monte Carlo simulations applied to lattice field theories became an important tool of contemporary physics. The famous example is Lattice Quantum Chromodynamics (QCD) which has grown up from its childhood and now goes hand-by-hand with experiments and beyond, e.g. by investigating the very non-trivial QCD phase diagram in the regime of coupling constants non-tractable by perturbative calculus. Despite many open questions, QCD has a well defined ultraviolet limit, where it becomes non-interacting *asymptotically free* theory and thus the high energy behaviour can be investigated perturbatively. The opposite thing happens when one tries to formulate a quantum theory of gravity (QG) by applying standard quantum field theory techniques to Einstein's General Relativity (GR). In that case the perturbative expansion around any fixed classical metric field fails at high energies due to the perturbative non-renormalizability of such a formulation [1, 2]. However, as conjectured by Steven Weinberg in his seminal paper [3], QG can be *asymptotically safe*, i.e. it can admit a well behaved non-perturbative high energy limit defined in the vicinity of a non-trivial fixed point of the renormalization group flow, where quantum gravity becomes scale-invariant and thus can be extrapolated to arbitrarily large energy scale. If the *asymptotic safety* scenario is valid[1] then (in the ultraviolet regime) QG must be formulated in a background-independent non-perturbative way making lattice approaches well suited to tackle this problem. In such formulations one discretizes geometric degrees of freedom on the lattice with (4-dimensional) lattice 'volume' N_4 and with a minimal (cut-off) spacing a, and in the ultraviolet regime one would like to get rid of the discretization by taking a continuum limit of $a \to 0$ and $N_4 \to \infty$ such that $N_4^{1/4} \cdot a$ is related to some physical length. In order to obtain non-trivial physical observables in the continuum limit, where $a \to 0$ and $N_4 \to \infty$, one would also like to have appropriately divergent correlation lengths $\ell_c \sim N_4^{1/4}$. Thus in a lattice approach the continuum limit

[1] There is growing evidence for the existence of a fixed point suitable for asymptotic safety coming from functional renormalization group studies [4–9], however a rigorous proof of its existence is still lacking.

should be associated with a higher order (continuous) phase transition. Therefore studies of the phase structure and orders of phase transitions are important steps towards defining an ultraviolet limit in a lattice formulation and thus testing the asymptotic safety scenario for gravity.

One of the most successful attempts of the lattice formulation of quantum gravity is that of Causal Dynamical Triangulations (CDT) (for reviews see [10, 11]), in the sense that it has a rich phase structure, where some of the transitions are higher order, which potentially can be used to define continuum limit and that it additionally has a well behaved low energy limit consistent with GR. CDT is based on the path integral formalism and makes only a few assumptions on the geometry of quantum space-time, namely it requires that the geometry can be globally foliated into space-like hypersurfaces, each with the same fixed topology Σ. The model is using the discretization of space-time following the method proposed by Regge [12]. The three-dimensional spatial states are constructed by gluing together in all possible ways regular tetrahedra with a common link length a_s to form a triangulation of a three-dimensional space with a (closed) topology Σ. The topology of states is fixed during the evolution of geometry in time, being the origin of the name *causality* in the model. To join states at different times t we need two types of 4-dimensional simplices. Tetrahedra become bases of 4-dimensional simplices $\{4,1\}$ (and $\{1,4\}$) with four vertices at a time layer t and one at $t+1$ (resp. $t-1$). In our notation the simplex $\{i,j\}$ has i vertices at a time t and j vertices at a time $t+1$. The time links are assumed to have a common link length a_t which may be different than a_s. To complete the manifold structure two additional simplex structures are necessary. These are $\{3,2\}$ and $\{2,3\}$ simplices. Pairs of simplices share a common three-dimensional face (tetrahedron). The construction works both for systems with Lorentzian signature and, after Wick rotation, for systems with Euclidean signature. Each space-time configuration can be interpreted as Lorentzian or Euclidean. The possibility of performing Wick rotation is crucial if we want to use numerical methods to analyze the properties of the model. In the following, we assume the Euclidean formulation is used. The discretization described above means that the four-dimensional volume of all $\{i,j\}$ simplices depends only on the type of a simplex. Similarly other geometric properties, like the angles, are universal for all simplices of a particular type.

The studied object is the Feynman amplitude $\mathcal{Z}$, which is expressed as a weighted sum over manifolds $\mathcal{T}$ joining the initial and final geometric states separated by time T. The weight is assumed to be expressed as a discretized version of the Hilbert-Einstein action $S_{\mathrm{EH}}(\mathcal{T})$

$$\mathcal{Z} = \sum_{\mathcal{T}} \frac{1}{C(\mathcal{T})} e^{-S_{\mathrm{EH}}}, \tag{1.1}$$

where $C(\mathcal{T})$ is the symmetry factor of a graph representing the manifold. In practice the choice of the initial and final states is replaced by assuming the system to be periodic with the period T. The discretized version of the Hilbert-Einstein action takes the form [13]

$$S_{\mathrm{EH}} = -\left(\kappa_0 + 6\Delta\right) N_0 + \kappa_4 \left(N_{4,1} + N_{3,2}\right) + \Delta N_{4,1}, \tag{1.2}$$

JHEP05(2020)030

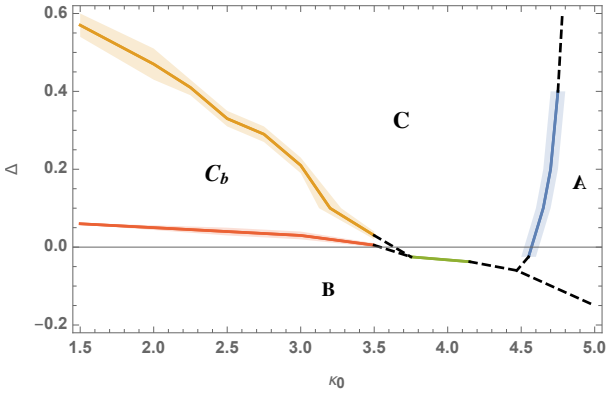

Figure 1. The phase structure of 4-dimensional CDT.

where $N_{i,j}$ denotes the number of 4-dimensional simplicial building blocks with i vertices on hypersurface t and j vertices on hypersurface $t \pm 1$, and N_0 is the number of vertices in the triangulation. κ_0, Δ and κ_4 are bare coupling constants. κ_0 and κ_4 are related to Newton's constant and the cosmological constant, respectively, and Δ depends on the ratio of the length of space-like and time-like links in the lattice. In the Monte Carlo simulations of CDT the parameter κ_4, which is proportional to the cosmological constant, is tuned such that one can take infinite-volume limit. As will be explained later, in numerical simulations we perform a series of measurements for systems with increasing (fixed) volume $N_{4,1}$ and try to determine the limiting behaviour for $N_{4,1} \to \infty$. In the consequence the phase diagram presented in figure 1 depends only on two bare couplings κ_0 and Δ. It is remarkable that such a simple model has a rich phase structure with four phases with very different physical properties. The analysis of the phase structure and, in particular, the order of phase transitions is fundamental to relate the model to a possible theory of quantum gravity.

2 Phase transitions in MC simulations of lattice field theories

According to Ehrenfest's classification, the order of a phase transition depends on the behaviour of the thermodynamic free energy. If all first $n-1$ order derivatives of the free energy are continuous functions of some thermodynamic variable, e.g. the coupling constant of the lattice theory, and the n-th order derivative exhibits a discontinuity at the transition point then the transition is the *n-th order* phase transition. Here we are especially interested to distinguish between the first- and the higher-order phase transitions, as the continuous limit of the lattice field theory should be associated with the latter type.

The derivatives of free energy are related to order parameters, which capture differences of thermodynamic properties of the system in two different phases separated by the transition point. For a first-order transition one should observe a discontinuity of the order parameter at the transition point and for the higher-order transition the order parameter should be continuous but its derivatives, e.g. its susceptibility, should diverge. Unfortunately measuring the (dis-)continuity of the (derivatives) of an order parameter in

JHEP05(2020)030

numerical simulations is a tedious task. Actually, in numerical Monte Carlo simulations, which are always performed for a finite lattice size N_4, one does not even observe phase transitions per se. The finite lattice size and the finite lattice spacing make all thermodynamic functions and their derivatives finite, even though they can become arbitrarily large for large lattice sizes. One should therefore carefully analyze finite (lattice) size effects and, if possible, take the infinite (lattice) volume limit $N_4 \to \infty$.

As phase transitions are usually related to breaking some symmetries of the studied lattice field theory, one can define order parameter(s) OP which capture these symmetry differences between various phases of the theory in question. One then usually performs numerical Monte Carlo (MC) simulations for some fixed lattice volume N_4 in many points of the theory parameter space (see e.g. the CDT phase diagram in figure 1) to find regions where the order parameter rapidly changes, see e.g. figure 4 where we show the mean value $\langle \mathrm{OP} \rangle$ of the four order parameters (for their definitions see equation (4.2)) used in CDT phase transition studies measured in the $B - C_b$ transition region. The precise position of the phase transition is signaled by a peak of the susceptibility of an order parameter

$$\chi_{\mathrm{OP}} \equiv \langle \mathrm{OP}^2 \rangle - \langle \mathrm{OP} \rangle^2 \tag{2.1}$$

related to its first-order derivative with respect to some thermodynamic variable, see e.g. figure 5. For a finite lattice volume N_4 one can only determine a position of the (volume dependent) pseudo-critical point. Positions of such points may in general depend on the order parameter or the method used. Only in $N_4 \to \infty$ limit they must coincide. Let $\Delta^c(N_4)$ be the pseudo-critical value of the thermodynamic variable Δ, e.g. the coupling constant, measured for a given phase transition for the lattice volume N_4. The typical (large) volume dependence is

$$\Delta^c(N_4) = \Delta^c(\infty) - \frac{C}{N_4^{1/\nu}}\,, \tag{2.2}$$

where the critical exponent ν is one for a first-order transition and larger than one for a higher-order transition. Thus by making a series of measurements of $\Delta^c(N_4)$ for different lattice volumes N_4 one can establish a value of the critical exponent ν and in effect determine the order of the phase transition.

Another way of distinguishing between the first- and the higher-order phase transitions in numerical Monte Carlo studies is to analyze the behaviour of the order parameter(s) measured precisely at (or in practice as close as possible to) the transition point. For a first-order transition the discontinuity of an order parameter can appear in its MC history as jumps between two different states. In such a case, the histogram of the order parameter measured at the pseudo-critical point should show two separate peaks centered around the values generic for the two different phases. Here one should also carefully analyze finite size effects related to the finite lattice volume N_4 fixed in the numerical studies. The separation of the peaks in the MC history histogram can either increase or decrease with the lattice volume which can imply the first- or the higher-order transition, respectively. If the separation of the states, generic for the first-order transition, is large enough one

JHEP05(2020)030

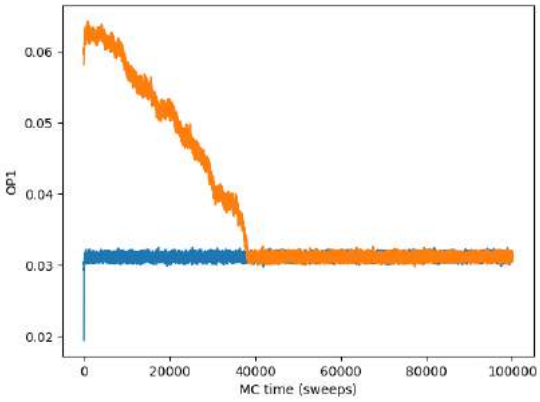

Figure 2. Thermalization check of Monte Carlo data series. The plot shows the OP_1 order parameter (for definition see equation (4.2)) measured in two independent MC simulations of CDT with toroidal spatial topology with exactly the same parameters, i.e. $N_{4,1} = 300\mathrm{k}$, $T = 4$, $\kappa_0 = 2.2$, $\Delta = 0.048$. One simulation was initiated with a configuration from phase B (blue line) and the other one started from a configuration from phase C_b (orange line). Both data series statistically agree from ca 40000 sweeps (1 sweep = 10^7 attempted MC moves). Data from earlier MC time history, called the *thermalization* period, are excluded from final measurements.

typically observes a hysteresis at the transition region. In order to check that, one can run two separate series of Monte Carlo simulations, one initiated with configurations generic for one phase and the other one initiated with configurations generic for the other phase. If hysteresis is present then one can observe a (statistically) different behaviour of the two series in the transition region, e.g. the pseudo-critical points measured in the two different series could be shifted versus each other. If hysteresis is absent the results of the two series should (statistically) agree. Running two independent series initiated with different staring configurations is also a good way of checking *thermalization* of the Monte Carlo data, i.e. checking if the MC simulation has run for long enough to reach the proper statistical equilibrium and thus if measurement data can be collected, see e.g. figure 2.

Another quantity of interest is the Binder cumulant[2]

$$B_{\mathrm{OP}} \equiv \frac{1}{3}\left(1 - \frac{\langle \mathrm{OP}^4 \rangle}{\langle \mathrm{OP}^2 \rangle^2}\right) = -\frac{1}{3}\frac{\langle (\mathrm{OP}^2)^2 \rangle - \langle \mathrm{OP}^2 \rangle^2}{\langle \mathrm{OP}^2 \rangle^2}, \tag{2.3}$$

which is always non-positive because $\langle (\mathrm{OP}^2)^2 \rangle - \langle \mathrm{OP}^2 \rangle^2 \geq 0$, and it reaches a minimum at the pseudo-critical point $\Delta^c(N_4)$, because there fluctuations are maximal. In the numerical MC simulations one can measure the (volume dependent) value of the Binder

[2]Note that here we use a definition of the Binder cumulant which is shifted (by a $-2/3$ constant) versus the original Binder's formulation [14–16]: $B_x = 1 - \frac{1}{3}\frac{\langle x^4 \rangle}{\langle x^2 \rangle^2}$. The definition (2.3) was used in previous CDT phase transition studies [17–19] and thus we keep it in order to ease comparison with these results. The virtue of using our definition is that, as explained in the text, the deviation of (critical) B_{OP} from zero with rising lattice volume may signal a first order transition, while the convergence to zero is characteristic of a higher order transition. One could as well use the original Binder's definition and look at the deviation from 2/3.

JHEP05(2020)030

OBSERVABLE	First-order transition	Higher-order transition
Critical exponent ν in scaling of $\Delta^c(N_4)$, eq. (2.2)	ν $= 1$	ν > 1
OP histograms measured at pseudo-critical points $\Delta^c(N_4)$	double peaks peak separation $\uparrow$ with $N_4 \to \infty$	single peak or peak separation $\downarrow$ with $N_4 \to \infty$
Hysteresis of MC data near pseudo-critical points $\Delta^c(N_4)$	YES hysteresis $\uparrow$ with $N_4 \to \infty$	NO or hysteresis $\downarrow$ with $N_4 \to \infty$
Binder cumulant (2.3) minima for $N_4 \to \infty$	$B^{\min}_{\rm OP}(N_4 \to \infty)$ < 0	$B^{\min}_{\rm OP}(N_4 \to \infty)$ $= 0$

Table 1. Characteristics of the first- and the higher-order phase transitions in MC studies.

cumulant minimum

$$B^{\min}_{\rm OP}(N_4) = B_{\rm OP}(\Delta^c(N_4)) \tag{2.4}$$

for different (fixed) lattice sizes N_4 and then analyze its behaviour in the large volume limit $N_4 \to \infty$. In the case of a higher-order phase transition the probability distribution of the order parameter OP approaches a Dirac delta around $\langle \mathrm{OP} \rangle$ in the infinite volume limit. And then $B^{\min}_{\rm OP}(\infty)$ should equal 0. In the case of the first-order transition the distribution of the parameter OP is a sum of two distributions centered at expectation values characteristic for the two different phases. In the infinite volume limit, when these distributions approach Dirac delta functions, the minimum of the Binder cumulant becomes:

$$B^{\min}_{\rm OP}(\infty) = -\frac{\langle \mathrm{OP}_B \rangle^2 + \langle \mathrm{OP}_{C_b} \rangle^2}{12 \langle \mathrm{OP}_B \rangle^2 \langle \mathrm{OP}_{C_b} \rangle^2} \tag{2.5}$$

where $\langle \mathrm{OP}_B \rangle$ and $\langle \mathrm{OP}_{C_b} \rangle$ are expectation values of the observable OP at two different phases, say "B" and "C_b", and the relative strength of Dirac delta functions is assumed to be $\frac{\langle \mathrm{OP}_B \rangle^2}{\langle \mathrm{OP}_B \rangle^2 + \langle \mathrm{OP}_{C_b} \rangle^2}$ and $\frac{\langle \mathrm{OP}_{C_b} \rangle^2}{\langle \mathrm{OP}_B \rangle^2 + \langle \mathrm{OP}_{C_b} \rangle^2}$, respectively.

In table 1 we summarize methods used in numerical MC simulations of lattice field theories to distinguish between the first- and the higher-order phase transitions. We will then apply these methods in section 4 to analyze the $B - C_b$ transition in CDT with the toroidal topology of spatial slices.

3 The properties of the bifurcation phase C_b

The existence of the bifurcation phase in the CDT model with a spherical spatial topology was discovered relatively late [20–22]. The reason why in the early studies only three phases were discussed was that the basic observable used in these approaches was the (average) spatial volume profile of configurations. A typical setup for numerical experiments was to use systems periodic in time, with a period T usually in the range 40–80. Using the spatial volume observable, the three phases, A, B and C, were characterized by completely different qualitative behavior. The phase A was characterized by large fluctuations of the spatial volume in the neighboring time slices. The observed average volume distribution in time corresponded to the unbroken symmetry of the time translations. In the phase B almost all

JHEP05(2020)030

spatial volume (except for the *stalk*, necessary to satisfy the periodic boundary conditions) was concentrated at a single time slice. This meant that for typical states in this phase the symmetry of the time translations was fully broken. The physically most interesting was the phase C, where the volume profile contained the *blob* and the *stalk*, again meaning that for a typical configuration the symmetry of the time translations was broken. Average volume distribution in the blob and its fluctuations could be very accurately explained using the effective mini-superspace model for the isotropic four-dimensional Euclidean space-time [23–25]. Most results were obtained for a particular point in the coupling constant space with $\kappa_0 = 2.2$ and $\Delta = 0.6$, where it was shown that volume distribution scaled with the total $N_{4,1}$ lattice volume in a way consistent with the Hausdorff dimension $d_H = 4$.

Similar measurements performed for decreasing values of Δ showed that, although qualitatively the volume profile still contained a blob and the stalk, the scaling properties did not follow those determined in the de Sitter phase C. It was observed that the scaling was consistent with that predicted for systems with the Hausdorff dimension $d_H = \infty$. The name *bifurcation phase* C_b appeared to describe the additional property observed in the volume profile: a different behavior in the even and odd time slices when the time period T was sufficiently small [20]. It was soon realized that the reason for the observed behavior came from the breaking of the isotropy of the spatial volume distribution in the new phase. For the time slices separated by two units in time, vertices with very high coordination numbers appeared, leading to a formation of highly nontrivial geometric objects, forming a chain in the time direction. A physical interpretation of these objects was conjectured to be a result of a local signature change from Euclidean to Lorentzian [21], producing objects with some qualitative similarity to a *black hole* or rather a series of *black points*. A detailed description of the microscopic mechanism producing such effects will be the subject of a separate paper.

As can be seen in figure 1, for decreasing values of Δ and a fixed value of κ_0, one observes a phase transition between the C_b and B phases. The properties of this phase transition were very accurately measured in the case of a spherical spatial topology [17, 18, 22], although originally the phase C_b was interpreted as being a part of the *de Sitter* phase C. Results indicated that the phase transition was higher order, a very important property from a theoretical point of view, as explained earlier. The purpose of the present analysis is to check if the position and properties of the phase transition remain the same for systems with the spatial topology Σ of a sphere S^3 and of a three-torus T^3.

The first question to be asked is: are the qualitative properties in the C_b phase similar or different when we consider systems with a different spatial topology. Again we may look at the simplest object, a volume profile for systems with the periodicity T of the same order as the one used in the spherical case. This is the observable which was found to behave differently in the C phase. The observed volume profile, in this case, was found to be flat rather than containing a blob [26, 27]. The reason of such a behavior could be explained using a mini-superspace spatially isotropic model for a system with the spatial topology of a three-torus. The averaged volume profile is flat since in the toroidal case the time translation symmetry remains unbroken [26, 27].

Investigations show that this is not the case in the bifurcation phase C_b. The volume

JHEP05(2020)030

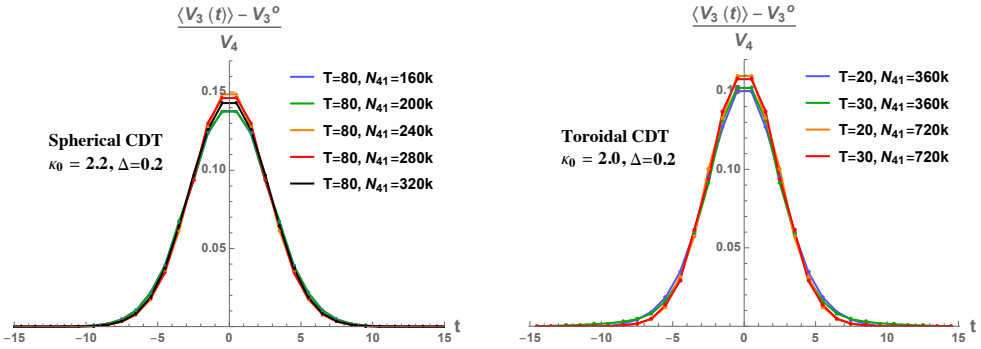

Figure 3. The (rescaled) average spatial volume profiles $\langle V_3(t)\rangle$ observed in the bifurcation phase C_b in the spherical (left plot) and the toroidal (right plot) CDT. In both plots the spatial volume profiles were presented with respect to the centre of volume, set at $t = 0$, and shifted by a (constant V_3^0) volume measured in the *stalk* range ($|t| >\sim 10$), V_3^0 being different for each volume profile (in general V_3^0 is bigger in the toroidal CDT where discretization effects are larger). Data measured for various total $N_{4,1}$ lattice volumes and different T were rescaled by $V_4 = \sum_t(\langle V_3(t)\rangle - V_3^0)$, i.e. in agreement with the Hausdorff dimension $d_H = \infty$.

profile observed for the point in the coupling constant space, typical for the bifurcation phase ($\kappa_0 = 2.0$ and $\Delta = 0.2$) shows the appearance of a blob and the stalk, see figure 3, the same way as it was observed in the spherical case. Also the scaling of the volume profile with the total $N_{4,1}$ lattice volume is consistent with the Hausdorff dimension $d_H = \infty$, the same as in the spherical CDT. The analysis of the geometric properties of configurations in the bifurcation phase C_b shows that also from a microscopic point of view the toroidal and spherical cases are very similar. In both topologies, we observe the high-order vertices, separated in time by two steps. The shape of the blob observed for periodicity T large enough ($T \geq 20$) again scales consistently with the infinite Hausdorff dimension. The difference is observed in the stalk, which has a much larger volume for a torus than that for a sphere. This is well understood and results from the fact that a minimal $3D$ spatial configuration depends strongly on the topology (see [26]).

As a conclusion, one may expect the critical properties of the phase transition between the C_b and B phases to be very similar in both topologically different realizations of the model. Below we show that this is indeed the case. The measurement of the critical behavior on the boundary between C_b and C phases may, on the other hand, be different, or at least difficult to be determined numerically.

4 The $B - C_b$ phase transition in the toroidal CDT

Below, we present the results of the $B - C_b$ phase transition study in CDT with the toroidal spatial topology. The $B - C_b$ transition was earlier studied in the spherical spatial topology [17, 18, 22] where it was classified to be the higher order transition. As explained in section 2 in order to investigate the phase transition one has to make a series of Monte

JHEP05(2020)030

Carlo simulations for various points in the CDT (κ_0, Δ) parameter space,[3] around the phase transition point. In this study all measurements were taken for one fixed value of $\kappa_0 = 2.2$ and for a sequence of Δ values.[4] In each simulation the $N_{4,1}$ lattice volume of the system (i.e. the total number of $\{4,1\}$ and $\{1,4\}$ simplices) is fixed or, more precisely, it fluctuates around the target value $\bar{N}_{4,1}$. The lattice volume is controlled by a volume-fixing potential

$$\delta V = \epsilon (N_{4,1} - \bar{N}_{4,1})^2 \tag{4.1}$$

added to the bare Einstein-Hilbert-Regge action of CDT (1.2) such that the volume is sharply peaked around a chosen value of $\bar{N}_{4,1}$, with a well-defined amplitude of fluctuations $\propto 1/\epsilon$. In the CDT Monte Carlo simulations one also has to set the length of the (periodic) time axis, i.e. the number of (integer) time slices T. In our case the number of time slices was equal $T = 4$, the numerical constant governing the magnitude of volume fluctuations was fixed at $\epsilon = 0.00002$ and measurements were performed every 10^7 attempted Monte Carlo moves (such that the measured $N_{4,1}$ volume could differ from the target $\bar{N}_{4,1}$ volume).[5]

In our analysis we will focus on the behaviour of four order parameters which have previously been successfully used in phase transition studies both in the spherical [18, 28, 29] and the toroidal [19, 30, 31] CDT,[6]

$$\begin{aligned} \mathrm{OP}_1 &= N_0/N_{4,1}, & \mathrm{OP}_2 &= N_{3,2}/N_{4,1}, \\ \mathrm{OP}_3 &= \sum_t (V_3(t+1) - V_3(t))^2, & \mathrm{OP}_4 &= \max_v O(v), \end{aligned} \tag{4.2}$$

where $V_3(t)$ is the spatial volume[7] in the time slice t and $O(v)$ is the vertex coordination number, i.e. the number of simplices sharing a given vertex v. The behaviour of the order parameters in all CDT phases has been summarized in table 2. Specifically when changing from the phase B to the phase C_b the OP_1, OP_2 and OP_4 increase in value while the OP_3 decreases, see figure 4. The MC simulations were performed for nine different (fixed) lattice volumes, i.e. for $\bar{N}_{4,1} = 40\mathrm{k}, 60\mathrm{k}, 80\mathrm{k}, 100\mathrm{k}, 120\mathrm{k}, 140\mathrm{k}, 160\mathrm{k}, 300\mathrm{k}, 400\mathrm{k}$. For each lattice volume $\bar{N}_{4,1}$ the approximate location of the $B - C_b$ phase transition point was found and then a series of precise measurement was performed for Δ in the range around the expected critical value Δ^c with a resolution of 0.001. Each measurement series was performed twice, each time for a different initial triangulation: one from phase B and one from phase C_b, and the two data series were compared in order to check thermalization

[3] In each Monte Carlo simulations the κ_4 is fine-tuned to the critical value, which depends on κ_0 and Δ and also on the lattice volume $N_{4,1}$.

[4] The same κ_0 value was earlier used in the $B - C_b$ transition studies in the spherical CDT.

[5] In principle MC simulation results could depend on the set of parameters used, such as the volume fixing method (one could e.g. fix the total N_4 volume instead of the $N_{4,1}$ volume) or the number of time slices T but as advocated in [19] the order of CDT phase transitions does not depend on that.

[6] Here we use a slightly different definition of OP_1 than in previous CDT phase transition studies, where it was: $\mathrm{OP}_1 \equiv N_0/N_4$. Current definition is more natural when $N_{4,1}$ volume is fixed (see equation (4.1)) which was the case in all MC simulations described herein.

[7] To ensure consistency with our earlier publications we define $V_3(t)$ as *twice* the number of spatial tetrahedra with the integer time coordinate t.

JHEP05(2020)030

	Phase A	Phase B	Phase C	Phase C_b
OP_1	large	small	medium	medium
OP_2	small	small	large	large
OP_3	medium	large	small	medium
OP_4	small	large	small	large

Table 2. Order parameters used in CDT phase transition studies.

and possible hysteresis, see e.g. figure 2. For each lattice volume $\bar{N}_{4,1}$ and each of the two measurement series ($s = B, C_b$) and each of the four order parameters OP_i ($i = 1, 2, 3, 4$) the precise position of the (volume dependent) pseudo-critical point $\Delta^c_{i,s}(N_{4,1})$ was established based on the peak of the $\mathrm{OP}_{i,s}$ susceptibility $\chi_{\mathrm{OP}_{i,s}}$, see figure 5 where we present the results of measurements for the lattice volume $\bar{N}_{4,1} = 100\mathrm{k}$. The values of $\Delta^c_{i,s}(N_{4,1})$ measured for different OP_i and in the two data series in general coincide up to the used Δ resolution. If the results for various OP_i or for various data series are different, usually shifted not more than by the Δ difference of 0.001, we simply take the arithmetic mean

$$\Delta^c(N_{4,1}) = \frac{1}{8} \sum_{s\in\{B,C_b\}} \sum_{i=1}^{4} \Delta^c_{i,s}(N_{4,1}) \tag{4.3}$$

and assign a correspondingly larger measurement error, e.g. for the lattice volume $\bar{N}_{4,1} = 100\mathrm{k}$ one has $\Delta^c(N_{4,1} = 100\mathrm{k}) = 0.0376 \pm 0.0016$.

Then we fit the finite size scaling relation (2.2) to the measured $\Delta^c(N_{4,1})$ values. The best fit of the true (infinite volume) critical point is $\Delta^c(\infty) = 0.073 \pm 0.004$, and the best fit of the critical scaling exponent is $\nu = 2.7 \pm 0.4$ which supports the higher-order nature of the $B - C_b$ phase transition, see also figure 6 where we plot the measured data together with the best fit of the scaling relation (2.2) and compare it to the fit with a forced value of $\nu = 1$ (typical for a first-order transition) showing that the quality of the latter fit is much worse. The measured values of the true critical point and the critical exponent also agree with $\Delta^c(\infty) = 0.077 \pm 0.004$ and $\nu = 2.51 \pm 0.03$ measured in CDT with the spherical spatial topology [18], giving strong evidence that the results are independent of the topology chosen (at least for the toroidal and the spherical one).

In order to corroborate this result, we have performed the detailed Monte Carlo history analysis of all order parameters at (and in the vicinity) of the measured pseudo-critical points, see figure 7 where we plot the MC history histograms of the OP_1 measured for the example $N_{4,1} = 100\mathrm{k}$ volume and for $\Delta = 0.037$ (peak of $\chi_{\mathrm{OP}_{1,B}}$) and $\Delta = 0.038$ (peak of $\chi_{\mathrm{OP}_{1,C_b}}$). In none of the cases have we observed the double peaks in the measured histograms nor the hysteresis of the measured data series. These results support the higher-order $B - C_b$ transition.

Finally, we have analyzed the behaviour of the Binder cumulants (2.3) in search of minima, see figure 8 where we plot data measured for $N_{4,1} = 100\mathrm{k}$. The value of pseudo-critical $\tilde{\Delta}^c_{i,s}(N_{4,1})$ defined by the minimum of the Binder cumulants $B_{\mathrm{OP}_{i,s}}$ in general coincides with the $\Delta^c_{i,s}(N_{4,1})$ value defined by the maximum of susceptibility $\chi_{\mathrm{OP}_{i,s}}$, the

JHEP05(2020)030

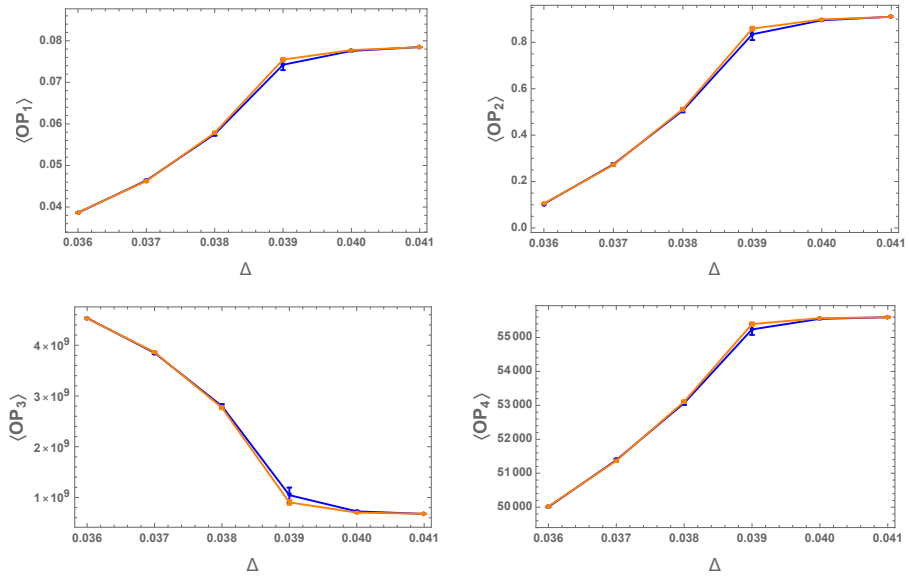

Figure 4. Mean values of the four order parameters (4.2) $\langle \mathrm{OP}_1 \rangle, \ldots, \langle \mathrm{OP}_4 \rangle$ as a function of Δ in the $B - C_b$ phase transition region in CDT with toroidal spatial topology for fixed $\kappa_0 = 2.2$ and the lattice volume $N_{4,1} = 100$k. Blue data points are for the MC series started from a triangulation in phase B while orange data points were started from a triangulation in phase C_b. Error bars were estimated using a single-elimination (binned) jackknife procedure, where the bin sizes were selected in such a way that the statistical errors are maximized.

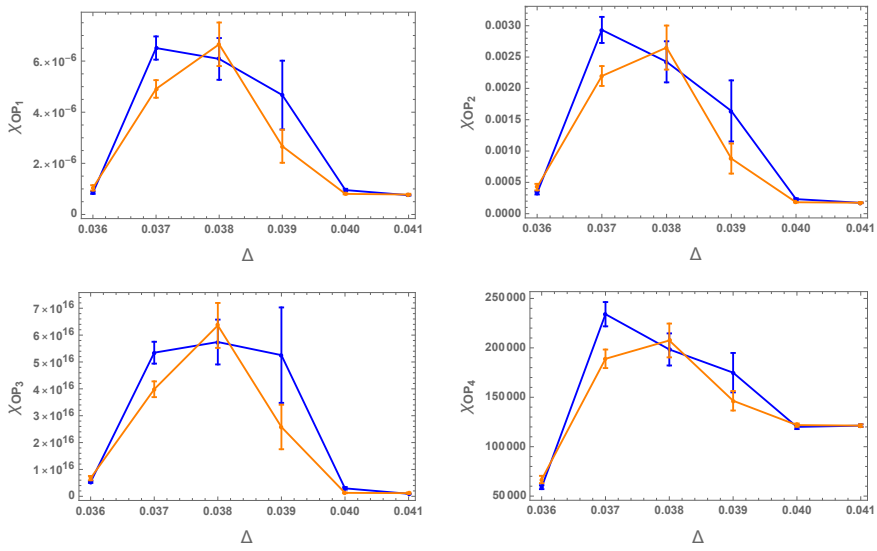

Figure 5. Susceptibilities (2.1) of the four order parameters (4.2) $\chi_{\mathrm{OP}_1}, \ldots, \chi_{\mathrm{OP}_4}$ as a function of Δ in the $B - C_b$ phase transition region in CDT with toroidal spatial topology for fixed $\kappa_0 = 2.2$ and the lattice volume $N_{4,1} = 100$k. Blue data points are for the MC series started from a triangulation in phase B while orange data points were started from a triangulation in phase C_b. Error bars were estimated using a single-elimination (binned) jackknife procedure, where the bin sizes were selected in such a way that the statistical errors are maximized.

JHEP05(2020)030

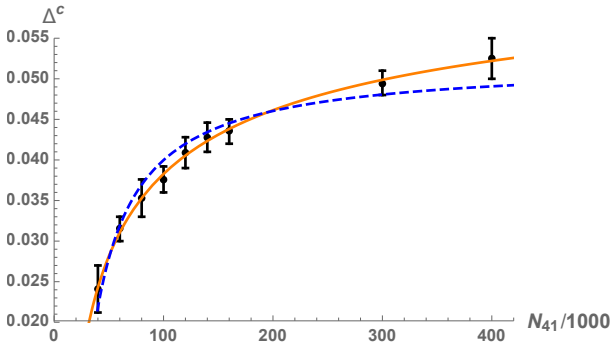

Figure 6. Lattice volume dependence of the pseudo-critical $\Delta^c(N_{4,1})$ values in CDT with toroidal spatial topology and for fixed $\kappa_0 = 2.2$ together with the fit of the finite size scaling relation (2.2) with critical exponent $\nu = 2.7$ (orange solid line) and the same fit with a forced value of $\nu = 1$ (blue dashed line).

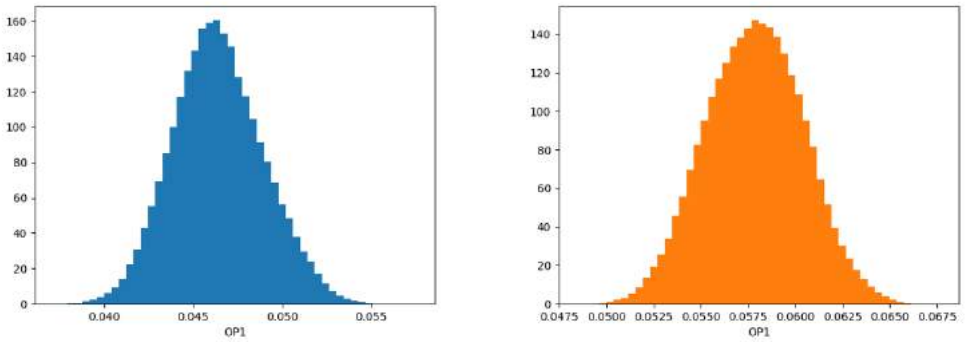

Figure 7. Histograms of the MC history of the OP_1 order parameter (4.2) measured in CDT with toroidal spatial topology for fixed $\kappa_0 = 2.2$ and the lattice volume $N_{4,1} = 100$k. The left plot is for data series started from configuration in phase B and $\Delta = 0.037$ (i.e. the peak of susceptibility χ_{OP_1} measured for this data series, see figure 5) while the right plot is for data series initiated in phase C_b and $\Delta = 0.038$ (peak of χ_{OP_1} for this data series).

possible shift is usually up to Δ difference of 0.001. In figure 9 we plot the measured values of $B^{\min}_{\mathrm{OP}_{i,s}}(N_{4,1}) \equiv B_{\mathrm{OP}_{i,s}}(\tilde{\Delta}^c_{i,s}(N_{4,1}))$ as the function of the lattice volume $N_{4,1}$.[8] All Binder cumulants measured for $\mathrm{OP}_1, \ldots, \mathrm{OP}_4$ visibly grow towards zero when $N_{4,1}$ is increased, which again favours the higher-order nature of the $B - C_b$ transition.

5 Summary and conclusions

Applying phase transition analysis methods described in section 2 to the $B - C_B$ transition in CDT with the toroidal spatial topology we have shown that the transition is most likely the higher-order phase transition. This result is supported both by the finite size scaling analysis of equation (2.2) showing the best fit scaling exponent $\nu = 2.7 > 1$, by the large

[8] In the plot we skip data measured for $N_{4,1} = 400$k which can be not accurate enough as these systems did not thermalize completely resulting in large measurements errors.

JHEP05(2020)030

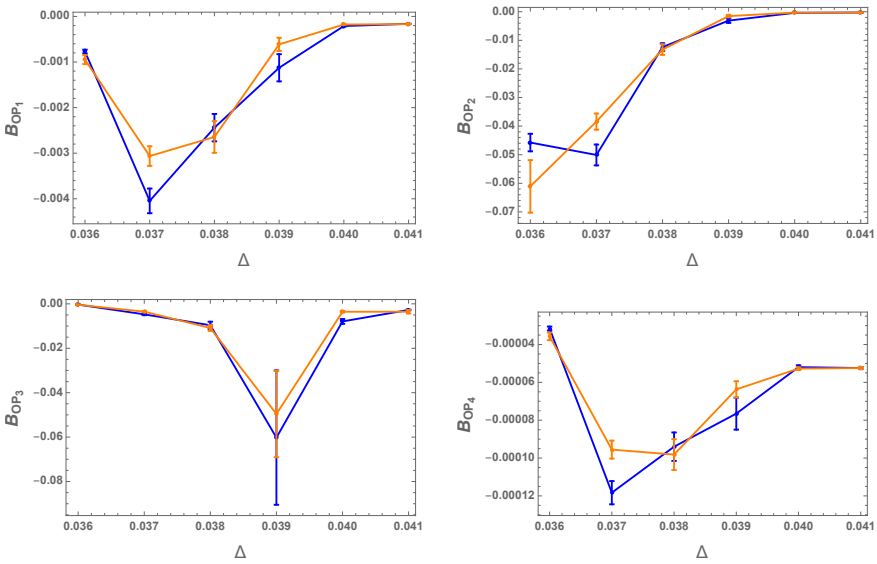

Figure 8. Binder cumulants (2.3) of the four order parameters (4.2) $B_{\mathrm{OP}_1}, \ldots, B_{\mathrm{OP}_4}$ as a function of Δ in the $B - C_b$ phase transition region in CDT with toroidal spatial topology for fixed $\kappa_0 = 2.2$ and the lattice volume $N_{4,1} = 100$k. Blue data points are for the MC series started from a triangulation in phase B while orange data points were started from a triangulation in phase C_b. Error bars were estimated using a single-elimination (binned) jackknife procedure, where the bin sizes were selected in such a way that the statistical errors are maximized.

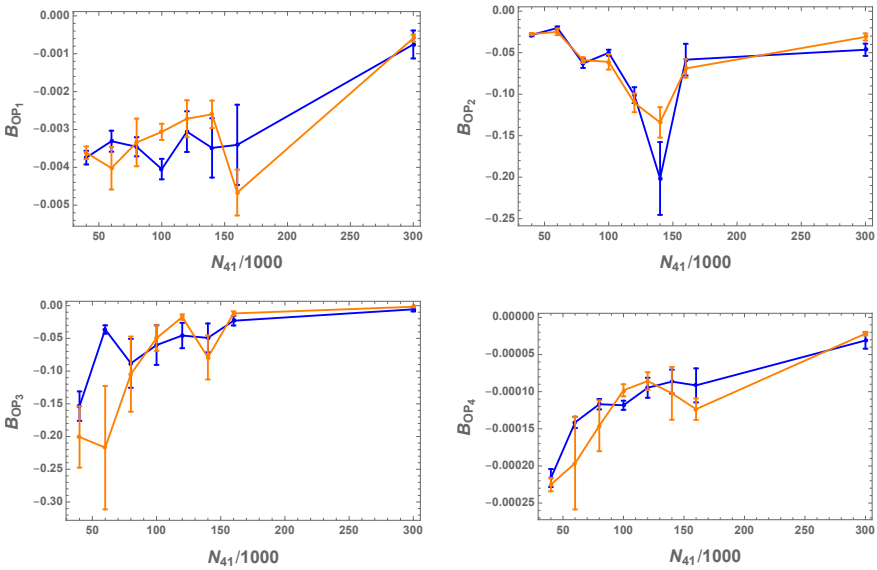

Figure 9. Lattice volume dependence of the Binder cumulant (2.3) minima $B^{\min}_{\mathrm{OP}_i}(N_{4,1})$ $(i = 1, \ldots, 4)$ in CDT with toroidal spatial topology and for fixed $\kappa_0 = 2.2$. Blue data points are for the MC series started from a triangulation in phase B while orange data points were started from a triangulation in phase C_b. Error bars were estimated using a single-elimination (binned) jackknife procedure, where the bin sizes were selected in such a way that the statistical errors are maximized.

JHEP05(2020)030

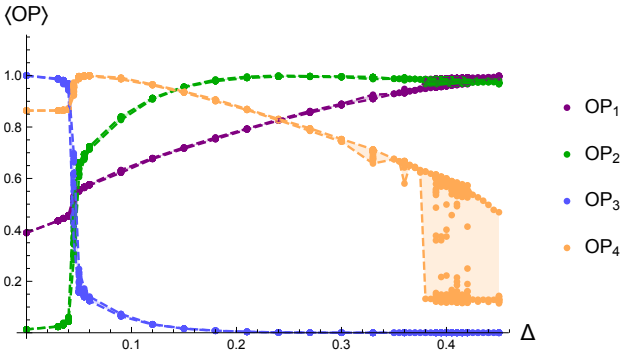

Figure 10. Rescaled order parameters $\langle \mathrm{OP}_1 \rangle, \ldots, \langle \mathrm{OP}_4 \rangle$ in CDT with the toroidal spatial topology measured for the (target) lattice volume $\bar{N}_{4,1} = 120k$ and $T = 4$ time slices. Data were measured for many different starting triangulations for each Δ ($\kappa_0 = 2.0$ is kept fixed), the number of starting configurations being different for various Δ. Each data point denotes $\langle \mathrm{OP}_i \rangle$ ($i = 1, 2, 3, 4$) measured from last 100k sweeps (1 sweep = 10^7 attempted MC moves), data from initial thermalization period were skipped. Shaded regions between the dashed lines denote the range of the measured data. Hysteresis is clearly visible for $\Delta \geq 0.38$, especially for the OP_4 parameter which is the most sensitive to the $C - C_b$ transition. This is not the case for the higher-order $B - C_b$ transition (described herein) observed around $\Delta \approx 0.05$.

volume behaviour of the Binder cumulant minima (2.4): $B^{\min}_{\mathrm{OP}_i}(N_{4,1} \to \infty) \to 0$ and by the lack of hysteresis/two-state jumping of the order parameters measured at the (pseudo) critical points.

The above result and also numerical values of the critical scaling exponent $\nu = 2.7 \pm 0.4$ and the true critical point $\Delta^c(\infty) = 0.073 \pm 0.004$ are also consistent with the $B - C_b$ transition measured in CDT with the spherical spatial topology for the same fixed value of the $\kappa_0 = 2.2$ parameter, where $\Delta^c(\infty) = 0.077 \pm 0.004$ and $\nu = 2.51 \pm 0.03$, respectively [18]. Thus the $B - C_b$ transition properties are the same in both spatial topologies. This is also the case for the $A - C$ transition which was found to be the first-order phase transition in both topologies — the detailed analysis of the $A - C$ transition in the spherical and the toroidal CDT for various Monte Carlo simulations' parameters (lattice volume fixing methods and lengths of the (integer) time period T) can be found in [19]. One can therefore formulate a conjecture that CDT results including the phase structure and the order of phase transitions are independent of the spatial topology choice, which is a parameter put in "by hand".

The question mark remains for the $C - C_b$ transition which was found to be the higher-order phase transition in the spherical CDT [28, 29][9] and has not been yet investigated in detail in the toroidal CDT. The reason is that in the toroidal CDT case one observes a very strong hysteresis in the $C - C_b$ transition region[10] (see figure 10) and therefore one is

[9] Recent studies based on spectral properties of three-dimensional time slices in the spherical CDT [32, 33] also indicate that the $C - C_b$ transition is most likely the higher-order phase transition.

[10] The hysteresis is observed for sufficiently large (target) lattice volumes $\bar{N}_{4,1}$ such that the the three-volume of each (integer) time slice $\sim \bar{N}_{4,1}/T$ is big enough to allow for creation of high-order vertices, for small $\bar{N}_{4,1}$ the bifurcation phase is not observed which is a finite-volume/discretization artifact.

JHEP05(2020)030

not able to perform precise MC measurements which would enable one to make finite size scaling analysis as it was explained in section 2. The very strong hysteresis would suggest that the $C - C_b$ transition is most likely the first-order transition in the toroidal CDT, i.e. the order of the transition would change due to the different spatial topology. But this can be as well an algorithmic issue of the MC code used in the CDT simulations and more advanced methods should be used in order to resolve this problem.[11] In the toroidal CDT one was also able to make MC simulations in the most interesting region of the CDT parameter space, namely in the vicinity of the two "triple" points where the $A - B - C$ and the $B - C - C_b$ phases meet (see the CDT phase diagram in figure 1), which was not possible in the spherical CDT where MC simulations got effectively "frozen" in this region of the phase diagram. As a result in the toroidal CDT one observes the direct $B - C$ transition which was classified to be the first-order transition, albeit with some atypical properties suggesting a possible higher-order transition [31]. Summing up, we have shown that the $B - C_b$ transition is the higher order transition which most likely makes the $B - C - C_b$ "triple" point the higher order transition point even though the $B - C$ and the $C - C_b$ transitions are possibly the first-order transitions. The above "triple" point is thus a natural candidate for an UV fixed point for QG [34, 35].

Acknowledgments

JA acknowledges support from the Danish Research Council grant no. 7014-00066B *Quantum Geometry*. JGS acknowledges support from the grant no. 2016/23/ST2/00289 from the National Science Centre, Poland. AG acknowledges support by the National Science Centre, Poland, under grant no. 2015/17/D/ST2/03479. JJ acknowledges support from the National Science Centre, Poland, grant no. 2019/33/B/ST2/00589. DN acknowledges support from the National Science Centre, Poland, under grants no. 2015/17/D/ST2/03479 and 2019/32/T/ST2/00389.

References

[1] G. 't Hooft and M.J.G. Veltman, *One loop divergencies in the theory of gravitation*, *Ann. Poincare Phys.Theor.* **A 20** (1974) 69.

[2] M.H. Goroff and A. Sagnotti, *The ultraviolet behavior of Einstein gravity*, *Nucl. Phys.* **B 266** (1986) 709 [INSPIRE].

[3] S. Weinberg, *General relativity, an Einstein centenary survey*, Cambridge University Press, Cambridge U.K. (1997).

[11] We are currently working on a "multi-canonical" Monte Carlo algorithm which should enable one to measure both sides of the hysteresis in a single MC run and thus to estimate the lattice volume dependence of the hysteresis size and the position of pseudo-critical points with much better precision.

JHEP05(2020)030

[4] M. Reuter, *Nonperturbative evolution equation for quantum gravity*, *Phys. Rev.* **D 57** (1998) 971 [hep-th/9605030].

[5] D.F. Litim, *Fixed points of quantum gravity*, *Phys. Rev. Lett.* **92** (2004) 201301 [hep-th/0312114] [INSPIRE].

[6] M. Niedermaier and M. Reuter, *The asymptotic safety scenario in quantum gravity*, *Living Rev. Rel.* **9** (2006) 5.

[7] A. Codello, R. Percacci and C. Rahmede, *Investigating the ultraviolet properties of gravity with a Wilsonian renormalization group equation*, *Annals Phys.* **324** (2009) 414 [arXiv:0805.2909] [INSPIRE].

[8] D. Benedetti, P.F. Machado and F. Saueressig, *Asymptotic safety in higher-derivative gravity*, *Mod. Phys. Lett.* **A 24** (2009) 2233 [arXiv:0901.2984] [INSPIRE].

[9] D.F. Litim, *Renormalisation group and the Planck scale*, *Phil. Trans. Roy. Soc. London* **A 369** (2011) 2759.

[10] J. Ambjørn, A. Görlich, J. Jurkiewicz and R. Loll, *Nonperturbative quantum gravity*, *Phys. Rept.* **519** (2012) 127 [arXiv:1203.3591] [INSPIRE].

[11] R. Loll, *Quantum gravity from causal dynamical triangulations: a review*, *Class. Quant. Grav.* **37** (2020) 013002 [arXiv:1905.08669] [INSPIRE].

[12] T. Regge, *General relativity without coordinates*, *Nuovo Cim.* **19** (1961) 558 [INSPIRE].

[13] J. Ambjørn, J. Jurkiewicz and R. Loll, *Dynamically triangulating Lorentzian quantum gravity*, *Nucl. Phys.* **B 610** (2001) 347 [hep-th/0105267] [INSPIRE].

[14] K. Binder, *Finite size scaling analysis of ising model block distribution functions*, *Z. Phys.* **B 43** (1981) 119.

[15] K. Binder, *Critical properties from monte carlo coarse graining and renormalization*, *Phys. Rev. Lett.* **47** (1981) 693 [INSPIRE].

[16] K. Binder and D.W. Heermann, *Monte Carlo simulation in statistical physics: an introduction*, Springer, Germany (2010).

[17] J. Ambjørn, S. Jordan, J. Jurkiewicz and R. Loll, *A second-order phase transition in CDT*, *Phys. Rev. Lett.* **107** (2011) 211303 [arXiv:1108.3932] [INSPIRE].

[18] J. Ambjørn, S. Jordan, J. Jurkiewicz and R. Loll, *Second- and first-order phase transitions in CDT*, *Phys. Rev.* **D 85** (2012) 124044 [arXiv:1205.1229] [INSPIRE].

[19] J. Ambjørn et al., *Critical phenomena in causal dynamical triangulations*, *Class. Quant. Grav.* **36** (2019) 224001 [arXiv:1904.05755] [INSPIRE].

[20] J. Ambjørn, J. Gizbert-Studnicki, A. Görlich and J. Jurkiewicz, *The effective action in 4-dim CDT. The transfer matrix approach*, *JHEP* **06** (2014) 034 [arXiv:1403.5940] [INSPIRE].

[21] J. Ambjørn, D.N. Coumbe, J. Gizbert-Studnicki and J. Jurkiewicz, *Signature Change of the Metric in CDT Quantum Gravity?*, *JHEP* **08** (2015) 033 [arXiv:1503.08580] [INSPIRE].

[22] J. Ambjørn et al., *Characteristics of the new phase in CDT*, *Eur. Phys. J.* **C 77** (2017) 152 [arXiv:1610.05245] [INSPIRE].

[23] J. Ambjørn, A. Görlich, J. Jurkiewicz and R. Loll, *Planckian birth of the quantum de Sitter universe*, *Phys. Rev. Lett.* **100** (2008) 091304 [arXiv:0712.2485] [INSPIRE].

JHEP05(2020)030

[24] J. Ambjørn, A. Görlich, J. Jurkiewicz and R. Loll, *The nonperturbative quantum de Sitter universe*, *Phys. Rev.* **D 78** (2008) 063544 [arXiv:0807.4481] [INSPIRE].

[25] J. Ambjørn et al., *The semiclassical limit of causal dynamical triangulations*, *Nucl. Phys.* **B 849** (2011) 144 [arXiv:1102.3929] [INSPIRE].

[26] J. Ambjørn et al., *Impact of topology in causal dynamical triangulations quantum gravity*, *Phys. Rev.* **D 94** (2016) 044010 [arXiv:1604.08786] [INSPIRE].

[27] J. Ambjørn et al., *Four-dimensional CDT with toroidal topology*, *Nucl. Phys.* **B 922** (2017) 226 [arXiv:1705.07653] [INSPIRE].

[28] D.N. Coumbe, J. Gizbert-Studnicki and J. Jurkiewicz, *Exploring the new phase transition of CDT*, *JHEP* **02** (2016) 144 [arXiv:1510.08672] [INSPIRE].

[29] J. Ambjørn et al., *New higher-order transition in causal dynamical triangulations*, *Phys. Rev.* **D 95** (2017) 124029 [arXiv:1704.04373] [INSPIRE].

[30] J. Ambjørn et al., *The phase structure of Causal Dynamical Triangulations with toroidal spatial topology*, *JHEP* **06** (2018) 111 [arXiv:1802.10434] [INSPIRE].

[31] J. Ambjørn et al., *Towards an UV fixed point in CDT gravity*, *JHEP* **07** (2019) 166 [arXiv:1906.04557] [INSPIRE].

[32] G. Clemente and M. D'Elia, *Spectrum of the Laplace-Beltrami operator and the phase structure of causal dynamical triangulations*, *Phys. Rev.* **D 97** (2018) 124022 [arXiv:1804.02294] [INSPIRE].

[33] G. Clemente, M. D'Elia and A. Ferraro, *Running scales in causal dynamical triangulations*, *Phys. Rev.* **D 99** (2019) 114506 [arXiv:1903.00430] [INSPIRE].

[34] J. Ambjørn et al., *Renormalization Group Flow in CDT*, *Class. Quant. Grav.* **31** (2014) 165003 [arXiv:1405.4585] [INSPIRE].

[35] J. Ambjørn et al., *Renormalization in quantum theories of geometry*, arXiv:2002.01693.

JHEP05(2020)030

Published for SISSA by Springer

Received: June 17, 2019
Accepted: July 9, 2019
Published: July 29, 2019

Towards an UV fixed point in CDT gravity

J. Ambjørn,[b,c] **J. Gizbert-Studnicki,**[a] **A. Görlich,**[a] **J. Jurkiewicz**[a] **and D. Németh**[a]

[a] *The M. Smoluchowski Institute of Physics, Jagiellonian University, Łojasiewicza 11, Kraków, PL 30-348, Poland*
[b] *The Niels Bohr Institute, Copenhagen University, Blegdamsvej 17, DK 2100 Copenhagen, Denmark*
[c] *IMAAP, Radboud University, PO Box 9010, Nijmegen, The Netherlands*

E-mail: ambjorn@nbi.dk, jakub.gizbert-studnicki@uj.edu.pl, andrzej.goerlich@uj.edu.pl, jerzy.jurkiewicz@uj.edu.pl, dnemeth@th.if.uj.edu.pl

Abstract: CDT is an attempt to formulate a non-perturbative lattice theory of quantum gravity. We describe the phase diagram and analyse the phase transition between phase B and phase C (which is the analogue of the de Sitter phase observed for the spherical spatial topology). This transition is accessible to ordinary Monte Carlo simulations when the topology of space is toroidal. We find that the transition is most likely first order, but with unusual properties. The end points of the transition line are candidates for second order phase transition points where an UV continuum limit might exist.

Keywords: Lattice Models of Gravity, Lattice Quantum Field Theory, Models of Quantum Gravity

ArXiv ePrint: 1906.04557

https://doi.org/10.1007/JHEP07(2019)166

JHEP07(2019)166

Contents

1 **Introduction** 1

2 **The phase structure of CDT** 5

3 **Order parameters** 9

4 **Conclusion and discussion** 13

JHEP07(2019)166

1 Introduction

Since the middle of last century physicists have been pursuing the idea of unifying the four fundamental interactions, the strong, the weak, the electromagnetic and the gravitational interactions. The framework of Quantum Field Theory (QFT) unified the first three of them in the so-called Standard Model. Including gravity remains an unsolved problem in a QFT context.[1] Difficulties appear when one tries to formulate a quantum version of Einstein's theory of General Relativity. The naive quantization leads to a perturbatively non-renormalizable theory which cannot be simply included in the unified model of all interactions. The idea of asymptotic safety introduced by Weinberg [1] is an attempt to formulate a non-perturbative QFT of gravity. It assumes that the renormalization group flow in the bare coupling constant space leads to a non-trivial finite-dimensional ultraviolet fixed point around which a new perturbative expansion can be constructed which leads to a predictive quantum theory of gravity. The so-called Exact Renormalization Group program [2–6] has tried to establish the existence of such a fixed point with a fair amount of success, but relies in the end, despite the name, on truncation of the renormalization group equations. Thus it would be reassuring if other non-perturbative QFT approaches could confirm the exact renormalization group results.

Lattice QFT is such a non-perturbative framework and it is well suited to deal precisely with the situation where one identifies fixed points, since these are where one wants to reach continuum physics by scaling the lattice spacing to zero in a way which keeps physics fixed. It has been very successful providing us with results for QCD which are not accessible via perturbation theory. There exists a number of lattice QFT of gravity. One of them, the so-called Dynamical Triangulation (DT) formalism [7–12] has provided us with a "proof of concept", in the sense that it has shown us, in the case of two-dimensional quantum gravity [13–16], that the continuum limit of the lattice theory of gravity coupled to conformal field theories agree with the corresponding continuum theories. Of course there are no propagating gravitational degrees of freedom in two dimensions, but the main issue

[1] Going beyond conventional QFT, string theory provides us with a theory unifying the interaction of matter and gravity. Likewise loop quantum gravity uses concepts beyond conventional QFT.

with the lattice regularization is whether or not diffeomorphism invariance is recovered when the lattice spacing goes to zero. That is the case in the DT formalism, and for the conformal field theories living on the lattice one obtains precisely the non-trivial critical scaling dimensions obtained also in the continuum, i.e. scaling dimensions which are different from the ones in flat spacetime (the so-called KPZ scaling [17–19]). The DT formalism was extended to higher dimensional gravity [20–27], but there it was less successful [28, 29]. It is not ruled out that the theory can provide us with a successful version of quantum gravity, but if so the formulation has to be more elaborate than the first models (see [30–33] for recent attempts). However, there is one modification of DT which seems to work in the sense that lattice theory might have a non-trivial continuum limit, the so-called Causal Dynamical Triangulations model (CDT). The model is more constrained than the DT models because one assumes global hyperbolicity, i.e. the existence of a global time foliation.

The CDT model of four-dimensional quantum gravity is realized by considering piecewise linear simplicial discretizations of space-time. The simplicial building blocks can be glued together, satisfying the basic topological constraints of global hyperbolicity (as mentioned) and a simplicial manifold structure. The quantum model is now defined using the Feynman path integral formalism, summing over all such geometries with a suitable action to be defined below. The spatial Universe with a fixed topology evolves in proper time. Geometric states at a fixed value of the (discrete) time are triangulated, using regular three-dimensional simplices (tetrahedra) glued along triangular faces in all possible ways, consistent with topology. The common length of the edges of spatial links is assumed to be a_s. Tetrahedra are the bases of four-dimensional $\{4,1\}$ and $\{1,4\}$ simplices with four vertices at time t connected by time links to a vertex at $t \pm 1$. All time edges are assumed to have a universal length a_t. To construct a four-dimensional manifold one needs two additional types of four-simplices: $\{3,2\}$ and $\{2,3\}$ (having three vertices at time t and two vertices at $t \pm 1$). The structure described above permits for every configuration the analytic continuation between imaginary a_t (Lorentzian signature) and real a_t (Euclidean signature). Even after Wick rotation the orientation of the time axis is remembered. The spatial and time links may have a different length, and are related by $\alpha a_s^2 = a_t^2$. The quantum amplitude between the initial and final geometric states separated by the integer time T is a weighted sum over all simplicial manifolds connecting the two states. In the Lorentzian formulation the weight is assumed to be given by a discretized version of the Hilbert-Einstein action.

$$\mathcal{Z}_{\mathcal{QG}} = \int \mathcal{D}_{\mathcal{M}}[g] e^{iS_{EH}[g]} \tag{1.1}$$

where $[g]$ denotes an equivalent class of metrics and $\mathcal{D}_{\mathcal{M}}$[g] is the integration measure over nonequivalent classes of metrics. A piecewise linear manifold where we have specified the length of links defines a geometry without the need to introduce coordinates. In the CDT approach the integration over equivalent classes of metrics is thus replaced by a summation over all triangulations $\mathcal{T}$ satisfying the constraints. After a Wick rotation the amplitude becomes a partition function

$$\mathcal{Z}_{\mathcal{CDT}} = \sum_{\mathcal{T}} e^{-S_R[\mathcal{T}]}, \tag{1.2}$$

JHEP07(2019)166

where S_R is a suitable form of the Einstein-Hilbert action on piecewise linear geometries. There exists such an action, which even has a nice geometric interpretation, the so-called Regge action S_R for piecewise linear geometries [34]. In our case it becomes very simple because we have only two kinds of four-simplices which we glue together to form our piecewise linear four-manifold:

$$S_R = -(K_0 + 6\Delta) \cdot N_0 + K_4 \cdot (N_{41} + N_{32}) + \Delta \cdot N_{41}, \tag{1.3}$$

where N_0 is the number of vertices in a triangulation $\mathcal{T}$, N_{41} and N_{32} are the numbers of $\{4,1\}$ plus $\{1,4\}$ and $\{3,2\}$ plus $\{2,3\}$ simplices, respectively. The action is parametrized by a set of three dimensionless bare coupling constants, K_0, related to the inverse gravitational constant, K_4 — the dimensionless cosmological constant and Δ — a function of the parameter α, the ratio of the spatial and time edge lengths (for a detailed discussion we refer to [35] and to the most recent review [36] and for the original literature to [37, 38]). The amplitude is defined for $K_4 > K_4^{\rm crit}$ and the limit $K_4 \to K_4^{\rm crit}$ corresponds to a (discrete) infinite volume limit. In this limit, the properties of the model depend on values of the two remaining coupling constants. The model was extensively studied in the case, where the spatial topology was assumed to be spherical (S^3) [39–45]. The model could not be solved analytically and the information about its properties was obtained using Monte Carlo simulations. It was found that the model has a surprisingly rich phase structure, with four different phases. The most interesting among the four phases is phase C, where the model dynamically develops a semiclassical background geometry which in some respect is like (Euclidean) de Sitter geometry, i.e. like the geometry of S^4. Both the semiclassical volume distribution and fluctuations around this distribution can be interpreted in terms of a minisuperspace model [46–49]. For increasing K_0 phase C is bounded by a first-order phase transition to phase A, where the time correlation between the consecutive slices is absent. For smaller Δ phase C has a phase transition to a so-called bifurcation phase, where one observes the appearance of local condensations of geometry around some vertices of the triangulation [50–53]. The phase transition is in this case of second or higher order. For still lower Δ the bifurcation phase is linked with the fourth phase, the so-called B phase, where one observes a spontaneous compactification of volume in the time direction, such that effectively all volume condenses in one time slice. The phase transition between the bifurcation phase and the B phase is also of second or higher order [44]. The behavior of the model near continuous phase transitions is crucial if one wants to define a *physical* large-volume limit (a careful discussion of this can be found in [54]). In this respect phase C stands out, the reason being that only in this phase the large scale structure of the average geometry is "observed" (via the Monte Carlo simulations) to be four-dimensional, isotropic and homogeneous, and one can define an infrared semiclassical limit with a correct scaling of the physical volume [42, 46]. Via phase C we thus want a renormalization group flow in the bare coupling constant space towards an UV fixed point (the asymptotic safety fixed point), while keeping physical observables fixed. The natural endpoint of such a flow would be a point in the phase diagram where several phases meet. In the early studies it was speculated that there could be a quadruple point, where all four phases meet. Unfortunately the numerical algorithm used was not efficient in this most physically interesting

JHEP07(2019)166

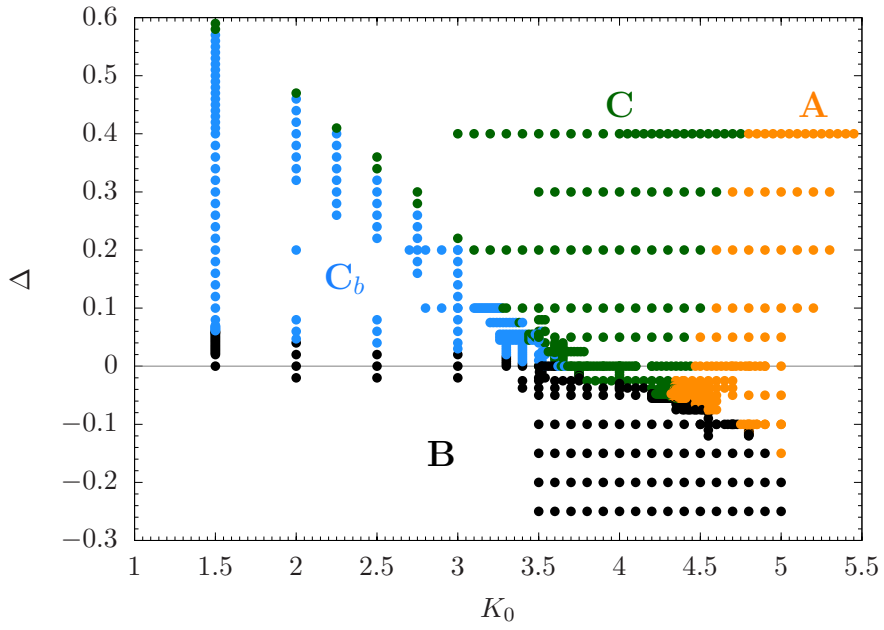

Figure 1. The phase structure of CDT for a fixed number of time slices $T = 4$ and average lattice volume $\bar{N}_{41} = 160$k. Blue color represents the bifurfaction phase, black color the crumpled phase, green color the C phase and orange color the A phase.

range in the coupling constant space. As a consequence it was not possible to analyze the model in this range.

The present article discusses a new formulation of the model, where the spatial topology is assumed to be that of a three-torus (T^3) [55–57], rather than that of a three-sphere, which was the topology used in all the former studies. It was found that the four phases in this case are the same as in the spherical model, with the position of phase boundaries shifted a little.[2] The additional, important bonus in this new formulation comes from the fact that the physically interesting region in the bare coupling constant space mentioned above becomes numerically accessible with the standard algorithm used in the earlier studies. We could then observe that the speculative quadruple point, maybe not surprisingly, separates into two triple points, connected by a phase transition line between phase C and the B phase, and not separated by the bifurcation phase (see figure 1). An important point is that we now have access to these triple points directly from phase C and it is thus possible to have a renormalization group flow from the infrared to the potential UV fixed point entirely in the "physical" C phase.

The phases of the model were identified for a system with $\bar{N}_{41} = 160$k, analyzing the structure of geometry at the grid of points in the coupling constant plane shown in figure 1, the different phases represented by dots with different colors. In the presented phase diagram the precise position of phase transitions was not determined. This requires a careful study of the infinite volume limit and scaling of the position of phase transition

[2]This may be a finite-size effect. The diagram was determined by analyzing systems with only one volume.

JHEP07(2019)166

lines with the lattice volume. The most interesting region is the one separating phase C and B where we may observe two triple points. The present paper is the first step in the analysis of this most physically interesting region. We will perform a detailed analysis of the behavior of the model at $K_0 = 4.0$ in the neighborhood of the phase transition line. We will try to determine the order of the phase transition at this point. We will show that the transition seems to be a first order transition. The results presented in this article show that the most interesting region in the bare parameter space can successfully be analyzed using the standard Monte Carlo algorithm used in the earlier simulations.

2 The phase structure of CDT

As mentioned, the phase diagram of the CDT model with a toroidal spatial topology permits us to investigate the properties of the model in an important range of the bare coupling constants, previously inaccessible to numerical measurements. For systems with a spherical spatial topology a detailed analysis of the phase diagram was performed following two lines in the bare coupling constant space. These were the vertical line with varying Δ at $K_0 = 2.2$ and the horizontal line at $\Delta = 0.6$. In the first case it was possible to analyze the phase transition between C and bifurcation phases and between the bifurcation and B phases. In the second case a transition between the C and A phases was studied (see [58] for recent results). The belief coming from the analysis of the spherical case was that if we decrease the value of Δ for a fixed value of K_0 we necessarily move from C phase to the bifurcation phase and only, for still lower Δ, to the B phase. However, changing to toroidal spatial topology we discovered that this is not the case, probably also in the spherical topology. There exists a range of bare coupling constants where C and B phases are directly neighboring. This happens close to the $\Delta = 0$ line in the range of K_0 between, approximately, 3.5 and 4.5. One may expect the existence of two triple points (instead of the previously conjectured quadruple point): one triple point where C, A and B phases meet, and a second triple point where C, bifurcation and B phases meet. Finding the precise location of the triple points may be numerically more difficult than analyzing the generic transition between phase C and B. As a first step in the detailed analysis we have chosen to determine the position and the order of the phase transition between C and B phases along a vertical line at $K_0 = 4.0$. This is approximately in the middle between the position of the two triple points. Since the characteristic behavior in the two phases corresponds to different symmetries of the configurations (we have translational symmetry in time in the C phase and a spontaneous breaking of this symmetry in the B phase) we expect a relatively large hysteresis when we cross the phase boundary. We want to find methods which make the hysteresis effect as small as possible. We also expect relatively large finite size effects. An important point in the analysis will be to check how the hysteresis behaves when the system size goes to infinity.

The analysis presented in the paper is based on a study of systems with a fixed time period $T = 4$ and different (almost) fixed volumes N_{41}. In the earlier studies, it was shown that reducing the period T does not produce significant finite-size effects [58]. On the other hand, in particular in the C phase, the average volume per time slice for a fixed total volume gets relatively large, which is very important. In the Monte Carlo simulations we

JHEP07(2019)166

enforce the lattice volume N_{41} to fluctuate around a chosen value $\bar{N}_{41}$, so that the measured $\langle N_{41} \rangle = \bar{N}_{41}$. This is realized by adding to the Regge action (1.3) a volume-fixing term

$$S_R \to S_R + \epsilon (N_{41} - \bar{N}_{41})^2. \tag{2.1}$$

In the thermalization process it is essential to fine-tune the value of K_4 in such a way that one gets stability of the system volume. This is realized by letting the value of K_4 dynamically change by small steps, until the required stable situation is realized. If a value of K_4 is too high, we observe that system volume stabilizes below the target value $\bar{N}_{41}$. Similarly, if we take it too small, the volume will be too large. Only for $K_4 \approx K_4^{\rm crit}(\bar{N}_{41})$ fluctuations of volume are centered around $\bar{N}_{41}$ with the width controlled by ϵ. During the thermalization part of the Monte Carlo simulations the algorithm tries to find the optimal value of K_4 for a given fixed set of parameters K_0, Δ and $\bar{N}_{41}$. The whole process of measurements is organized in the following way:

- We start a sequence of thermalization runs at a set of Δ values in the neighborhood of the expected position of the phase transition. The initial configuration of the system is taken to be the small hyper-cubic configuration discussed in reference [55]. We choose the target volume $\bar{N}_{41}$ and let the system size grow towards $\bar{N}_{41}$ and adapt the K_4 value from the guessed initial value. The initial K_4 can be chosen either a little below or a little above the guessed critical value.

- We find that on the grid of Δ values we can determine ranges corresponding to the appearance of two different phases, with a relatively sudden jump between the phases. In general the jump is observed between two neighboring values on the grid of Δ. The corresponding values of K_4 are markedly different in the two phases. Typically the value is smaller for the C phase than for the B phase. We can determine the phase of the system by the measured values of the order parameters (see later for definitions), which are very different in the different phases.

- The value of Δ where the phase transition is observed depends on the initial value of K_4 used in the thermalization process. As a consequence, we observe in general two values $\Delta^{\rm crit}_{\rm low}(N_{41})$ and $\Delta^{\rm crit}_{\rm high}(N_{41})$. Both values are determined with the accuracy depending on the grid of Δ.

- We repeat the analysis on a finer grid, which covers the range where we observed phase transitions. We found the most effective procedure is to restart the Monte Carlo evolution from the same small initial configuration as before, but using as the initial values of K_4 the ones determined for the C or the B phase from earlier runs in the neighborhood of the transitions, corresponding to $\Delta^{\rm crit}_{\rm low}(N_{41})$ or $\Delta^{\rm crit}_{\rm high}(N_{41})$ respectively.

- A finer grid permits to determine the two positions of the phase transition with better accuracy. The different position of jumps between the two phases (*low* or *high*) can be interpreted as the hysteresis effect in a process where we slowly increase the value of the Δ parameter or slowly decrease its value. *We observe that the size*

JHEP07(2019)166

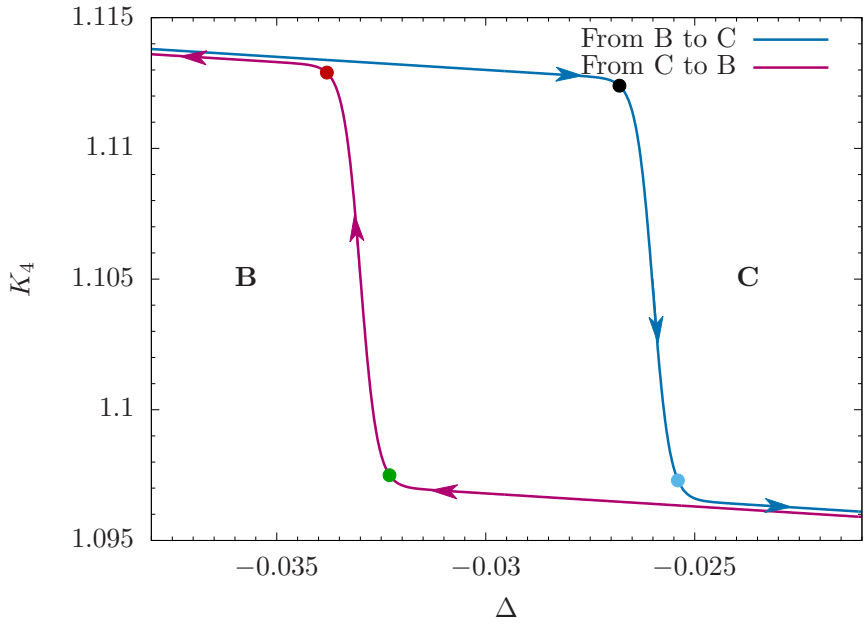

Figure 2. The plot illustrates the hysteresis measured during simulations for the target volume $\bar{N}_{41} = 160$k. The green and blue dots correspond to the location of the phase C side of the phase-transition, while the red and black dots correspond to the location of the phase B side of the phase-transition. The same colors will be used in the next plots, where we compare results for different volumes.

of the hysteresis for a particular choice of $\bar{N}_{41}$ *does not decrease within reasonable thermalization times. By taking a finer grid in* Δ *we can only determine the end points of a hysteresis curve with a better accuracy.* We illustrate the situation in figure 2. The lines shown were obtained from the measured values of Δ and K_4 for $\bar{N}_{41} = 160$k.

- In the range of Δ values between $\Delta^{\rm crit}_{\rm low}(N_{41})$ and $\Delta^{\rm crit}_{\rm high}(N_{41})$, depending on the initial value of K_4 a system ends either in the B or C phase. This can be interpreted as a range of parameters, where the two phases may coexist. The distribution of the values of the order parameters (to be defined below), characteristic for the two phases, is very narrow. As a consequence, a tunnelling between the two phases is never observed after we have reached a "stable" ensemble of configurations in the thermalization stage.

The thermalization path chosen above means in practice, that in the beginning, the system grows in a relatively random way from the initially small configuration to the desired target volume $\bar{N}_{41}$ and the geometry evolves to a stable range in the configuration space. The first step can be interpreted as a step in the direction typical for the phase A, where correlations between the spatial configurations in the consecutive time slices are small or absent. Only afterwards we reach the domains corresponding to the two phases we study. As a consequence, we expect that the described method will be very well suited to the future analysis of the triple point involving the A phase.

JHEP07(2019)166

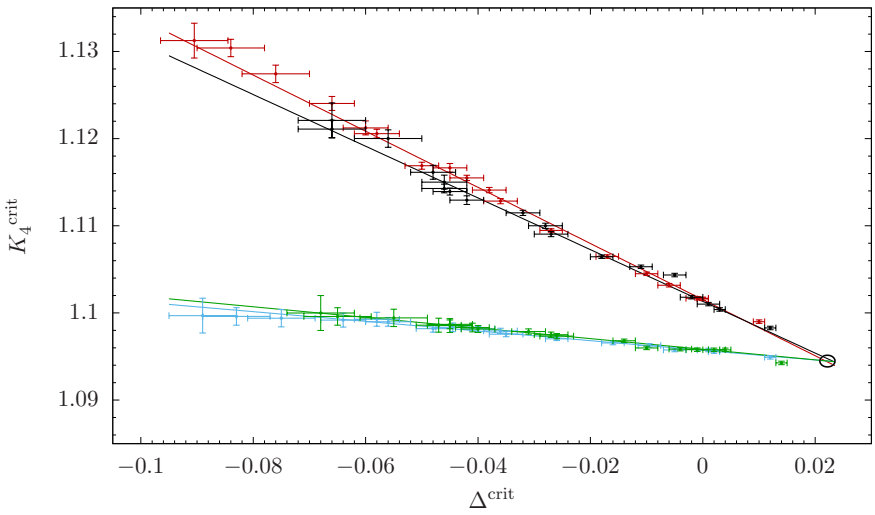

Figure 3. The pseudo-critical value $K_4^{\rm crit}(N_{41})$ as a function of $\Delta^{\rm crit}(N_{41})$. The data points measured for increasing lattice volume $\bar{N}_{41}$ are going from left to right. Center of the black ellipse corresponds to the estimated position of $(\Delta^{\rm crit}(\infty)\,,\ K_4^{\rm crit}(\infty))$ and its radii correspond to the estimated uncertainties. Colors of the fits follow the convention used in figure 2.

The behavior of the pseudo-critical values $K_4^{\rm crit}(N_{41})$ is very similar to that of $\Delta^{\rm crit}(N_{41})$. This can be seen in figure 3, where we show the values of $K_4^{\rm crit}(N_{41})$ plotted as a function of $\Delta^{\rm crit}(N_{41})$. On both sides of the hysteresis the dependence is approximately linear, which means that values of both pseudo-critical parameters ($K_4^{\rm crit}$ and $\Delta^{\rm crit}$) scale in the same way with the lattice volume $\bar{N}_{41}$. Extrapolating the lines to a point where they cross permits to determine values for $K_4^{\rm crit}$ and $\Delta^{\rm crit}$ in the limit $\bar{N}_{41} \to \infty$. The fit gives $K_4^{\rm crit}(\infty) = 1.095 \pm 0.001$ and $\Delta^{\rm crit}(\infty) = 0.022 \pm 0.002$. The errors on this and other plots are the estimated statistical errors and include the grid spacing for Δ.

Although the size of the hysteresis shrinks with volume $\bar{N}_{41}$, the plots indicate that the shrinking process is relatively slow and thus in order to get rid of the hysteresis one should use extremely large lattice volumes, not tractable numerically. The dependence of $\Delta^{\rm crit}$ on the lattice volume, ranging between $\bar{N}_{41} = 40$k and $\bar{N}_{41} = 1600$k is presented in figure 4. As it was explained above, the plot contains four sets of data corresponding to the four different points describing the hysteresis (see figure 2). The data points can be fitted with the curve

$$\Delta^{\rm crit}(\bar{N}_{41}) = \Delta^{\rm crit}(\infty) - A \cdot \bar{N}_{41}^{-1/\gamma}. \tag{2.2}$$

The best fit for the combined sets of data (with fixed $\Delta^{\rm crit}(\infty) = 0.022$ determined above) was obtained for $\gamma = 1.64 \pm 0.18$. An alternative fit with $\gamma = 1$ (and the same value of $\Delta^{\rm crit}(\infty)$) is excluded as can be seen in figure 4 (the dashed line). The value $\gamma = 1$ would be a strong evidence for a first order transition. The fits were based on data measured for volumes ranging from $\bar{N}_{41} = 40$k to $\bar{N}_{41} = 720$k. The largest volume $\bar{N}_{41}$ =1600k was used only for checking consistency with the extrapolations The analogous plot presenting the four sets of the pseudo-critical $K_4^{\rm crit}(\bar{N}_{41})$ values for the same range of volumes is shown in

JHEP07(2019)166

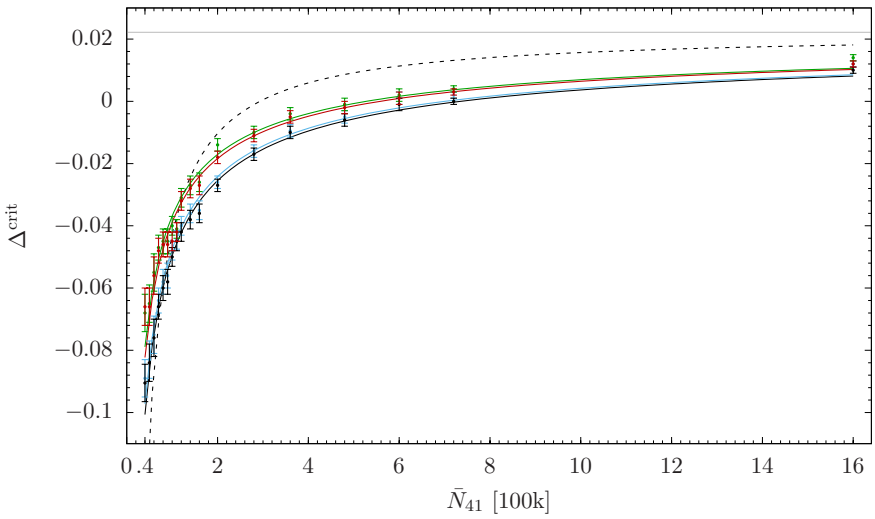

Figure 4. The pseudo-critical value $\Delta^{\rm crit}$ as a function of $\bar{N}_{41}$. The solid lines are (one parameter) fits of formula (2.2) with fixed common values of $\gamma = 1.64$ and $\Delta^{\rm crit}(\infty) = 0.022$. Colors of the fits follow the convention used in figure 2. The dashed line shows a common fit of all data points to the scaling function (2.2) with enforced value of $\gamma = 1$ and $\Delta^{\rm crit}(\infty) = 0.022$.

figure 5. The experimental points are again well fitted by the formula

$$K_4^{\rm crit}(\bar{N}_{41}) = K_4^{\rm crit}(\infty) - B \cdot \bar{N}_{41}^{-1/\gamma}, \tag{2.3}$$

where the measured value of $\gamma = 1.62 \pm 0.25$ agrees well with the result obtained for $\Delta^{\rm crit}$. The fits are represented by curves with different colors, which again follow the convention used in figure 2. On the scale used in this plot the green and blue curves practically overlap.

3 Order parameters

To identify the phases of CDT with toroidal spatial topology we follow methods used in the previous studies. These are based on the analysis of order parameters which have a different behavior in the different phases. We use order parameters which characterize both global and local properties of the simplicial manifolds. The global order parameters were called $\mathcal{O}_1$ and $\mathcal{O}_2$, where

$$\mathcal{O}_1 = \frac{N_0}{N_{41}}, \quad \mathcal{O}_2 = \frac{N_{32}}{N_{41}}. \tag{3.1}$$

In each phase the distributions of N_0 and N_{32} are very narrow, and practically Gaussian. Phases B and C are characterized by very different average values for the two distributions. The dependence of the order parameters $\mathcal{O}_1$ and $\mathcal{O}_2$ on $\bar{N}_{41}$ at the endpoints of the hysteresis is presented in figure 6. The colors follow the convention used in figure 2.

The data presented on the plots correspond for each $\bar{N}_{41}$ to the four values of the $\Delta^{\rm crit}(N_{41})$ points, following again the notation of figure 2. It is seen that although both pseudo-critical values $K_4^{\rm crit}(N_{41})$ and $\Delta^{\rm crit}(N_{41})$ become very close for increasing $\bar{N}_{41}$, *this is not the case for the order parameters, which in fact behave in a way similar to that*

JHEP07(2019)166

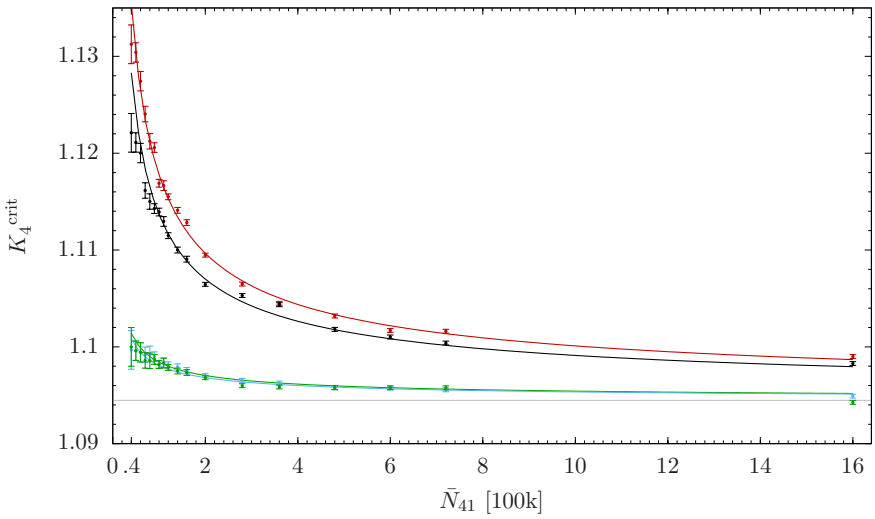

Figure 5. The pseudo-critical value $K_4^{\rm crit}$ as a function of $\bar{N}_{41}$. The solid lines are (one parameter) fits of formula (2.3) with fixed common values of $\gamma = 1.62$ and $K_4^{\rm crit}(\infty) = 1.095$. Colors of the fits follow the convention used in figure 2.

characterizing the first order transition. It means that a transition between the B and C phases becomes very rapid. On the other hand, due to the observed hysteresis, the method used in this analysis chooses a position of measured values for the order parameters slightly away from the *true* transition point (located inside the hysteresis region) and thus in fact we were not able to perform stable simulations exactly at $K_4^{\rm crit}(N_{41})$ and $\Delta^{\rm crit}(N_{41})$ corresponding to such a transition point.[3]

A similar behavior is observed for the set of local order parameters $\mathcal{O}_3$ and $\mathcal{O}_4$ defined by

$$\mathcal{O}_3 = \sum_t (n_{t+1} - n_t)^2, \quad \mathcal{O}_4 = \max o_p. \tag{3.2}$$

Here n_t is the number of tetrahedra shared by $\{4,1\}$ and $\{1,4\}$ four-simplices with bases at time t and $\sum_t n_t = \sum_t \frac{1}{2} N_{41}(t) = \frac{1}{2} N_{41}$. $\max o_p$ is the maximal order of a vertex in a triangulation. The typical behavior of these two order parameters is expected to be different in phases B and C. Phase B is characterized by having a macroscopic fraction of the four-volume concentrated at a single spatial slice corresponding to some time t (in the sense that almost all $\{4,1\}$ and $\{1,4\}$ four-simplices have four vertices at this spatial slice). This is accompanied by the appearance of two singular vertices located at times $t \pm 1$ and shared by a macroscopic number of four-simplices in a triangulation. As a consequence, in phase B $\frac{\mathcal{O}_3}{\bar{N}_{41}^2}$ and $\frac{\mathcal{O}_4}{\bar{N}_{41}}$ should be of order one. In phase C there is no such degeneracy and for large $\bar{N}_{41}$ both $\frac{\mathcal{O}_3}{\bar{N}_{41}^2}$ and $\frac{\mathcal{O}_4}{\bar{N}_{41}}$ should approach zero. The behavior of these two order parameters is presented in figure 7.

[3] We are currently working on the numerical algorithm which would enable tunneling between both sides of the hysteresis region in a single Monte Carlo run and thus enable to define a more precise position of the transition point.

JHEP07(2019)166

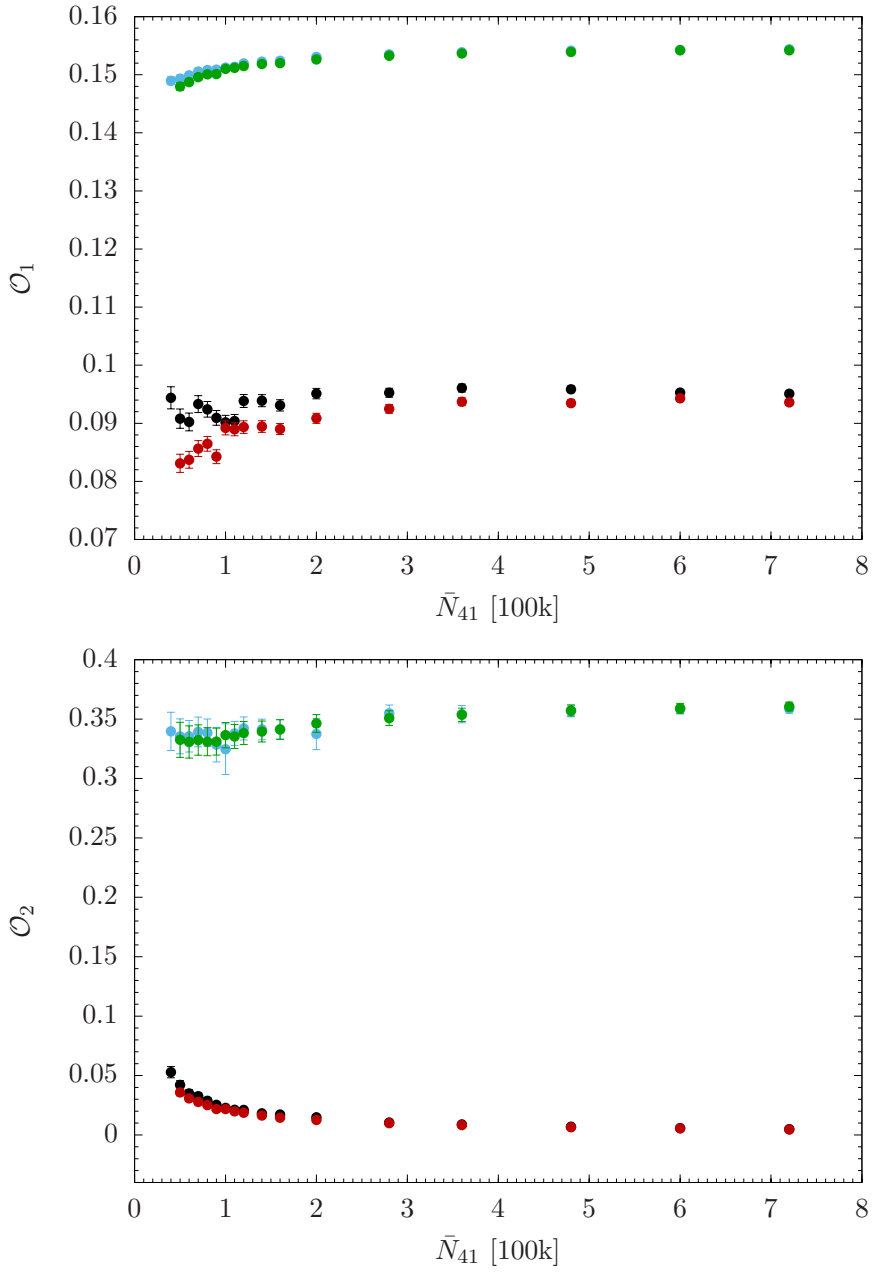

Figure 6. The order-parameters $\mathcal{O}_1$ and $\mathcal{O}_2$ as a function of $\bar{N}_{41}$ at the endpoints of the hysteresis. The colors correspond to the convention used in figure 2.

JHEP07(2019)166

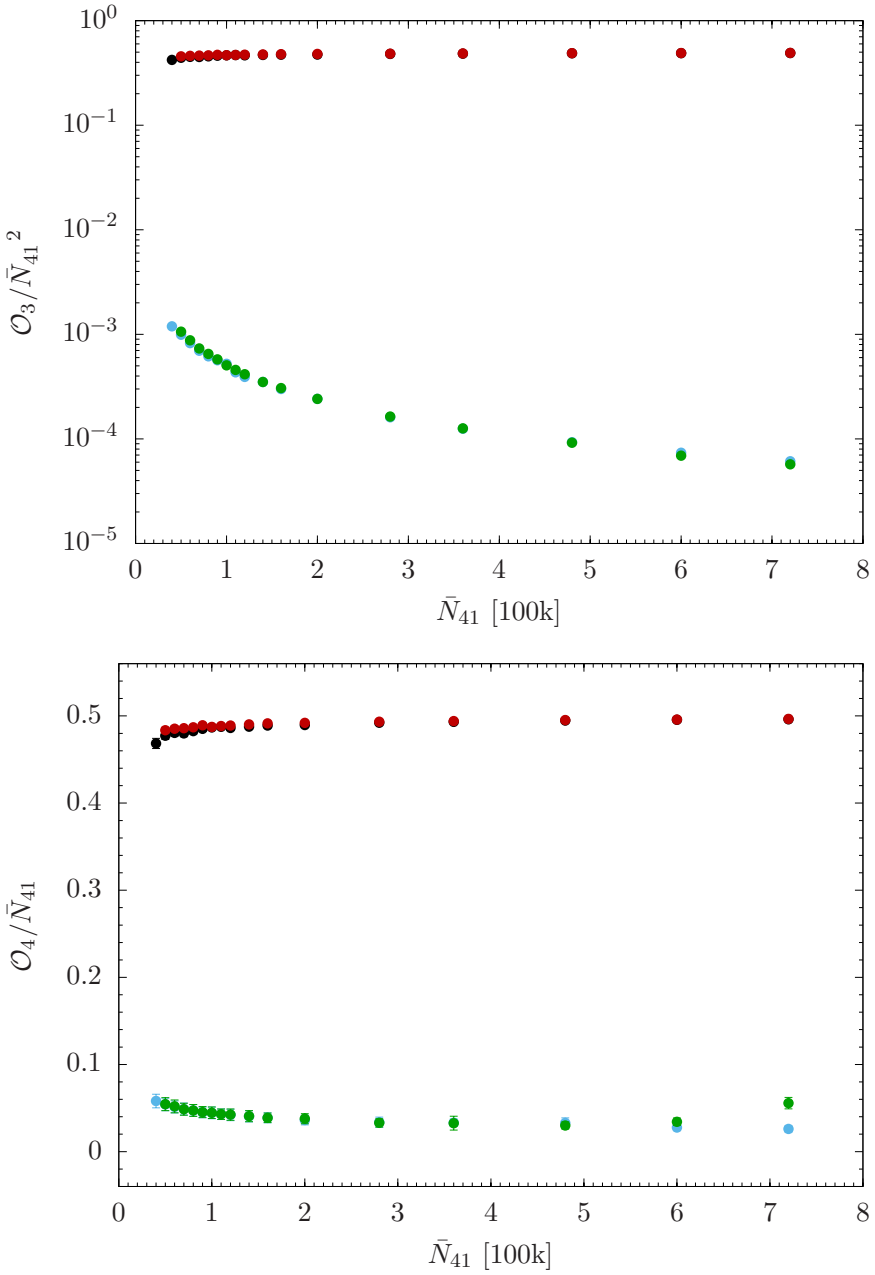

Figure 7. The order-parameters $\mathcal{O}_3/\bar{N}_{41}^2$ and $\mathcal{O}_4/\bar{N}_{41}$ as a function of $\bar{N}_{41}$ at the endpoints of the hysteresis. The colors correspond to the convention used in figure 2.

JHEP07(2019)166

4 Conclusion and discussion

In the present article we made a detailed study of the phase transition observed between the phase C and the phase B at the value of the dimensionless gravitational coupling constant $K_0 = 4.0$. The transition appears to be located close to $\Delta = 0$. The identification of this region, and the possibility that one can move all the way to the triple points of the phase diagram, staying entirely inside the "physical" C phase, is a good news for the renormalization group program started in [54] (and temporarily put on hold by the discovery of the bifurcation phase). The renormalization group analysis is probably the cleanest way to connect CDT lattice gravity approach to asymptotic safety. The analysis of the relevant coupling constant region was made possible by switching from spherical spatial topology to toroidal spatial topology. In this first study of the interesting region we positioned ourselves in the middle of the B-C phase transition line, between the two triple endpoints and from the analysis of the Monte Carlo data we conclude that the transition is most likely of first order. Since endpoints of phase transition lines often are of higher order, the triple points might well be of second order and one of them could then serve as a UV fixed point for a quantum theory of gravity. We are actively pursuing this line of research.

Let us end by some remarks about our quantum gravity model, viewed as a statistical system of four-dimensional geometries. Despite the almost trivial action (1.3), the model has an amazingly rich phase structure, with four different phases, each characterized by very different dominating geometries. In addition, some of the phase transitions have quite unusual characteristics. The transition between phase B and the bifurcation phase is a second order transition [44], but superficially, for a finite volume, it looked like a first order transition. However, analyzing the behavior as a function of the increasing lattice volume the first order nature faded away. Moving towards larger values of K_0, i.e. towards the region we have been investigating in this article, the transition became more and more like a first order transition. With the spherical spatial topology used in [44] one could not get to the region investigated in the present article, but it is natural to conjecture that passing the triple point moving from the bifurcation-B line to the C-B line, the transition changes from second order to first order. However, this first order transition is still somewhat unusual. Firstly, it has kept the characteristics of the second order bifurcation-B transition that the finite size behavior of the pseudo-critical points, given by eqs. (2.2) and (2.3) have non-trivial exponents γ. Secondly, the hysteresis gap goes to zero with increasing volume, which is a non-standard behavior in the case of a first order transition. However, the jumps of the order parameters seem volume independent and that is the main reason that we classify the transition as being a first order transition. The large finite size effects we observe might be related to the global changes of dominant configurations which take place between phase C and phase B, and these global rearrangements might, for finite volumes, have a different "phase-space" in the case of spherical and toroidal topologies. That might explain why our Monte Carlo algorithm can access the B-C transition only in the case of toroidal topology. The statistical theory of geometries is a fascinating area which is almost unexplored for spacetime dimensions larger than two.

JHEP07(2019)166

Acknowledgments

DN would like to thank Renate Roll the fruitful discussions and hospitality during his stay at Radboud University in Nijmegen. JGS acknowledges support from the grant UMO-2016/23/ST2/00289 from the National Science centre, Poland. JA acknowledges support from the Danish Research Council grant *Quantum Geometry*, grant 7014-00066B. AG and DN acknowledges support by the National Science Centre, Poland, under grant no. 2015/17/D/ST2/03479.

JHEP07(2019)166

References

[1] S. Weinberg, *Ultraviolet divergences in quantum theories of gravitation*, in *General relativity: Einstein centenary survey*, S.W. Hawking and W. Israel eds., Cambridge University Press, Cambridge, U.K. (1979), pg. 790 [INSPIRE].

[2] M. Reuter, *Nonperturbative evolution equation for quantum gravity*, *Phys. Rev.* **D 57** (1998) 971 [hep-th/9605030] [INSPIRE].

[3] A. Codello, R. Percacci and C. Rahmede, *Investigating the ultraviolet properties of gravity with a Wilsonian renormalization group equation*, *Annals Phys.* **324** (2009) 414 [arXiv:0805.2909] [INSPIRE].

[4] M. Reuter and F. Saueressig, *Functional renormalization group equations, asymptotic safety and quantum Einstein gravity*, in *Geometric and topological methods for quantum field theory*, Cambridge University Press, Cambridge, U.K. (2010), pg. 288 [arXiv:0708.1317] [INSPIRE].

[5] M. Niedermaier and M. Reuter, *The asymptotic safety scenario in quantum gravity*, *Living Rev. Rel.* **9** (2006) 5 [INSPIRE].

[6] D.F. Litim, *Fixed points of quantum gravity*, *Phys. Rev. Lett.* **92** (2004) 201301 [hep-th/0312114] [INSPIRE].

[7] F. David, *Planar diagrams, two-dimensional lattice gravity and surface models*, *Nucl. Phys.* **B 257** (1985) 45 [INSPIRE].

[8] A. Billoire and F. David, *Microcanonical simulations of randomly triangulated planar random surfaces*, *Phys. Lett.* **B 168** (1986) 279 [INSPIRE].

[9] J. Ambjørn, B. Durhuus and J. Fröhlich, *Diseases of triangulated random surface models and possible cures*, *Nucl. Phys.* **B 257** (1985) 433 [INSPIRE].

[10] J. Ambjørn, B. Durhuus, J. Fröhlich and P. Orland, *The appearance of critical dimensions in regulated string theories*, *Nucl. Phys.* **B 270** (1986) 457 [INSPIRE].

[11] V.A. Kazakov, A.A. Migdal and I.K. Kostov, *Critical properties of randomly triangulated planar random surfaces*, *Phys. Lett.* **B 157** (1985) 295 [INSPIRE].

[12] D.V. Boulatov, V.A. Kazakov, I.K. Kostov and A.A. Migdal, *Analytical and numerical study of the model of dynamically triangulated random surfaces*, *Nucl. Phys.* **B 275** (1986) 641 [INSPIRE].

[13] V.A. Kazakov, *The appearance of matter fields from quantum fluctuations of 2D gravity*, *Mod. Phys. Lett.* **A 4** (1989) 2125 [INSPIRE].

[14] J. Ambjørn and Yu. M. Makeenko, *Properties of loop equations for the Hermitean matrix model and for two-dimensional quantum gravity*, *Mod. Phys. Lett.* **A 5** (1990) 1753 [INSPIRE].

[15] J. Ambjørn, J. Jurkiewicz and Yu. M. Makeenko, *Multiloop correlators for two-dimensional quantum gravity*, *Phys. Lett.* **B 251** (1990) 517 [INSPIRE].

[16] J. Ambjørn, L. Chekhov, C.F. Kristjansen and Yu. Makeenko, *Matrix model calculations beyond the spherical limit*, *Nucl. Phys.* **B 404** (1993) 127 [*Erratum ibid.* **B 449** (1995) 681] [hep-th/9302014] [INSPIRE].

[17] V.G. Knizhnik, A.M. Polyakov and A.B. Zamolodchikov, *Fractal structure of 2D quantum gravity*, *Mod. Phys. Lett.* **A 3** (1988) 819 [INSPIRE].

[18] F. David, *Conformal field theories coupled to 2D gravity in the conformal gauge*, *Mod. Phys. Lett.* **A 3** (1988) 1651 [INSPIRE].

[19] J. Distler and H. Kawai, *Conformal field theory and 2D quantum gravity*, *Nucl. Phys.* **B 321** (1989) 509 [INSPIRE].

[20] J. Ambjørn and S. Varsted, *Three-dimensional simplicial quantum gravity*, *Nucl. Phys.* **B 373** (1992) 557 [INSPIRE].

[21] J. Ambjørn and S. Varsted, *Entropy estimate in three-dimensional simplicial quantum gravity*, *Phys. Lett.* **B 266** (1991) 285 [INSPIRE].

[22] J. Ambjørn, D.V. Boulatov, A. Krzywicki and S. Varsted, *The vacuum in three-dimensional simplicial quantum gravity*, *Phys. Lett.* **B 276** (1992) 432 [INSPIRE].

[23] M.E. Agishtein and A.A. Migdal, *Three-dimensional quantum gravity as dynamical triangulation*, *Mod. Phys. Lett.* **A 6** (1991) 1863 [*Erratum ibid.* **A 6** (1991) 2555] [INSPIRE].

[24] D.V. Boulatov and A. Krzywicki, *On the phase diagram of three-dimensional simplicial quantum gravity*, *Mod. Phys. Lett.* **A 6** (1991) 3005 [INSPIRE].

[25] J. Ambjørn and J. Jurkiewicz, *Four-dimensional simplicial quantum gravity*, *Phys. Lett.* **B 278** (1992) 42 [INSPIRE].

[26] J. Ambjørn and J. Jurkiewicz, *Scaling in four-dimensional quantum gravity*, *Nucl. Phys.* **B 451** (1995) 643 [hep-th/9503006] [INSPIRE].

[27] M.E. Agishtein and A.A. Migdal, *Simulations of four-dimensional simplicial quantum gravity*, *Mod. Phys. Lett.* **A 7** (1992) 1039 [INSPIRE].

[28] P. Bialas, Z. Burda, A. Krzywicki and B. Petersson, *Focusing on the fixed point of 4D simplicial gravity*, *Nucl. Phys.* **B 472** (1996) 293 [hep-lat/9601024] [INSPIRE].

[29] S. Catterall, R. Renken and J.B. Kogut, *Singular structure in 4D simplicial gravity*, *Phys. Lett.* **B 416** (1998) 274 [hep-lat/9709007] [INSPIRE].

[30] J. Ambjørn, L. Glaser, A. Görlich and J. Jurkiewicz, *Euclidian 4d quantum gravity with a non-trivial measure term*, *JHEP* **10** (2013) 100 [arXiv:1307.2270] [INSPIRE].

[31] J. Laiho and D. Coumbe, *Evidence for asymptotic safety from lattice quantum gravity*, *Phys. Rev. Lett.* **107** (2011) 161301 [arXiv:1104.5505] [INSPIRE].

[32] D. Coumbe and J. Laiho, *Exploring Euclidean dynamical triangulations with a non-trivial measure term*, *JHEP* **04** (2015) 028 [arXiv:1401.3299] [INSPIRE].

JHEP07(2019)166

[33] J. Laiho, S. Bassler, D. Coumbe, D. Du and J.T. Neelakanta, *Lattice quantum gravity and asymptotic safety*, *Phys. Rev.* **D 96** (2017) 064015 [arXiv:1604.02745] [INSPIRE].

[34] T. Regge, *General relativity without coordinates*, *Nuovo Cim.* **19** (1961) 558 [INSPIRE].

[35] J. Ambjørn, A. Görlich, J. Jurkiewicz and R. Loll, *Nonperturbative quantum gravity*, *Phys. Rept.* **519** (2012) 127 [arXiv:1203.3591] [INSPIRE].

[36] R. Loll, *Quantum gravity from causal dynamical triangulations: a review*, arXiv:1905.08669 [INSPIRE].

[37] J. Ambjørn, J. Jurkiewicz and R. Loll, *Dynamically triangulating Lorentzian quantum gravity*, *Nucl. Phys.* **B 610** (2001) 347 [hep-th/0105267] [INSPIRE].

[38] J. Ambjørn, J. Jurkiewicz and R. Loll, *A nonperturbative Lorentzian path integral for gravity*, *Phys. Rev. Lett.* **85** (2000) 924 [hep-th/0002050] [INSPIRE].

[39] J. Ambjørn, J. Jurkiewicz and R. Loll, *Reconstructing the universe*, *Phys. Rev.* **D 72** (2005) 064014 [hep-th/0505154] [INSPIRE].

[40] J. Ambjørn, J. Jurkiewicz and R. Loll, *Emergence of a 4D world from causal quantum gravity*, *Phys. Rev. Lett.* **93** (2004) 131301 [hep-th/0404156] [INSPIRE].

[41] J. Ambjørn, J. Jurkiewicz and R. Loll, *Spectral dimension of the universe*, *Phys. Rev. Lett.* **95** (2005) 171301 [hep-th/0505113] [INSPIRE].

[42] J. Ambjørn, A. Görlich, J. Jurkiewicz and R. Loll, *The nonperturbative quantum de Sitter universe*, *Phys. Rev.* **D 78** (2008) 063544 [arXiv:0807.4481] [INSPIRE].

[43] J. Ambjørn, A. Görlich, J. Jurkiewicz and R. Loll, *Planckian birth of the quantum de Sitter universe*, *Phys. Rev. Lett.* **100** (2008) 091304 [arXiv:0712.2485] [INSPIRE].

[44] J. Ambjørn, S. Jordan, J. Jurkiewicz and R. Loll, *Second- and first-order phase transitions in CDT*, *Phys. Rev.* **D 85** (2012) 124044 [arXiv:1205.1229] [INSPIRE].

[45] J. Ambjørn, S. Jordan, J. Jurkiewicz and R. Loll, *A second-order phase transition in CDT*, *Phys. Rev. Lett.* **107** (2011) 211303 [arXiv:1108.3932] [INSPIRE].

[46] J. Ambjørn, J. Jurkiewicz and R. Loll, *Semiclassical universe from first principles*, *Phys. Lett.* **B 607** (2005) 205 [hep-th/0411152] [INSPIRE].

[47] J. Ambjørn, A. Görlich, J. Jurkiewicz, R. Loll, J. Gizbert-Studnicki and T. Trześniewski, *The semiclassical limit of causal dynamical triangulations*, *Nucl. Phys.* **B 849** (2011) 144 [arXiv:1102.3929] [INSPIRE].

[48] J. Ambjørn, J. Gizbert-Studnicki, A. Görlich and J. Jurkiewicz, *The transfer matrix in four-dimensional CDT*, *JHEP* **09** (2012) 017 [arXiv:1205.3791] [INSPIRE].

[49] J. Ambjørn, J. Gizbert-Studnicki, A. Görlich and J. Jurkiewicz, *The effective action in 4-dim CDT. The transfer matrix approach*, *JHEP* **06** (2014) 034 [arXiv:1403.5940] [INSPIRE].

[50] J. Ambjørn, D.N. Coumbe, J. Gizbert-Studnicki and J. Jurkiewicz, *Signature change of the metric in CDT quantum gravity?*, *JHEP* **08** (2015) 033 [arXiv:1503.08580] [INSPIRE].

[51] D.N. Coumbe, J. Gizbert-Studnicki and J. Jurkiewicz, *Exploring the new phase transition of CDT*, *JHEP* **02** (2016) 144 [arXiv:1510.08672] [INSPIRE].

[52] J. Ambjørn, J. Gizbert-Studnicki, A. Görlich, J. Jurkiewicz, N. Klitgaard and R. Loll, *Characteristics of the new phase in CDT*, *Eur. Phys. J.* **C 77** (2017) 152 [arXiv:1610.05245] [INSPIRE].

JHEP07(2019)166

[53] J. Ambjørn, D. Coumbe, J. Gizbert-Studnicki, A. Görlich and J. Jurkiewicz, *New higher-order transition in causal dynamical triangulations*, *Phys. Rev.* **D 95** (2017) 124029 [arXiv:1704.04373] [INSPIRE].

[54] J. Ambjørn, A. Görlich, J. Jurkiewicz, A. Kreienbuehl and R. Loll, *Renormalization group flow in CDT*, *Class. Quant. Grav.* **31** (2014) 165003 [arXiv:1405.4585] [INSPIRE].

[55] J. Ambjørn, Z. Drogosz, J. Gizbert-Studnicki, A. Görlich, J. Jurkiewicz and D. Nemeth, *Impact of topology in causal dynamical triangulations quantum gravity*, *Phys. Rev.* **D 94** (2016) 044010 [arXiv:1604.08786] [INSPIRE].

[56] J. Ambjørn, J. Gizbert-Studnicki, A. Görlich, K. Grosvenor and J. Jurkiewicz, *Four-dimensional CDT with toroidal topology*, *Nucl. Phys.* **B 922** (2017) 226 [arXiv:1705.07653] [INSPIRE].

[57] J. Ambjørn, J. Gizbert-Studnicki, A. Görlich, J. Jurkiewicz and D. Németh, *The phase structure of causal dynamical triangulations with toroidal spatial topology*, *JHEP* **06** (2018) 111 [arXiv:1802.10434] [INSPIRE].

[58] J. Ambjørn, D. Coumbe, J. Gizbert-Studnicki, A. Görlich and J. Jurkiewicz, *Critical phenomena in causal dynamical triangulations*, arXiv:1904.05755 [INSPIRE].

JHEP07(2019)166

Published for SISSA by Springer

Received: *February 17, 2022*
Accepted: *March 23, 2022*
Published: *April 19, 2022*

Topology induced first-order phase transitions in lattice quantum gravity

J. Ambjorn,[a,b] **J. Gizbert-Studnicki,**[c,d] **A. Görlich**[c,d] **and D. Németh**[c]

[a] *The Niels Bohr Institute, Copenhagen University, Blegdamsvej 17, 2100 Copenhagen, Denmark*
[b] *IMAAP, Radboud University, Nijmegen, PO Box 9010, The Netherlands*
[c] *Institute of Theoretical Physics, Jagiellonian University, Łojasiewicza 11, Kraków, 30-348, Poland*
[d] *Mark Kac Complex Systems Research Center, Jagiellonian University, Łojasiewicza 11, Kraków, 30-348, Poland*

E-mail: ambjorn@nbi.dk, jakub.gizbert-studnicki@uj.edu.pl, andrzej.goerlich@uj.edu.pl, nemeth.daniel.1992@gmail.com

Abstract: Causal Dynamical Triangulations (CDT) is a lattice formulation of quantum gravity, suitable for Monte-Carlo simulations which have been used to study the phase diagram of the model. It has four phases characterized by different dominant geometries, denoted phase A, B, C and C_b. In this article we analyse the $A-B$ and the $B-C$ phase transitions in the case where the topology of space is that of the three-torus. This completes the phase diagram of CDT for such a spatial topology. We observe that the order of a phase transition of spacetime geometries can depend on the topology of spacetime.

Keywords: Lattice Models of Gravity, Models of Quantum Gravity, Phase Transitions

ArXiv ePrint: 2202.07392

https://doi.org/10.1007/JHEP04(2022)103

JHEP04(2022)103

Contents

1 Introduction **1**
- 1.1 Causal Dynamical Triangulations 1
- 1.2 Phase transition methodology 2

2 The phase diagram of CDT **3**

3 The $A-B$ phase transition **7**

4 Revisiting the $B-C$ phase transition **9**

5 Discussion and conjecture **13**

A Machine learning locations of the CDT phase transitions **14**

JHEP04(2022)103

1 Introduction

1.1 Causal Dynamical Triangulations

Causal Dynamical Triangulations (CDT) is a lattice formulation of quantum gravity [1, 2] based on the path integral approach of Feynman, where certain piecewise linear geometries provide the lattice structure and the UV cut-off. The action used is the Einstein-Hilbert action provided for such geometries by Regge [3]. It is the hope that it can be as successful as Lattice QCD has been in regard to testing non-perturbative aspects of the theory via numerical simulations. The difference between CDT and Lattice QCD is that in the latter case the lattice structure is fixed and is just representing the underlying flat spacetime, while in CDT the geometry is encoded in the lattice connectivity. Since we want to integrate over geometries in the path integral, we have to use lattices with different connectivity structure. More precisely, within the framework of CDT, the formal path integral of quantum gravity is defined as a sum over geometries constructed by gluing together simplicial building blocks satisfying certain topological constraints. The most important constraint is that the quantum geometries admit a global time-foliation into spatial slices of fixed topology which is conserved in the time evolution. In all cases studied before, the topology of the spatial slices was chosen to be either spherical (S^3) or toroidal (T^3). Even though the formulation seems to be discrete in nature, it is important to stress that the lengths of links (i.e., the edges of the simplicial building blocks) play a role of the UV cut-off, which is supposed to be removed in the continuum limit, if it exists. In 3+1 dimensional spacetime the simplicial manifolds are constructed from two types of building blocks: the $\{4,1\}$ and the $\{3,2\}$ simplices, where the first number denotes the number of vertices at the (discrete) lattice time t and the second one is the number of vertices at time $t\pm1$. Within each four-simplex, all vertices with the same time coordinate are connected by space-like links and vertices at the neighboring time layers are connected by time-like links. The lengths

of all spatial links are fixed to be a_s and of all time-like links to be $a_t^2 = -\alpha\, a_s^2$, where the asymmetry parameter $\alpha > 0$ if the signature of spacetime is Lorentzian. The simplices are then glued together along their three-dimensional faces (tetrahedra) in such a way that no topological defects are introduced and the assumed spatial topology and time-foliation structure of the simplicial manifolds are preserved. The imposed global time-foliation allows for a well-defined analytic continuation between Lorentzian and Euclidean signatures. The quantum amplitude can be calculated as a weighted sum over all such discretized four-dimensional geometries, later called *triangulations* or *configurations*, joining two geometric states. In practice, one usually identifies the initial and final states and thus assumes time-periodic boundary conditions, leading to the global topology of the CDT manifolds being either $T^1 \times S^3$ or T^4, in what we call the *spherical* or the *toroidal* CDT, respectively, depending on the (fixed) spatial topology choice. In the continuum formulation, the path integral is formally defined as:

$$\mathcal{Z}_{\mathrm{QG}} = \int \mathcal{D}_{\mathcal{M}}[g] e^{iS_{EH}[g]} \tag{1.1}$$

where $[g]$ denotes the equivalence class of metrics with respect to diffeomorphisms and $\mathcal{D}_{\mathcal{M}}$[g] is the integration measure over nonequivalent classes of metrics. This expression becomes meaningful only if one introduces a regularization. In CDT we make a particular choice by introducing the piecewise linear regularization described above, and when performing the Wick rotation from Lorentzian to Euclidean signature, the path integral becomes a partition function:

$$\mathcal{Z}_{\mathrm{CDT}} = \sum_{\mathcal{T}} e^{-S_R[\mathcal{T}]} \tag{1.2}$$

with the Regge action [4]:

$$S_R = -(\kappa_0 + 6\Delta) \cdot N_0 + \kappa_4 \cdot (N_{41} + N_{32}) + \Delta \cdot N_{41}, \tag{1.3}$$

where N_0 is the number of vertices in a triangulation $\mathcal{T}$, N_{41} and N_{32} are the numbers of $\{4,1\}$ and $\{3,2\}$ simplices, respectively. The action is parametrized by a set of three dimensionless bare coupling constants, κ_0, κ_4 and Δ corresponding respectively to the inverse gravitational bare coupling constant, the dimensionless cosmological constant and a function of the asymmetry parameter α. The model is analytically solvable in 1+1 dimensions [5] and the 2+1 dimensional model can be associated with matrix models [6–8]. The 3+1 dimensional model discussed here can be analyzed via Monte Carlo simulations.

1.2 Phase transition methodology

The phase structure is such that for given κ_0 and Δ there exists a κ_4^{crit} such that for $\kappa_4 > \kappa_4^{\mathrm{crit}}$ the average value of $N_4 = N_{41} + N_{32}$ will be finite, while for $\kappa_4 < \kappa_4^{\mathrm{crit}}$ the partition function is not well defined. We are interested in the limit where $N_4 \to \infty$. In order to obtain that in a controlled way, in the numerical simulations where N_4 will fluctuate, we add to the action (1.3) a quadratic volume fixing term: $\epsilon\,(N_{41} - \bar{N}_{41})^2$. Then, to achieve that N_{41} actually fluctuates around $\bar{N}_{41}$ in the large-volume limit, one has to add the volume fixing term and fine-tune the bare cosmological constant κ_4 to its pseudo-critical

JHEP04(2022)103

value $\kappa_4^{\rm crit}(\bar{N}_{41})$. Only for $\bar{N}_{41} \to \infty$ will $\kappa_4^{\rm crit}(\bar{N}_{41})$ approach the true critical value $\kappa_4^{\rm crit}$. The nontrivial behavior of κ_4 near $\kappa_4^{\rm crit}$ is transferred to the volume dependence of κ_4 on $\bar{N}_{41}$. It means that for each $\bar{N}_{41}$ we effectively fix the pseudo-critical value of the coupling constant $\kappa_4^{\rm crit}(\bar{N}_{41})$ and we study the properties of the model parametrized by the two remaining coupling constants: κ_0 and Δ. Observing the geometric structures of individual triangulations and their extracted averaged properties, one may find regions where these properties differ from one another. In this way the two-dimensional phase diagram of the model can be determined, and it reveals a rich structure with many phase transition lines, see figure 1. The phase transitions in CDT have so far been analyzed using standard techniques. It has been shown that the peak in the variance of an order parameter typically designates, with high accuracy, the location of the phase transitions, and also the Binder cumulant can be used to predict the value of the infinite volume limit of a given coupling constant using finite volume scaling measurements [9–13]. Typically, one selects a value of a coupling constant (κ_0 or Δ) and creates a set of configurations with fixed values of one coupling (e.g., κ_0) and changed values of the other coupling (e.g., Δ) with step-size $\delta\kappa_0$ or $\delta\Delta$. After thermalizing these configurations one collects statistics of various observables for different geometries. Collecting large enough statistics is necessary to calculate averages of these observables with high accuracy. Each line (or grid) of measurements gives information about the location of the phase transition and the pseudo-critical value of the observed quantities for fixed $\bar{N}_{41}$.[1] Taking the limit $\bar{N}_{41} \to \infty$ gives the continuum behavior of the chosen observable, and the critical exponents can be extracted. The finite size dependence of the observables (which are functions of Δ and κ_0) is non-trivial. In this paper we try to use this dependence to determine the properties of the CDT phase transitions in the infinite volume limit, i.e., when $\bar{N}_{41} \to \infty$ and $\kappa_4 \to \kappa_4^{\rm crit}$.

One should also note that in the phase transition studies described herein, we have tested and used a new method of finding locations of the phase transition points based on machine learning techniques, namely the so-called *logistic regression* method which turned out to be very efficient. More details can be found in the appendix.

2 The phase diagram of CDT

The geometry of a CDT triangulation can be investigated by analyzing various *observables*.[2] They can be general quantities characterizing global properties of a triangulation, e.g., the ratios: $\mathcal{O}_1 \equiv N_0/N_{41}$ or $\mathcal{O}_2 \equiv N_{32}/N_{41}$. They can be as well more local quantities, e.g., the distribution of the spatial three-volume as a function of the (lattice) time coordinate, which can be measured both in the spherical and the toroidal version of CDT, as it is presented in figure 2. Other examples of local observables are the recently introduced space-time coordinates [14], which map a triangulation onto four scalar fields, enabling one

[1] Note that in a lattice formulation for any finite lattice size $\bar{N}_{41}$ the free energy is finite and thus one has a cross-over rather than a true phase transition, thus we talk about *pseudo-criticality*. Only in the limit where $\bar{N}_{41} \to \infty$ one recovers a true phase transition.

[2] Here what we call *observable* is a quantity which can be measured in numerical simulations. It does not have to be a gauge / diffeomorphism invariant observable.

JHEP04(2022)103

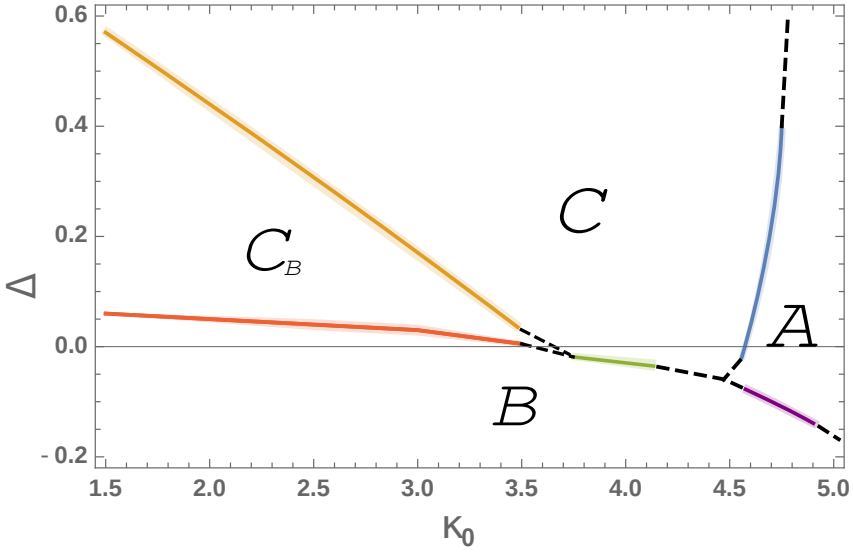

Figure 1. Phase-diagram of CDT with the four phases. The plot shows the position of phase transitions measured for fixed lattice volume $\bar{N}_{41} = 160$k in the toroidal CDT. In the spherical CDT case the phase structure is similar, although the phase transition between C and B phases (denoted by the green solid line) was inaccessible by numerical simulations.

to measure and visualize four-volume density distribution in all spacetime directions within the toroidal version of CDT, see figure 3.

Geometric properties of *generic triangulations* dominating the path integral (1.2), and thus the typical behavior of the above-mentioned observables, will vary depending on the choice of the bare coupling constants: κ_0 and Δ.[3] Even though the bare action of CDT (1.3) is very simple, the $3+1$-dimensional model reveals a surprisingly rich phase structure, see figure 1, which seems to be universal, independent of the spatial topology choice [15]. So far, four phases with distinct geometric properties were discovered — called A, B, C and C_b, respectively.

For large values of the bare inverse gravitational constant κ_0 one encounters phase A. This phase is characterized by the spatial volumes at different (lattice) time layers being uncorrelated [16], which is seen clearly in the upper left panel in figure 2. Approaching phase A from the phase C, where one has an effective minisuperspace action [17] (see below), the coefficient in front of the kinetic term, which couples spatial volume in the neighboring time layers, vanishes reflecting the lack of correlation between spatial volumes. On the A-side the system is described by an effective action without kinetic term. On the other hand, the generic geometry of the spatial slices themselves seems to be isotropic and homogeneous, see figure 3, left upper panel.

For small or negative values of the asymmetry parameter Δ one observes phase B, where the typical spatial volume distribution is collapsed into a single time layer with the three-volume distribution pinched to the cut-off size in the remaining part of a generic

[3] As explained above the κ_4 is fine tuned to the pseudo-critical value $\kappa_4^{\rm crit}(\bar{N}_{41})$ dependent on the fixed lattice volume $\bar{N}_{41}$.

JHEP04(2022)103

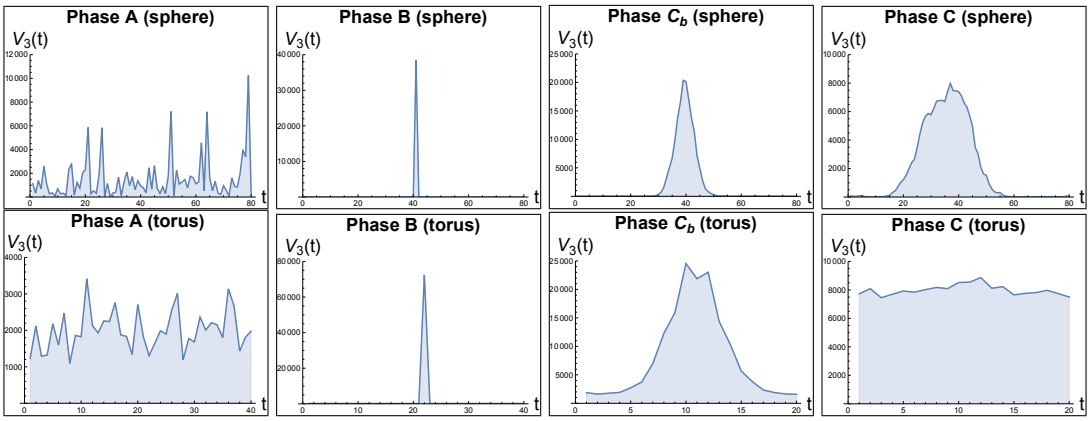

Figure 2. Spatial volume profiles of generic CDT configurations in different phases. Top: Spherical CDT: A, B, C_b, C; Bottom: Toroidal CDT: A, B, C_b, C, respectively.

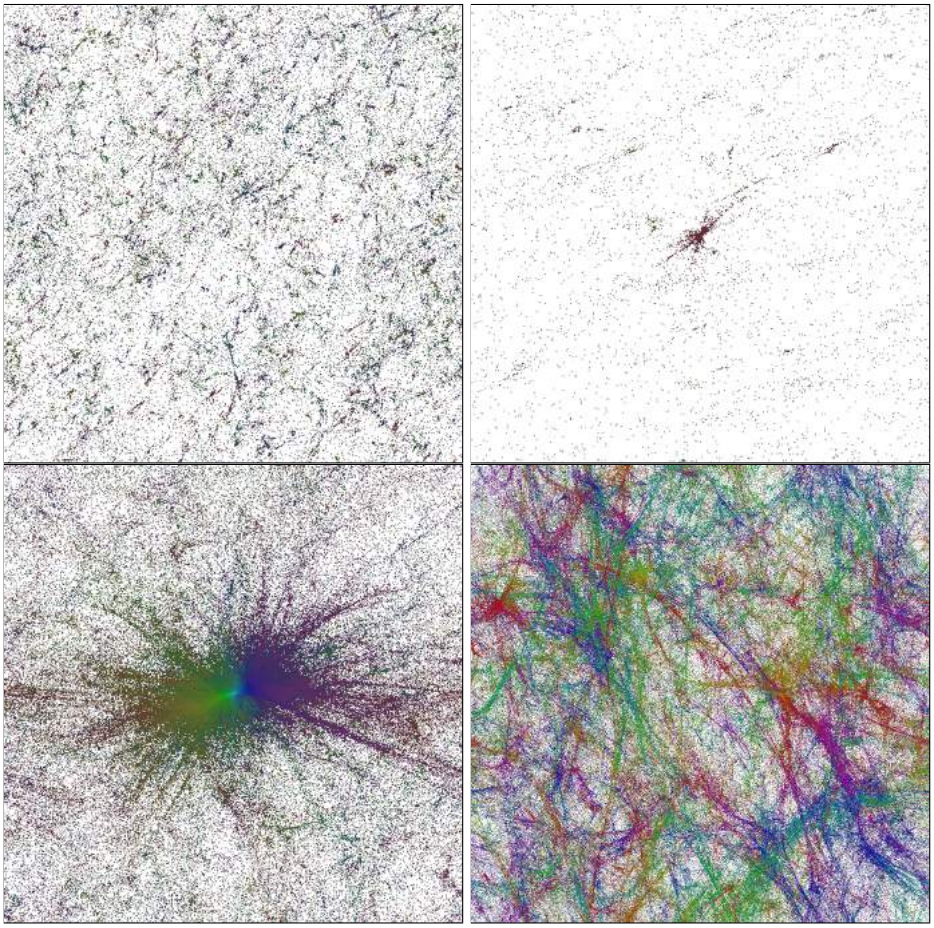

Figure 3. The structure of the geometry of phase A (top left), B (top right), C_b (bottom left), and C (bottom right), respectively, using the scalar field mapping method defined in [14]. The plots show four-volume density distribution of generic CDT configurations in each phase projected on two spatial directions.

JHEP04(2022)103

triangulation, see figure 2. Thus, the four-dimensional geometry is effectively reduced to a three-dimensional geometry, in the sense that all four-volume is contained in a thin slab surrounding a single time layer. Moreover, in such a generic configuration, the isotropy and homogeneity of three-dimensional space is itself maximally broken, in the sense that the whole volume is concentrated around a few vertices. This is illustrated in figure 3, top right panel.

For not too large κ_0, increasing Δ one moves from the B phase to the so-called bifurcation phase, C_b. In this phase the number of constant time layers where the spatial volume is significantly different from the minimal value starts to increase and forms a *blob*, see figure 2. However, when one increases the four-volume N_{41} sufficiently, the extension of this blob ceases to increase as $N_{41}^{1/4}$. This implies that in the limit where $N_{41} \to \infty$, the *stalk*, where the spatial volumes are of cut-off scale, will dominate if we allow the time direction to be of order at least $N_{41}^{1/4}$. In addition, if we look at the spatial geometry inside time layers belonging to the blob, it shows the same characteristics as the spatial geometry in the B phase: isotropy and homogeneity are broken for a generic configuration by the presence of a few high-order vertices. These high-order vertices are correlated from slice to slice within the blob. As we continue to increase Δ or κ_0 this effect becomes less and less pronounced [18]: the order of the high-order vertices decreases and the blob broadens but it does not disappear. A stalk will remain. The lower left panel in figure 3 shows that not only in the time direction, but also in the spacial directions, the geometry is more extended than in the B phase, but still inhomogeneous. Increasing Δ or κ_0 even further bring us into phase C.

In phase C, which is also denoted the de Sitter phase or the semiclassical phase, the spatial volume profiles seem to depend on the choice of spatial topology, as illustrated in the right panels in figure 2. In the case where the spatial topology is S^3 the volume profiles form a blob, like in the bifurcation phase. The crucial difference is that the extension of the blob scales as $N_{41}^{1/4}$ and a typical spatial volume in the blob scales as $N_{41}^{3/4}$. Thus, one might obtain a semiclassical geometry of the blob in the limit $N_{41} \to \infty$. Similarly, the generic spatial slices seem to be isotropic and homogeneous without the high-order vertices of phase B and phase C_b. In the case where the spatial topology is T^3 we do not observe a blob, but rather a constant volume profile with superimposed (small) fluctuations. In both cases, the spatial geometries (except for the geometry in the stalk in the case where the spatial topology is S^3) of generic configurations seem to be isotropic and homogeneous on large scales while on shorter scales one can observe volume density fluctuations forming voids-and-filaments [14, 19], surprisingly similar to structures formed by matter content of the real Universe, as illustrated in the lower right panel in figure 3. In accordance with this, the volume profiles are well described by minisuperspace actions similar to the Hartle-Hawking minisuperspace action [20–24], and the kinetic term in the minisuperspace actions has the same coefficient in the two cases.

The $A-C$ transition has been determined to be a first-order transition [9, 12], while the $B-C_b$ transition has been determined to be a second-order transition [9, 13] in both S^3 and T^3 spatial topology choices. The $C-C_b$ transition was found to be a second-order transition in the case where the spatial topology was S^3 [10, 11] and (seemingly) a first-

JHEP04(2022)103

order transition when the spatial topology was T^3 [15]. The $B-C$ transition and the $A-B$ transition could be studied by MC simulations in the case where the spatial topology is T^3. Preliminary results for the $B-C$ transition were reported in [25], but herein we will improve the data for the $B-C$ transition and complete the phase diagram by measuring the yet unexplored $A-B$ transition. As a result, we will see an interesting pattern emerge, to be discussed in section 5.

3 The $A-B$ phase transition

The phase transition between phases A and B was not analyzed earlier in detail. This transition is important because there is a point in the phase diagram which is the common endpoint of the $A-C$, $A-B$ and $B-C$ phase transitions (the $A-B-C$ triple point), see figure 1, which is a potential candidate of the UV fixed point of CDT. Thus, understanding the nature of all surrounding phase transitions is crucial. We perform a finite volume scaling analysis and determine the order of the $A-B$ phase transition for three different fixed values of $\kappa_0 = 4.8$, 4.6 and 4.5 (and the corresponding observables will be denoted with their corresponding κ_0 coupling as a lower right index). At this phase transition, the time-reduced collapsed configurations on the B side of the transition compete with time-uncorrelated configurations on the A side (see figure 2). For consistency, the scaling exponent is measured for the three fixed values of κ_0 independently by varying the values of Δ to find the (pseudo-)critical values $\Delta^{\text{crit}}(\bar{N}_{41})$ together with the scaling exponents γ. We performed simulations for various volumes (ranging between $\bar{N}_{41} = 20\text{k}$ and 720k) to find the scaling exponents for each fixed κ_0 measurement set. Our assumption about the critical behavior of $\Delta^{\text{crit}}(\bar{N}_{41})$ in the limit $\bar{N}_{41} \to \infty$ is a (standard) power function, the same as used in the previous phase transition studies cited before:

$$\Delta^{\text{crit}}(\bar{N}_{41}) = \Delta^{\infty} - \tilde{C} \cdot \bar{N}_{41}^{-1/\gamma}, \tag{3.1}$$

where $\tilde{C}$ is a constant, Δ^{∞} is the value of the asymmetry parameter corresponding to the infinite volume limit at fixed κ_0 and γ is the scaling exponent.

The best fits for the scaling exponents γ were measured to be $\gamma_{4.8} = 1.088 \pm 0.101$, $\gamma_{4.6} = 1.029 \pm 0.178$, and $\gamma_{4.5} = 1.151 \pm 0.379$ for the three κ_0 values considered. As the best fitted exponent values are all consistent with the first-order behavior, i.e., $\gamma = 1$, we used fixed $\gamma = 1$ to fit relation (3.1) to our data, as presented in figure 4. By extrapolating the fits to the infinite volume limits Δ^{crit} were determined to be $\Delta^{\infty}_{4.8} = -0.110 \pm 0.001$, $\Delta^{\infty}_{4.6} = -0.077 \pm 0.001$ and $\Delta^{\infty}_{4.5} = -0.059 \pm 0.001$ for the three cases respectively.

In the following analysis, we will assume that near the phase transition point not only the critical coupling(s) $\Delta^{\text{crit}}(\bar{N}_{41})$, but also other relevant order parameters scale similarly to eq. (3.1) with the critical exponent fixed at $\gamma = 1$. This is indeed supported by our data. In figure 5 we show the results for the $\mathcal{O}_2 \equiv N_{32}/N_{41}$ observable measured for each side of the phase transition independently.

The fits shown in figure 5 have a close to zero value of $\mathcal{O}_2^{\infty}$ for all cases, but on the A side of the transition the approach to $\mathcal{O}_2^{\infty} \approx 0$ becomes slower with decreasing κ_0, i.e., slower when we approach the $A-B-C$ triple point.

JHEP04(2022)103

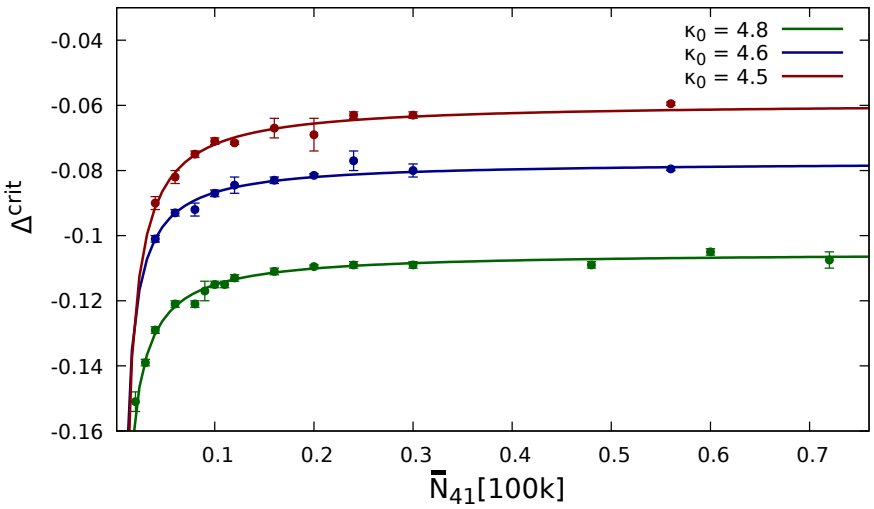

Figure 4. (Pseudo-)critical values of $\Delta^{\text{crit}}(\bar{N}_{41})$ measured for $\kappa_0 = 4.8$ (green), $\kappa_0 = 4.6$ (blue), and $\kappa_0 = 4.5$ (red) together with the fits of eq. (3.1). The solid curves were fitted with the critical exponent fixed to $\gamma = 1$ for all three data sets.

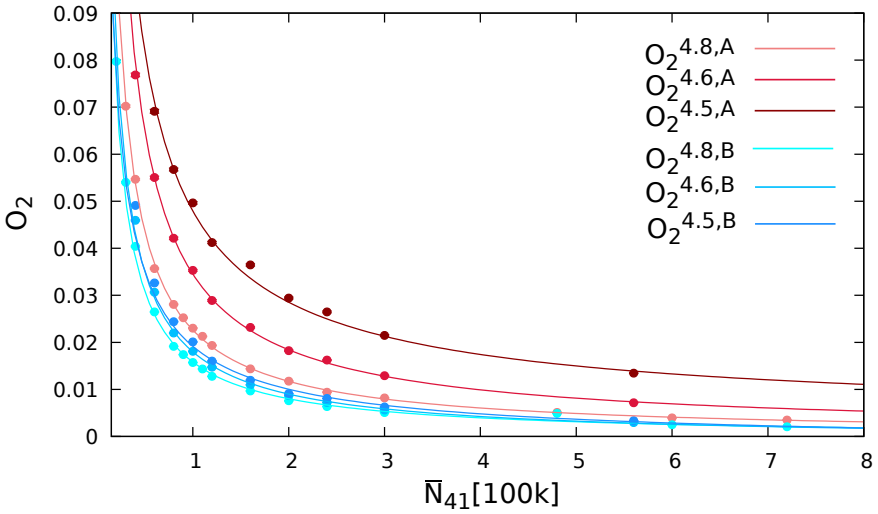

Figure 5. The running of $\mathcal{O}_2$ for $\kappa_0 = 4.8$, $\kappa_0 = 4.6$ and $\kappa_0 = 4.5$. Blue colors correspond to data measured in phase B and red in phase A closest to the phase transition point, and the darker the color the lower the corresponding κ_0 coupling, i.e., the closer to the $A-B-C$ triple point. The error bars are smaller than the size of the data-points. The solid curves correspond to the fits of a relation similar to eq. (3.1) with the critical exponent fixed to be $\gamma = 1$ for all data sets.

JHEP04(2022)103

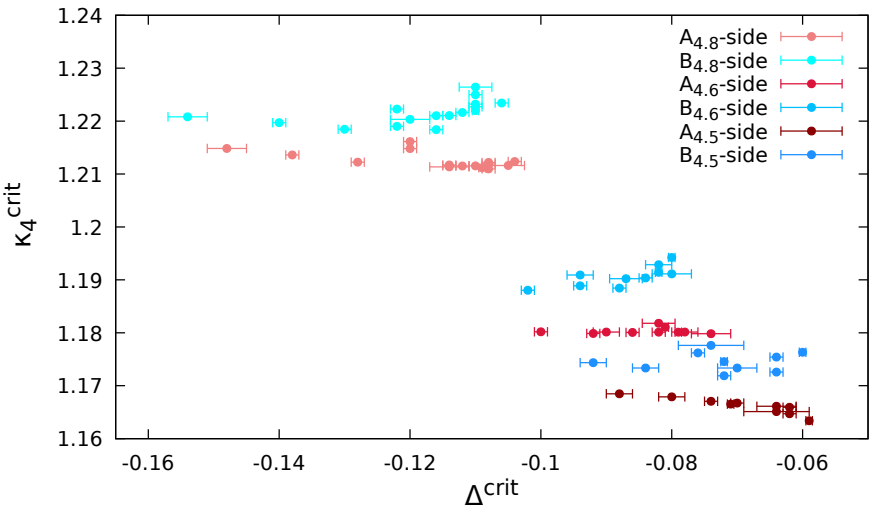

Figure 6. Values of the critical $\kappa_4^{\rm crit}(\bar{N}_{41})$ coupling measured as a function of $\Delta^{\rm crit}(\bar{N}_{41})$ in phase A (red) and phase B (blue) closest to the phase transition points. The darker the color the lower the corresponding κ_0 coupling, i.e., the closer to the $A-B-C$ triple point. Data suggest the lack of a common value of κ_4^{∞} for the A and B phases at the infinite volume limit.

A final observation corroborating the first-order nature of the $A-B$ transition is the fact that the values $\kappa_4^{\rm crit}(\bar{N}_{41})$ observed in the A phase and the B phase data closest to the transition point do not converge to a common value for $\bar{N}_{41} \to \infty$. This is shown in figure 6 (where we have used data from figure 4 to express $\bar{N}_{41}$ in terms of $\Delta^{\rm crit}$). It is seen that when we increase $\bar{N}_{41}$, which corresponds to higher $\Delta^{\rm crit}$ in the plot, the gap between $\kappa_4^{\rm crit}$(A- side) and $\kappa_4^{\rm crit}$(B- side) increases. This shows that the MC simulations collect very different configurations on the A and the B phase transition side, a situation typical for a first-order transition.

Summarizing, in this section we have analyzed the behavior of the A–B phase transition for three different fixed values of κ_0 via the scaling of the asymmetry parameter $\Delta^{\rm crit}(\bar{N}_{41})$ and $\mathcal{O}_2$ on the two sides of the phase transition. For all measured values of κ_0, the fitted values of the scaling exponent γ are consistent with the first-order behavior ($\gamma = 1$). Thus, we conclude that the $A-B$ phase transition is a first-order phase transition. The order of the $A-B$ phase transition does not exclude the possibility that exactly at the endpoint ($A-B-C$ triple point) the phase transition could be of higher-order.

4 Revisiting the $B-C$ phase transition

Recently, using manifolds with toroidal spatial topology, we were able, for the first time, to measure the properties of the $B-C$ phase transition [25] at fixed $\kappa_0 = 4.0$. This result was important since this region of the phase diagram is between the two common endpoints of CDT phase transition lines (the $A-B-C$ and the C_b-B-C triple points), see figure 1. We determined the critical behavior based on measurements for a sequence of values of Δ approaching the phase transition from B and C sides of the phase diagram. Using the

JHEP04(2022)103

approach presented in [25] we established a range of coupling constants, within which, for a given finite value of $\bar{N}_{41}$, the system jumps between the two phases. We determined the limits of this hysteresis region and measured the (volume dependent) pseudo-critical values of the coupling constants Δ and κ_4 as close to the phase transition as we could get with respect to the hysteresis. We observed that, similarly to the $A-B$ transition case, the position of the phase transition line moves towards larger Δ and κ_0 values when $\bar{N}_{41}$ is increased. Again, the true phase transition is observed in the infinite volume limit $\bar{N}_{41} \to \infty$ which corresponds to $\kappa_4 \to \kappa_4^{\rm crit}(\kappa_0, \Delta)$. In [25] we assumed the standard finite volume scaling for $\Delta^{\rm crit}(\bar{N}_{41})$, $\kappa_0^{\rm crit}(\bar{N}_{41})$ and $\kappa_4^{\rm crit}(\bar{N}_{41})$, analogous to eq. (3.1):

$$\begin{aligned} \Delta^{\rm crit}(\bar{N}_{41}) &= \Delta^{\infty} - A \cdot \bar{N}_{41}^{-1/\gamma} \\ \kappa_0^{\rm crit}(\bar{N}_{41}) &= \kappa_0^{\infty} - B \cdot \bar{N}_{41}^{-1/\gamma'} \\ \kappa_4^{\rm crit}(\bar{N}_{41}) &= \kappa_4^{\infty} - C \cdot \bar{N}_{41}^{-1/\gamma''}. \end{aligned} \tag{4.1}$$

We showed that in the limit $\bar{N}_{41} \to \infty$, the hysteresis shrinks to zero. Furthermore, we observed that on both sides of the phase transition $\Delta^{\rm crit}(\bar{N}_{41})$ and $\kappa_4^{\rm crit}(\bar{N}_{41})$ scale in the same way. The scaling analysis of this behavior could be characterized by a common critical exponent $\gamma \approx 1.62 \pm 0.25$, potentially signaling a higher-order phase transition. As we will show below, an equally good fit to the data can be obtained using $\gamma = 1$ and a higher-order correction given by a universal small constant shift of N_{41} for data measured on both sides of the transition line. This indicates that the transition might be first-order, which is supported by the analysis of the order parameters $\mathcal{O}_1 \equiv N_0/N_{41}$ and $\mathcal{O}_2 \equiv N_{32}/N_{41}$ showing a strong discontinuity between the two phases even in the infinite volume limit, as already noted in [25].

Herein we have repeated the analysis for $\kappa_0 = 4.0$ with much larger statistics and we have also performed new measurements for $\kappa_0 = 4.2$, which is closer to the $A-B-C$ triple point. The lattice volumes used ranged from $\bar{N}_{41} = 40$k and 1600k. We denote the measurements performed at fixed $\kappa_0 = 4.0$ and 4.2 as *vertical* since in the (κ_0, Δ) coupling-constant plane only Δ varies. Similarly, we have performed measurements with fixed $\Delta = 0$ and -0.02 varying κ_0 values. We refer to these as *horizontal* measurements. In the horizontal measurements, the lattice volumes ranged from $\bar{N}_{41} = 40$k to 800k. n the following, we will present results in pairs related to the two values of the fixed coupling constant in the horizontal and the vertical measurement, respectively. Even though we now have much better statistics than in [25] and have measured the $B-C$ phase transition at various bare coupling constant locations, approaching the transition line in different ways (vertically and horizontally), a fit to eq. (4.1) still does not allow a very good determination of the scaling exponents γ, γ' and γ'', indicating that for the considered range of lattice volumes the assumed functional form (4.1) might not be optimal. Typically, we could only determine γ to be between 1.6 and 2.6, but on the other hand $\gamma = 1$ does not seem to be a good fit. This leads to the conclusion that higher-order corrections should be included as they can be important for smaller volumes. Below we propose a very simple finite size correction of the kind considered in [26], namely we perform a shift $\bar{N}_{41} \to \bar{N}_{41} - \text{const}$. Thus, instead of using eq. (4.1), we will use a slightly modified scaling relation, which can

JHEP04(2022)103

Fit	$\chi^2_{\kappa_0=4.0}$	$\chi^2_{\kappa_0=4.2}$	$\chi^2_{\Delta=0}$	$\chi^2_{\Delta=-0.02}$
free γ	1.3e-04	6.4e-05	2.3e-02	3.6e-02
$\gamma = 1$	1.7e-05	4.6e-05	1.9e-02	4.7e-02

Table 1. The χ^2 values related to the individual fits of eq. (4.1) (free γ) and eq. (4.2) ($\gamma = 1$) to finite volume scaling of the coupling constants: $\Delta^{\rm crit}$ (vertical measurements in the left two columns) and $\kappa_0^{\rm crit}$ (horizontal measurements in the right two columns).

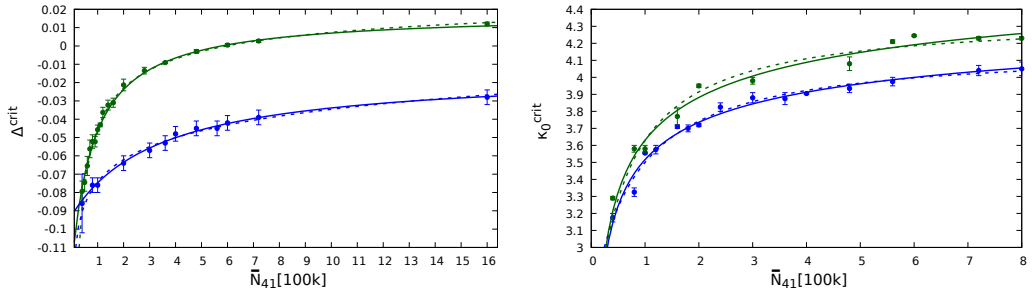

Figure 7. Finite volume scaling of the coupling constants $\Delta^{\rm crit}$ (left panel) and $\kappa_0^{\rm crit}$ (right panel). The dashed and solid curves represent fits to eq. (4.1) and eq. (4.2), respectively. In the left panel (vertical measurements), green data-points are for fixed $\kappa_0 = 4.0$ and blue are for $\kappa_0 = 4.2$. In the right panel (horizontal measurements), green data-points are for fixed $\Delta = -0.02$ and blue are for $\Delta = 0$.

be viewed as corresponding to the first-order transition (fixed $\gamma = 1$), but with a specific form of a finite size correction:

$$\begin{aligned} \Delta^{\rm crit}(\bar{N}_{41}) &= \Delta^{\infty} - A \cdot (\bar{N}_{41} - {\rm const}_1)^{-1}, \\ \kappa_0^{\rm crit}(\bar{N}_{41}) &= \kappa_0^{\infty} - B \cdot (\bar{N}_{41} - {\rm const}_2)^{-1}, \\ \kappa_4^{\rm crit}(\bar{N}_{41}) &= \kappa_4^{\infty} - C \cdot (\bar{N}_{41} - {\rm const}_3)^{-1}. \end{aligned} \tag{4.2}$$

Both scaling relations of eq. (4.1) and eq. (4.2) have the same number of free parameters, i.e., they require a three-parameter fit. We can now compare the two different classes of fits. The parameters for the best fits of the critical scaling of $\Delta^{\rm crit}$ (vertical measurements) and $\kappa^{\rm crit}$ (horizontal measurements) using equations (4.1) and (4.2) were found via the least squares method. In table 1 we show values of χ^2 corresponding to the fits presented in figure 7.

In figure 7 the vertical measurements (for fixed κ_0) are in the left plot and the horizontal ones (for fixed Δ) are in the right plot. In both cases, the dashed lines show the fits of eq. (4.1) and solid lines are the fits of eq. (4.2). Table 1 and figure 7 clearly show that the two classes of fits are really close to each other in all cases; thus, using this information alone, it is hard to distinguish the order of the $B-C$ transition. Additional hint comes from analysis of the $\kappa_4^{\rm crit}$ parameter measured on both sides of the transition, i.e., using data on both sides of the hysteresis region as close to the transition as one can get. This is presented in figure 8 where we compare fits of eq. (4.1) and eq. (4.2) to these data. The vertical measurements are shown in the left panel of figure 8 and the corresponding χ^2

JHEP04(2022)103

Fit	$\chi^2_{\kappa_0=4.0,C}$	$\chi^2_{\kappa_0=4.0,B}$	$\chi^2_{\kappa_0=4.2,C}$	$\chi^2_{\kappa_0=4.2,B}$
free γ	1.15e-06	5.2e-05	1.3e-06	6.3e-06
$\gamma = 1$	1.05e-06	1.6e-05	8.1e-07	4.2e-06

Table 2. The χ^2 values related to the individual fits of eq. (4.1) (free γ) and eq. (4.2) ($\gamma = 1$) to finite volume scaling of the $\kappa_4^{\rm crit}$ in vertical measurements (κ_0 fixed). The C or B indices indicate which side of the phase transition the fitted data belong to.

Fit	$\chi^2_{\Delta=0,C}$	$\chi^2_{\Delta=0,B}$	$\chi^2_{\Delta=-0.02,C}$	$\chi^2_{\Delta=-0.02,B}$
free γ	1.2e-04	2.2e-04	1.6e-04	4.1e-04
$\gamma = 1$	1.2e-04	1.0e-04	2.1e-04	3.8e-04

Table 3. The χ^2 values related to the individual fits of eq. (4.1) (free γ) and eq. (4.2) ($\gamma = 1$) to finite volume scaling of the $\kappa_4^{\rm crit}$ in horizontal measurements (Δ fixed). The C or B indices indicate which side of the phase transition the fitted data belong to.

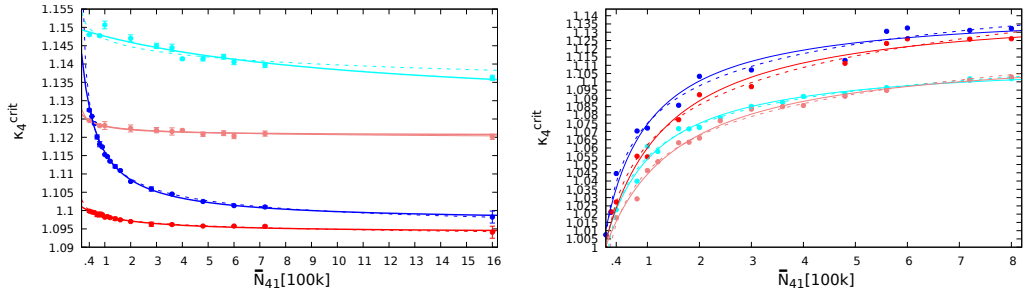

Figure 8. Finite volume scaling of the $\kappa_4^{\rm crit}$ in vertical measurements with fixed $\kappa_0 = 4.2$ and 4.0 (left panel) and horizontal measurements with fixed $\Delta = 0$ and -0.02 (right panel). The dashed and solid curves represent fits to eq. (4.1) and eq. (4.2), respectively. In both plots blue color corresponds to data measured in phase B and red in phase C — closest to the phase transition (hysteresis) region. Darker colors correspond to lower values of the fixed coupling constant.

values in table 2. The horizontal ones are in the right panel of figure 8 and the χ^2 values can be found in table 3. Again, the difference between the two classes of fits is not large, however, our data favor slightly the first-order fits.

Summarizing, we have shown that the first-order type of critical scaling relation (with the proposed finite size correction) fits our data at least as well or even better than the (standard) higher-order fits. Therefore, taking into account the behavior of order parameters which, as already shown in [25] and discussed above, on both sides of the transition behave discontinuously even when extrapolated to the infinite volume limit, we conclude that the data favor a first-order B–C transition, but with the admittedly strange property that in the limit $\bar{N}_{41} \to \infty$ the region of hysteresis shrinks to zero.

JHEP04(2022)103

5 Discussion and conjecture

In this paper, we have analyzed the previously not measured $A-B$ phase transition at three different locations of fixed $\kappa_0 = 4.8$, 4.6, and 4.5. The finite size scaling analysis of $\Delta^{\text{crit}}(\bar{N}_{41})$ revealed a scaling exponent γ close to value 1, which points to a first-order phase transition. Next, we analyzed the $B-C$ phase transition, improving the statistics and extending the previous research to another fixed value of the $\kappa_0 = 4.2$. We also analyzed the finite size scaling when approaching the critical line along the perpendicular direction in the coupling constant space where Δ was fixed at 0 and -0.02. We concluded that the $B-C$ phase transition was also a first-order transition, although we had to use a slightly modified fitting function to obtain acceptable agreement with data. Let us stress that the phase transitions considered are non-standard from the point of view of ordinary phase transitions, since they involve changes in spacetime, rather than changes in field configurations on a fixed spacetime. From the above and our earlier measurements, an interesting pattern emerges, relating the order of the CDT phase transition to changes in the topology of spacetime and it leads to the following conjecture: *phase transitions which involve a change in topology will be first-order transitions.*

First, let us clarify that by topology we mean *effective* topology. This is exemplified by the configurations we observe in the C phase if the topology of space is S^3 and we have time-periodic boundary conditions. Thus, from the outset the topology of the triangulations is that of $T^1 \times S^3$. This is encoded in the initial configuration when we start our MC simulations. By construction, any MC update of the configuration does not change the imposed topology. However, after many MC updates, a typical generic configuration will effectively look like an S^4-triangulation where the *north-pole* and the *south-pole* of this S^4 are connected by a thin *stalk* of cut-off scale. While technically the triangulation still has the topology $T^1 \times S^3$, it is clear that if allowed by the updating algorithm, the preferred configurations would have the topology of S^4. Secondly, recall from the discussion of the nature of generic configurations in section 2, that we observed a second-order transition between phase B and phase Cb, where there is no change in the effective topology. Likewise, in the case when the spatial topology is S^3 there is no real change in topology when we move from phase C_b to phase C and again we observe a second-order transition. All other phase transitions observed are first-order transitions and they are related to a change of the effective topology. In the case of toroidal spatial topology, the $C_b - C$ transition involves a change from S^4 in phase C_b to T^4 in phase C. Similarly, the $B - C$ transition involves a change from S^4 to T^4. The effective topology of phase A may be best characterized as the topology of a disjoint union of spatial geometries of various extensions (see upper left panel in figure 2). Thus, it is different from the topologies encountered in phase C and phase B. Again, the observed phase transitions between phase C and phase A, as well as the transition between phase B and phase A, are first-order transitions.

With hindsight, it is not surprising that a change in the topology of spacetime at the phase transition might result in a first-order transition, since often one would need some major rearrangements of the configurations to implement the change. In this way, a barrier for such a change can be created and lead to pronounced hysteresis. Such phenomena are

JHEP04(2022)103

of course well known in field theories, where the topology of field configurations might change. The new thing here is that we are discussing the topology of spacetime itself. We were alerted to the relation between topology change of spacetime and phase transitions when we studied scalar fields coupled to geometry [19, 27], but the phenomena seen there are in fact already present in the pure theory of geometry as discussed here.

In the CDT theory, our main interest is to find a second-order phase transition where we might be able to define a continuum limit and maybe even a UV fixed point. Since only phase C seems to offer acceptable *infrared* configurations, it is natural to look for phase transition lines in or at the border of phase C. From the results reported here, we cannot use toroidal spatial topology in such studies, since the transitions will be first-order. One should note that there is still a chance that even though the phase transition lines bordering the C phase are first-order, the triple points where the lines end and meet may be of higher-order. This may be indeed the case of the $C_b - B - C$ triple point as the higher-order $B - C_b$ transition line ends in this point as well. Nevertheless, this scenario is not very natural and it is hard to be proven numerically. However, if the spatial topology is S^3, the $C_b - C$ transition is a second-order transition. In addition it is then possible that the $B-C$ transition will also be second-order and it makes the C_b-B-C triple point an interesting candidate for a UV-fixed point. At least it would then be a point where three second-order transition lines meet. In addition, the $C_b - C$ transition has in that case the simple interpretation as the phase transition related to the breaking of isotropy and homogeneity. One could then imagine that the shadow of such a breaking could be important for inhomogeneities in our universe.

Acknowledgments

J.G-S. and A.G. acknowledge support from the grant 2019/33/B/ST2/00589 from National Science Centre Poland. This research was funded by the Priority Research Area Digiworld under the program Excellence Initiative — Research University at the Jagiellonian University in Krakow. We would also like to acknowledge our deep gratitude to Prof. Jerzy Jurkiewicz (from Institute of Theoretical Physics of the Jagiellonian University in Krakow) who collaborated with us in this research; unfortunately he unexpectedly passed away on 30th November 2021, before we finished this work.

A Machine learning locations of the CDT phase transitions

As already noted in section 1.2, in all phase transition studies described herein we have tested and used a new method of finding locations of the (pseudo-)critical points based on machine learning techniques. We have tried many machine learning (ML) methods[4] but the one which turned out to be both very simple and at the same time most efficient has been based on a *logistic regression* model. A detailed discussion of the logistic regression in the

[4]Detailed results of using Machine Learning in CDT data analysis will be published in a separate article. Here we just focus on the Logistic Regression used in the current study.

JHEP04(2022)103

context of ML can be found, e.g., in [28], so below we only shortly summarise this approach and describe most important aspects of its implementation in the context studied here.

Logistic regression is a so-called supervised ML technique which can be applied when one has labeled training data sets. It is commonly used in classification problems, where some new, yet unlabeled, data have to be divided into sub-classes attributed with labels of the training set. A simple example studied here concerns data measured in Monte Carlo simulations which can be classified as belonging to one of two different phases, labeled P_0 and P_1. Each data point p_j within the MC measurements is characterized by a set of features (observables): $\{x_i(p_j)\}$. In the binary classification problem, where one has only two classes, the probability that a data point p_j belongs to class P_1 is estimated by a logistic function:

$$\Pr(p_j \in P_1) = \frac{1}{1 + b^{-\sum_i w_i x_i(p_j)}} \tag{A.1}$$

and the probability that p_j belongs to class P_0 is then $\Pr(p_j \in P_0) = 1 - \Pr(p_j \in P_1)$. In the learning process a numerical algorithm optimises parameters of the logistic function, i.e., b and w_i (weights), by minimizing a *cost function*, usually defined as the cross-entropy of the (labeled) training data set:[5]

$$\text{cost function} = -\frac{1}{N}\sum_{j=1}^{N}\left(l_j \ln \Pr(p_j \in P_1) + (1 - l_j)\ln \Pr(p_j \in P_0)\right), \tag{A.2}$$

where $l_j = 1$ if $p_j \in P_1$ and $l_j = 0$ otherwise. In practice one usually adds $L_1 = \lambda_1 \sum_i |w_i|$ (Lasso regularization) or $L_2 = \lambda_2 \sum_i w_i^2$ (Ridge regularization) to the *cost function*, where λ_1 and λ_2 are metaparameters of the model. Including non-zero λ_1 or λ_2 reduces the number of non-zero weights w_i which effectively acts as a penalty for the number of parameters and thus enhances model prediction accuracy and interpretability.[6]

For each phase transition studied here, we create a training data set by *manually* attributing phase labels to CDT data measured deep into each phase and use these data to learn (fit) the logistic regression model. Then we use the learned model to classify other data, measured closer to the transition region, as belonging to one of the two phases. The phase transition point is signalled by a sudden change of the probability (A.1) of the measured data to belong to a given phase from ~ 0 to ~ 1, see figure 9. We have decided to look at data measured for each chosen value of the fixed coupling constant and each lattice volume independently, i.e., for each such a choice we create an independent training set, fit our model and use it to find the critical point. Take, e.g., the $A-B$ transition analysis done for some fixed value of κ_0 and fixed $\bar{N}_{41}$ volume based on data measured for

[5] Often, the learning data are additionally split into the *training* and the *test* sets. Parameter optimization (fitting) is done using the training set but model accuracy is checked using the test set.

[6] The metaparameters λ_1 and λ_2 can themselves be optimized by fitting many models with different λ_1 and λ_2 and choosing the one with the highest accuracy. In all cases studied here the optimal models had very small values of these metaparameters.

JHEP04(2022)103

different values of the Δ coupling: $\Delta_{\min}, \Delta_1, \ldots, \Delta_k, \Delta_{\max}$, see section 3. The procedure to find $\Delta^{\text{crit}}(\bar{N}_{41})$ is the following:[7]

1. take all data measured for the highest value of $\Delta = \Delta_{\max}$ (deep in phase A) and label it as P_1 (or "phase A"),
2. take all data measured for the lowest value of $\Delta = \Delta_{\min}$ (deep in phase B) and label it as P_0 (or "phase B"),
3. take a subset of data from points 1 and 2 as a (labeled) *training set*,
4. learn (fit) the logistic regression model using the training set;[8] this step also includes optimizing metaparameters of the model (λ_1 and λ_2 regularization coefficients),
5. check accuracy of the fitted model using all data from points 1 and 2 (in all cases analyzed the accuracy was 100%, i.e., the model was able to distinguish between the P_1 and P_2 data perfectly),
6. use the fitted model to classify other, yet unlabeled, data measured for Δ: $\Delta_1, \ldots, \Delta_k$, i.e., closer to a phase transition region than data from points 1 and 2,
7. compute the probability of all classified data points to be in phase P_1: $\Pr(p_j \in P_1)$, see eq. (A.1),
8. compute the mean value $\langle \Pr(p_j \in P_1) \rangle_\Delta$ (and the error: standard deviation) of the probability of all data points measured for a given Δ,
9. find the transition point $\Delta^{\text{crit}}(\bar{N}_{41})$, where $\langle \Pr(p_j \in P_1) \rangle_\Delta$ jumps from ~ 0 to ~ 1, see figure 9.

Then we repeat the analysis (model learning and classification) for a different lattice volume $\bar{N}_{41}$, and then also for each different κ_0 independently.

It is important to stress that in the data analysis described above we used only geometric information about triangulations (configurations) generated in MC simulations, i.e., the set of features used in the ML model fitting and classification does not include any information about the values of the CDT coupling constants or other MC simulation parameters. Therefore we can say, that the method learned to distinguish the phases purely on (some) geometric features of the triangulations. We used a set of 30 geometric observables, including both global parameters of the triangulations: N_0, N_1, N_2, N_4, N_{41}, MO, i.e., the total number of vertices, links, triangles, four-simplices, $\{4,1\}$-simplices and maximal coordination number of vertices, respectively, as well as "per-time-slab" data: $N_{41}(t)$, $N_{32}(t)$, $N_{23}(t)$, $N_{14}(t)$, $N_0(t)$, $MO(t)$, i.e., the number of $\{4,1\}$, $\{3,2\}$, $\{2,3\}$ and $\{1,4\}$-simplices in

[7] For the $B-C$ transition, see section 4, P_1 denotes "phase C", and in the *vertical* measurements the procedure is exactly the same while in the *horizontal* measurements one fixes Δ and changes κ_0 (thus $\kappa_0 \leftrightarrow \Delta$).

[8] During ML process we have chosen not to split the learning data into independent training and test sets. Instead we make a global check of the model accuracy — see point 5.

JHEP04(2022)103

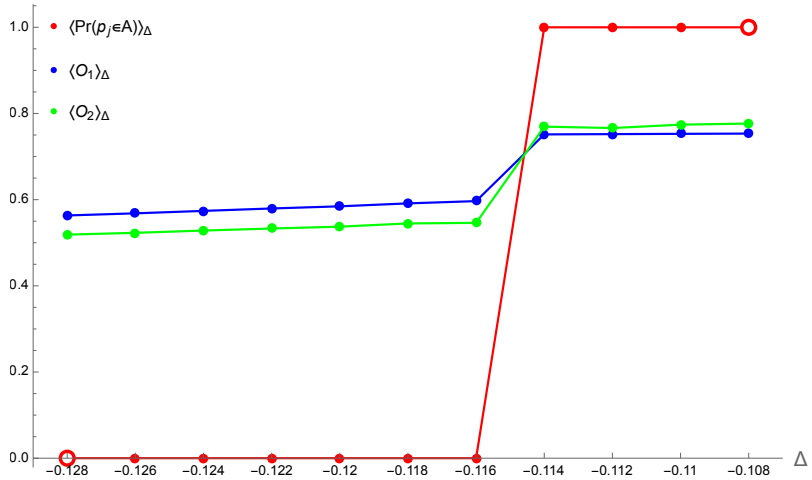

Figure 9. Machine learning analysis of the $A-B$ transition for fixed $\kappa_0 = 4.8$ and $\bar{N}_{41} = 100$k. Red points are the mean probabilities $\langle \Pr(p_j \in P_1) \rangle_\Delta$ that all MC measurements performed for a given value of Δ belong to phase A. The probabilities were computed using the logistic regression model (A.1) learned (fitted) using only part of data measured for the lowest and the highest Δ (denoted by empty dots). For comparison we also plot the *traditional* order parameters $\mathcal{O}_1$ (rescaled by $5\times$) and $\mathcal{O}_2$ (rescaled by $35\times$).

a given slab between (lattice) time coordinate t and $t+1$, the number and maximal coordination number of all vertices with a time coordinate t, respectively. In all cases $t = 1, 2, 3, 4$ (with periodic boundary conditions). In order to increase statistics of our data set and also to encode information about a time shift symmetry of the CDT model, we have quadrupled the data by performing a time shift of all "per-time-slab" features by (periodically) changing their time coordinates $t = (1, 2, 3, 4) \to (4, 1, 2, 3) \to (3, 4, 1, 2) \to (2, 3, 4, 1)$. The values of the global features kept unchanged.

The above-mentioned observables also enable one to compute *traditional* order parameters, which were earlier used to distinguish between the CDT phases, e.g., $\mathcal{O}_1 \equiv N_0/N_{41}$ or $\mathcal{O}_2 \equiv N_{32}/N_{41}$ and thus check if the automatic ML classification algorithm is consistent with our former results, see figure 9. We implemented the logistic regression model in *Wolfram Mathematica 12* using the built-in function:

```
Classify[..., Method -> "LogisticRegression"]
```

with standard parameters. In all cases analyzed the model classified both $A-B$ and $C-B$ phase transition data correctly, with a 100% accuracy, see figure 9 as an example.

JHEP04(2022)103

References

[1] R. Loll, *Quantum Gravity from Causal Dynamical Triangulations: A Review*, *Class. Quant. Grav.* **37** (2020) 013002 [arXiv:1905.08669] [INSPIRE].

[2] J. Ambjørn, Z. Drogosz, J. Gizbert-Studnicki, A. Görlich, J. Jurkiewicz and D. Nèmeth, *CDT Quantum Toroidal Spacetimes: An Overview*, *Universe* **7** (2021) 79 [arXiv:2103.15610] [INSPIRE].

[3] T. Regge, *General relativity without coordinates*, *Nuovo Cim.* **19** (1961) 558 [INSPIRE].

[4] J. Ambjørn, A. Görlich, J. Jurkiewicz and R. Loll, *Nonperturbative Quantum Gravity*, *Phys. Rept.* **519** (2012) 127 [arXiv:1203.3591] [INSPIRE].

[5] J. Ambjørn and R. Loll, *Nonperturbative Lorentzian quantum gravity, causality and topology change*, *Nucl. Phys. B* **536** (1998) 407 [hep-th/9805108] [INSPIRE].

[6] J. Ambjørn, J. Jurkiewicz, R. Loll and G. Vernizzi, *Lorentzian* $3-D$ *gravity with wormholes via matrix models*, *JHEP* **09** (2001) 022 [hep-th/0106082] [INSPIRE].

[7] J. Ambjørn, J. Jurkiewicz, R. Loll and G. Vernizzi, $3-D$ *Lorentzian quantum gravity from the asymmetric ABAB matrix model*, *Acta Phys. Polon. B* **34** (2003) 4667 [hep-th/0311072] [INSPIRE].

[8] A. Eichhorn, A.D. Pereira and A.G.A. Pithis, *The phase diagram of the multi-matrix model with ABAB-interaction from functional renormalization*, *JHEP* **12** (2020) 131 [arXiv:2009.05111] [INSPIRE].

[9] J. Ambjørn, S. Jordan, J. Jurkiewicz and R. Loll, *Second- and First-Order Phase Transitions in CDT*, *Phys. Rev. D* **85** (2012) 124044 [arXiv:1205.1229] [INSPIRE].

[10] D.N. Coumbe, J. Gizbert-Studnicki and J. Jurkiewicz, *Exploring the new phase transition of CDT*, *JHEP* **02** (2016) 144 [arXiv:1510.08672] [INSPIRE].

[11] J. Ambjørn, D. Coumbe, J. Gizbert-Studnicki, A. Görlich and J. Jurkiewicz, *New higher-order transition in causal dynamical triangulations*, *Phys. Rev. D* **95** (2017) 124029 [arXiv:1704.04373] [INSPIRE].

[12] J. Ambjørn, D. Coumbe, J. Gizbert-Studnicki, A. Görlich and J. Jurkiewicz, *Critical Phenomena in Causal Dynamical Triangulations*, *Class. Quant. Grav.* **36** (2019) 224001 [arXiv:1904.05755] [INSPIRE].

[13] J. Ambjørn, G. Czelusta, J. Gizbert-Studnicki, A. Görlich, J. Jurkiewicz and D. Németh, *The higher-order phase transition in toroidal CDT*, *JHEP* **05** (2020) 030 [arXiv:2002.01051] [INSPIRE].

[14] J. Ambjørn, Z. Drogosz, J. Gizbert-Studnicki, A. Görlich, J. Jurkiewicz and D. Németh, *Cosmic voids and filaments from quantum gravity*, *Eur. Phys. J. C* **81** (2021) 708 [arXiv:2101.08617] [INSPIRE].

[15] J. Ambjørn, J. Gizbert-Studnicki, A. Görlich, J. Jurkiewicz and D. Németh, *The phase structure of Causal Dynamical Triangulations with toroidal spatial topology*, *JHEP* **06** (2018) 111 [arXiv:1802.10434] [INSPIRE].

[16] J. Ambjørn, J. Gizbert-Studnicki, A. Görlich and J. Jurkiewicz, *The effective action in 4-dim CDT. The transfer matrix approach*, *JHEP* **06** (2014) 034 [arXiv:1403.5940] [INSPIRE].

[17] J.B. Hartle and S.W. Hawking, *Wave Function of the Universe*, *Phys. Rev. D* **28** (1983) 2960 [INSPIRE].

JHEP04(2022)103

[18] J. Ambjørn, J. Gizbert-Studnicki, A. Görlich, J. Jurkiewicz, N. Klitgaard and R. Loll, *Characteristics of the new phase in CDT*, *Eur. Phys. J. C* **77** (2017) 152 [arXiv:1610.05245] [INSPIRE].

[19] J. Ambjørn, Z. Drogosz, J. Gizbert-Studnicki, A. Görlich, J. Jurkiewicz and D.a. Németh, *Scalar fields in causal dynamical triangulations*, *Class. Quant. Grav.* **38** (2021) 195030 [arXiv:2105.10086] [INSPIRE].

[20] J. Ambjørn, A. Görlich, J. Jurkiewicz and R. Loll, *The Nonperturbative Quantum de Sitter Universe*, *Phys. Rev. D* **78** (2008) 063544 [arXiv:0807.4481] [INSPIRE].

[21] J. Ambjørn, A. Görlich, J. Jurkiewicz, R. Loll, J. Gizbert-Studnicki and T. Trześniewski, *The Semiclassical Limit of Causal Dynamical Triangulations*, *Nucl. Phys. B* **849** (2011) 144 [arXiv:1102.3929] [INSPIRE].

[22] J. Ambjørn, J. Gizbert-Studnicki, A. Görlich and J. Jurkiewicz, *The transfer matrix in four-dimensional CDT*, *JHEP* **09** (2012) 017 [arXiv:1205.3791] [INSPIRE].

[23] J. Ambjørn, Z. Drogosz, J. Gizbert-Studnicki, A. Görlich, J. Jurkiewicz and D. Nèmeth, *Impact of topology in causal dynamical triangulations quantum gravity*, *Phys. Rev. D* **94** (2016) 044010 [arXiv:1604.08786] [INSPIRE].

[24] J. Ambjørn, J. Gizbert-Studnicki, A. Görlich, K. Grosvenor and J. Jurkiewicz, *Four-dimensional CDT with toroidal topology*, *Nucl. Phys. B* **922** (2017) 226 [arXiv:1705.07653] [INSPIRE].

[25] J. Ambjørn, J. Gizbert-Studnicki, A. Görlich, J. Jurkiewicz and D. Németh, *Towards an UV fixed point in CDT gravity*, *JHEP* **07** (2019) 166 [arXiv:1906.04557] [INSPIRE].

[26] J. Ambjørn, J. Jurkiewicz and Y. Watabiki, *On the fractal structure of two-dimensional quantum gravity*, *Nucl. Phys. B* **454** (1995) 313 [hep-lat/9507014] [INSPIRE].

[27] J. Ambjørn, Z. Drogosz, J. Gizbert-Studnicki, A. Görlich, J. Jurkiewicz and D. Németh, *Matter-Driven Change of Spacetime Topology*, *Phys. Rev. Lett.* **127** (2021) 161301 [arXiv:2103.00198] [INSPIRE].

[28] G. James, D. Witten, T. Hastie and R. Tibshirani, *An Introduction to Statistical Learning: with Applications in R*, Springer (2013).

JHEP04(2022)103

Eur. Phys. J. C (2021) 81:708
https://doi.org/10.1140/epjc/s10052-021-09468-z

THE EUROPEAN PHYSICAL JOURNAL C

Letter

Cosmic voids and filaments from quantum gravity

J. Ambjørn[1,2], **Z. Drogosz**[3], **J. Gizbert-Studnicki**[3], **A. Görlich**[3], **J. Jurkiewicz**[3], **D. Németh**[3,a]

[1] The Niels Bohr Institute, Copenhagen University, Blegdamsvej 17, 2100 Copenhagen Ø, Denmark
[2] IMAPP, Radboud University Nijmegen, Heyendaalseweg 135, AJ 6525 Nijmegen, The Netherlands
[3] Institute of Theoretical Physics, Jagiellonian University, Łojasiewicza 11, 30-348 Kraków, Poland

Received: 17 March 2021 / Accepted: 20 July 2021 / Published online: 7 August 2021

Abstract Using computer simulations, we study the geometry of a typical quantum universe, i.e., the geometry one might expect before a possible period of inflation. We display it using coordinates defined by means of four classical scalar fields satisfying the Laplace equation with nontrivial boundary conditions. They are a close analogue of the harmonic coordinate condition used in the context of GR (Kuchar and Torre in Phys Rev D 43:419–441, 1991). It is highly nontrivial that these ideas can be applied to understand the structures which appear in very irregular and fluctuating geometries. The field configurations reveal cosmic web structures surprisingly similar to the ones observed in the present-day universe.

1 Introduction

One major unsolved problem in theoretical physics is how to unite the theory of general relativity and quantum mechanics. It is hoped that such a unification will allow us to understand physics at the Planck scale, where the assumed quantum nature of gravity most likely plays a dominant role. Furthermore, the idea of an inflationary period in the history of our Universe has taught us that these quantum fluctuations at or near the Planck scale can, owing to an exponential growth of the size of the Universe, freeze and be expanded into the seeds of macroscopic large-scale structures. Results presented in this article suggest that the scenario of cosmic filaments and voids that we observe in the Universe today might have its source at the very early stage of cosmic evolution of quantum geometric degrees of freedom.

[a] e-mail: daniel.nemeth@doctoral.uj.edu.pl (corresponding author)

2 Lattice quantum universes

To discuss universes of the size of a few Planck lengths and their fluctuating quantum geometry, one needs a non-perturbative model of quantum gravity. We will discuss here a particular model called Causal Dynamical Triangulations (abbreviated to CDT; see [2,3] for a comprehensive introduction and an explanation of its somewhat technical name), but we believe that our results are generic and will be present in any reasonable quantum model of gravity. In CDT, spacetime is a triangulation built by joining together fixed-size four-dimensional simplices in a way that satisfies certain topological requirements. The edge length ε of the four-simplices acts as an ultraviolet (UV) cutoff. Its choice also fixes the geometry of a triangulation. The way in which simplicial building blocks are connected codes the information about the curvature of the particular configuration. A natural geometric way of calculating the classical Einstein-Hilbert action on such piecewise linear manifolds leads to the so-called Regge action. The lattice regularized path integral of quantum gravity is then given by

$$\mathscr{Z}_{QG} = \int \mathscr{D}_{\mathscr{M}_H}[g_L]\, e^{iS_{EH}[g_L]} \to \sum_{T_E \in \mathscr{T}_E} e^{-S_R[T_E]}, \qquad (1)$$

where $\mathscr{M}_H$ is a globally defined hyperbolic Lorentzian manifold and $\mathscr{D}_{\mathscr{M}_H}[g_L]$ denotes the integration over equivalence classes $[g_L]$ of Lorentzian metrics on $\mathscr{M}_H$. $\mathscr{T}_E$ is a suitable set of Wick-rotated Euclidean triangulations. The Regge action $S_R[T_E]$ for a triangulation $T_E \in \mathscr{T}_E$ contains the bare couplings related to the cosmological and Newton constants. In principle, we want to adjust the bare coupling constants such that we can take the UV cutoff ε to zero while keeping the physics unchanged (see [4] for a recent review). In accordance with the imposed global hyperbolicity, CDT introduces a time foliation of the four-dimensional manifolds into three-dimensional leaves, which are three-dimensional spatial sub-manifolds with a global time t and a fixed topol-

ogy. The explicit CDT construction permits a Wick rotation of the time coordinate t (still denoted t), whereby CDT becomes a statistical model that can be studied using Monte-Carlo simulations. Each configuration obtained in the simulations can be viewed as the quantum evolution of a three-dimensional quantum geometric state in the imaginary time. This allows us inter alia, to measure the time dependence of some global quantities such as the spatial volume. It was shown [5–12] that, for suitable choices of the bare coupling constants, both the average spatial volume and its fluctuations can, with a large degree of accuracy, be described by the Hartle–Hawking minisuperspace model, which assumes isotropy and homogeneity of the Universe such that the only dynamical variable is the scale factor $a(t)$. It should be emphasized that the isotropy and homogeneity are not put in by hand in CDT but follow from integrating out all degrees of freedom other than the scale factor, and the typical geometries encountered in the quantum path integral are not at all close to the classical homogeneous solution of GR. The approximate agreement with the classical minisuperspace solution is obtained from an average of an ensemble of highly fluctuating geometric states and is caused by a nontrivial interplay between the physical action and the entropy of configurations.

The CDT model is background independent and, in the spatial directions, coordinate free. There is no background geometry in the definition of the path integral. Geometric information provided by the model is local, in the form of the neighborhood relations between the elements of the geometry. We may determine the geodesic distance between the simplices, but capturing the global properties of the system without a good choice of coordinates is difficult [13–15]. It is not a priori clear if such a choice is at all possible for a locally highly fluctuating geometry. Below we will show that such a choice is not only possible but can also give us a much better understanding of the structures present in quantum geometric configurations.

3 Boundary conditions

We will now consider a version of CDT where the piecewise linear manifolds are periodic both in time and space directions. Such a toroidal topology can be viewed as being extended to an infinite four-dimensional space, in which a four-dimensional elementary cell, bounded by a set of four independent non-contractible three-dimensional boundaries is periodically repeated in all directions. These boundaries are not physical entities, are not unique, and can be locally deformed as long as they still form an elementary cell, and yet they can serve as a reference frame for a coordinate system on a given triangulation. The nontrivial fractal structure of the encountered geometries makes it difficult to introduce spatial coordinates in a chosen elementary cell in a constructive geometric way, using only the geodesic distance from a boundary. Below we will introduce an alternative method, where four massless classical scalar fields, which satisfy the Laplace equation with nontrivial boundary conditions will be used to fully parametrize the fractal geometry. In the case discussed in this paper, the fields depend on the geometry, but they do not modify it, providing us, for each configuration, with a system of external coordinates. One can say that they act as a microscope which uncovers the complicated four-dimensional structure of density fluctuations. Even for a configuration with a very irregular geometry, such fields allow us to define periodic pseudo-continuous coordinates and provide generalized foliations in all space-time directions. Consequently, it becomes possible to visualize and measure multidimensional correlations in all directions. As will be reported below, what we see is a quantum universe which seems surprisingly similar to our present day macroscopic universe.

3.1 Scalar fields as coordinates with values on S^1

We want to find nontrivial harmonic maps between two Riemannian manifolds $\mathscr{M}(g_{\mu\nu}) \to \mathscr{N}(h_{\alpha\beta})$, where $g_{\mu\nu}$ is an arbitrary metric and $h_{\alpha\beta}$ is a flat one. If $\mathscr{N}$ has the topology of T^4, then it can be defined by four scalar fields ϕ^α, $\alpha = 1, 2, 3, 4$, where $\phi^\alpha(x)$ is a map $\mathscr{M} \to S^1$, such that the following action is minimized:

$$S_M[\phi, \mathscr{M}] = \frac{1}{2}\int \mathrm{d}^4x\sqrt{g(x)}\; g^{\mu\nu}(x)\; h_{\rho\sigma}(\phi^\gamma(x)) \times \partial_\mu\phi^\rho(x)\partial_\nu\phi^\sigma(x)). \tag{2}$$

Because we have chosen the trivial metric $h_{\rho\sigma}$ on $\mathscr{N}$, Eq. (2) splits up into four independent equations for the four scalar fields ϕ^σ. Minimizing Eq. (2) leads to the set of Laplace equations:

$$\Delta_x\phi^\sigma(x) = 0, \quad \Delta_x = \frac{1}{\sqrt{g(x)}}\partial_\mu\sqrt{g(x)}g^{\mu\nu}(x)\partial_\nu. \tag{3}$$

Thus ϕ^σ becomes a harmonic map $\mathscr{M} \to (S^1)^4$ preserving a dependence of ϕ^σ on $g^{\mu\nu}$. Let us consider a trivial one-dimensional example. In this case, let $\mathscr{M}$ be S^1 with a unit circumference and a positive and strictly periodic density $\sqrt{g(x)}$. We want $x \to \phi(x)$ to be a non-trivial map $S^1 \to S^1$ such that ϕ can serve as a coordinate instead of x. One way to implement this is to find a solution satisfying

$$\phi(x + n) = \phi(x) + n\delta, \tag{4}$$

which maps the circle with a unit circumference to a circle with a circumference δ. The solution to the Laplace equation in this case satisfies

$$\mathrm{d}\phi(x) = \delta \cdot \sqrt{g(x)}\,\mathrm{d}x. \tag{5}$$

By rescaling the field, we can always enforce $\delta = 1$. The solution $\phi(x)$ is fixed by picking x_0 where $\phi(x_0) = 0$. The map $x \to \phi(x)$ becomes a monotonically increasing invertible map in the whole domain $\mathbb{R}$ with the geometry periodically repeated with the period δ. If we parametrize the one-dimensional manifold $\mathscr{M}$ in terms of ϕ instead of x, we will find the volume density in the range ϕ to $\phi+\mathrm{d}\phi$ to be proportional to $\sqrt{g(x)}\,\mathrm{d}x$, so that effectively $g(\phi) = 1$. We can also consider a function $\psi(x) = \mathrm{mod}(\phi(x)-\phi(x_1), \delta)$. This function satisfies the Laplace equation in the range between x_1 (where $\psi(x) = 0$) and x_1+1 (where $\psi(x) = \delta$). The equation satisfied by $\psi(x)$ becomes a Poisson equation with the extra inhomogeneous local term, producing jumps at boundary points $x = x_1$ and $x = x_1 + 1$. It can still be considered to be a Laplace equation with a non-trivial boundary "jump" condition. Generalizing this to $\mathscr{M}$ with the topology of T^4, we want a solution to the Laplace Eq. (3) that wraps around S^1 in a particular direction once, and, in addition, we want the points x in $\mathscr{M}$ that satisfy $\phi^\sigma(x) = c$ to form hypersurfaces $H^\sigma(c)$ whose union for c varying in a range of length 1 covers the whole $\mathscr{M}$.

3.2 Classical scalar fields with a jump

In CDT, the four-dimensional manifolds are represented by regular four-dimensional triangulations constructed by gluing together four-simplices so that each face is shared by exactly two simplices. Denote the number of four-simplices in the triangulation by N_4. Each triangulation we consider is generated by a Monte Carlo simulation, using the CDT partition function. We call such a generated triangulation a configuration. For each configuration, we keep information about the position of the four boundaries of the elementary cell. This information is non-dynamical: it does not influence the Monte Carlo process. Each boundary is a connected set of three-dimensional faces, each of which separates two simplices, for instance, i and j, belonging to two neighboring elementary cells. The connection $i \to j$ can have either a positive or negative orientation, depending on the direction in which we cross the boundary. The boundary between the neighboring elementary cells in a direction σ can be parametrized by the $N_4 \times N_4$ anti-symmetric matrix $\mathbf{B}^\sigma_{ij} = -\mathbf{B}^\sigma_{ji}$ with the elements

$$\mathbf{B}^\sigma_{ij} = \begin{cases} \pm 1 & \text{if } i \to j \text{ crosses the boundary,} \\ 0 & \text{otherwise.} \end{cases} \tag{6}$$

The number of directed boundary faces of a simplex i is given by $b^\sigma_i = \sum_j \mathbf{B}^\sigma_{ij}$, with the obvious constraints $-5 < b^\sigma_i < 5$ and $\sum_i b^\sigma_i = 0$. For any simplex i adjacent to a boundary, the values $\mathbf{B}^\sigma_{ij}$ are all positive or zero (on one side of the boundary), or all negative or zero (on the other side). We consider four scalar fields ϕ^σ_i located in the centers of simplices and solve the minimization problem for the following discrete version of the continuous action in Eq. (2), for each field ϕ^σ_i:

$$S^{CDT}_M[\phi^\sigma, T_E] = \frac{1}{2}\sum_{i\leftrightarrow j}(\phi^\sigma_i - \phi^\sigma_j - \delta\mathbf{B}^\sigma_{ij})^2. \tag{7}$$

The simplicity of the action does not mean that the geometric information about the connections between simplices is lost. Its form is purely a result of the fact that the system is built from simplices with an equal size. In (7) the sum is over all pairs of neighboring four-simplices in the triangulation T_E representing the manifold $\mathscr{M}(g_{\mu\nu})$ in Eq. (2). The parameter δ plays the same role as in the one-dimensional example considered previously, and here too, by rescaling the field, we can always set $\delta = 1$. The action (7) has two important symmetries. The first one is the invariance under a constant shift of the scalar field (the Laplacian zero mode). The second is a local invariance under a modification of the boundary $\mathbf{B}^\sigma_{ij}$ and a shift by ± 1 (depending on the side of the boundary) of the field value in a simplex i adjacent to the boundary. This is equivalent to moving the simplex to the other side of the boundary and compensating for the change of the field in its center. After such a move, the number of faces belonging to the boundary will in general be changed, but the action (7) will remain constant. The classical field, henceforth denoted as ϕ^σ_i, minimizes the action (7), and thus has to satisfy the non-homogeneous Poisson-like equation

$$\mathbf{L}\phi^\sigma = b^\sigma, \tag{8}$$

where $\mathbf{L} = 5\mathbb{1} - \mathbf{A}$ is the $N_4 \times N_4$ Laplacian matrix, and $\mathbf{A}_{ij}$ is the adjacency matrix with entries of value 1 if simplices i and j are neighbors and 0 otherwise. The Laplacian matrix $\mathbf{L}$ has a constant zero mode but can be inverted if we fix a value of the field $\phi^\sigma_{i_0} = 0$ for an arbitrary simplex i_0. Although $\mathbf{L}$ is a sparse matrix, inverting it is a major numerical challenge for a system typically of size $N_4 \approx 10^6$. After we nevertheless obtain the classical solution ϕ^σ, the multi-dimensional analogue of the one-dimensional function $\psi(x)$ is given by ψ^σ_i:

$$\psi^\sigma_i = \mathrm{mod}(\phi^\sigma_i, 1). \tag{9}$$

A new boundary is defined by $\bar{b}^\sigma = \mathbf{L}\psi^\sigma$. This allows us to reconstruct a new three-dimensional hypersurface H, separating the elementary cell from its copies in the direction σ and characterized by the fact that the field jumps from 0 to 1 when crossing H. This hypersurface can be moved to another position if we consider a family of hypersurfaces $H(\alpha^\sigma)$ obtained from

$$\psi^\sigma_i(\alpha^\sigma) = \mathrm{mod}(\phi^\sigma_i - \alpha^\sigma, 1), \quad \bar{b}^\sigma(\alpha^\sigma) = \mathbf{L}\psi^\sigma(\alpha^\sigma). \tag{10}$$

Changing $0 \le \alpha^\sigma < 1$, we shift the position of the hypersurface and cover the whole elementary cell defined

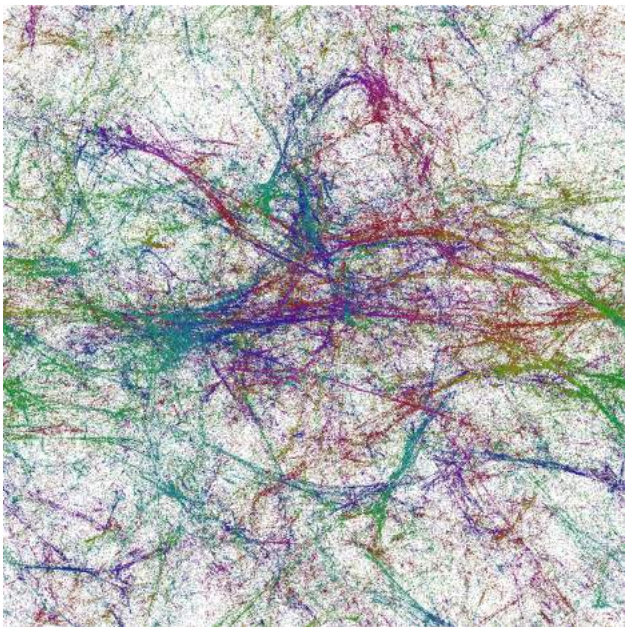

Fig. 1 The projection of four-volume on the xy-plane, as defined by (11) for a CDT configuration. Different colors correspond to different times t of the original t-foliation

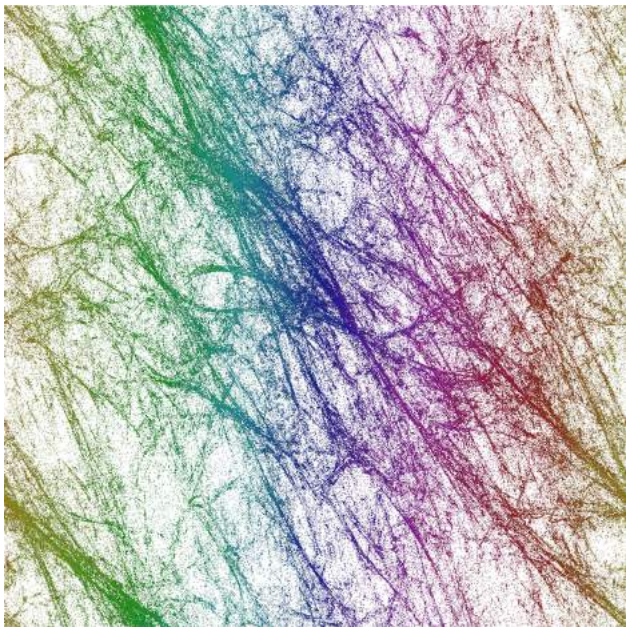

Fig. 2 The projection of four-volume on the tx-plane for a CDT configuration. There is a strong correlation between the original t-foliation (color) and new time coordinate ψ^t (horizontal axis)

by the boundary (10), and in this way we obtain a foliation in the direction σ. We may now use $\psi_i^\sigma = \psi_i^\sigma(0)$ as a coordinate in the σ-direction. The same construction can be repeated in all directions $\sigma \in \{x, y, z, t\}$ for any configuration obtained in the numerical simulations, and in this way every simplex i will be assigned a unique set of coordinates $\{\psi_i^x, \psi_i^y, \psi_i^z, \psi_i^t\}$, all in the range between 0 and 1. A solution to the Laplace equation has the property that the coordinates of each simplex are equal to the mean value of the coordinates of its neighbors (up to the shift of the field at the boundary), i.e., it preserves the triangulation structure. This is the required map from our configuration with a topology of T^4 to $(S^1)^4$ (which of course also has the topology T^4). Note that the coordinate ψ_i^t is not the same as the one coming from the original foliation of the CDT model. The parametrization defined above permits to analyze the distribution of the four-volume (the number of simplices) contained in hypercubic blocks with sizes $\{\Delta\psi_i^x, \Delta\psi_i^y, \Delta\psi_i^z, \Delta\psi_i^t\}$, which is equivalent to measuring the integrated $\sqrt{g(\psi)}$:

$$\Delta N(\psi) = \sqrt{g(\psi)} \prod_\sigma \Delta\psi^\sigma = N(\psi) \prod_\sigma \Delta\psi^\sigma. \tag{11}$$

We can measure the full four-dimensional distribution $N(\psi)$. In Figs. 1 and 2 we show projections of the volume density distribution of a typical configuration on two-dimensional parameter subspaces, the xy-plane and the tx-plane respectively, integrating over the remaining two directions. One observes a remarkable pattern of voids and filaments, which qualitatively looks quite similar to the pictures of voids and filaments observed in our real Universe (see e.g. [16]; the plots can be found on the web [17,18]). Using the new coordinates, we observe a pattern of volume concentrations in the spatial directions. The higher-density domains tend to attract each other, forming denser clouds, which survive in the imaginary time evolution in a quantum trajectory (see Fig. 2). There seems to appear a sequence of scales, characterizing a gradual condensation of gravitationally interacting "objects", but one should remember that there is no matter in this system, only pure geometry, which behaves as if quantum fluctuations could produce massive interacting objects, somewhat analogous to dark matter. This indicates that quantum geometric fluctuations are highly correlated, an effect which could not be easily analyzed without introducing a global set of coordinates. Of course, we are talking about quantum objects of Planckian size, but if a more extended model exhibited inflation, one could imagine that aspects of these objects would be frozen when entering the horizon, like the standard Gaussian fluctuations in simple inflationary models, and then would re-enter the horizon at a later stage, after reheating, as classical densities.

4 Discussion

CDT presents us with a model of what we believe are generic fluctuations of geometry at the Planck scale. We hope that measurements of space-time correlations will allow us to determine "experimentally" (i.e., using Monte Carlo data) the

effective continuum action that governs our lattice model not only in time, but also in spatial directions. The construction of such an effective action will help us to understand if CDT is an UV-complete quantum field theory of gravity, as imagined in the so-called asymptotic safety scenario, or only an effective quantum theory of geometries.

Acknowledgements Z.D. acknowledges support from the National Science Centre, Poland, Grant 2019/32/T/ST2/00390. J.G.-S. acknowledges support of the Grant UMO-2016/23/ST2/00289 from the National Science Centre Poland. A.G. acknowledges support by the National Science Centre, Poland, under Grant no. 2015/17/D/ST2/03479. J.J. acknowledges support from the National Science Centre, Poland, Grant 2019/33/B/ST2/00589. D.N. acknowledges support from National Science Centre, Poland with Grant no. 2019/32/T/ST2/00389.

Data Availibility Statement The data and code based on which this manuscript was written will not be deposited. [Author comment: All data included in this manuscript are available upon request by contacting with the corresponding author.]

Declarations

Conflict of interest Not applicable.

Funded by SCOAP[3].

References

1. K.V. Kuchar, C.G. Torre, Phys. Rev. D **43**, 419–441 (1991)
2. J. Ambjorn, A. Goerlich, J. Jurkiewicz, R. Loll, Phys. Rep. **519**, 127 (2012)
3. R. Loll, Class. Quantum Gravity **37**, 013002 (2020)
4. J. Ambjorn, J. Gizbert-Studnicki, A. Görlich, J. Jurkiewicz, R. Loll, Front. Phys. **8**, 247 (2020)
5. J. Ambjorn, J. Jurkiewicz, R. Loll, Phys. Lett. B **607**, 205–213 (2005)
6. J. Ambjorn, A. Gorlich, J. Jurkiewicz, R. Loll, J. Gizbert-Studnicki, T. Trzesniewski, Nucl. Phys. B **849**, 144 (2011)
7. J. Ambjorn, J. Jurkiewicz, R. Loll, Phys. Rev. D **72**, 064014 (2005)
8. J. Ambjorn, J. Jurkiewicz, R. Loll, Phys. Rev. Lett. **93**, 131301 (2004)
9. J. Ambjorn, A. Görlich, J. Jurkiewicz, R. Loll, Phys. Rev. D **78**, 063544 (2008)
10. J. Ambjorn, A. Görlich, J. Jurkiewicz, R. Loll, Phys. Rev. Lett. **100**, 091304 (2008)
11. J. Ambjorn, Z. Drogosz, J. Gizbert-Studnicki, A. Görlich, J. Jurkiewicz, D. Németh, Phys. Rev. D **94**, 044010 (2016)
12. J. Ambjorn, J. Gizbert-Studnicki, A. Görlich, K. Grosvenor, J. Jurkiewicz, Nucl. Phys. B **922**, 226–246 (2017)
13. J. Ambjørn, Z. Drogosz, J. Gizbert-Studnicki, A. Görlich, J. Jurkiewicz, Nucl. Phys. B 114626 (2019)
14. J. Ambjorn, Z. Drogosz, A. Görlich, J. Jurkiewicz, Phys. Rev. D **103**, 086022 (2021)
15. J. Ambjorn, Z. Drogosz, J. Gizbert-Studnicki, A. Görlich, J. Jurkiewicz, D. Németh. arXiv:2105.10086 [gr-qc]
16. J.N. Burchett, O. Elek, N. Tejos, J.X. Prochaska, T.M. Tripp, R. Bordoloi, A.G. Forbes, Astrophys. J. Lett. **891**, L35 (2020)
17. https://aasnova.org/2018/01/05/galaxies-growing-up-on-the-edge-of-the-void/
18. https://astronomynow.com/2016/08/12/astronomers-use-cosmic-voids-to-study-the-universe/

Matter-Driven Change of Spacetime Topology

J. Ambjørn,[1,*] Z. Drogosz,[2,†] J. Gizbert-Studnicki,[2,‡] A. Görlich,[2,§] J. Jurkiewicz,[2,‖] and D. Németh[2,¶]
[1]The Niels Bohr Institute, Copenhagen University, Blegdamsvej 17, DK-2100 Copenhagen Ø, Denmark
[2]Institute of Theoretical Physics, Jagiellonian University, Łojasiewicza 11, Kraków, PL 30-348, Poland

(Received 13 March 2021; revised 26 June 2021; accepted 13 September 2021; published 12 October 2021)

Using Monte Carlo computer simulations, we study the impact of matter fields on the geometry of a typical quantum universe in the causal dynamical triangulations (CDT) model of lattice quantum gravity. The quantum universe has the size of a few Planck lengths and the spatial topology of a three-torus. The matter fields are multicomponent scalar fields taking values in a torus with circumference δ in each spatial direction, which acts as a new parameter in the CDT model. Changing δ, we observe a phase transition caused by the scalar field. This discovery may have important consequences for quantum universes with nontrivial topology, since the phase transition can change the topology to a simply connected one.

DOI: 10.1103/PhysRevLett.127.161301

Introduction.—The problem of merging general relativity and quantum mechanics in a theory of quantum gravity has been approached from many directions (string theory [1], loop quantum gravity [2], and the so-called asymptotic safety program using conventional quantum field theory [3], to mention some of the approaches), but no completely satisfactory formulation has yet been found. Difficulties occur already for the pure gravity case, but an additional complication comes from the fact that any realistic theory of quantum gravity should also include coupling to matter fields. The question arises: what type of matter can be included in a particular approach and what impact does it have on the underlying (quantum) geometric degrees of freedom? In this Letter we argue that the impact of matter can be quite dramatic even leading to a change of the topology of the Universe.

Causal dynamical triangulations.—Our attempt to examine the above-mentioned question is via a nonperturbative lattice approach to quantum gravity with the name causal dynamical triangulations (CDT)—see [4] for its detailed formulation and [5] for a recent review. It is an approach which lies within the asymptotic safety program and is only using ordinary quantum field theory concepts. In CDT, the (formal) path integral of quantum gravity is lattice regularized as a sum over four-dimensional simplicial complexes, called triangulations, which encode geometric degrees of freedom; crucially, they are assumed to be endowed with a causal structure of a globally hyperbolic manifold (i.e., spacetime is foliated into spatial hypersurfaces of fixed and identical topology), which allows a well-defined Wick rotation of the time coordinate. Thus,

$$\mathcal{Z}_{QG} = \int \mathcal{D}_{\mathcal{M}_H}[g] \int \mathcal{D}\phi\, e^{iS_{\rm EH}[g]+iS_M[\phi,g]} \to \\ \to \sum_{T\in\mathcal{T}} \int \mathcal{D}\phi e^{-S_R[T]-S_M^{\rm CDT}[\phi,T]} = \mathcal{Z}_{\rm CDT}, \quad (1)$$

where $\mathcal{M}_H$ is a globally hyperbolic Lorentzian manifold, $\mathcal{D}_{\mathcal{M}_H}[g]$ denotes the integration over geometries, i.e., equivalence classes of metrics $[g]$ on $\mathcal{M}_H$ with respect to diffeomorphisms, and $\mathcal{T}$ is a suitable set of Wick-rotated (now Euclidean) triangulations. The action $S_R[T]$ for a triangulation $T \in \mathcal{T}$ is the Einstein-Hilbert action $S_{\rm EH}$ computed using Regge's method of describing piecewise-linear geometries [6] and containing the bare couplings related to the cosmological and Newton constants. The second term of the action $S_M^{\rm CDT}[\phi, T]$ is the discrete version of the continuous action S_M for matter field(s) ϕ.

Quantum matter fields in CDT.—The simplest quantum matter that can be added to the quantum geometry of CDT is a d-component massless scalar field ϕ. In general, one can assume that the field ϕ has a nontrivial target space, i.e., it is a map $\mathcal{M}_H(g_{\mu\nu}) \to \mathcal{N}(h_{\alpha\beta})$ between an arbitrary manifold $\mathcal{M}_H$ [from the path integral (1)] with a metric $g_{\mu\nu}$ and a target space $\mathcal{N}$ with some fixed metric $h_{\alpha\beta}$ and fixed topology. The continuous (Euclidean) action S_M takes the form

$$S_M[\phi, g] = \frac{1}{2}\int d^4x \sqrt{g(x)}\, g^{\mu\nu}(x)\, h_{\rho\sigma}[\phi^\gamma(x)] \\ \times \partial_\mu\phi^\rho(x)\partial_\nu\phi^\sigma(x). \quad (2)$$

Here, we choose the target space $\mathcal{N}$ of the scalar field to have either Euclidean $\mathbb{R}^d$ or toroidal $(S^1)^d$ topology, and we fix the flat metric $h_{\rho\sigma} = \delta_{\rho\sigma}$ on $\mathcal{N}$. Consequently, the action (2) reads

$$S_M[\phi, g] = \frac{1}{2}\sum_{\sigma=1}^{d} \int d^4x \sqrt{g(x)} \partial^\nu \phi^\sigma(x) \partial_\nu \phi^\sigma(x), \quad (3)$$

and the various components decouple for different σ because the target space metric is diagonal. For a particular sample geometry $[g]$, quantum fluctuations of ϕ^σ will occur around a semiclassical solution $\bar{\phi}^\sigma$ satisfying the Laplace equation

$$\Delta_x \bar{\phi}^\sigma(x) = 0, \qquad \Delta_x = \frac{1}{\sqrt{g(x)}} \partial_\mu \sqrt{g(x)} g^{\mu\nu}(x) \partial_\nu. \quad (4)$$

Let us now start with a simple case where the target space of the scalar field is $\mathcal{N} = \mathbb{R}^d$. In CDT we consider the scalar field as located at the centers of equilateral simplexes, and thus the discrete counterpart of the action (3) takes a very simple form

$$S_M^{\mathrm{CDT}}[\phi, T] = \frac{1}{2}\sum_{\sigma=1}^{d} \sum_{i \leftrightarrow j} (\phi_i^\sigma - \phi_j^\sigma)^2 = \sum_{\sigma,i,j} \phi_i^\sigma \mathbf{L}_{ij}(T) \phi_j^\sigma. \quad (5)$$

The sum $\sum_{i\leftrightarrow j}$ is over the five pairs of neighboring four-simplexes of each simplex i in the triangulation T of the manifold $\mathcal{M}_H(g_{\mu\nu})$ and $\mathbf{L} = 5\mathbb{1} - \mathbf{A}$ is the Laplacian matrix, where $\mathbf{A}_{ij}$ is the adjacency matrix with entries of value 1 if simplexes i and j are neighbors and 0 otherwise. The discrete version of the Laplace equation (4) for each component of the classical scalar field is then

$$\mathbf{L}\bar{\phi}^\sigma = 0, \quad (6)$$

which is solved by $\bar{\phi} = \text{const}$ (the Laplacian zero mode) for any compact simplicial manifold T. After the decomposition of the field

$$\phi^\sigma = \bar{\phi}^\sigma + \xi^\sigma \quad (7)$$

into the classical part $\bar{\phi}^\sigma$ and the quantum part ξ^σ and an application of (6), the contribution from the classical field vanishes, leaving

$$S_M^{\mathrm{CDT}}[\phi, T] = \frac{1}{2}\sum_{\sigma=1}^{d} \sum_{i \leftrightarrow j} (\xi_i^\sigma - \xi_j^\sigma)^2 = \sum_{\sigma,i,j} \xi_i^\sigma \mathbf{L}_{ij}(T) \xi_j^\sigma. \quad (8)$$

The Gaussian form of the matter action (8) means that, in principle, the field can be integrated out, contributing to the geometric action $S_R[T] \to S_R[T] + S_M^{\mathrm{eff}}[T]$ with a term

$$S_M^{\mathrm{eff}}[T] = \frac{d}{2} \log \det[\mathbf{L}'(T)], \quad (9)$$

where $\mathbf{L}'(T)$ is the Laplacian matrix $\mathbf{L}(\mathbf{T})$ in the subspace orthogonal to the constant zero mode of $\mathbf{L}$. The dependence of Eq. (9) on the geometry rests in the dependence of $\mathbf{L}'(T)$ on the adjacency matrix $\mathbf{A}$ defined for a given triangulation T. Using numerical Monte Carlo simulations we checked that the dependence of the determinant $S_M^{\mathrm{eff}}[T]$ on T is weak and, in practice, we can treat it as a constant.

Quantum scalar fields with values on $(S^1)^d$.—The new aspect studied here is based on two major generalizations of the CDT model: (1) We choose the spatial topology of the time foliation leaves to be $(S^1)^3$, and for technical reasons we assume the time boundary conditions to be periodic as well. Thus, each triangulation has the toroidal topology $(S^1)^4$ and can equivalently be represented as an elementary cell periodically repeated in four dimensions. There is a lot of freedom in the selection of the elementary cell; one way to determine it is to choose four independent noncontractible three-dimensional boundaries delimiting it. The boundaries are connected sets of three-dimensional faces, each shared by two four-simplexes located in different copies of the elementary cell. We assume each boundary to be oriented, and we encode the information about the position of the four boundaries (labeled by $\sigma = 1, 2, 3, 4$) in a triangulation T within four matrices $\mathbf{B}^\sigma$, whose elements are

$$\mathbf{B}_{ij}^\sigma = \begin{cases} \pm 1 & \text{if the face shared by simplexes } i \text{ and } j \\ & \text{exists and belongs to the boundary} \\ 0 & \text{otherwise.} \end{cases} \quad (10)$$

The number of directed boundary faces of a simplex i is given by $b_i^\sigma = \sum_j \mathbf{B}_{ij}^\sigma$, and the boundary three-volume is $V^\sigma = \frac{1}{2}\sum_{ij} (\mathbf{B}_{ij}^\sigma)^2$. Despite being fictitious constructs having no impact on the physics, the boundaries can be used to define a coordinate system, as described in [7,8].

(2) The d-component scalar field ϕ is assumed to take values on a symmetric torus $\mathcal{N} = (S^1)^d$ with circumference δ in each direction. We require that each component of the field $\phi^\sigma \in S^1$ winds around the circle once as we go around any noncontractible loop in T that crosses a boundary in direction σ. This requirement completely changes the dynamics of the interaction between geometry and the scalar field. For the scalar field taking values in $\mathbb{R}^d$, the classical solution is constant and does not contribute to the matter action, which depends therefore only on quantum fluctuations. For $\phi^\sigma \in S^1$, however, the constant solution is not allowed, since it has winding number zero; as we will show below, the new nontrivial classical solution does contribute to the effective matter action. The winding condition can technically be obtained by considering a field

$\phi^\sigma \in \mathbb{R}$ that jumps by $\delta \times \mathbf{B}^\sigma_{ij}$ on any face shared by simplexes i and j and identifying

$$\phi^\sigma_i \equiv \phi^\sigma_i + n \times \delta, \qquad n \in \mathbb{Z}. \tag{11}$$

The (discrete) matter action becomes

$$S^{\mathrm{CDT}}_M[\phi, T] = \frac{1}{2}\sum_{\sigma=1}^{d}\sum_{i\leftrightarrow j}(\phi^\sigma_i - \phi^\sigma_j - \delta \times \mathbf{B}^\sigma_{ij})^2 \tag{12}$$

leading to the following equation for the classical field $\bar{\phi}^\sigma$:

$$\mathbf{L}\bar{\phi}^\sigma = \delta \times b^\sigma, \tag{13}$$

which now acquires a boundary term and thus admits nontrivial solutions for $\bar{\phi}^\sigma$. Note that the action (12) is invariant under a local shift of the σ-boundary with a simultaneous change of the scalar field value $\phi^\sigma_i \to \phi^\sigma_i \pm \delta$. Thus the choice of a specific boundary does not influence the path integral (1) in any way. Decomposition (7) of the field into the classical and the quantum part yields

$$S^{\mathrm{CDT}}_M[\phi, T] = \sum_{\sigma,i,j}\xi^\sigma_i \mathbf{L}_{ij}(T)\xi^\sigma_j + S^{\mathrm{CDT}}_M[\bar{\phi}, T]. \tag{14}$$

Since ϕ^σ and $\bar{\phi}^\sigma$ have winding number one, the fluctuation field ξ^σ is a scalar field with winding number zero, i.e., an ordinary scalar field taking values in $\mathbb{R}$. The action (14) is then again Gaussian and can be integrated out, now leading to $S_R[T] \to S_R[T] + S^{\mathrm{eff}}_M[T] + S^{\mathrm{CDT}}_M[\bar{\phi}, T]$, where the determinant $S^{\mathrm{eff}}_M[T]$ is the same as in Eq. (9). Thus the only difference between the impact of the scalar field in $(S^1)^d$ and that of the ordinary field in $\mathbb{R}^d$ is the dependence of the effective matter action on the nontrivial classical solution $\bar{\phi}$; note that the size of the jump δ fixes the scale of the classical field. For $\delta = 0$ one recovers the $\mathbb{R}^d$ case where $S^{\mathrm{CDT}}_M[\bar{\phi}, T]$ is zero (the absolute minimum), as $\bar{\phi} = \mathrm{const}$ for any quantum geometry T. For $\delta > 0$ the constant solution is not allowed, and the action $S^{\mathrm{CDT}}_M[\bar{\phi}, T]$ depends on the specific geometry T. By adjusting the geometry in a rather drastic way, one is still able to reduce the matter action almost to zero. This is illustrated in Fig. 1 in the simple case of a two-dimensional torus with a one-dimensional field ϕ changing in the vertical direction, but the argument is clearly valid in higher dimensions, and in fact it only depends on one direction being periodic. The topology in the "transverse" directions can be anything. On the left plot we have a torus with volume V and vertical length L_V, which is pinched to a cylinder of circumference ε and length L. The total matter action of the field configuration alluded to on the plot is

$$S^{\mathrm{CDT}}_M[\phi, T_L] = \left(\frac{\delta}{L}\right)^2 L\varepsilon = \delta^2\frac{\varepsilon}{L}, \tag{15}$$

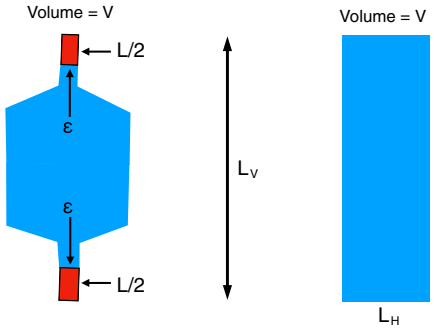

FIG. 1. Left: a torus (opposite sides identified) with a pinch. The region in red is the region where ϕ changes from 0 to δ. In the blue part it stays constant. ϕ is constant in the horizontal direction. Right: a torus where ϕ is constant in the horizontal direction and uniformly increases from 0 to δ from bottom to top.

and the minimal action for a classical field configuration $S^{\mathrm{CDT}}_M[\bar{\phi}, T_L]$ for this geometry is even lower. This can clearly be made arbitrarily small when $\varepsilon \to 0$, and this is even more true in higher dimensions. On the right plot we also have a torus with volume V and vertical length L_V. For this geometry, the action is minimal for a field changing uniformly from 0 to δ, when we move from bottom to top, thus obtaining an action

$$S^{\mathrm{CDT}}_M[\bar{\phi}, T_R] = \left(\frac{\delta}{L_V}\right)^2 L_V L_H = \delta^2\frac{V}{L_V^2}, \quad V = L_H L_V, \tag{16}$$

which is bounded from below when V and L_V are fixed. Let us discuss the consequence of this in the full quantum theory defined by the path integral (1). The classical action $S^{\mathrm{CDT}}_M[\bar{\phi}, T]$ depends in a crucial way on the triangulation T. The triangulations that are pinched as shown in Fig. 1 will have the smallest matter action, but the geometric Einstein-Hilbert part of the action will be larger for such pinched configurations than for "regular" triangulations. A simple minisuperspace model, like the Hartle-Hawking model [9], suggests that for small jumps δ the geometric part of the action dominates and the generic configurations in the path integral are quite similar to the ones which dominate when no matter field with a jump is present. However, for large δ the total action will be the lowest for pinched configurations and the system will instead fluctuate around pinched configurations. Thus, the system might undergo a phase transition as a function of the jump magnitude δ.

Results for scalar fields winding around spatial directions.—Below, using numerical Monte Carlo simulations, we study a CDT model with a $d = 3$ component massless scalar field taking values in a symmetric torus $\mathcal{N} = (S^1)^3$ with circumference δ, i.e., ϕ^σ jumps by $\pm\delta$ when crossing a three-dimensional boundary orthogonal to one of three independent noncontractible loops winding around the toroidal spatial direction $\sigma = x, y, z$ in a

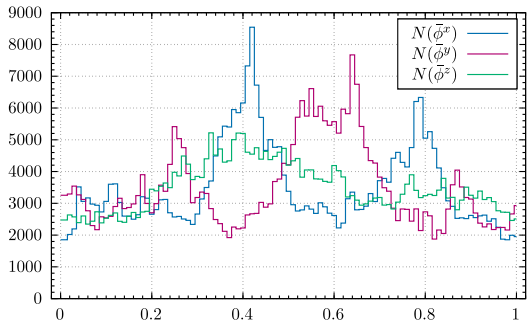

FIG. 2. The projection of four-volume, as defined by (17), on one spatial direction (x, y, or z) for a typical CDT configuration with small jump magnitude ($\delta = 0.1$). The horizontal axis is $\bar{\phi}/\delta$.

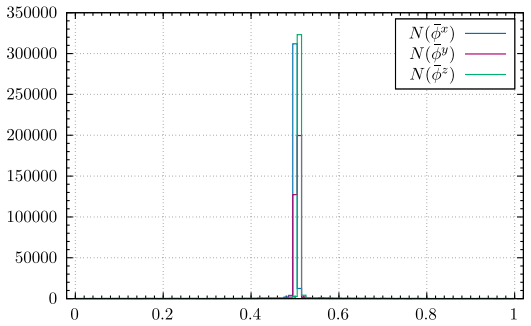

FIG. 4. The projection of four-volume, as defined by (17), on one spatial direction (x, y, or z) for a typical CDT configuration with large jump magnitude ($\delta = 1.0$). The horizontal axis is $\bar{\phi}/\delta$.

triangulation T. This type of matter system was earlier introduced to define a semiclassical coordinate system for a given CDT triangulation [8]. Now we want to make the scalar field a dynamical (quantum) object and let it evolve together with the geometry. Then, for a given geometric configuration T, one can simply compute the expectation value of the field $\langle\phi\rangle = \bar{\phi}$ by solving the Laplace equation (13) and use it as spatial coordinates. The analyzed systems were all in the same point in the CDT parameter space inside the so-called semiclassical (or de Sitter) phase [10–12], and the only variable parameter was the jump magnitude δ. For each analyzed value of δ we pick a generic quantum geometry (a triangulation T) appearing in the path integral (1), and we use the methodology introduced in [8] to assign a unique set of spatial coordinates for each simplex i defined by the classical solution of the scalar field $(\bar{\phi}_i^x, \bar{\phi}_i^y, \bar{\phi}_i^z)$ computed for that geometric configuration. Note that in CDT one has the time coordinate "for free" as the classical solution of the field $\bar{\phi}_i^t$ can be computed using the imposed proper-time foliation. In order to visualize changes in a typical quantum geometry triggered by the increasing jump magnitude, we measure the four-volume density distribution $N(\bar{\phi})$, i.e., the number of simplexes contained in hypercubic blocks with sizes $(\Delta\bar{\phi}_i^x, \Delta\bar{\phi}_i^y, \Delta\bar{\phi}_i^z, \Delta\bar{\phi}_i^t)$, which is equivalent to measuring the integrated $\sqrt{g(\bar{\phi})}$:

$$\Delta N(\bar{\phi}) = \sqrt{g(\bar{\phi})}\prod_\sigma \Delta\bar{\phi}^\sigma = N(\bar{\phi})\prod_\sigma \Delta\bar{\phi}^\sigma. \quad (17)$$

In Figs. 2 and 4 we plot projections of the volume density distribution $N(\bar{\phi})$ in a typical toroidal CDT configuration on one spatial direction (x, y, or z), and in Figs. 3 and 5 the projections on two-dimensional (x-y directions) parameter

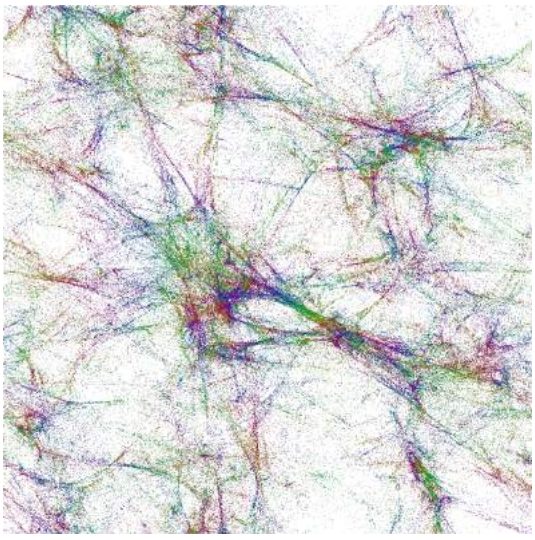

FIG. 3. The projection of four-volume, as defined by (17), on the xy plane for a typical CDT configuration with small jump magnitude ($\delta = 0.1$). Different colors correspond to different times t of the original (lattice) time foliation.

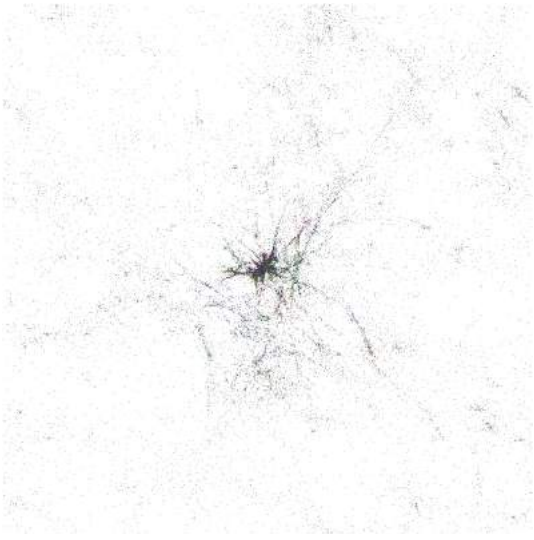

FIG. 5. The projection of four-volume, as defined by (17), on the xy plane for a typical CDT configuration with large jump magnitude ($\delta = 1.0$). Different colors correspond to different times t of the original (lattice) time foliation.

subspace, integrating over the remaining directions. Figures 2 and 3 are for a small ($\delta = 0.1$), while Figs. 4 and 5 for a relatively large ($\delta = 1.0$) jump magnitude, respectively. One clearly observes that the change of the jump magnitude causes a substantial change in a typical CDT geometry. For a small jump ($\delta = 0.1$) one observes a geometry which resembles the pure gravity case, see [8]. For a large jump ($\delta = 1.0$), in line with expectations, one observes that the geometry is "pinched" in all spatial directions (which manifests itself as the small-volume region in Fig. 4 and the low-density region in Fig. 5).

Discussion.—We have shown that if spacetime is globally hyperbolic and has the toroidal spatial topology, i.e., has three nonequivalent noncontractible loops in the spatial directions, then the three-component scalar field with matching topological boundary conditions imposed can have a dramatic effect on the geometries that dominate the CDT path integral. If the spatial topology is simply connected, this effect is absent. This new kind of coupling between the topology of the matter fields and the topology of spacetime is likely to result in a phase transition for sufficiently strong coupling (sufficiently large δ in our model), a transition where the path integral will be dominated by spatial geometries with pinched regions fluctuating close to zero sizes (but still connected due to topological restrictions imposed by our model). This is schematically shown in Fig. 1 and for actual configurations in the path integral in Figs. 4 and 5, using as coordinates in the noncontractible "directions" the classical scalar fields with nontrivial boundary conditions in these directions, and what is also visible using other coordinate systems, e.g., the ones introduced in [7]. Extrapolating this result to a large volume limit we get a picture with a small toroidal part of cutoff size and the dominating geometry with an (almost) spherical topology. Concluding, the effect of scalar fields can be much more drastic than previously appreciated, with possible implications for cosmological model building and even in other areas of physics related to phase transitions of topological nature.

Z. D. acknowledges support from the National Science Centre, Poland, Grant No. 2019/32/T/ST2/00390. J. G.-S. acknowledges support of Grant No. 2016/23/ST2/00289 from the National Science Centre Poland. A. G. acknowledges support by the National Science Centre, Poland, under Grant No. 2015/17/D/ST2/03479. J. J. acknowledges support from the National Science Centre, Poland, Grant No. 2019/33/B/ST2/00589. D. N. acknowledges support from National Science Centre, Poland with Grant No. 2019/32/T/ST2/00389.

*ambjorn@nbi.dk.
†zbigniew.drogosz@doctoral.uj.edu.pl
‡jakub.gizbert-studnicki@uj.edu.pl
§andrzej.goerlich@uj.edu.pl
‖jerzy.jurkiewicz@uj.edu.pl
¶nemeth.daniel.1992@gmail.com

[1] J. Polchinski, *String Theory* (Cambridge University Press, Cambridge, England, 1998), Vols. 1 and 2.
[2] T. Thiemann, *Modern Canonical Quantum General Relativity* (Cambridge University Press, Cambridge, England, 2010).
[3] M. Reuter and F. Saueressig, *Quantum Gravity and the Functional Renormalization Group: The Road Towards Asymptotic Safety* (Cambridge University Press, Cambridge, England, 2019).
[4] J. Ambjørn, A. Görlich, J. Jurkiewicz, and R. Loll, Phys. Rep. **519**, 127 (2012).
[5] R. Loll, Classical Quantum Gravity **37**, 013002 (2020).
[6] T. Regge, Nuovo Cimento **19**, 558 (1961).
[7] J. Ambjørn, Z. Drogosz, J. Gizbert-Studnicki, A. Görlich, and J. Jurkiewicz, Nucl. Phys. **943**, 114626 (2019); J. Ambjørn, Z. Drogosz, A. Görlich, and J. Jurkiewicz, Phys. Rev. D **103**, 086022 (2021).
[8] J. Ambjørn, Z. Drogosz, J. Gizbert-Studnicki, A. Görlich, J. Jurkiewicz, and D. Németh, Eur. Phys. J. C **81**, 708 (2021).
[9] J. B. Hartle and S. W. Hawking, Phys. Rev. D **28**, 2960 (1983).
[10] J. Ambjø rn, J. Jurkiewicz, and R. Loll, Phys. Rev. Lett. **93**, 131301 (2004); Phys. Lett. B **607**, 205 (2005); J. Ambjørn, A. Görlich, J. Jurkiewicz, R. Loll, J. Gizbert-Studnicki, and T. Trzesniewski, Nucl. Phys. **B849**, 144 (2011).
[11] J. Ambjørn, J. Jurkiewicz, and R. Loll, Phys. Rev. D **72**, 064014 (2005); J. Ambjørn, A. Görlich, J. Jurkiewicz, and R. Loll, Phys. Rev. D **78**, 063544 (2008); Phys. Rev. Lett. **100**, 091304 (2008).
[12] J. Ambjørn, Z. Drogosz, J. Gizbert-Studnicki, A. Görlich, J. Jurkiewicz, and D. Németh, Phys. Rev. D **94**, 044010 (2016); J. Ambjørn, J. Gizbert-Studnicki, A. Görlich, K. Grosvenor, and J. Jurkiewicz, Nucl. Phys. **B922**, 226 (2017).

Scalar fields in causal dynamical triangulations

OPEN ACCESS
IOP Publishing
Classical and Quantum Gravity
Class. Quantum Grav. **38** (2021) 195030 (59pp) https://doi.org/10.1088/1361-6382/ac2135

Scalar fields in causal dynamical triangulations

Jan Ambjorn[1,2], Zbigniew Drogosz[3], Jakub Gizbert-Studnicki[3], Andrzej Görlich[3,*], Jerzy Jurkiewicz[3] and Dániel Németh[3]

[1] The Niels Bohr Institute, Copenhagen University, Blegdamsvej 17, DK-2100 Copenhagen Ø, Denmark
[2] IMAPP, Radboud University, Nijmegen, PO Box 9010, The Netherlands
[3] Institute of Theoretical Physics, Jagiellonian University, Łojasiewicza 11, Kraków, PL 30-348, Poland

E-mail: ambjorn@nbi.dk, zbigniew.drogosz@doctoral.uj.edu.pl, jakub.gizbert-studnicki@uj.edu.pl, andrzej.goerlich@uj.edu.pl, jerzy.jurkiewicz@uj.edu.pl and nemeth.daniel.1992@gmail.com

Received 4 June 2021, revised 29 July 2021
Accepted for publication 25 August 2021
Published 16 September 2021

Abstract

A typical geometry extracted from the path integral of a quantum theory of gravity may be quite complicated in the UV region. Even if a single configuration is not physical, its properties may be of interest to understand the details of its nature, since some universal features can be important for the physics of the model. If the formalism describing the geometry is coordinate independent, which is the case in the model studied here, such understanding may be facilitated by the use of suitable coordinate systems. In this article we use scalar fields that solve Laplace's equation to introduce coordinates on geometries with a toroidal topology. Using these coordinates we observe what we identify as the cosmic voids and filaments structure, even if matter is only a tool to visualize the geometry. We also show that if the scalar fields we used as coordinates are dynamically coupled to geometry, they can change it in a dramatic way, leading to a modification of the spatial topology.

Keywords: quantum gravity, lattice field theory, dynamical triangulations

(Some figures may appear in colour only in the online journal)

*Author to whom any correspondence should be addressed.

1. Introduction

Lattice approaches based on the path integral formalism constitute an important tool with which one can investigate non-perturbative aspects of many quantum field theories. The general idea is the following: given a continuum field theory with a classical action, one defines a quantum theory via the (lattice regularized) path integral, where the length of lattice links provides an ultraviolet (UV) cut-off. A continuum quantum field theory might then be defined if there exists a so-called UV fixed point such that it is possible to keep the physical observables fixed while taking the lattice spacing to zero. There is a number of practical issues and open questions which need to be addressed, especially when trying to apply this approach to the quantization of Einstein's general relativity (GR):

(a) GR is perturbatively non-renormalizable. Moreover, it is not clear if GR exists as a quantum field theory with a well-defined non-perturbative UV limit.

(b) The quantum theory of GR should be diffeomorphism invariant. It is not clear how to obtain this, starting from a lattice theory where the concept of diffeomorphisms, if defined at all, might be different from that defined in the continuum. In addition it is not clear how then to relate lattice measurements to other, more analytical approaches.

(c) Studies of a lattice theory usually require the use of numerical Monte-Carlo (MC) methods, which is technically possible only in spacetimes with Euclidean signature. Although it is known how to relate correlation functions calculated in *flat* spacetimes with Euclidean and Lorentzian signatures (the so-called Osterwalder–Schrader axioms), nothing like that is known when GR is involved[4].

(d) A realistic quantum theory of gravity should also include coupling to quantum matter fields—what types of fields can and should be included in this approach? Furthermore, what impact do the matter fields have on the underlying geometric degrees of freedom?

Let us briefly try to answer these questions in the lattice model of quantum gravity defined by causal dynamical triangulations (CDT).

(a) It is well known that Einstein's gravity as a perturbative field theory is non-renormalizable [2]. However, as suggested by Weinberg's asymptotic safety conjecture [3], it may be renormalizable in a non-perturbative way. A necessity for such a scenario is that the renormalization group flow of the gravitational coupling constants can lead to a nontrivial ultraviolet fixed point (UVFP). Some evidence of such an UVFP is provided by calculations in $2 + \epsilon$ dimensions [4] and from the use of the so-called exact renormalization group [5, 6], but none of the methods have yet provided us with a generally accepted proof that such a fixed point exists. Thus, one of the aims of studying a lattice theory of quantum gravity is to test the asymptotic safety conjecture.
In the lattice formulation, the UVFP should be associated with a second- or higher-order phase transition point. In addition, it should be possible to define the renormalization group flow lines in the lattice coupling constant space leading from an infrared limit to the UVFP. This in general requires finding a region in the lattice coupling constant space where the semiclassical limit (consistent with the classical GR) can be defined, together with some physical observables. These physical observables should be such that keeping their values fixed defines a path in the lattice coupling constant space that allows the interpretation of a

[4] The Osterwalder–Schrader axioms in the context of GR were discussed e.g. in [1].

decreasing lattice spacing when moving away from the semiclassical region. If the lattice spacing goes to zero at the endpoint of the path, this endpoint will be an UVFP.

The CDT approach (described in more detail in section 2) has at least some of the required features of a successful lattice field theory in the sense described above, i.e. it has a semiclassical region in the lattice coupling constant space [7–9], while some of the boundaries of the semiclassical phase are higher order phase transition lines/points [10, 11]. One can define and measure the renormalization group flow lines [12] in the lattice coupling constant space, however it has not yet been possible to define a suitable continuum limit; it is not ruled out that it will be possible in the future, using better observables (see [13] for a more detailed discussion of this issue).

Although the existence of the UVFP in a lattice theory of quantum gravity is still a conjecture, it can nevertheless be argued that even if the continuum limit were not to exist, the lattice theory would still be useful in investigating non-perturbative aspects of quantum gravity, treated as an effective theory valid up to some finite energy scale. A simple example of such a situation goes all the way back to the first proof of confinement in a gauge theory, where Polyakov showed that three-dimensional compact $U(1)$ lattice theory contained all the non-perturbative physics responsible for the confinement in the Georgi–Glashow model, despite having itself no such non-perturbative continuum limit [14].

(b) The physics of GR is invariant under diffeomorphisms. In his seminal work [15], Regge provided a prescription for how to assign local curvature to piecewise linear (simplicial) geometries without the use of coordinates. That formulation is manifestly coordinate free and thus diffeomorphism invariant. In that approach, the geometry of a piecewise linear (simplicial) manifold and the resulting Regge action S_{R} (the Einstein–Hilbert action S_{EH} for the triangulated manifold) are entirely determined by geometric quantities such as the length of edges (links) and the adjacency relations of the d-dimensional simplices glued together to form the manifold. Regge's idea was to describe simplicial discretizations of classical continuously differentiable manifolds with arbitrary precision in a coordinate-independent way. However, the classical theory of Regge is not easily transferred to the path integral of the corresponding quantum theory [16]. A more suitable lattice path integral over *Euclidean* geometries is known as Euclidean dynamical triangulations (EDT)[5]. In this approach, the simplicial manifolds used in the path integral are obtained by gluing together identical four-simplices whose links have length a, the UV cut-off in the lattice theory. The geometry of such a manifold is the piecewise linear geometry defined by Regge, and the action associated with such a configuration is the Regge action associated with the piecewise linear geometry. An important feature of the EDT formalism is that each triangulation in the EDT ensemble corresponds to a different geometry, and the basic assumption is that as the link distance $a \to 0$, the EDT ensemble of geometries becomes dense in some suitable way in the set of continuous geometries that appears in the continuum path integral. This seems to be true in two-dimensional quantum gravity where both the continuum theory and the lattice theory can be solved analytically and they agree (see [20] for a review). In higher-dimensional quantum gravity, we do not know if this is true since the continuum path integral has not been rigorously defined and the EDT theory of gravity can only be studied via numerical simulations.

[5] The use of EDT goes back to attempts to provide a regularization of the bosonic string theory [17], which can be viewed as 2D gravity coupled to Gaussian fields. It was first used in the context of higher dimensional gravity in [18, 19].

If the asymptotic safety scenario discussed above is valid, one should in principle be able to shrink the lattice spacing (the size of the elementary simplicial building blocks) to zero, and thus to get rid of the discretization and recover the continuum limit of the putative quantum theory of gravity. In this limit one could in principle compute expectation values of correlators of some physical observables, although they are not so easily defined in a theory of quantum gravity without matter fields. One 'problem' is that the EDT formalism is 'coordinate free'. While this seems a major achievement from a GR point of view, it comes with its own issues. One of these is that it makes it difficult to relate the results obtained in the lattice theory to more analytical approaches where coordinate systems are used (even if physics of course should be independent of a specific coordinate system). The issue of reintroducing suitable coordinate systems in the lattice theory of gravity has been extensively studied recently by our group [21, 22], and in this article we will discuss a new promising way of doing it by using scalar fields—see section 3.

(c) The formulation of the EDT lattice field theory of (Euclidean) quantum GR is simple. The path integration over continuous Euclidean geometries is replaced by the summation over the EDT piecewise linear geometries. If we consider GR in d dimensions, each such piecewise linear geometry is described by an abstract triangulation, and we thus obtain a summation over abstract d-dimensional triangulations, each with the Boltzmann weight given by the Regge action of the corresponding piecewise linear geometry. Thus we write

$$\mathcal{Z}_{\rm QG} = \int \mathcal{D}_{\mathcal{M}}[g_{\rm L}]\, {\rm e}^{{\rm i}S_{\rm EH}[g_{\rm L}]} \to \int \mathcal{D}_{\mathcal{M}}[g_{\rm E}]\, {\rm e}^{-S_{\rm EH}[g_{\rm E}]} \to \mathcal{Z}_{\rm EDT} = \sum_{\mathcal{T}} {\rm e}^{-S_{\rm R}[\mathcal{T}]}, \quad (1)$$

where the first path integral is over geometries with Lorentzian signature and the second path integral is over geometries with Euclidean signature. $S_{\rm EH}[g]$ denotes the Einstein–Hilbert action, and $S_{\rm R}[\mathcal{T}]$ is the Regge action of the triangulation $\mathcal{T}$.

While it is easy to define $\mathcal{Z}_{\rm EDT}$, it can be calculated analytically only in two dimensions. As mentioned above, the very encouraging outcome is that the continuum limit can be taken, and the resulting theory agrees with the continuum two-dimensional Euclidean quantum gravity theory (the so-called quantum Liouville theory), which can also be solved analytically. In higher dimensions the best one can do is to study the theory using Monte Carlo simulations. The model has been studied extensively in three and four dimensions [18, 19], together with generalizations where matter fields were added to the action [24]. However, no suitable UVFP was found [25].[6]

This failure led to a reformulation of the model, with the Lorentzian starting point of GR taken more seriously [27]. In this approach, denoted CDT, the starting assumption is that the continuum path integral should include only Lorentzian geometries that are globally hyperbolic. To regularize the path integral, a discretization based on building blocks (d-dimensional simplices), similar in spirit to EDT, is introduced. Now each d-dimensional simplex has space- and timelike links. Moreover, it is possible to perform a Wick rotation of each simplex to an 'Euclidean' simplex, and the triangulation built from Lorentzian simplices is then analytically Wick-rotated to an Euclidean triangulation, with the Regge action of the triangulation changed accordingly. The change from Lorentzian geometries

[6] Recently attempts have been made to find higher order transitions in generalized EDT models [26], but so far with no clear success.

alluded to in (1) thus becomes a real analytical continuation, and we can write

$$\mathcal{Z}_{\rm QG} = \int \mathcal{D}_{\mathcal{M}_{\rm H}}[g_{\rm L}]\, {\rm e}^{{\rm i}S_{\rm EH}[g_{\rm L}]} \to \mathcal{Z}_{\rm CDT} = \sum_{\mathcal{T}_{\rm L}} {\rm e}^{{\rm i}S_{\rm R}[\mathcal{T}_{\rm L}]} \to \sum_{\mathcal{T}_{\rm E}} {\rm e}^{-S_{\rm R}[\mathcal{T}_{\rm E}]}, \qquad (2)$$

where $\mathcal{M}_{\rm H}$ denotes globally hyperbolic geometries, $\mathcal{T}_{\rm L}$ a corresponding Lorentzian triangulation, and $\mathcal{T}_{\rm E}$ the Wick-rotated Euclidean triangulation. When we talk about $\mathcal{Z}_{\rm CDT}$ below, we will always have in mind the summation over Euclidean triangulations in (2), but contrary to the situation in EDT shown in (1) there is now a clear relation between the Lorentzian and the Euclidean theory. However, it comes at the price of introducing a preferred foliation of the triangulated manifolds, which may be incompatible with general 4D spacetime diffeomorphism invariance[7]. The question remains whether introducing such a foliation can be treated as a specific gauge choice in a quantum version of GR or if it would rather make CDT fall into some other universality class of quantum gravity theories, e.g. Hořava–Lifshitz gravity [28].

Hořava–Lifshitz-gravity is indeed a natural candidate for a continuum limit of CDT, since also in this theory there is a time foliation. One can show analytically that two-dimensional CDT corresponds to a quantum version of two-dimensional Hořava–Lifshitz gravity [29], but for higher-dimensional gravity the situation is much less clear since the Hořava–Lifshitz gravity in higher dimensions contains important action terms that are not GR-terms and are not included in the CDT action. In three dimensions there is some evidence that the physics of the CDT model does not depend in a crucial way on the existence of a time foliation [30]. In four dimensions it has not yet been possible to address this question. However, one step in this direction is at least to be able to talk about different time-foliations of the same CDT four-geometry, and to check if and how the results depend on the choice of foliation. In section 4 we make a first step toward this goal by showing how to use scalar fields to define alternative spacetime foliations for the CDT triangulations.

(d) Last but not least, a realistic theory of quantum gravity should not only describe the pure gravity sector but also investigate the impact of quantum matter coupled to geometric degrees of freedom. There are no technical problems associated with the introduction of bosonic matter coupled to the geometry in CDT. That was done already in EDT, as mentioned above [24], and the same discretized prescriptions as used there can be applied in CDT. While matter did not have a great impact in EDT, the situation is potentially much more interesting in CDT, where there *are* second order phase transitions and thus probably some kind of continuum physics of geometry, which could be influenced in important ways by matter and vice versa. So far, interesting results were obtained for simple 2D CDT models coupled to scalar [31] and gauge [32] fields, where matter fields seemingly have a significant impact on the geometry. As regards the more interesting but also more complicated four-dimensional CDT model, we have recently analyzed systems with (multiple copies of) massless scalar fields coupled to the geometry [11], and we have also studied point particles (mass lines)[8]. Disappointingly, our previous results did not show any substantial impact of the scalar field(s) on spacetime geometry nor the position of phase transition lines in the CDT coupling constant space. In the present study, we investigate the impact of introducing nontrivial boundary conditions for the scalar field(s), such that

[7] In this case full 3D (spatial) diffeomorphism invariance remains, but the time direction is distinguished and treated on a special footing.

[8] Results of the mass line studies will be published in a separate article.

the field jumps on the boundary of a periodic elementary cell, which in our setup can be defined. Our formulation is topological, i.e. the matter action does not depend on the specific (unphysical) position of the boundary but just on the value of the jump. Such systems seem to undergo a new type of phase transition where spacetime geometry dramatically changes for large values of the jump vs the (almost pure gravity) geometry observed for small values of the jump; see section 5 for details.

The remaining part of the article is organized as follows: in section 2 we outline the CDT approach to quantum gravity; in section 3 we discuss how classical scalar fields can be used to define coordinates in fixed simplicial geometries, and how they in turn help better to understand the geometric structures observed in CDT triangulations; in section 4 we describe how the classical scalar fields can serve as a tool to define alternative proper-time foliations of the CDT manifolds; finally in section 5 we analyze the impact of dynamical scalar fields with non-trivial boundary conditions.

2. Causal dynamical triangulations

As already mentioned in the introduction, CDT is a background-independent and diffeomorphism-invariant lattice field theory aiming at providing a non-perturbative definition of quantum gravity. Below we provide for completeness a short description of the actual lattice construction of the geometries. For a complete account, we refer the reader to the review [33] (and to [34, 35] for an update on the recent results). CDT provides a definition of the (formal) continuum gravitational path integral appearing in (2) as a sum over an ensemble of triangulations $\mathcal{T}$ constructed from several types of elementary simplicial building blocks. The edge lengths of the simplices are assumed to be fixed[9] and act as the UV cut-off of the lattice theory. The geometries appearing in the formal path integral (2) are by assumption globally hyperbolic, and the piecewise linear geometries represented by the triangulations are constructed to reflect it: they have spatial hypersurfaces of constant 'lattice time' t, and the construction is such that it is actually possible to perform an analytic continuation in the lattice time t to piecewise linear geometries with Euclidean signature, as alluded to in (2) (see [33] for a detailed discussion of the analytic continuation).

In the four-dimensional case, which is the one we are the most interested in, a spatial 3D geometric state with a given fixed topology in a slice with integer (lattice) time coordinate t is constructed by gluing together equilateral tetrahedra (with fixed length of all edges/lattice links: a_s). Similarly, an independent 3D geometry with the same topology is constructed in the spatial slice at time $t+1$. These two 3D geometries are now connected by 4D simplices filling out the four-dimensional 'slab' between the two hypersurfaces. This is done by introducing two types of 4D simplices—the (4, 1) and the (3, 2) simplices[10]—whose timelike edges (links) have a fixed length a_t. In the Lorentzian setting, $a_t^2 = -\alpha a_s^2$, with the asymmetry parameter $\alpha > 0$. The rotation to an Euclidean four-simplex is performed by rotating α to the negative real axis in the lower complex plane (for restrictions on the value of α on the negative real axis see [33]). Since the four-dimensional simplices are glued together in such a way that no topological defects are introduced in the slab between the three-dimensional triangulations at t and

[9] In computer simulations we set the length of (spatial) links to be one (in abstract lattice units), and then by performing measurements of certain observables and relating them to a continuous theory we measure the effective lattice spacing in physical units, say Planck lengths $\ell_{\rm Pl}$. For a given set of parameters (CDT bare couplings), the lattice spacing is constant and fixed, but it does change from one point to another in the parameter space (see e.g. [36] for more details).

[10] The (i, j) simplex has i vertices in a spatial slice with integer (lattice) time coordinate t and j vertices in the neighboring spatial slice with $t \pm 1$.

$t+1$, it is possible to assign non-integer time and piecewise linear 3D geometries to spatial hypersurfaces between t and $t+1$. This construction is analogously extended to hypersurfaces $t+2$, $t+3$, etc and the corresponding slabs in between. In the path integral $\mathcal{Z}_{\rm CDT}$ in (2), the summation is performed over all 3D geometries (of the given topology) at $t = 1, 2, \ldots$ and all 4D slab geometries connecting them as described. All four-simplices (and their subsimplices) are assumed to be flat (their interior being a fragment of either Minkowski or Euclidean spacetime, depending on whether or not we have performed the analytic continuation).

In the Regge prescription, the nontrivial spacetime curvature of the four-dimensional triangulation is localized on the two-dimensional subsimplices, i.e. triangles, and depends on the number of four-simplices sharing a given triangle. Using the Regge prescription [15], one can derive the Einstein–Hilbert action for such simplicial geometries, the Regge action $S_{\rm R}$ mentioned above, which for CDT takes a very simple form after the rotation to Euclidean signature has been made (see e.g. [33]):

$$S_{\rm R}[\mathcal{T}] = -\left(\kappa_0 + 6\Delta\right) N_0 + \kappa_4 \left(N_{4,1} + N_{3,2}\right) + \Delta N_{4,1}, \tag{3}$$

where $N_{i,j}$ denotes the number of four-simplices of the type (i, j) (see above), and N_0 is the number of vertices in the triangulation $\mathcal{T}$. κ_0, Δ and κ_4 are bare dimensionless coupling constants, related to Newton's constant, the cosmological constant, and the asymmetry parameter α (see above). In principle, one could choose some fixed initial (at $t = 1$) and final (at $t = T$) 3D geometric states, but for the purpose of this article it is convenient instead to impose time-periodic boundary conditions such that a 3D spatial geometry at time t is identified with the geometry at time $t + T$.

At present, the only tool we have available to investigate four-dimensional CDT is Monte Carlo simulations. This is a method to generate configurations with a probability distribution in accordance with the Boltzmann distribution dictated by the action of the system. However, to function, it requires a real probability distribution. This is why we have to rotate to geometries with Euclidean signatures in (2), as described. More precisely, our rotation of a configuration $\mathcal{T}_{\rm L} \to \mathcal{T}_{\rm E}$ is such that $iS_{\rm R}[\mathcal{T}_{\rm L}] \to -S_{\rm R}[\mathcal{T}_{\rm E}]$, which implies that the Boltzmann weight $e^{iS_{\rm R}[\mathcal{T}_{\rm L}]} \to e^{-S_{\rm R}[\mathcal{T}_{\rm E}]}$. With this analytic continuation to an ensemble of geometries $\{\mathcal{T}_{\rm E}\}$, we can now view $\mathcal{Z}_{\rm CDT}$ in (2) as a statistical theory of random geometries with Euclidean signature. A special feature of the gravity system is that the volume of spacetime is not fixed but instead is a dynamical variable. In our simulations, this implies that the number of four-simplices is not fixed. For a positive cosmological constant Λ, the corresponding term in Euclidean Einstein–Hilbert action, $\Lambda \int d^4x\sqrt{g(x)}$, will try to force the spacetime volume to be as small as possible. The same term is present in the discretized Regge action (3), and it will appear with a Boltzmann weight $e^{-\kappa_4 N_4(\mathcal{T})}$, where $N_4(\mathcal{T}) = N_{4,1} + N_{3,2}$ is the number of four-simplices in the triangulation $\mathcal{T}$. This seems to hint that for a positive dimensionless coupling constant κ_4 there should be very few four-simplices. However, there are many triangulations with a given number N_4 of four-simplices. In fact, up to the leading order, the number grows exponentially [37], approximately like $e^{\kappa_4^c N_4}$. In the MC simulations, we are interested in as large N_4's as possible, and this is achieved by fine-tuning κ_4 to κ_4^c from above. From a practical point of view, it is convenient to keep N_4 or $N_{4,1}$ fixed when measuring observables and then to perform the measurements for different values. In addition, this allows us to use powerful techniques of finite-size scaling, borrowed from the study of critical phenomena in statistical physics, to evaluate the behavior of systems of infinite size from those of finite size. It is such techniques that we use to determine the phase diagram and the corresponding phase transitions (for details we refer to the review [33]).

Below we briefly summarize the most important CDT results; for more details we direct the reader to the review articles [33–35]. Despite the relative simplicity of its formulation and

a small number of parameters (three coupling constants), CDT has a surprisingly rich phase structure, which seems to be independent of the spatial topology choice [38].[11] Four phases of quantum geometry with distinct physical features have been observed for various combinations of the bare coupling parameters (κ_0, Δ); see the phase diagram in figure 1.[12] At this point it is worth reminding the reader that no background geometry is introduced by hand. So even if the building blocks are four-dimensional simplices, *a priori* it is in no way clear what kind of geometries will be observed. The experience from the old four-dimensional EDT simulations was that it was close to impossible to obtain something that even vaguely resembled four-dimensional universes. From that point of view it is non-trivial and very encouraging that in one of the phases, the so-called C-phase (also called the semiclassical or de Sitter phase) we observe what looks like a four-dimensional Universe where the scale factor admits a semi-classical description [7–9]. This is different in other phases, called A, B and C_b, which most likely do not have a good semiclassical interpretation[13]. The four phases are separated by first-($A-B$, $A-C$ and $B-C$)[14] and higher-order ($B-C_b$ and $C-C_b$)[15] phase transition lines [10, 39], meeting in two *triple points*, which are natural candidates for the UV fixed point of quantum gravity, if it exists. A key issue in CDT is how to define good observables, whose expectation values or correlation functions can be measured in the Monte Carlo simulations. One example is the spatial volume distribution in (lattice) proper time. Using this observable, we were able to measure the effective action for the scale factor of CDT, which in phase C is consistent with the (discretized) minisuperspace action of GR [7–9].

Some progress toward defining new coordinate-free observables in CDT has recently been made [40], but in general it would be beneficial to have a notion of coordinates not only in time but also in spatial directions. They would, for example, be instrumental in measuring a more general effective action of CDT, taking into account not only the scale factor but also the spatial degrees of freedom. They would also help better to understand properties of the C_b phase, where spatial homogeneity is strongly broken by very nontrivial geometric structures appearing in generic triangulations. Therefore, we have recently started a research program aimed at restoring spatial coordinates in CDT, whose formulation is *ab initio* (space-)coordinate free. The choice of a toroidal spatial topology seems convenient for this purpose. In the toroidal CDT, conversely to the spherical case, one can define three (or four, including the time direction) families of 3D surfaces, called boundaries, which are orthogonal to each other and non-contractible in spatial directions; see figure 2 for a lower-dimensional visualization[16]. These boundaries are nonphysical, and their position does not affect the underlying geometries (triangulations) in any way. One of the possibilities is then to use the boundaries as reference

[11] So far we have investigated only two cases, namely the spherical S^3 and the toroidal T^3 topologies.

[12] In the Monte Carlo simulations of CDT, the parameter κ_4, which is proportional to the cosmological constant, is tuned so that the infinite-volume limit can be taken (as described above), which effectively leaves a two-dimensional coupling constant space.

[13] Phases A and B may be realizations of some exotic geometries not observed in the real Universe, and phase C_b, also called the bifurcation phase, may be a realization of a quantum spacetime with a singularity, however it has not been proven rigorously.

[14] The $B-C$ transition was examined only in CDT with toroidal spatial topology as in the spherical topology it could not be analyzed because of technical issues. It has some properties that may indicate a higher order phase transition and some suggesting a first order transition. This issue has not been completely resolved. The $A-B$ transition is currently examined in CDT with toroidal spatial topology, and it is most likely a first-order transition.

[15] The order of $C-C_b$ transition was measured only in CDT with spherical spatial topology; in the toroidal case we observe a strong hysteresis in the transition region which may suggest that the order of the transition has changed because of the topology change, but it can be an algorithmic issue as well.

[16] In our approach we also require the volume of each such boundary to be (locally) minimal, which seems to lead to three universal boundaries, one in each spatial direction; see [21] for details.

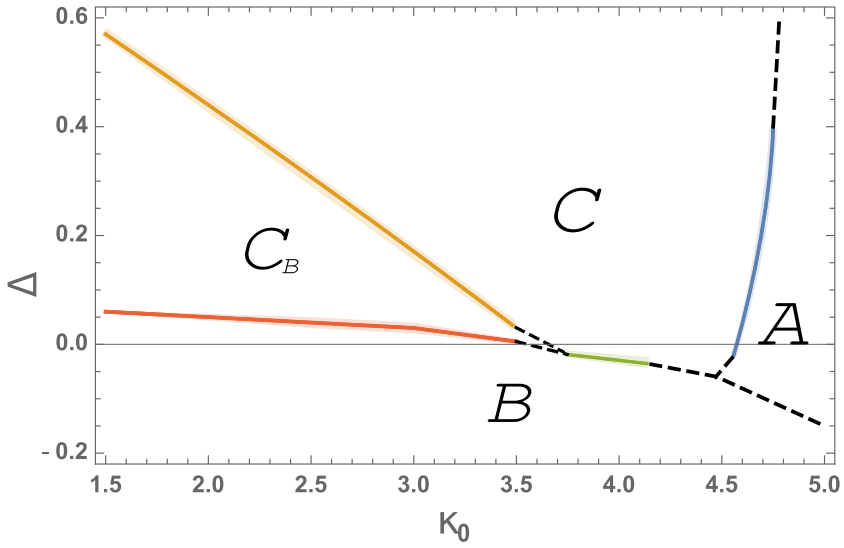

Figure 1. The phase structure of four-dimensional CDT in the (κ_0, Δ) parameter space. Blue color denotes first-order and red color higher-order phase transition lines. See footnotes 13 and 14 for additional remarks.

frames and to define coordinates by geodesic distances from them [21]. Such a proposal has some drawbacks as the coordinates are in general dependent on the position of nonphysical boundaries, but it led nevertheless to a better understanding of generic CDT geometries, which in phase C can be described as a semiclassical torus with a number of quantum fractal outgrowths; see figure 3. Another way of analyzing such geometric structures was proposed in [22], where the boundaries were used to define the shortest loops (starting at any four-simplex) with nontrivial winding numbers in all three spatial directions and in the time direction. The length of such loops measured in a given geometry (triangulation) is 'topological' as it does not depend on the position of the boundaries. These concepts led us to the proposal introduced in [41], and discussed in detail in section 3 below, of using scalar fields as spatial coordinates.

3. Classical scalar fields as coordinates in CDT

3.1. Classical scalar fields

The idea of introducing matter fields as coordinates (dynamical reference 'clock-and-rods' fields) and using them to define relational observables (as functions of the reference fields) is already present in many approaches to gravity [42]. Now we want to use a similar concept in CDT. Our CDT configurations come from the path integral. Usually, in the continuum, in order to perform the path integral, we would choose a coordinate system, for instance x^μ, on the manifold defining the whole setup, and we would talk about the equivalence classes of metrics $[g_{\mu\nu}(x)]$ defining the geometry, which would promote the manifold to a Riemannian manifold. In the EDT and the CDT formalism (except for the time-coordinate in CDT), the situation is in a way purified from the GR point of view. No coordinate system is given, only the relations between vertices (belonging to the same link or not, belonging to the same triangle or not, etc), and from those data one can reconstruct a coordinate system and, in addition, the geometry. While beautiful from the GR point of view, the lack of a coordinate system has sometimes

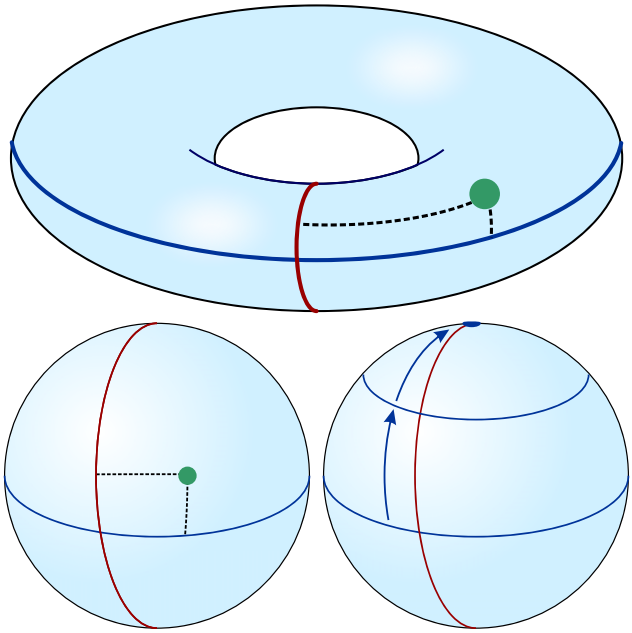

Figure 2. In the 2D toroidal case two orthogonal non-contractible loops can be constructed and used to define coordinates (top chart). This is not possible in a spherical case, where all loops are contractible to a point (bottom chart).

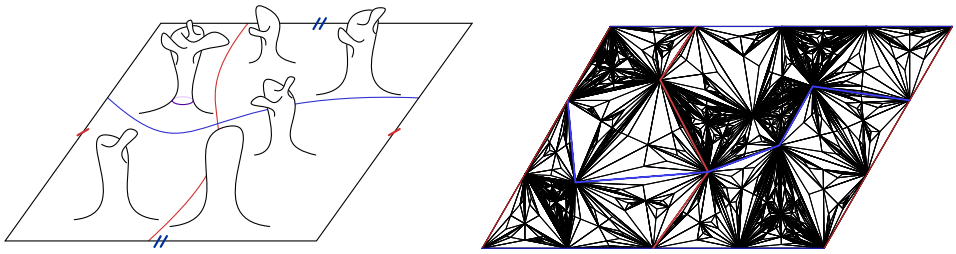

Figure 3. Left: a 2D visualization of a fractal structure of a quantum manifold with sizable outgrowths originating from the toroidal center (the boundaries of the rectangular cell are pairwise identified, making it a topological torus). Right: a visualization of 2D toroidal triangulation with outgrowths. In CDT all triangles are assumed to be identical, but a triangulation can be transformed by a conformal map to the regular square lattice with non-identical triangles. The quantum outgrowths are represented by denser regions. For similar pictures coming from 'real' computer simulations of 2D quantum gravity see [23].

been quite cumbersome and not very enlightening from the point of view of understanding the basic characteristics of the geometries encountered in the path integral. To explore the geometric characteristics of a 'typical' quantum CDT configuration, i.e. a configuration coming from the path integral, it would be beneficial to have a coordinate system which is *natural* for the given geometry. This is what we want to achieve below for typical CDT configurations. The coordinate systems will thus be different for different configurations, contrary to the situation

described above, where x^μ was given from the beginning. To discuss the general principles going into the construction of a coordinate system using scalar fields on a given CDT configuration, let us for a moment use a continuum notation. The topology of the CDT configurations we extract from our MC simulations will be that of $T^4 = S^1 \times S^1 \times S^1 \times S^1$. In principle, we know the geometry of each configuration since we view it as a piecewise linear manifold $\mathcal{M}$, and from the knowledge of the connectivity of the graph representing the configuration we can reconstruct all distances between points on $\mathcal{M}$. Let us consider $\mathcal{M}$ as a Riemannian manifold with the geometry given by some metric $g_{\mu\nu}$ and T^4 as a Riemannian manifold $\mathcal{N}$ with the trivial, flat metric $h_{\alpha\beta}$. We want to use as our coordinates a 'good' nontrivial harmonic map $\mathcal{M} \to \mathcal{N}$. To define one, we can use four scalar fields ϕ^α, $\alpha = 1, 2, 3, 4$, $\phi^\alpha(x)$ being a map $\mathcal{M} \to S^1$ minimizing the action

$$S_{\mathrm{M}}[\phi] = \frac{1}{2} \int \mathrm{d}^4x \sqrt{g(x)}\, g^{\mu\nu}(x)\, h_{\alpha\beta}(\phi^\gamma(x))\, \partial_\mu \phi^\alpha(x) \partial_\nu \phi^\beta(x). \tag{4}$$

The choice of the trivial metric $h_{\alpha\beta}$ on $\mathcal{N}$ reduces equation (4) to four decoupled equations for the scalar fields ϕ^α, so for the moment let us concentrate on the scalar field $\phi(x)$ that minimizes (4) and is thus a harmonic map $\mathcal{M} \to S^1$. The minimization of (4) yields the Laplace equation

$$\Delta_x \phi(x) = 0, \quad \Delta_x = \frac{1}{\sqrt{g(x)}} \frac{\partial}{\partial x^\mu} \left(\sqrt{g(x)}\, g^{\mu\nu}(x) \right) \frac{\partial}{\partial x^\nu}, \quad \phi(x) \in S^1. \tag{5}$$

If $\phi(x)$ were a scalar field taking values in $\mathbb{R}$, then the constant mode would be the only solution to $\Delta_x \phi(x) = 0$ on a compact manifold $\mathcal{M}$. Thus, here it is important that $\phi(x) \in S^1$. Let the circumference of S^1 be δ. One way to force $\phi(x) \in S^1$ is to let $\phi(x)$ take values in $\mathbb{R}$ but to identify $\phi(x)$ and $\phi(x) + n \cdot \delta$. We thus write

$$\phi(x) \equiv \phi(x) + n\,\delta, \quad n \in \mathbb{Z}. \tag{6}$$

The map

$$\phi \to \psi = \frac{\delta}{2\pi}\, \mathrm{e}^{2\pi \mathrm{i} \phi/\delta}, \tag{7}$$

which maps ϕ to a circle in the complex plane, is unchanged by this equivalence. We are mainly interested in the situation where we have a function $\phi(x)$ that is continuous except for a jump that is a multiple of δ when x crosses a hypersurface in $\mathcal{M}$. The corresponding function $\psi(x)$ will then be a continuous function. The constant mode is still a trivial harmonic map $\phi(x)$ from $\mathcal{M}$ to S^1, but that is clearly an uninteresting choice if we want $\phi(x)$ to act as a coordinate on $\mathcal{M}$. However, because $\phi(x)$ belongs to S^1, we now have other possibilities. Let us illustrate this in the simplest case where $\mathcal{M}$ is also S^1 with the same circumference δ as the target space for ϕ. Then we are considering maps $S^1 \to S^1$, and a solution to (5) which winds k times around S^1 is simply

$$\phi_k(x) = k \cdot x + c, \quad x \in [0, \delta], \quad k \in \mathbb{Z}. \tag{8}$$

Solutions with different k cannot be deformed continuously into each other. Since $\mathcal{M}$ has the topology of T^4, we seek a solution to (5) with winding number one, and we want the points $x \in \mathcal{M}$ satisfying $\phi(x) = c$ to constitute hypersurfaces $H(c) \subset \mathcal{M}$ whose union for c varying in a range of length δ covers $\mathcal{M}$. We now turn to the implementation of this program for triangulations $\mathcal{T}$ that describe our piecewise linear manifolds $\mathcal{M}$.

In all our previous studies of CDT and also in all cases discussed in the present study, we consider the field ϕ_i to be located in the four-simplices and, for the sake of simplicity, we do

not distinguish between different simplex types. Therefore, we consider the following discrete counterpart of the continuous action (4) or, more precisely, one of its components in a given 'direction':

$$S_{\mathrm{M}}^{\mathrm{CDT}}[\{\phi\},\mathcal{T}] = \frac{1}{2}\sum_{i\leftrightarrow j}(\phi_i-\phi_j)^2 = \sum_{i,j}\phi_i L_{ij}\phi_j \equiv \phi^T \boldsymbol{L}\phi, \tag{9}$$

where the first sum is over all pairs of neighboring four-simplices and the second sum is over all four-simplices in the triangulation $\mathcal{T}$. $\boldsymbol{L}$ is the discrete Laplacian matrix. For every four-dimensional triangulation, there are an associated graph and a corresponding five-valent dual graph[17] where a vertex corresponds to a four-simplex in the triangulation, and a link denotes a connection between two adjacent four-simplices, i.e. it can be viewed as connecting the centers of the four-simplices across the tetrahedron they share. Given such a dual graph, one can define the $N_4 \times N_4$ symmetric adjacency matrix $\mathbf{A}$,

$$A_{ij} = \begin{cases} 1 & \text{if(the link } i \leftrightarrow j) \in \text{dual lattice,} \\ 0 & \text{otherwise,} \end{cases} \tag{10}$$

where N_4 is the number of vertices in the dual lattice or, equivalently, the number of simplices in the original triangulation. Using the dual lattice notation, the Laplacian matrix $\boldsymbol{L}$ in equation (9) can be expressed as

$$\mathbf{L} = 5\mathbb{1} - \mathbf{A}, \tag{11}$$

where $\mathbb{1}$ is the $N_4 \times N_4$ unit matrix. Let us first treat ϕ_i as a field taking values in $\mathbb{R}$. Then, a field ϕ_i which minimizes the action (9) satisfies the discrete Laplace equation

$$\mathbf{L}\phi = 0. \tag{12}$$

For any finite triangulation of a compact manifold without boundary, there is a trivial solution:

$$\phi_i = \text{const.} \tag{13}$$

If we project out this zero mode, we can invert the Laplacian matrix (or, in the continuum, the Laplace operator). Thus, if ϕ_i is a field taking values in $\mathbb{R}$, the solutions (13) are the only type of field configurations that minimize (9). However, as discussed above, we are really interested in fields ϕ_i minimizing the action (9) under the constraint that $\phi_i \in S^1$ and that ϕ_i winds around S^1 once, which allows for new solutions examplified by (8). Of course, a concept such as the winding number is not strictly defined in our discretized version, but as we will show, we can obtain ϕ_i configurations that approximate it well. We thus define the discretized analogue of (6):

$$\phi_i \equiv \phi_i + n\cdot\delta, \quad n\in\mathbb{Z} \quad \forall\, i \in \mathcal{T}, \tag{14}$$

where S^1 has 'circumference' δ. In the following, for convenience we will take $\delta = 1$, except in section 5. With this definition, (12) has solutions ϕ_i that can serve as coordinates. There are four independent non-contractible loops winding around the toroidal CDT triangulation $\mathcal{T}$. Let us choose one of them and a closed hypersurface that intersects the loop only once. For a

[17] Each four-simplex in a four-dimensional triangulation has exactly five neighbors (CDT forbids topological defects, and four-simplices are glued together along all their five 3D faces).

description of how to actually choose such hypersurfaces for our CDT triangulations, we refer to [21, 22]. Let the field ϕ_i jump by $\delta = 1$ when crossing the hypersurface. This is precisely what happened in the continuum solution (8), and viewed as belonging to S^1 it does not jump at all. However, to solve the equations for ϕ_i it is convenient temporarily to view it as an ordinary scalar field in $\mathbb{R}$ with a jump at the hypersurface. As we will show below, this ensures that we have a unique solution to (14) orthogonal to the constant mode, which by definition is 'stretched' by $\delta = 1$ moving around the manifold along the (or any) non-contractible loop intersecting the hypersurface. Although it seems that we have introduced a discontinuity of the field ϕ_i along the chosen hypersurface, we want again to emphasize that this is not the case when we view ϕ_i as a field belonging to S^1, and thus the hypersurface does not have any physical reality since we cannot identify it if we only know ϕ_i expressed as a field with values in S^1.[18] We want to apply this construction also to the three other independent non-contractible loops in our triangulation $\mathcal{T}$ so that we have four scalar fields $(\phi_i^{(x)}, \phi_i^{(y)}, \phi_i^{(z)}, \phi_i^{(t)})$, which provide us with a map from $\mathcal{T}$ to $S^1 \times S^1 \times S^1 \times S^1$, and which we can use (with some modifications) as coordinates for $\mathcal{T}$. We now turn to the precise description of how to do that.

3.2. Scalar fields as coordinates with values on S^1

The jump condition

We will now discuss how to implement the jump and solve the corresponding discretized Laplace equation. Suppose we have a given *oriented* boundary or hypersurface (again, see [21, 22] for explicit constructions), defined as a non-contractible (in a given spatial or time direction) connected subset of 3D tetrahedral faces of four-simplices or, equivalently, as a subset of links on the dual lattice. The field ϕ_i in a simplex i adjacent to the boundary will perceive the value of the field ϕ_j in a simplex j on the other side of the boundary as shifted by $\pm\delta$ (the sign depends on the orientation of the boundary); see figure 4 for a 2D illustration. Since the classical scalar field solution will trivially scale with the jump magnitude δ, in the following *we will assume* $\delta = 1$ (as already noted above), but we can always release this assumption and change $\phi_i \to \delta\phi_i$, depending on possible physical requirements[19]. One can define an antisymmetric *jump matrix*

$$B_{ij} = \begin{cases} +1 & \text{if the dual link } \ i \to j \ \text{ crosses the boundary in the positive direction,} \\ -1 & \text{if the dual link } \ i \to j \ \text{ crosses the boundary in the negative direction,} \\ 0 & \text{otherwise} \end{cases} \tag{15}$$

and a *boundary (jump) vector*

$$b_i = \sum_j B_{ij}. \tag{16}$$

The three-volume (i.e. the number of tetrahedra) of the boundary is then given by:

$$V = \frac{1}{2}\sum_{ij} B_{ij}^2 = \frac{1}{2}\sum_i |b_i|, \tag{17}$$

[18] In appendix A1 we show that if we view ϕ_i as a field taking values in $\mathbb{R}$ rather than in S^1, the hypersurface represents indeed a physical surface. In the language of electrostatics, it is a dipole sheet with constant dipole density.

[19] We release this assumption in section 5 where we discuss dynamical scalar fields coupled to geometric degrees of freedom. The jump magnitude δ will have an important impact on the underlying generic geometries.

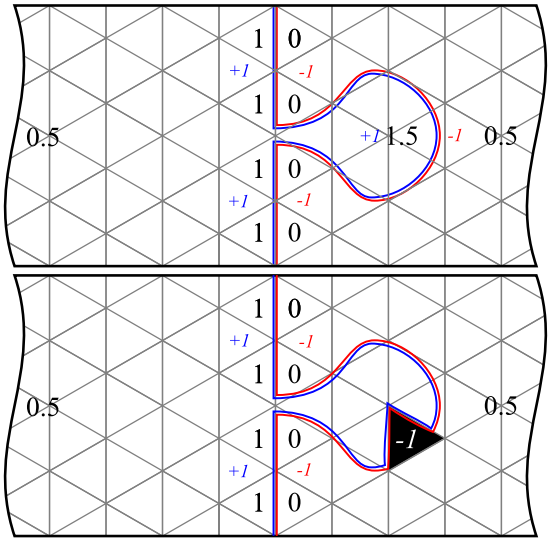

Figure 4. Top: an example boundary with a bubble, for which the field values do not fit into an interval of width 1. Bottom: a step of the boundary redefinition procedure. The black triangle is flipped to the other side of the boundary. Its field value is decreased by 1.

as the boundary vector b_i is integer-valued in the range $-5 \leqslant b_i \leqslant 5$ and measures the number of tetrahedral faces a particular four-simplex i has on the boundary[20]. To accommodate to the jump $\delta = 1$, we modify the scalar field action to

$$S_{\mathrm{M}}^{\mathrm{CDT}}[\{\phi\}, \mathcal{T}] = \frac{1}{2}\sum_{i\leftrightarrow j}(\phi_i - \phi_j - B_{ij})^2$$
$$= \sum_{i,j}\phi_i L_{ij}\phi_j - 2\sum_i \phi_i b_i + V \equiv \phi^T \mathbf{L}\phi - 2\phi^T b + V, \tag{18}$$

where we used definitions (16) and (17). The action (18) is invariant under a constant shift in the scalar field values (the Laplacian zero mode) and, as we will argue below, it is also invariant under a shift of the boundary, provided that one also modifies the field values in a trivial way that is compatible with the equivalence definition (14). Thus, it follows that, viewed as taking values on S^1, the field is not changed at all, and the classical solution is then independent of the specific choice of boundaries which can be 'continuously' (in a sense defined suitably for the lattice) deformed into each other.

The classical solution

A classical solution for ϕ_i that minimizes the action (18) will now satisfy the discrete Laplace[21] equation with a boundary term:

$$\mathbf{L}\phi = b. \tag{19}$$

[20] b_i will later be used to find a position of a (redefined) boundary. The sign depends on the flow of the winding number, i.e. whether the four-simplex is on the positive or negative side of the oriented boundary.

[21] Even though the equation (19) formally looks like a Poisson equation, we will call it the Laplace equation since b is not a source term when we view the field as a field with values in S^1.

Formally, the solution to equation (19) is given by $\phi = \mathbf{L}^{-1}b$. However, as already discussed, the Laplacian matrix $\mathbf{L}$ is not invertible as it has a zero mode ($\mathbf{L}e^{(0)} = 0$, where $e^{(0)} = [1, 1, \ldots, 1]^{\mathrm{T}}$ is a constant eigenvector). Equation (19) is still solvable since the jump vector b is orthogonal to the zero mode ($e^{(0)} \cdot b = \sum_i b_i = 0$), which is due to the translational symmetry of the action (the action is invariant under a constant shift of the field). For the sake of simplicity, we shift the field values so that for some simplex (labeled i_1) $\phi_{i_1} = 0$. This can be done by adding a term $\varepsilon \cdot \phi_{i_1}^2$ to the action (18), where ε is positive (not necessarily small). The modification can then be absorbed into the Laplacian matrix,

$$L_{ij} \;\rightarrow\; L_{ij} + \varepsilon\delta_{ii_1}\delta_{ji_1}, \tag{20}$$

and one obtains a unique solution:

$$\bar{\phi} = \mathbf{L}^{-1}b, \qquad \bar{\phi}_{i_1} = 0. \tag{21}$$

All other solutions to the original Laplace equation (19) with the zero mode are thus given by translations $\phi_i = \bar{\phi}_i + \text{const}$. Computing the classical solution numerically is itself a technical challenge since the Laplacian matrix is large ($N_4 \times N_4$, where $N_4 \sim 10^5 - 10^6$). Nevertheless, we managed to construct numerical algorithms that solve this problem with machine precision in relatively short computer time. Technicalities are discussed in appendix A2. The classical solution $\bar{\phi} = \mathbf{L}^{-1}b$ has the property

$$\bar{\phi}_i = \frac{1}{5}\left(b_i + \sum_{j\to i}\bar{\phi}_j\right). \tag{22}$$

This is just a discretized version of the mean value property of continuous harmonic functions, where at the boundary one should view the field as taking values in S^1 rather than in $\mathbb{R}$. An interesting consequence of equation (22) is that the field condensates in the fractal outgrowths observed in CDT triangulations. This is because the (artificial) local boundary surrounding an outgrowth is typically small in size, and therefore the field changes only a little on that local boundary, leaving the field values almost constant in all simplices building the geometric outgrowth. The condensation is observed in all spatial and time directions and for each of the four scalar fields ($\phi_i^{(x)}, \phi_i^{(y)}, \phi_i^{(z)}, \phi_i^{(t)}$). Consequently, if one represents each simplex i by a point with coordinates ($\phi_i^{(x)}, \phi_i^{(y)}, \phi_i^{(z)}, \phi_i^{(t)}$), the fractal outgrowths will constitute dense clouds of points. Examples of such maps are presented in figures 6–9. The maps (or at least 2D projections) will therefore qualitatively resemble the conformal map in figure 3 discussed above, where dense regions are also fractal outgrowths.

Boundary redefinition

The scalar field action with a jump at the boundary (18) is invariant under a local shift of the boundary (such that one simplex, labeled i, is transferred from one to the other side of the boundary) with a simultaneous change of the scalar field value $\phi_i \rightarrow \phi_i \pm \delta$ (the sign depends on whether the simplex is shifted from the negative to the positive side of the oriented boundary or vice versa). This is illustrated by a simple 2D example triangulation with a boundary presented in figure 4. Let us consider repeated changes in the position of the boundary, which preserve its nature as a hypersurface with the topology of T^3, and at the same time the corresponding changes in the field ϕ_i. Clearly the field ϕ_i viewed as a field with values on S^1 is not changed at all; nevertheless, it is convenient to think about such a change of the boundary and the field ϕ_i. The reason is that the solution $\bar{\phi}_i$ given by (21) need not be constant on the hypersurface with the jump $\delta(=1)$ nor does it necessarily take values in the range $[0, 1]$ (as illustrated in figure 4), even after adjusting the global constant. Let us now argue that we can

deform the hypersurface of the field jump and correspondingly change $\bar{\phi}_i$ so that $\bar{\phi}_i$ is zero on one side of the modified hypersurface and takes the value 1 on its other side. We apply the following procedure to the original classical field solution $\bar{\phi}_i$:

(a) Shift all field values by a constant so that the smallest value is 0.
(b) Choose a simplex with the largest field value. As follows from the maximum principle for a harmonic function, the simplex has to touch the boundary with at least one face.
(c) Modify the boundary so that the simplex is flipped to its other side and decrease the corresponding field value by $\delta = 1$.
(d) Repeat steps (b) and (c) until the maximal field value is below 1.

The argument above shows, using the fact that $\bar{\phi}_i$ is a discrete harmonic function, that it is possible to find a hypersurface such that the (new) $\bar{\phi}_i$ defined by it takes values in the range $[0, 1]$. One could obtain such a surface 'in one go' by defining a new field

$$\tilde{\phi}_i(0) = \mathrm{mod}(\bar{\phi}_i, 1). \tag{23}$$

This removes the original hypersurface and replaces it with the one where $\bar{\phi}_i$ passes through 0 (or an integer $n \in \mathbb{Z}$), at the same time ensuring that the range of $\tilde{\phi}_i(0)$ is $[0, 1]$. Literally mapped to a circle of circumference 1 in the complex plane,

$$\psi_i = \frac{1}{2\pi} \exp\left(2\pi \mathrm{i} \bar{\phi}_i\right) = \frac{1}{2\pi} \exp\left(2\pi \mathrm{i} \tilde{\phi}_i(0)\right), \tag{24}$$

which illustrates again that from an S^1 perspective the hypersurfaces play no role (as long as they are 'continuously' deformable to each other). We have now achieved our goal of finding a harmonic map from the triangulation $\mathcal{T}$ to S^1 with winding number 1. The hypersurfaces $H(\alpha)$ in $\mathcal{T}$ characterized by being mapped to a fixed point $\mathrm{e}^{\mathrm{i}2\pi\alpha}/2\pi$ on the circle of circumference 1 cover $\mathcal{T}$, and α can serve as the coordinate in $\mathcal{T}$ 'orthogonal' to these hypersurfaces. Thus,

$$H(\alpha) = \{i \in \mathcal{T} \mid \psi_i = \mathrm{e}^{2\pi \mathrm{i}\alpha}/2\pi\}. \tag{25}$$

$H(0)$ is precisely the hypersurface where $\tilde{\phi}_i(0)$ jumps from 0 to 1 constructed above, and we can generalize this construction to find $H(\alpha)$ explicitly. Define

$$\tilde{\phi}_i(\alpha) = \mathrm{mod}(\bar{\phi}_i - \alpha, 1), \quad 0 \leqslant \alpha < 1. \tag{26}$$

Again, the original hypersurface of the jump in $\bar{\phi}_i$ is removed and replaced by the new hypersurface where $\bar{\phi}_i$ passes though α (or α plus an integer $n \in \mathbb{Z}$), i.e. where $\tilde{\phi}_i(\alpha)$ jumps from 0 to 1. By construction we have

$$\psi_i = \mathrm{e}^{2\pi \mathrm{i}\alpha}\, \mathrm{e}^{2\pi \mathrm{i}\tilde{\phi}_i(\alpha)}/2\pi, \tag{27}$$

so $H(\alpha)$ is indeed the hypersurface with the described property. Since $\tilde{\phi}_i(\alpha)$ is still a solution to equation (19), we can explicitly find $H(\alpha)$ by using equation (22) to reconstruct the boundary jump vector from $\tilde{\phi}_i(\alpha)$:

$$b(\tilde{\phi}_i(\alpha)) = 5\tilde{\phi}_i(\alpha) - \sum_{j \to i} \tilde{\phi}_j(\alpha) = \sum_j L_{ij} \tilde{\phi}_j(\alpha). \tag{28}$$

As already mentioned, the (integer) value of $b(\tilde{\phi}_i(\alpha))$ counts the number of faces (tetrahedra) the simplex i shares with the boundary (the value is 0 for no boundary faces shared, or either positive or negative depending on which side of the boundary the simplex is located, as

described above). Thus, knowing $b(\tilde{\phi}_i(\alpha))$, we know $H(\alpha)$. There are several issues related to the hypersurfaces $H(\alpha)$, which we will discuss below: are they really hypersurfaces? How do they change with α ($\bar{\phi}_i$ is a set of discrete variables, and α is a continuous parameter)? What is the size of a typical hypersurface $H(\alpha)$? Is α really a *good* coordinate for a typical path integral configuration? We will address these questions in section 4. Assuming that the issues mentioned have satisfactory answers, let us return to our original problem: for a given toroidal triangulation we have defined in some way (see [21, 22]) four independent non-contractible boundaries which we can label with x, y, z, t, and we want to use the corresponding classical solutions $\bar{\phi}_i^\mu$, $\mu = x, y, z, t$ as coordinates, but without any explicit reference to the chosen boundaries and the specific range of these solutions. We have managed to do that by introducing the coordinate system $(\alpha_x, \alpha_y, \alpha_z, \alpha_t)$ where $\alpha_\mu \in [0, 1]$ and the corresponding scalar fields $\tilde{\phi}_i^\mu(\alpha_\mu)$ are characterized by being solutions to the Laplace equations that jump from 0 to 1 at the α_μ-hypersurface. Sometimes, it can be convenient to represent the torus as a periodic structure on $\mathbb{R}^4$. If we choose to let the jumps of $\tilde{\phi}_i^\mu(\alpha_\mu)$ define the periodic structure, we can turn the functions $\tilde{\phi}_i^\mu(\alpha_\mu)$ into functions without a jump by adding ± 1 to them when they cross the boundaries where they jump. We can also label the new regions we enter in $\mathbb{R}^4$ by corresponding integer labels that tell us how many multiples of ± 1 we should add to the corresponding functions $\tilde{\phi}_i^\mu(\alpha_\mu)$ in that particular region in order to ensure it is a 'continuous' function (i.e. a function without the jumps) on $\mathbb{R}^4$. We have tried to illustrate this in figure 5, where we show how different choices of α lead to different representations of the torus on $\mathbb{R}^4$. With the choice of the coordinate system given by (α_μ), we are interested in the volume density $\sqrt{g(\alpha)}$ defined as

$$\mathrm{d}V(\alpha) = \sqrt{g(\alpha)} \prod_\mu \Delta\alpha_\mu = \#\,\text{simplices in volume element} \prod_\mu \Delta\alpha_\mu. \tag{29}$$

The easiest way to obtain an idea of the volume density is to fix a coordinate point α_μ^0 and calculate the four scalar fields $\tilde{\phi}_i^\mu(\alpha_\mu^0)$. If we implement $\tilde{\phi}_i^\mu(\alpha_\mu^0)$ on $\mathbb{R}^4$ as described above (without any jumps), then by definition (since the α-hypersurfaces are the hypersurfaces of constant $\bar{\phi}_i$ or, equivalently, of constant $\tilde{\phi}_i^\mu(\alpha_\mu^0)$) the density of simplices around a simplex i where $\tilde{\phi}_i^\mu(\alpha_\mu^0) = \alpha_\mu$,[22] measured using the scalar fields $\tilde{\phi}_i^\mu(\alpha_\mu^0)$, will agree with the density $\sqrt{g(\alpha)}$ defined in (29). We can thus write:

$$\mathrm{d}V(\tilde{\phi}_i^\mu(\alpha_\mu^0)) = \sqrt{g(\tilde{\phi}_i^\mu(\alpha_\mu^0))} \prod_\mu \Delta\tilde{\phi}_i^\mu(\alpha_\mu^0). \tag{30}$$

Now we turn to the measurement of $\sqrt{g(\tilde{\phi}_i^\mu(\alpha_\mu^0))}$.

3.3. Density measurements for generic geometries in various CDT phases

Below we present the results of scalar fields measurements for generic triangulations observed in all the four phases (C, C_b, B and A) of CDT with the toroidal spatial topology and a periodic time coordinate. The time period used was either $T = 4$ or $T = 20$, and the $N_{4,1}$ volume was set to fluctuate around 160k and 720k simplices, respectively. In each case, we picked just one typical configuration and solved for the classical scalar fields $(\tilde{\phi}^{(x)}(\alpha_x), \tilde{\phi}^{(y)}(\alpha_y), \tilde{\phi}^{(z)}(\alpha_z), \tilde{\phi}^{(t)}(\alpha_t))$ in such a way that the field values are within the range $[0, 1]$ (we put $\delta = 1$), and the elementary

[22] For clarity of presentation we have made this discussion a little imprecise, treating the simplices i as points in a continuum so that there is locally a one-one map between i and its coordinates $\alpha_\mu(i)$.

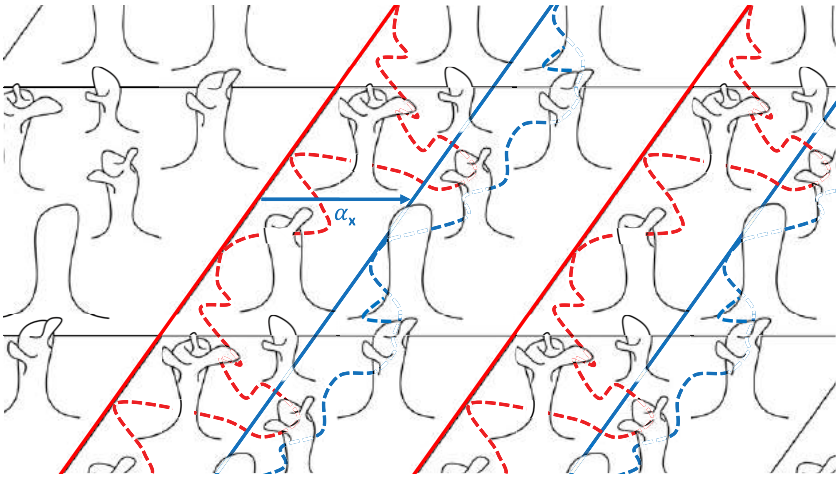

Figure 5. A 2D visualization of the (toroidal) periodic geometric structure. The solid red and blue lines are drawn to guide the eye. The dashed red lines show the periodic structure starting out with the hypersurface corresponding to, say, $\alpha_x = 0$. The dashed blue lines show the periodic structure starting out with the hypersurface corresponding to some other α_x.

cell boundaries are set at $\tilde{\phi}^\mu(\alpha_\mu) = 0, 1$ as described above. We chose α_μ such that in each direction the field values are centered around 0.5.

3.3.1. Density maps in $\tilde{\phi}$ coordinates. In principle, a density plot of $(\tilde{\phi}_i^{(x)}(\alpha_x), \tilde{\phi}_i^{(y)}(\alpha_y), \tilde{\phi}_i^{(z)}(\alpha_z), \tilde{\phi}_i^{(t)}(\alpha_t))$ would provide us with the desired quantity $\sqrt{g(\tilde{\phi}_i^\mu(\alpha_\mu))}$. However, this distribution depends on four fields and is difficult to visualize[23]. We have thus opted to plot in figures 6–9 the periodic 2D projections (in various directions), where each dot represents a simplex with coordinates determined by the classical scalar field solution $(\tilde{\phi}^\mu(\alpha_\mu), \tilde{\phi}^\nu(\alpha_\nu))$. Thus, in a given small area

$$\mathrm{d}A_{\mu\nu} = \Delta\tilde{\phi}^\mu(\alpha_\mu)\Delta\tilde{\phi}^\nu(\alpha_\nu) \tag{31}$$

we count the total number of four-simplices i with coordinates $(\tilde{\phi}_i^\mu(\alpha_\mu), \tilde{\phi}_i^\nu(\alpha_\nu))$ in the region $\Delta\tilde{\phi}^\mu(\alpha_\mu)\Delta\tilde{\phi}^\nu(\alpha_\nu)$. With the $(\tilde{\phi}^\mu(\alpha_\mu), \tilde{\phi}^\nu(\alpha_\nu))$-plane serving as a photographic plate, all points above and below are projected on it and leave a mark. In terms of the original $\sqrt{g(\tilde{\phi}_i^\mu(\alpha_\mu))}$, we can write (in continuum notation), instead of (30),

$$\mathrm{d}V_{\mu\nu} = \left(\int_0^1\int_0^1 \mathrm{d}\tilde{\phi}^\kappa(\alpha_\mu)\mathrm{d}\tilde{\phi}^\lambda(\alpha_\nu)\,\sqrt{g(\tilde{\phi}_i^\rho(\alpha_\rho))}\right)\,\mathrm{d}A_{\mu\nu}, \quad \kappa,\lambda \neq \mu,\nu. \tag{32}$$

Since we have the original coordinate t freely at our disposal, we have chosen to include this information in the plots by a color code. The color of each point thus depends on the position

[23] Under the link: https://cs.if.uj.edu.pl/plots/10-alphaft_xyz_t_3 one can find a '4D' visualization for a $T = 4$ configuration from phase C. Each dot in a 3D frame from the animation represents a simplex with coordinates $(\tilde{\phi}_i^{(x)}(\alpha_x), \tilde{\phi}_i^{(y)}(\alpha_y), \tilde{\phi}_i^{(z)}(\alpha_z), \tilde{\phi}_i^{(t)}(\alpha_t))$ where spatial coordinates are the 3D Euclidean coordinates of the dot and the time coordinate is related to the animation time.

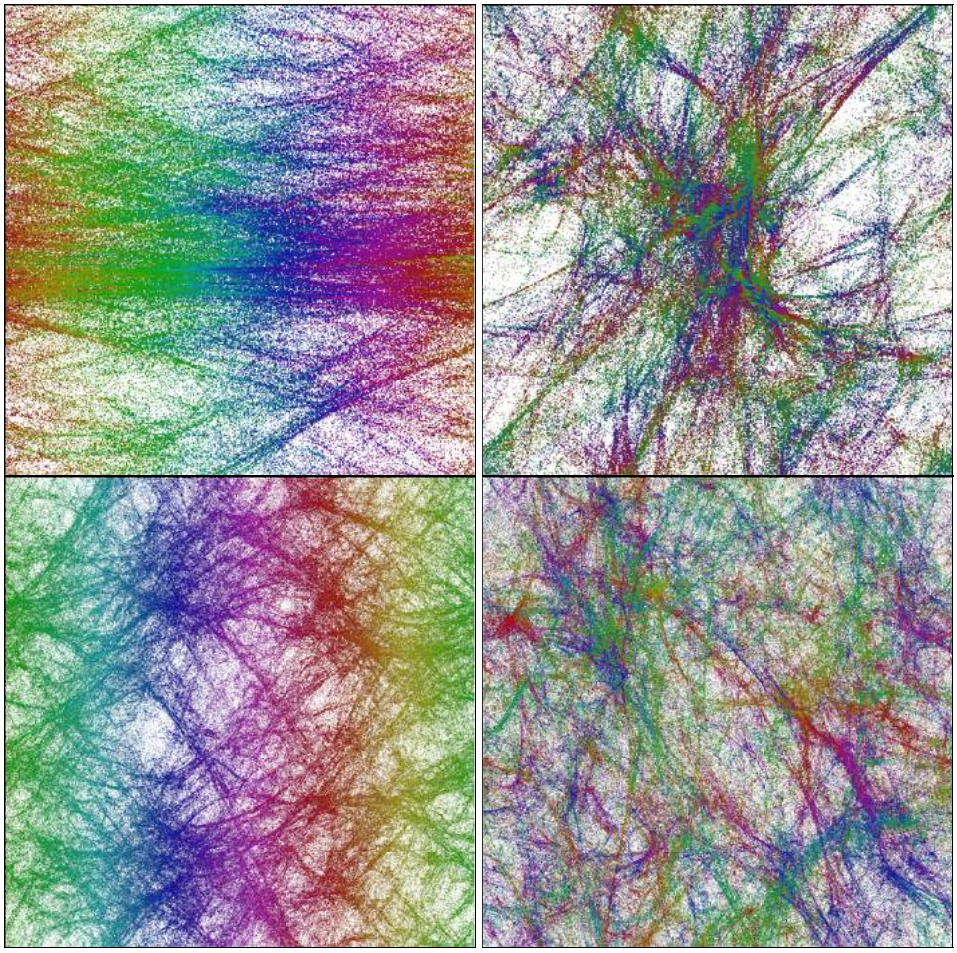

Figure 6. Cosmic voids and filaments for configurations in phase C. Top: a configuration with $T = 4$ ($\kappa_0 = 2.2$, $\Delta = 0.6$). Bottom: a configuration with $T = 20$ ($\kappa_0 = 3.0$, $\Delta = 0.2$). The left-hand side charts are projections on the $t - x$ plane, the right-hand side charts are projections on the $x - y$ plane. Notice that for the two bottom plots the period T is larger than that for the upper plots, which also explains why the observed structures are more dense.

of a given simplex in the original proper-time foliation t. To each $(4, 1)$ simplex with four vertices (a spatial tetrahedron) in t and one vertex in $t + 1$ we assign an integer time coordinate t. As going from such a simplex to a simplex of the same type in the next $t + 1$ layer requires at least 4 steps: $(4, 1) \to (3, 2) \to (2, 3) \to (1, 4) \to (4, 1)$, we assign non-integer time coordinates $t + \frac{1}{4}$, $t + \frac{1}{2}$ and $t + \frac{3}{4}$ to the $(3, 2)$, $(2, 3)$ and $(1, 4)$ simplices, respectively. Thus, we have in total $4 \times T$ various time coordinates (and the corresponding colors), and we can trace the location of each simplex in the (original) time foliation. In figure 6 we show configurations measured in the semiclassical phase C for $T = 4$ (top charts) and $T = 20$ (bottom charts), respectively. The left-hand side charts are projections on the $t - x$ plane, while the right-hand side charts are projections on the $x - y$ plane. One can easily see that the scalar field with a jump in the time direction follows the original time slicing (depicted by colors) quite closely, whereas

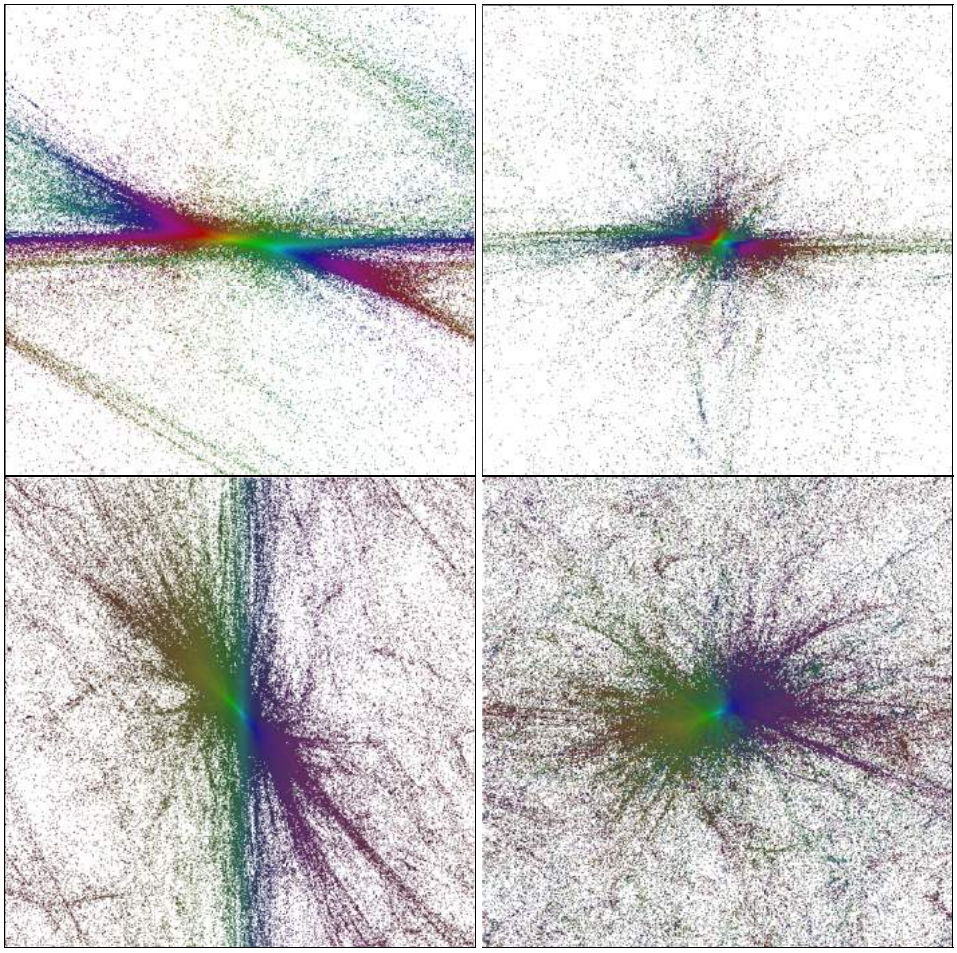

Figure 7. Configurations in phase C_b. Top: a configuration with $T = 4$ ($\kappa_0 = 2.0$, $\Delta = 0.1$). Bottom: a configuration with $T = 20$ ($\kappa_0 = 2.5$, $\Delta = 0.2$). The left-hand side charts are projections on the $t - x$ plane, the right-hand side charts are projections on the $x - y$ plane.

the new coordinates defined by the scalar fields are smeared around the original proper-time slicing. The large-scale structure is quite isotropic in all spatial directions, i.e. it looks qualitatively the same for all $x - y$, $x - z$ and $y - z$ projections (in the plots we show just the $x - y$ projection). This is also the case for the time direction when both $T = 20$ and $N_{4,1} = 720$k are large, i.e. the $t - x$ (and also $t - y$ and $t - z$) projection looks qualitatively similar to the $x - y$ projection[24]. For the larger triangulation, the large-scale geometry is also quite homogeneous in all directions, in the sense that shifting all coordinates by constants will produce pictures looking qualitatively the same. Summing up, in the semiclassical phase *C* one observes a homogeneous and isotropic geometry on large scales. This large-scale homogeneity and isotropy is

[24] For $T = 4$ the correlation length in the time direction is larger than the fixed time period, and thus the system is too small to allow for the full structure formation in this direction, but this is simply a finite size effect.

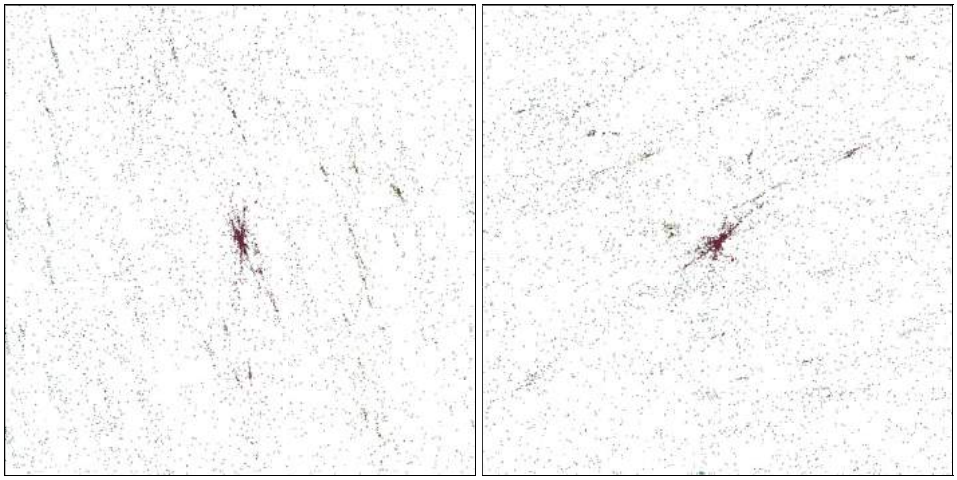

Figure 8. A configuration in phase B with $T = 4$ ($\kappa_0 = 4.4$, $\Delta = -0.7$). The left-hand side chart is a projection on the $t - x$ plane, the right-hand side chart is a projection on $x - y$ plane.

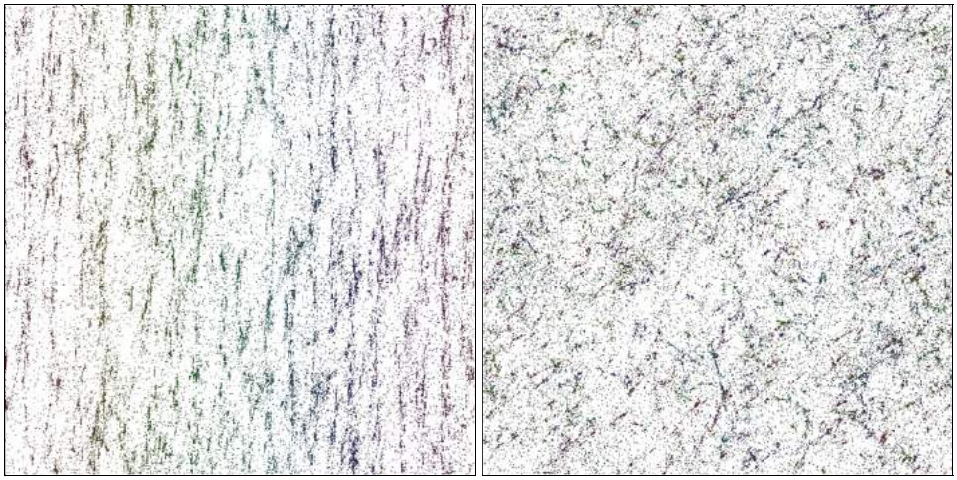

Figure 9. A configuration in phase A with $T = 20$ ($\kappa_0 = 5.0$, $\Delta = 0.2$). The left-hand side chart is a projection on the $t - x$ plane, the right-hand side chart is a projection on the $x - y$ plane.

broken on smaller scales, with sparse regions representing the 'central' toroidal part and dense regions showing fractal outgrowths. The outgrowths are very non-trivially correlated, forming the characteristic cosmic voids and filaments structure. Remarkably, even though we analyze the pure gravity case (i.e. the classical scalar fields do not impact the CDT geometry in any way), and the measured 'universes' are only a few Planck lengths in diameter [33], they qualitatively reproduce the basic features of the real Universe, including the large-scale cosmic voids and filaments structure observed in nature. From this perspective, one can imagine that the geometric fractal outgrowths serve as 'seeds' of some matter field condensations (this is

indeed the case for quantum scalar fields coupled to geometry, discussed in section 5), leading to nontrivial structure formation caused by quantum gravity effects.

Similar analysis can be performed for geometric configurations measured in the other CDT phases. In figure 7 we plot 2D projections of the density maps measured in the bifurcation phase C_b for $T = 4$ (top charts) and $T = 20$ (bottom charts). Here again, at least for the large $T = 20$ and $N_{4,1} = 720$k configuration, the geometry appears quite isotropic in all directions (we will return to this in the next subsection) but is no longer homogeneous. The lack of homogeneity in the time direction is well explained by the nonuniform spatial volume distribution in the proper-time coordinate as the volume profile in this phase is blob-like rather than flat as in phase C (the effect is visible only for large T). It is equally well known that the characteristic feature of generic phase C_b triangulations is the emergence of dense volume clusters around high-order vertices observed in every second spatial slice, which makes the spatial volume distribution inhomogeneous also in the spatial directions. In the C_b phase maps in figure 7, unlike in the C phase, no nontrivial structure of fractal outgrowths can be observed as the geometry viewed from any direction seems to concentrate in just one large outgrowth. This effect is even more pronounced in phase B; see figure 8, showing a configuration with $T = 4$. In this case, the geometry in all directions becomes effectively compactified to a point. Thus, time and spatial homogeneity are both maximally broken. This, again, was expected from the previous analyses of geometric configurations observed in this phase. Finally, figure 9 shows a generic phase A configuration, with $T = 20$. In that case, the dense regions, i.e. the geometric outgrowths, are separated and uncorrelated, and they do not form any nontrivial structures. This kind of behavior was previously noticed in the time direction, but now it can also be observed in the spatial directions. As a result, a generic configuration measured in phase A is highly homogeneous and isotropic on both large and small scales.

3.3.2. Density maps in alternative β coordinates. To visualize and analyze in detail the internal structure of geometric outgrowths, i.e. of the dense clouds of points in figures 6–9, another parametrization might be more suitable. It can be introduced by first sorting all $\tilde{\phi}$ field values so that

$$0 \leqslant \tilde{\phi}_{i_1} \leqslant \tilde{\phi}_{i_2} \leqslant \cdots \leqslant \tilde{\phi}_{i_{N_4}} < 1, \tag{33}$$

and then defining the map

$$\tilde{\phi} \to \beta : \beta_i = \frac{i}{N_4}, \tag{34}$$

where i is the index (field position) in the sorted list (33). β is by definition in the range. $[0, 1]$. Since $\tilde{\phi}$ is a (discrete) harmonic function, β monotonically interpolates between both sides of the elementary cell and thus can serve as a coordinate. It follows from the definition that the new β coordinates will be stretched in the range where $\tilde{\phi}$ is dense and compressed where $\tilde{\phi}$ is sparse. As a result, the fractal geometric outgrowths get magnified relative to the 'central' part of a triangulation; see figures 10–13. Interestingly, the qualitative picture of generic triangulations does not change significantly in the semiclassical phase C, which suggests that the geometric outgrowths observed in this phase are small and shallow, as in figure 10, where the voids and filaments structure is still visible in the β coordinates. This is not the case in the other phases, as shown in figures 11–13, where the new coordinates reveal much finer structures inside bigger and deeper outgrowths.

The new coordinates do not change qualitatively the results of the analysis of a phase A configuration, where one still observes a number of separated and uncorrelated spacetime points

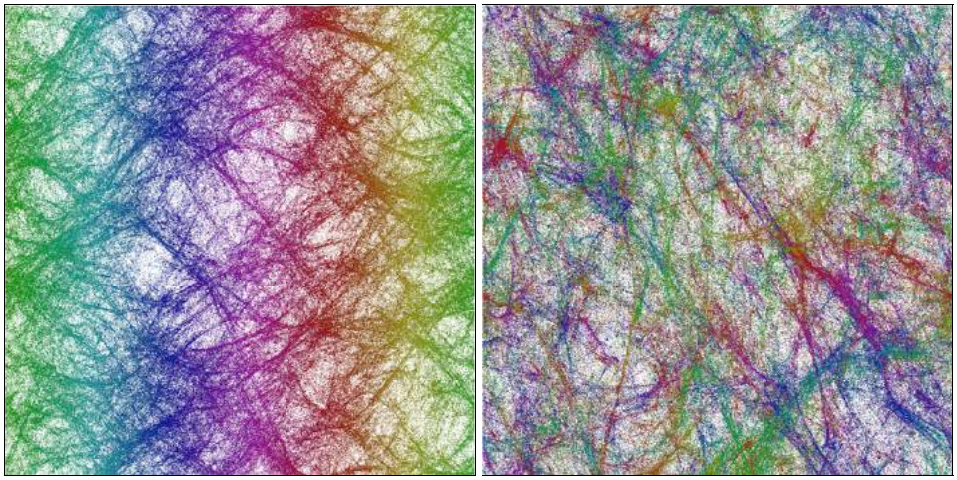

Figure 10. A configuration in phase C with $T = 20$ ($\kappa_0 = 3.0$, $\Delta = 0.2$) in β coordinates. The left-hand side chart is a projection on the $t - x$ plane, the right-hand side chart is a projection on the $x - y$ plane.

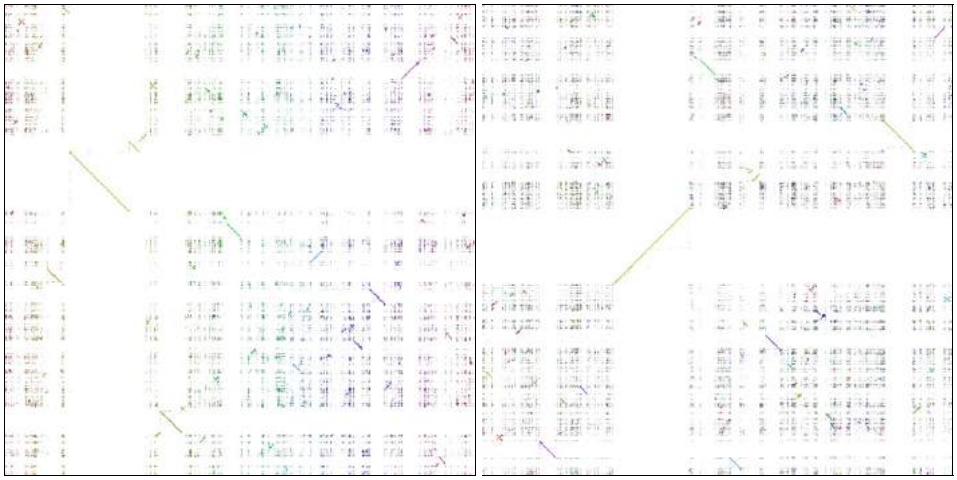

Figure 11. A configuration in phase A with $T = 20$ ($\kappa_0 = 5.0$, $\Delta = 0.2$) in β coordinates. The left-hand side chart is a projection on the $t - x$ plane, the right-hand side chart is a projection on the $x - y$ plane.

giving rise to a quite homogeneous and isotropic geometry. The results observed in the bifurcation phase C_b are more interesting, and they seem to change as one goes from the $C - C_b$ phase transition toward the $C_b - B$ phase transition; see figure 12 where we plot configurations for fixed $\Delta = 0.2$ and various $\kappa_0 = 2.5$ (close to phase C), $\kappa_0 = 2.0$ (in the middle of phase C_b) and $\kappa_0 = 1.5$ (close to phase B). The top charts in figure 12 can be interpreted as a magnification of a single fractal outgrowth observed for $\kappa_0 = 2.5$ in figure 7 (bottom) in various directions, while middle and bottom charts are magnifications of similar outgrowths observed for $\kappa_0 = 2.0$ and $\kappa_0 = 1.5$, respectively. In each case, one clearly observes the time evolution

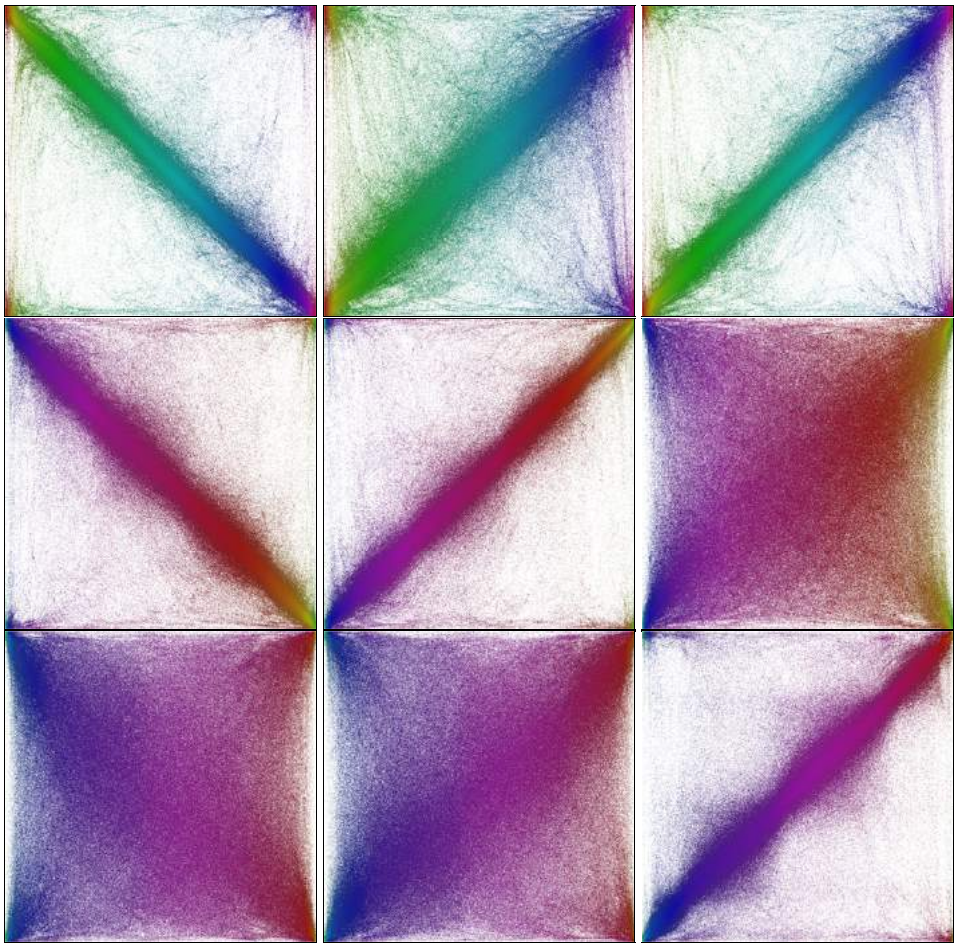

Figure 12. Configurations in phase C_b in β coordinates for $T = 20$, $\Delta = 0.2$ and $\kappa_0 = 2.5$ (top), $\kappa_0 = 2.0$ (middle), $\kappa_0 = 1.5$ (bottom). The left-hand side charts are projections on the $t - x$ plane, the middle charts on the $t - y$ plane and the right-hand side charts on the $t - z$ plane.

of a very compact geometric object with no clear internal fine structure. For the configuration closest to phase C, the geometry is isotropic in all directions (top charts). This isotropy is broken as one approaches phase B (middle and bottom charts). At the same time, the internal structure of the outgrowth becomes increasingly homogeneous, which manifests itself as a 'pillow-like' picture[25]. It would be tempting to interpret such configurations as quantum spacetimes collapsing to a singularity, and in that case the observed anisotropy could be consistent with the BKL scenario. Finally, in phase B the qualitative picture is quite similar, as shown in figure 13, where no fine structure of the magnified outgrowth (i.e. the point in figure 8) is observed, and the configuration looks quite isotropic in all directions.

[25] We checked very carefully that the lack of any fine structures is not a result of finite numerical precision of the classical scalar field solution.

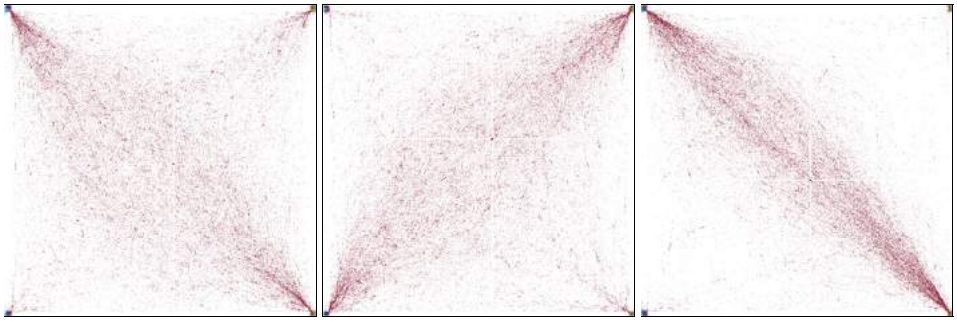

Figure 13. A configuration in phase B for $T = 4$ ($\kappa_0 = 4.4$, $\Delta = -0.7$) in β coordinates. The left-hand side chart is a projection on the $t - x$ plane, the middle chart on the $t - y$ plane and the right-hand side chart on the $t - z$ plane.

4. Alternative spacetime foliations

As already mentioned in sections 1 and 2, CDT introduces a preferred spacetime foliation parametrized by the (lattice) proper-time coordinate t. As a result, the spatial slices (3D hypersurfaces built from tetrahedra in each integer time coordinate t) constitute a set of boundaries orthogonal to the time direction. The new idea introduced in section 3 was to consider scalar field(s) with nontrivial jump(s) of magnitude $\delta = 1$ on the boundaries in the time (or in spatial) direction(s). The scalar field solutions can then act as new time coordinates, with a natural choice of

$$\tilde{\phi}_i^{(t)}(\alpha_t) = \mathrm{mod}(\bar{\phi}_i^{(t)} - \alpha_t, 1), \tag{35}$$

where $\bar{\phi}_i^{(t)}$ is the classical solution of the scalar field with a jump on some of the time boundaries (spatial slices), and which can be viewed as a field taking values in S^1. The solution is parametrized by the real quantity α_t ($0 \leqslant \alpha_t < 1$). The field $\tilde{\phi}_i^{(t)}(\alpha_t)$ is by definition in the range $[0, 1]$ and is periodic in α_t with period one. As already explained, one can consider an integer quantity $b(\tilde{\phi}_i^{(t)}(\alpha_t))$, defined in equation (28), which measures the position of the jump of the scalar field (35), i.e. the position of the new boundary $H(\alpha_t)$ orthogonal to the time direction. The nonzero (integer) values of $b(\tilde{\phi}_i^{(t)}(\alpha_t))$ indicate the number of new boundary faces (depending on α_t) of a particular simplex. For a particular value of α_t there is a set of simplices for which $b(\tilde{\phi}_i^{(t)}(\alpha_t)) > 0$ and a set where $b(\tilde{\phi}_i^{(t)}(\alpha_t)) < 0$. These simplices lie on two opposite sides of the (α_t-dependent) boundary. Note that in general $b(\tilde{\phi}_i^{(t)}(\alpha_t))$ and $b(\bar{\phi}_i^{(t)})$ are not the same, and thus the new 3D boundary $H(\alpha_t)$ is different than the original one, i.e. the spatial slice in t. The three-volume (the number of tetrahedra) of the $H(\alpha_t)$ hypersurface is

$$V(\alpha_t) = \frac{1}{2}\sum_i |b(\tilde{\phi}_i^{(t)}(\alpha_t))|. \tag{36}$$

We can determine the vertices of the boundary tetrahedra by considering a simplex with $b(\tilde{\phi}_i^{(t)}(\alpha_t)) > 0$ and checking the neighboring simplices j to find those for which $b(\tilde{\phi}_i^{(t)}(\alpha_t)) < 0$. Each such case defines a boundary face (tetrahedron). We repeat the same procedure for all simplices with $b(\tilde{\phi}_i^{(t)}(\alpha_t)) > 0$ to obtain a list of all boundary tetrahedra. Once the list is constructed, we check the neighborhood relations between the tetrahedra. Finally, we obtain a list of boundary tetrahedra where for each element the first four entries are the vertex labels of

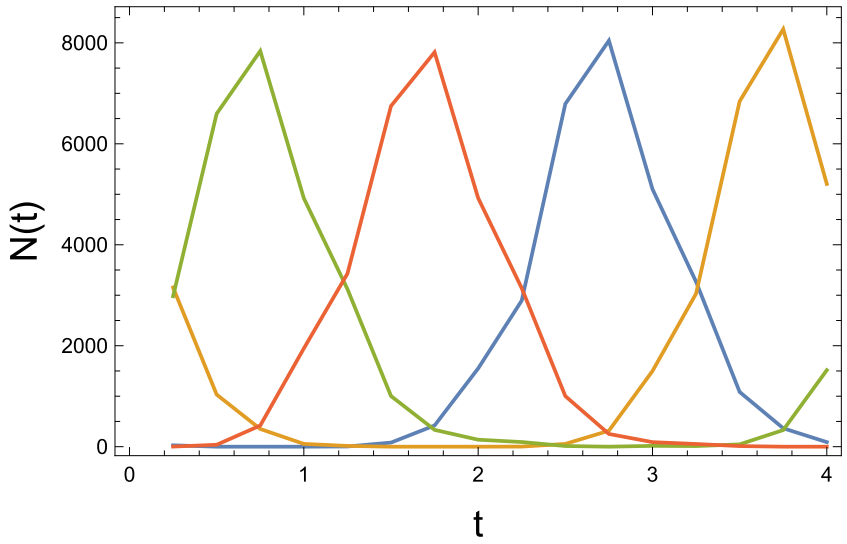

Figure 14. $N(t)$ denotes the number of simplices at the original proper-time coordinate t adjacent to the new boundary $H(\alpha_t)$ defined by the jump of the scalar field (35) for $\alpha_t = 0$ (green), 0.25 (red), 0.5 (blue) and 0.75 (orange). The data were measured for a generic triangulation in phase C. The time position of the simplices, and thus also the boundary, shifts with α_t. In the histograms we used non-integer t coordinates, depending on the simplex type, as explained in section 3.3.

the tetrahedron, and the remaining four are the indices of tetrahedra opposite to the vertices (similar to the way we code 4D simplices in a CDT triangulation). The list is the analogue of a 3D foliation we used before to describe spatial slices, but now it is parametrized by α_t. In all cases described here, the systems were periodic in time with the period $T = 4$. The new 3D hypersurfaces $H(\alpha_t)$ shift with α_t as expected and are smeared along the original proper-time coordinate, as illustrated in figure 14.

Obviously, in the toroidal spatial topology case examined here, a similar analysis can be performed also in the spatial directions. One can introduce a set of four fields $\tilde{\phi}^\mu$, $\mu = x, y, z, t$ and the corresponding boundaries $H(\alpha_\mu)$ in the way already discussed, and then the hypersurfaces will be parametrized (shifted) by α_x, α_y, α_z and α_t, respectively.

4.1. The topology of the hypersurfaces $\boldsymbol{H(\alpha)}$

The first question to be asked is whether the 3D hypersurfaces obtained by the new foliation method outlined above are connected. This can easily be checked. We start from a random tetrahedron belonging to the hypersurface and move out measuring the volume distribution at the geodesic distance r and, eventually, the total volume of the connected part of the hypersurface. We know the total volume $V(\alpha_t)$ defined by equation (36) and can check if all tetrahedra were visited. In all studied cases, they were all visited, and all hypersurfaces in the time direction (and similar hypersurfaces in all spatial directions) were fully connected. The studied cases were configurations from various CDT phases, and we checked the connectivity for many values of α in each spacetime direction. The conclusion is that in the case of CDT with the toroidal

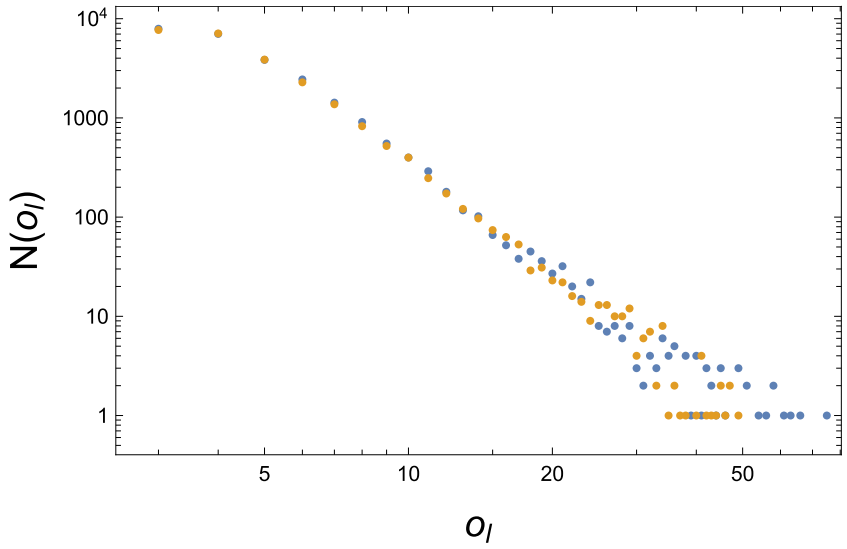

Figure 15. Histograms of the order of links (related to 3D curvature) for $\alpha_t = 0$ (blue) and $\alpha_t = 0.5$ (orange) for a generic configuration in the *C* phase ($\kappa_0 = 2.2$, $\Delta = 0.6$ and $T = 4$).

spatial topology[26] the proposed method permits to define a set of connected 3D hypersurfaces in all spacetime directions. In each direction, these can be viewed as spacetime foliations, similar to those studied in a standard approach with the t time foliation and 3D geometric states formed by tetrahedra. The second question is whether the 3D hypersurfaces satisfy the regular manifold conditions and thus preserve the 3D toroidal topology of the original spatial slices. This implies, for instance, that each triangle belonging to a hypersurface is a face of exactly two tetrahedra. In other words, each tetrahedron should have exactly four neighbors. We analyzed the neighborhood relations between tetrahedra belonging to the hypersurfaces and found that across a triangular face a tetrahedron could have 1, 3, 5 or a larger odd number of neighbors. This means that a triangle could belong, respectively, to 2, 4, 6 or more tetrahedra. Consequently, tetrahedra could have more than four neighbors. Their numbers are always even, and we found cases where the number of neighbors was 14, but larger even values are not excluded. We checked hypersurfaces in the *C* phase for $\alpha_t = 0$ and $\alpha_t = 0.5$. In both cases we measured the Euler characteristic

$$\chi = N_3 - N_2 + N_1 - N_0, \tag{37}$$

(here N_0, N_1, N_2, N_3 are the numbers of vertices, links, faces and tetrahedra forming a given hypersurface $H(\alpha)$) which was large and negative (-208 and -142 respectively). In figure 15 we show distributions of the order of links in the two cases. We also checked the order of vertices. They range up to approximately 1200, see figure 16.

The conclusion at this point is that the new 3D foliation leaves $H(\alpha_t)$ *are not regular manifolds* and that multiple realizations of a sub-simplex with the same set of vertex labels do appear.

[26] Here we consider systems with the toroidal spatial topology, so one can also define boundaries orthogonal to all three spatial directions, but one can study in the described way the scalar field coordinates and foliations in time direction for systems with a spherical or any other spatial topology.

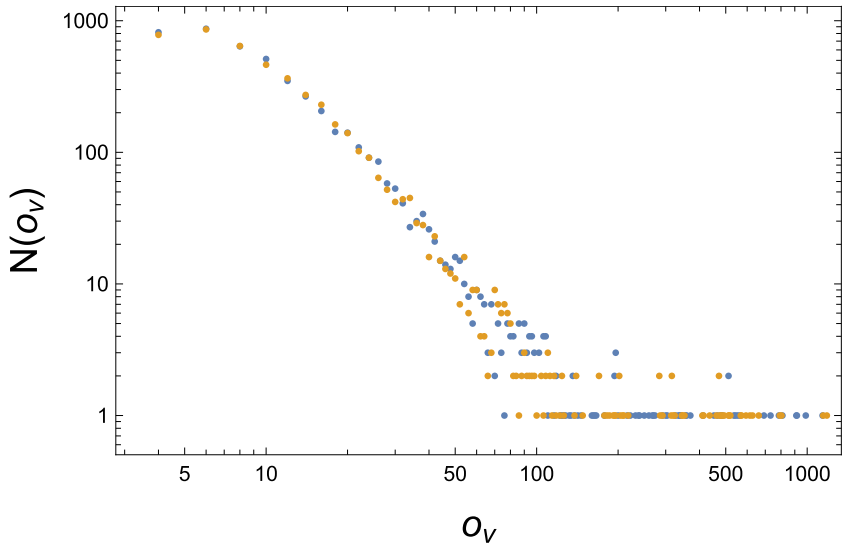

Figure 16. Histograms of the order of vertices for $\alpha_t = 0$ (blue) and $\alpha_t = 0.5$ (orange) for a generic configuration in the *C* phase ($\kappa_0 = 2.2$, $\Delta = 0.6$ and $T = 4$).

However, the connectivity condition is still satisfied. In our Monte Carlo algorithm, we explicitly check the manifold (topology) conditions for the original time foliation into spatial slices. This is apparently not controlled by the Laplace solution of the classical scalar field. Looking also at the spatial directions, one may ask whether the original (locally minimal) boundaries used in our code are free of the topological defects described above. As already said, this is obviously true for the original time foliation, but checking the properties of spatial boundaries one finds that the algorithms we use produce geometric irregularities on boundaries of a similar nature as the α-hypersurfaces. In the code we do not check if such irregularities appear, and indeed they may be produced.

Finally, one may ask the question whether our interpretation of using α_t hypersurfaces (and similar hypersurfaces for α_x, α_y and α_z) as boundaries separating elementary cells is valid? What we mean is that irregularities of such hypersurfaces may lead to a situation where a part of a 4D elementary cell gets disconnected from the bulk by the irregular outgrowth on the hypersurface. We explicitly checked that such a situation never happens, i.e. each elementary cell is fully connected by 4D dual links, which do not cross the hypersurface. In the next subsection we will explain these observations.

4.2. The hypersurfaces $H(\alpha)$ evolved via 3D Pachner moves

Superficially, one may think that the variable α is continuous and that by varying it we get a continuous evolution of the three-hypersurface $H(\alpha)$ defined by the jump of the classical scalar field solution (35). On a discretized manifold this is however not the case. Suppose we analyze the hypersurface $H(\alpha)$ obtained for a particular value of α in one of the four directions, and the range of values for the field for this α is $\epsilon \leqslant \tilde{\phi}_i(\alpha) < 1$, where $\epsilon > 0$ is the minimal value of the field distribution observed at some (single) simplex $i_{\min}$. If then we change α to $\alpha + \Delta\alpha$, where $\Delta\alpha < \epsilon$, it is clear that

$$b(\tilde{\phi}_i(\alpha + \Delta\alpha)) = b(\tilde{\phi}_i(\alpha)), \tag{38}$$

and, consequently, the two hypersurfaces $H(\alpha)$ and $H(\alpha + \Delta\alpha)$ are identical. Only if $\Delta\alpha$ becomes a little larger than ϵ, the value of $b(\tilde{\phi}_{i_{\min}}(\alpha + \Delta\alpha))$ changes, and the simplex $i_{\min}$ is moved to the other side of the boundary. The two hypersurfaces differ only by the position of this single simplex. Let us analyze what it means for the hypersurface $H(\alpha)$. The effect can be viewed as performing one of the so-called 3D Pachner moves on the hypersurface. Let us here recall that for triangulations in d dimensions the Pachner moves are local changes described as follows: consider n d-dimensional simplices in the triangulations, $n = 1, \ldots, d + 1$, which are glued together in such a way that they form a part of the boundary of a $d + 1$-dimensional simplex. The (closed) boundary of the $d + 1$-dimensional simplex has $d + 2 - n$ other d-dimensional simplices, which are also glued together. These two sets of d-dimensional simplices share a boundary consisting of $d - 1$-dimensional simplices. Thus, one can replace the n d-dimensional simplices in the original triangulation with the other $d + 2 - n$ simplices from the boundary of the $d + 1$-dimensional simplex. There are $d + 1$ types of such moves, one for each n. It is clear that this is precisely the situation we have in our case. We are given a hypersurface $H(\alpha)$, i.e. a three-dimensional triangulation. The way we change it is by 'moving' a four-dimensional simplex that contains a certain number of three-simplices of the hypersurface to the other side of the boundary. In other words, we declare that the original three-simplices which belonged both to the hypersurface $H(\alpha)$ and to the given four-simplex do not belong to the hypersurface $H(\alpha + \Delta\alpha)$; instead, it is the other three-simplices of the four-simplex that belong to the new hypersurface $H(\alpha + \Delta\alpha)$: we have moved the four-simplex to the other side of the (new) hypersurface. There are only two problems with this: the Pachner moves can lead to degenerate triangulations (but with the same topology), and they may not lead to a three-dimensional manifold as viewed from the perspective of the embedding space of a given four-dimensional triangulation, as is the situation here. The situation is generic and occurs in any dimension d and the reason is very simple: when performing the Pachner moves, new indices are assigned to the new vertices which were not part of the original d-dimensional simplicial complex. However, if the vertices are already part of a given $d + 1$-dimensional triangulation, and have some labels there, which we do keep, there is a chance that while performing the Pachner move we meet a vertex with the same label several times. This results in a situation where the d-dimensional triangulation may have self-intersections when viewed from the $d + 1$-dimensional triangulation perspective, while from the point of view of Pachner moves in d-dimensions, the self-intersection vertices would have gotten different indices with no reference to an embedding space. This is precisely what we have observed, and we have illustrated the situation in the simplest of all cases, namely $d = 1$, in figure 17.

Consequently, one can conclude that:

- The evolution of a hypersurface $H(\alpha)$ is not continuous in α but can be viewed as a discrete series of modifications of a boundary hypersurface. In each step, one or more simplices of the manifold are moved to the other side of the boundary. This happens only for a discrete set of values of α, which is an effect of the finite system size and of the discreteness of geometry.
- Each shift of the boundary $H(\alpha)$ can be viewed as a result of performing a number of 3D Pachner moves of the boundary.
- $H(\alpha)$ hypersurfaces, viewed as embedded in a 4D CDT manifold, will in general not be 3D manifolds, but they are *almost* manifolds in some sense, since a suitable additional labeling can turn them into 3D manifolds with the topology of three-torus. A lower-dimensional analogy is a crumpled piece of paper smeared with glue, which causes the folding points to stick together.

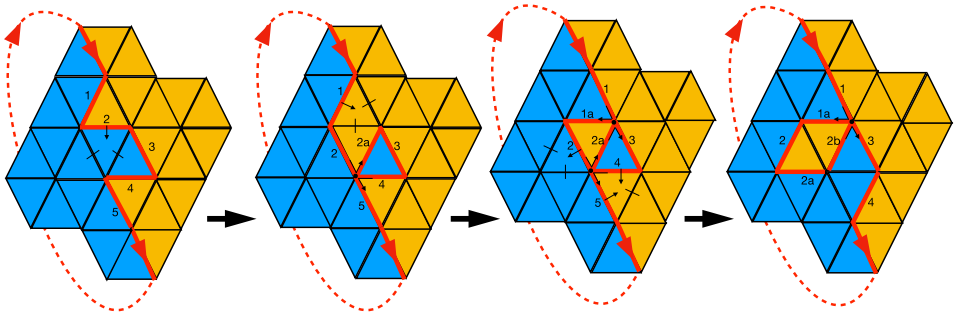

Figure 17. Shown is a part of a triangulation of a two-dimensional torus and a non-contractible boundary. First, we perform a Pachner move to transfer a blue triangle to the other side of the boundary. We thereby create an outgrowth, as seen from the two-dimensional triangulation. The Euler characteristics χ decreases from 0 (the value for a closed curve) to -1, unless (as we would do if we viewed the Pachner move entirely from a one-dimensional point of view) we assign two vertices to the pinching point (or the intersection). In the next move, we create another outgrowth and another pinching point, and the Euler characteristics changes to -2. Finally, the last move removes an outgrowth, but there still remains one outgrowth and the Euler characteristics is -1.

- Our algorithm to modify a (locally minimal) boundary in the 4D setup can also be interpreted in this setting.

To summarize, the interpretation of the change of the hypersurfaces $H(\alpha)$ with α as a sequence of Pachner moves explains the properties of the surfaces that we have observed in subsection 4.1 above[27].

4.3. The spatial volume distribution of the $H(\alpha)$-hypersurfaces

Varying α_t in the range between 0 and 1, for each configuration, one can measure the distribution of $V(\alpha_t)$, defined by equation (36), called here the α_t-*profile*. Below we illustrate the shape of α_t-profiles for generic configurations in different CDT phases, starting with the semi-classical phase C, see figure 18. Values of α in each plot were taken in 100 steps of .01 (so $\alpha_\mu^i \equiv (i-1)/100, i = 1, \ldots, 100$). All measured systems were single configurations with the proper-time coordinate period $T = 4$. In the plots we also show the volume profiles in the original proper-time coordinate (rescaled to fit the [0, 1] range), the t-profiles. We use generalized t coordinates, in which we assign integer t to each (4, 1) simplex and non-integer time coordinates $t + \frac{1}{4}$, $t + \frac{1}{2}$ and $t + \frac{3}{4}$ to the (3, 2), (2, 3) and (1, 4) simplices, respectively, as discussed in section 3.3. The original proper-time foliation (t-profile) volume structure is also apparent in the new α_t-profile function.

One can also measure the covariance function

$$C(\Delta\alpha_\mu) = \frac{1}{\mathcal{N}} \sum_i (V(\alpha_\mu^i) - \bar{V})(V(\mathrm{mod}(\alpha_\mu^i + \Delta\alpha_\mu, 1)) - \bar{V}). \tag{39}$$

[27] It should be noted that in the EDT simulations one usually uses the Pachner moves in a more restricted way, requiring that the moves should only create new triangulations where simplices are uniquely defined by their vertices. That will in general not be the case in an unrestricted use of the Pachner moves. However, even with their unrestricted use the underlying topology of the triangulation is not changed. The spurious change in topology we observe comes entirely from the embedding, as explained above.

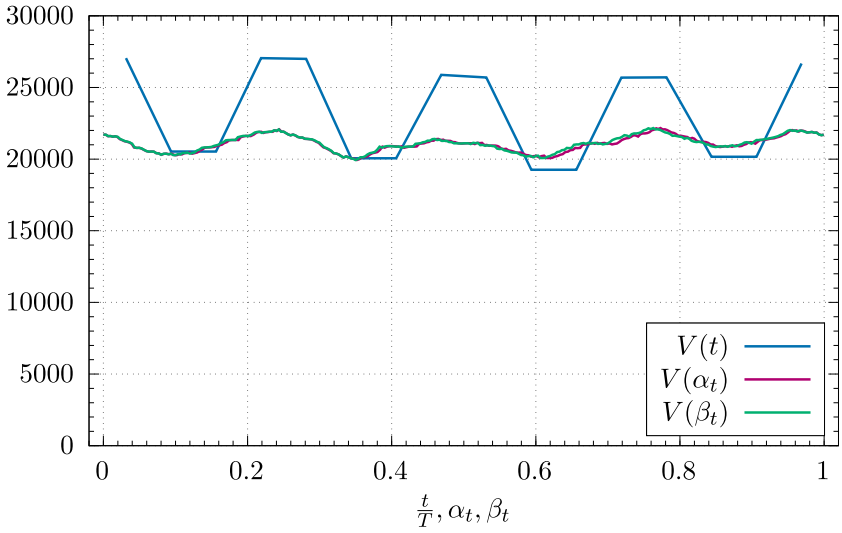

Figure 18. The volumes of α_t and β_t profiles in a single configuration in phase $C(\kappa_0 = 2.2, \Delta = 0.6)$ with $T = 4$, and the corresponding t-profile. The t-profile $V(t)$ was shifted to match the time values corresponding to the maxima of the α_t profile (see figure 14). Note that t variable changes in discrete steps but α_t and β_t change in much smaller steps.

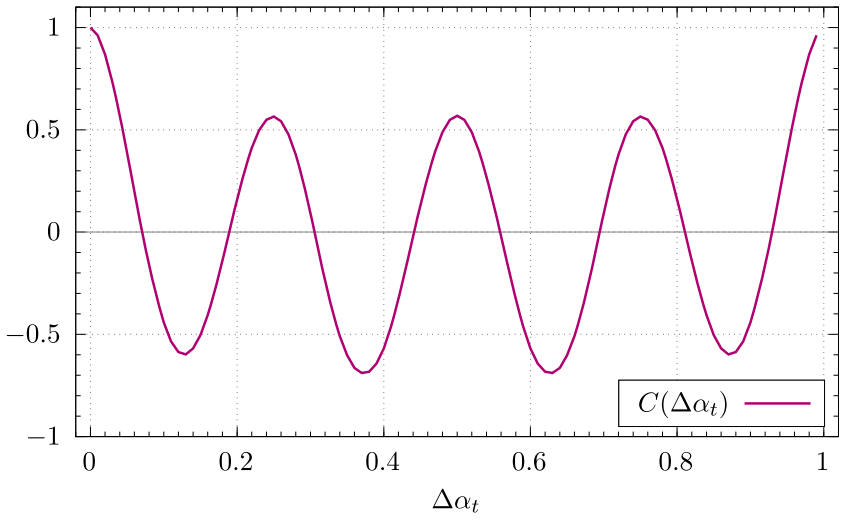

Figure 19. Covariance of the α_t-profile as a function of $\Delta\alpha_t$ (normalized by $C(0) = 1$) in a single configuration in phase $C(\kappa_0 = 2.2, \Delta = 0.6)$ with $T = 4$. Averaging over all initial points produces a relatively smooth curve even for a single configuration.

$C(\Delta\alpha_t)$, normalized to be 1 at $\Delta\alpha_t = 0$, for a single configuration in the C phase is plotted in figure 19. In this plot, the four layers are even more visible. Remember that the steps of α_t are .01, and one has all possible layers ((4, 1), (3, 2), (2, 3) and (1, 4)).

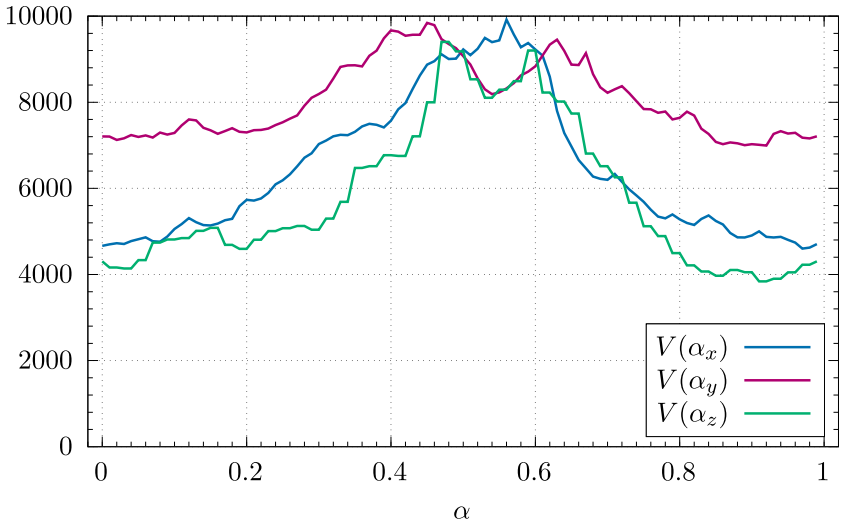

Figure 20. The volumes of α_x, α_y and α_z-profiles in a generic configuration in phase C. The plots were shifted in such a way that the maxima are approximately at $\alpha = 0.5$.

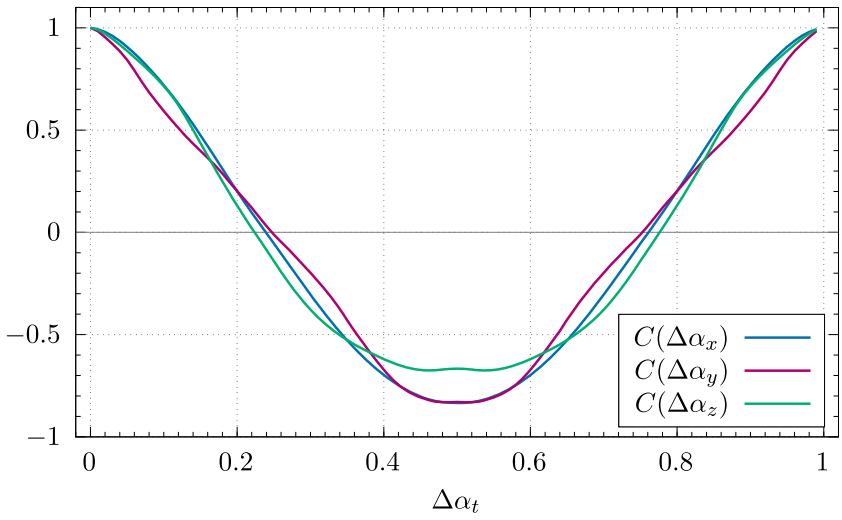

Figure 21. Covariance functions in the x, y, z directions in a generic configuration in phase C, normalized by $C(0) = 1$. Averaging over all initial points produces a relatively smooth curve even for a single configuration.

For the toroidal CDT, the α volume and covariance functions can also be measured in all spatial directions. For illustration, in figure 20 we show (volume) α-profiles and in figure 21 the covariance functions in the three spatial directions for the same configuration in phase C. The profiles can be averaged over many measured configurations, which may eventually lead to the reconstruction of the effective CDT action, now not only in time (as it was done for the original t coordinate) but also in the spatial directions.

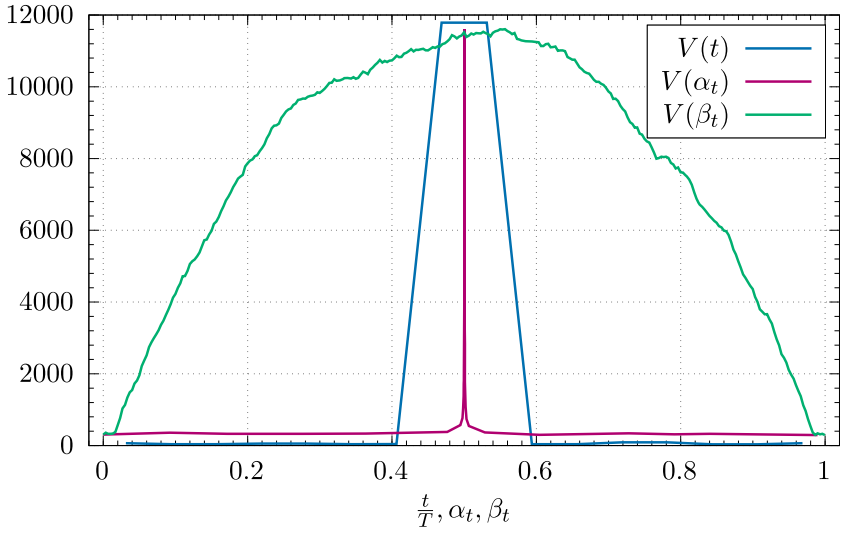

Figure 22. The volumes of α_t and β_t profiles in a single configuration in phase $B(\kappa_0 = 4.4, \Delta = -0.07)$ with $T = 4$, and the corresponding t-profile. Both profiles were shifted to place the maxima in the center of the plot. The t-profile $V(t)$ was additionally scaled by a factor 0.15. Superficially, the t-profile looks wider than the α_t-profile, but this simply results from a low 'resolution' of the t-profile which takes only $4 \times T = 16$ values in the time direction.

As can be seen from the volume α-profile functions, the spatial distributions are concentrated around a certain value of α_μ^i, and consequently the covariance functions in the spatial directions look different than the one in the time direction. Interpretation of these results requires further studies.

Similar plots for the α_t-profiles in phases B and C_b are shown in figures 22 and 23. One can see the appearance of time compactification in the B phase and the typical saw-like volume structure in the C_b phase, although in this case the α_t-profile seems distorted compared to the t-profile. We will return to this in the next subsection.

4.4. The spatial volume distributions in the β-parametrization

By means of equations (33) and (34) in section 3.3 we introduced the β-coordinates, which, as we will now argue, are useful for measuring distances between the different foliation leaves $H(\alpha)$. Let us consider the evolution of a boundary between $\alpha = 0$ and $\alpha = 1$. One can see that for increasing α, gradually all the simplices in the manifold are moved from one side of the boundary to the other. It is tempting to define a distance between two boundaries at different values of α as the number of transfers of simplices necessary to evolve the boundary α into the boundary α'. For each α we may define $\beta(\alpha)$ as the number of transfers between the $\alpha = 0$ boundary (where $\beta = 0$) and the α boundary, normalized by the total number of simplices N_4. Note that this is exactly equivalent to the definition of β used in section 3.3 (equation (34)) if we set $\beta(\alpha) = \beta_i$, where i is the index (field position) in the sorted list (33) of a simplex that joins the $H(\alpha)$ hypersurface at a given step of the boundary evolution. The new parameter β is again in the range $0 \leqslant \beta < 1$ and can easily be measured for any configuration in each direction. In figure 24 we show β_t as a function of α_t (the index denotes again the time direction) in a configuration in phase C. One can see that the two definitions coincide

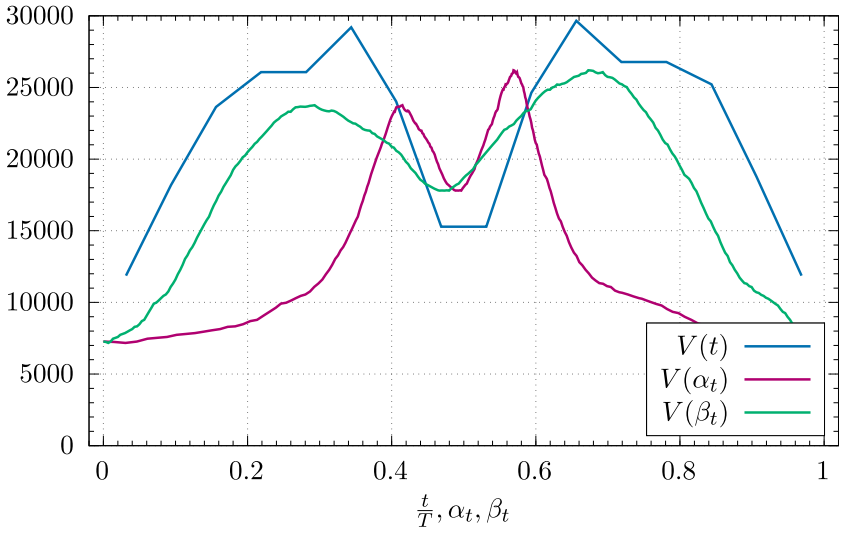

Figure 23. The volumes of α_t and β_t profiles in a single configuration in phase $C_b(\kappa_0 = 2.0, \Delta = 0.1)$ with $T = 4$, and the corresponding t-profile.

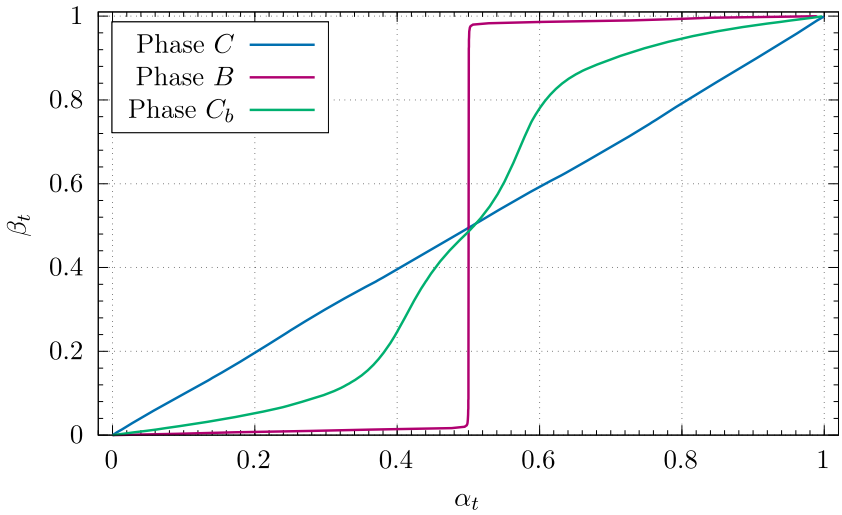

Figure 24. β_t as a function of α_t in a configuration in phases C, B and C_b.

in this case, and in practice $\beta_t \approx \alpha_t$. Consequently, the β_t-profile is almost identical to the α_t-profile, as shown in figure 18. This is different in other phases. A plot of β_t as a function of α_t in a configuration in phase B is shown in figure 24. In this case, the whole change in β_t is concentrated in a very narrow neighborhood of $\alpha_t \approx 0.5$, for which value we observe a blob in the α_t-profile (conf. figure 22). As a result, almost all boundary transfers happen in this neighborhood, and the distribution of $V(\beta_t)$ is completely different than that of $V(\alpha_t)$. The difference is conspicuous in figure 22, where the narrow peak in the α_t-profile is greatly expanded in the new β_t parametrization. In the C_b phase, the relation between α_t and β_t is

different yet again non-trivial, as exemplified in figures 24 and 23. Both the peaks of the α_t-profile are squeezed in a part of the [0, 1) range, leaving the rest of the profile much flatter, whereas the β_t-profile is much more regular.

5. Dynamical scalar fields

The simplest quantum matter which can be added to the quantum geometry of CDT is a scalar field. Models of this type were studied in EDT and CDT, mostly for the spherical spatial topology but recently also for the toroidal spatial topology. For such models, the lattice regularized path integral of quantum gravity (2) includes also an integral over scalar fields ϕ:

$$\mathcal{Z}_{\rm CDT} = \sum_{\mathcal{T}} \int \mathcal{D}[\phi] \mathrm{e}^{-\left(S_{\rm R}[\mathcal{T}]+S_{\rm M}[\{\phi\},\mathcal{T}]\right)}. \tag{40}$$

The dynamical scalar field ϕ was in all cases located in the simplices, and the following action of a massless field was considered:

$$S_{\rm M}[\{\phi\},\mathcal{T}] = \frac{1}{2}\sum_{i\leftrightarrow j}(\phi_i-\phi_j)^2 = \sum_{i,j}\phi_i L_{ij}\phi_j, \tag{41}$$

where, in the 4D case, the discrete Laplacian is given by

$$L_{ij} = 5\delta_{ij} - A_{ij}, \tag{42}$$

with $A_{ij} = 1, 0$ being the symmetric adjacency matrix on the dual lattice; see section 3 for a discussion. The Gaussian form of the field means that in principle the field can be integrated out using the flat measure

$$\mathcal{D}[\phi] = \prod_i{}' \frac{\mathrm{d}\phi_i}{\sqrt{\pi}}, \tag{43}$$

contributing to the geometric action $S_{\rm R}[\mathcal{T}] \to S_{\rm R}[\mathcal{T}] + S^{\rm eff}_{\rm quant}[\mathcal{T}]$ a term

$$S^{\rm eff}_{\rm quant}[\mathcal{T}] = \frac{1}{2}\,\log\,\det(\mathbf{L}'(\mathcal{T})), \tag{44}$$

where $\mathbf{L}'(\mathcal{T})$ is the Laplacian matrix $\mathbf{L}(\mathcal{T})$ in the subspace orthogonal to the constant zero-mode of $\mathbf{L}$. In the measure we also eliminate the integration over the zero mode (hence the 'prime' index in equation (43)). The dependence on geometry sits in the dependence of $\mathbf{L}'(\mathcal{T})$ on the adjacency matrix $\mathbf{A}$ defined for a given triangulation $\mathcal{T}$, which is modified by geometric moves. The dynamical field ϕ can be rescaled $\phi \to \lambda\phi$, but this rescaling can be eliminated by the change of measure and in effect included in the redefinition of the cosmological constant.

To summarize the results of our earlier research: the inclusion of an interaction of geometry with the massless scalar field(s) did not change the geometric properties observed without such fields, at most shifting values of the coupling constants by finite numbers [11]. Including a potential (like a mass term) suppresses field fluctuations but also does not lead to a visible change of the geometric phase structure. We also tried to increase the number of scalar fields, considering several copies of the field

$$S_{\rm M}[\{\phi\},\mathcal{T}] \to \sum_{\mu} S_{\rm M}[\{\phi^\mu\},\mathcal{T}]. \tag{45}$$

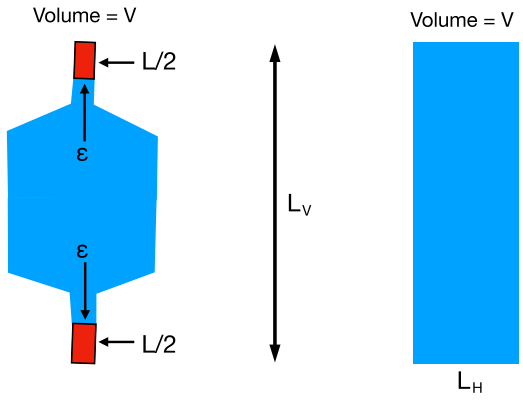

Figure 25. Left: a pinched torus with the opposite sides identified. Going from the bottom to the top, ϕ increases from 0 to δ; specifically, in the lower red part it changes from 0 to $\delta/2$, in the blue region it stays constant and equal to $\delta/2$, and in the upper red part it changes from $\delta/2$ to δ. ϕ is constant in the horizontal direction. The volume of the red region, the only region of the field change, is $L \cdot \epsilon$. Right: a torus where ϕ is constant in the horizontal direction and uniformly increases from 0 to δ from bottom to top. The two tori are assumed to have the same vertical length $L_{\rm V}$ and the same volume V (which for the right figure can be written as $V = L_{\rm V} L_{\rm H}$).

The effect was the same as with a single scalar field. We conclude that the dependence of the determinant $S^{\rm eff}_{\rm quant}[\mathcal{T}]$ on $\mathcal{T}$ is weak and, in practice, we can treat it as a constant.

5.1. Jumps

The new aspect introduced in [43] and studied in detail here is based on two major generalizations of the CDT model:

- The spatial topology was chosen to be toroidal T^3. Effectively the topology is toroidal T^4 since we also assume periodicity in the time direction. The system can be treated as infinite, with the elementary cell repeated periodically in four directions.
- The scalar field was defined as taking values on a circle of circumference δ rather than in $\mathbb{R}$ and forced to wind around the circle when moving around a non-contractible loop in one of the directions on T^4. This can alternatively be viewed as a field taking values in $\mathbb{R}$ with a jump of magnitude δ when crossing the (unphysical) boundary of an elementary cell; see section 3 for details.

The latter modification thoroughly changes the dynamics of the geometry–matter interaction[28]. Previously, for the $\mathbb{R}$-valued scalar field without jumps imposed, the constant field configuration (i.e. the classical solution) resulted in the absolute minimum (zero) of the matter action. Now, this solution with a zero winding number is excluded, yet there is a way of rearranging the geometry that makes the action decrease virtually to zero. For an illustration in the simple case of a two-dimensional torus see figure 25. The argument is independent of the number of dimensions as long as at least one direction is periodic.

[28] Scalar fields with non-trivial winding numbers may arise in topological configurations of gauge and Higgs fields in GUT theories.

The left-hand side picture shows a torus with volume V and vertical length $L_{\rm V}$, which is pinched to a cylinder of circumference ϵ and length L. The scalar field winds once around a circle of circumference δ when we move around a non-contractible loop in the vertical direction, or, equivalently, the field jumps by δ when passing a boundary between the lower and the upper edge of the picture (the opposite sides of the picture are identified). We consider a specific field configuration, where the field ϕ changes uniformly from 0 to $\delta/2$ over a distance $L/2$ in the lower red part, stays constant and equal to $\delta/2$ in the blue part and changes from $\delta/2$ to δ in the upper red part. The region where the field changes is joined smoothly to the region where it is constant. The total matter action of this field configuration is

$$S_{\rm M}[\{\phi\},\delta,\mathcal{T}_{\rm L}] = \left(\frac{\delta}{L}\right)^2 L\,\epsilon = \delta^2\frac{\epsilon}{L}, \tag{46}$$

and the minimal action for a classical field configuration for this geometry is even lower[29]. Clearly, this value can be made arbitrarily small when $\epsilon \to 0$, and this is even more true in higher dimensions. The right-hand side picture in figure 25 also shows a torus with volume V and vertical length $L_{\rm V}$. For this geometry, the action is minimal for a field changing uniformly from 0 to δ when we move from bottom to top, and is equal to

$$S_{\rm M}[\{\phi\},\delta,\mathcal{T}_{\rm R}] = \left(\frac{\delta}{L_{\rm V}}\right)^2 L_{\rm V}L_{\rm H} = \delta^2\frac{V}{L_{\rm V}^2}, \quad V = L_{\rm H}L_{\rm V}, \tag{47}$$

which is bounded from below when V and $L_{\rm V}$ are fixed. Let us discuss the consequence of this for the full quantum theory. We consider the action of a single scalar field,

$$S_{\rm M}[\{\phi\},\delta,\mathcal{T}] = \frac{1}{2}\sum_{i\leftrightarrow j}(\phi_i-\phi_j-\delta B_{ij})^2 = \sum_{i,j}\phi_i L_{ij}\phi_j - 2\delta\sum_i \phi_i b_i + \delta^2\cdot V. \tag{48}$$

Here $B_{ij} = \pm 1$, when the boundary face $i \to j$ is crossed in the positive (negative) direction, and $B_{ij} = 0$ otherwise; $b_i = \sum_j B_{ij}$ and $V = \frac{1}{2}\sum_{i,j} B_{ij}^2$. Note that now the size of the jump δ fixes the scale of the field ϕ. The action (48) is still Gaussian but with a linear term. Like before, the field ϕ can be integrated out. We use the standard method to eliminate the term linear in ϕ by a shift. We decompose the field into the classical part $\bar{\phi}_i$ and the quantum part ξ_i:

$$\phi_i = \bar{\phi}_i + \xi_i. \tag{49}$$

Since both ϕ_i and $\bar{\phi}_i$ have winding number 1, the fluctuation field ξ_i is a scalar field with winding number 0, like an ordinary scalar field taking values in $\mathbb{R}$. We modify the integration measure

$$\mathcal{D}[\phi] = \mathcal{D}[\xi] \tag{50}$$

[29] Note that the field configuration used in (46), even if smoothly joining the regions where ϕ changes and where ϕ is constant, will in general fail to satisfy Laplace's equation, i.e. it will not have the minimum value of the action (41). We only use it to show that by changing geometry the actual solution to Laplace's equation with winding number 1 can be made arbitrarily small. On the other hand, the solution ϕ used in (47) is the minimum for the given geometry since it has winding number 1 and satisfies Laplace's equation.

and rewrite the action (48) as

$$S_{\mathrm{M}}[\{\phi\},\delta,\mathcal{T}] = \sum_{i,j}\xi_i L_{ij}\xi_j + \sum_{i,j}\bar{\phi}_i L_{ij}\bar{\phi}_j - 2\delta\sum_i \bar{\phi}_i b_i + \delta^2\cdot V$$
$$= \sum_{i,j}\xi_i L_{ij}\xi_j + S_{\mathrm{M}}[\{\bar{\phi}\},\delta,\mathcal{T}]. \tag{51}$$

After integrating out the quantum field, we see that now the field with a jump contributes to the geometric action

$$\tilde{S}^{\mathrm{eff}}_{\mathrm{quant}}[\mathcal{T},\delta] = S^{\mathrm{eff}}_{\mathrm{quant}}[\mathcal{T}] + \Delta S^{\mathrm{eff}}[\mathcal{T},\delta], \quad \Delta S^{\mathrm{eff}}[\mathcal{T},\delta] = S_{\mathrm{M}}[\{\bar{\phi}\},\delta,\mathcal{T}]. \tag{52}$$

The extra correction term $\Delta S^{\mathrm{eff}}[\mathcal{T},\delta]$ is nothing else than the scalar field action (48) evaluated at the classical solution $\bar{\phi}$. It can be written in many equivalent ways, e.g.

$$\Delta S^{\mathrm{eff}}[\mathcal{T},\delta] = -\delta\sum_i \bar{\phi}_i b_i + \delta^2\cdot V$$
$$= -\delta^2\sum_{i,j}\left(b_i\tilde{L}^{-1}_{ij}b_j - \frac{B^2_{ij}}{2}\right)$$
$$= -\frac{1}{2}\sum_{i,j}\delta B_{ij}(\bar{\phi}_i - \bar{\phi}_j - \delta B_{ij}), \tag{53}$$

where we used the fact that the classical field $\bar{\phi}$ satisfies

$$\sum_j L_{ij}\bar{\phi}_j = \delta\cdot b_i, \quad \bar{\phi}_i = \delta\sum_j \tilde{L}^{-1}_{ij}b_j. \tag{54}$$

It is worth mentioning that, according to (53), the action $S_{\mathrm{M}}[\{\bar{\phi}\},\delta,\mathcal{T}]$ of the classical solution $\bar{\phi}$ can be written entirely in terms of the values of $\bar{\phi}_i$ next to the boundary with the jump, despite the fact that the action itself is independent of the precise location of the boundary. The purely quantum contribution $S^{\mathrm{eff}}_{\mathrm{quant}}[\mathcal{T}]$ is thus exactly the same as for the case with no jump ($\delta = 0$) and the (purely classical) correction $\Delta S^{\mathrm{eff}}[\mathcal{T},\delta] = S_{\mathrm{M}}[\{\bar{\phi}\},\delta,\mathcal{T}]$ is quadratic in the jump size δ. We now have the following situation: for a given geometry, i.e. a given triangulation $\mathcal{T}$, the contribution from the quantum fluctuations of the scalar field is the same whether the scalar field takes value in $\mathbb{R}$ (and thus just fluctuates around 0) or in a circle S^1 of circumference δ (and fluctuates around the classical solution $\bar{\phi}_i$ with winding number 1). However, in the latter case the minimum of the classical action $S_{\mathrm{M}}[\{\bar{\phi}\},\delta,\mathcal{T}]$ depends in a crucial way on the triangulation $\mathcal{T}$. Triangulations that are pinched as shown in figure 25 have the smallest matter action but, in general, the geometric Regge (Einstein–Hilbert) part of the action is larger for them than for non-pinched triangulations. Thus, there is a competition between matter and the geometric action. In the case of a scalar field winding around the time direction, this can easily be illustrated using a simple minisuperspace approximation. We refer to appendix A3 for details. The conclusion is that for a small jump magnitude $\delta < \delta_{\mathrm{c}}$, the geometric part of the action prevails, and generic triangulations in the path integral are quite similar to the ones that dominate when no matter field with a jump is present. However, for a large jump magnitude $\delta > \delta_{\mathrm{c}}$, the total (geometric + matter) action is the lowest for pinched triangulations, and the system fluctuates around them. Thus, we have a picture where for small $\delta < \delta_{\mathrm{c}}$, the effect of the scalar field is small, and we can say that the scalar field couples to and follows

the geometry. However, when $\delta > \delta_c$, the scalar field pinches the geometry to a spatial volume which is small or maybe even zero, and (almost) all changes of ϕ take place in this region of very small volume. Thus, ϕ basically splits a spacetime with a non-trivial winding number in the time direction into two parts: one (of cutoff size) with a nonzero winding number and one (dominating) with a zero winding number. Therefore, for $\delta = \delta_c$ we should observe a new type of a phase transition caused entirely by the scalar field, a phase transition in which the effective spacetime topology can change from toroidal to a simply connected one. This analysis is of course based on a very simple minisuperspace action (see appendix A3), which might be a good description in the time direction but not necessarily in the spatial directions, where there is no minisuperspace approximation. Therefore we now turn to numerical Monte Carlo simulations. In section 5.2 we discuss the case of an S^1 scalar field in the time direction in CDT with the T^3 spatial topology[30]. Then, in section 5.3 we investigate the case of three scalar fields winding around spatial directions.

5.2. Results for a single scalar field with a jump in the time direction

Below we present the results obtained for one dynamical scalar field with a jump of magnitude δ, or, in other words, a scalar field taking values in a circle of circumference δ in the time direction. All measured systems were toroidal CDT configurations inside the semiclassical C phase region ($\kappa_0 = 2.2$, $\Delta = 0.6$), and the Monte Carlo simulations were performed for the lattice volume $N_{4,1} = 160$k and the proper-time periods $T = 10$ and $T = 20$. In the Monte Carlo code, the jump was effectuated on the crossing between the $t = T$ and the $t = 1$ (periodic) proper-time coordinate, i.e. between the field values inside the $(1, 4)$ simplices (with 1 vertex in $t = T$ and 4 vertices in $t = 1$) and the $(4, 1)$ simplices (with 4 vertices in $t = 1$ and 1 vertex in $t = 2$), so that the time-boundary was the spatial slice in the layer $t = 1$.[31] Spatial volume t-profiles (in the original t coordinate: $V(t) =$ number of tetrahedra in a spatial slice t) for single generic configurations with several different jump magnitudes $\delta = 1, 2, 4, 8$ are presented in figure 26. To facilitate the comparison, the profiles measured for various δ were shifted in the (periodic) proper-time axis so that the maxima are placed at the centers of the charts.

For small jump magnitudes ($\delta = 1, 2$) one observes flat volume profiles characteristic for toroidal CDT in the pure gravity case (i.e. without the scalar field), while for large jump magnitudes ($\delta = 4, 8$) the volume profiles are completely changed, showing the blob-like configurations (somewhat similar to the left-hand side picture in figure 25). The pinching becomes more pronounced for larger T. In view of the discussion in the last subsection, this is very understandable. With the same four-volume V, it is a larger deformation of the geometry to perform a pinching of $V(t)$ to small values if T is small and thus the minimal value of $V(t)$ is larger. Figure 26 also provides a clear illustration of the fact that the precise location of the hypersurface where the scalar field jumps has no effect on the interaction between the scalar field and the geometry. In the figure we have shown the location of the jump in the numerical code, and it is clearly unrelated to the position of the region where the geometry is pinched by the scalar field, even though when looking at equation (53) (as already mentioned there) one

[30] We stated above that in this situation the phenomenon of pinching should be independent of the spatial topology. This is presumably true. However, we might fail to discern it if the spatial topology is S^3 and the system is in the semiclassical phase C. The reason is that in this case we generally already have a geometric pinching, in fact a whole 'stalk' of cut-off size width, even without a scalar field. In that situation there will be no problem for the scalar field to produce a jump of δ in the stalk, and there should not be any real difference in the effect of a scalar field with values in $\mathbb{R}$ and a scalar field with values in S^1 and a non-trivial winding number.

[31] As already discussed, the formulation is independent of the boundary position, and thus one could as well use any other spatial layer or a more complicated boundary in time direction.

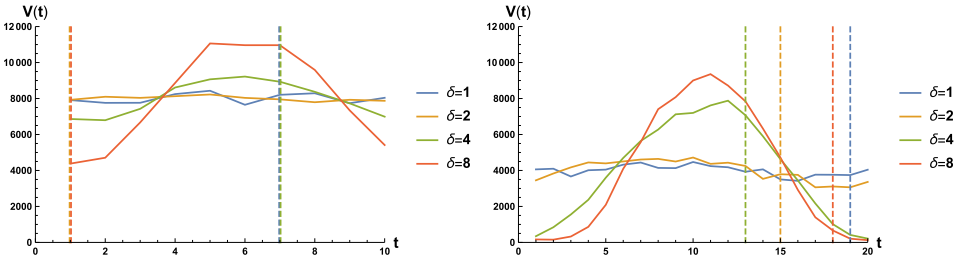

Figure 26. Spatial volume t-profiles in single generic configurations inside the semi-classical phase C ($\kappa_0 = 2.2, \Delta = 0.6$) for $T = 10$ (left) and $T = 20$ (right) with scalar field jump magnitudes $\delta = 1, 2, 4, 8$. For each configuration the position of a jump of the scalar field is denoted by a dashed vertical line.

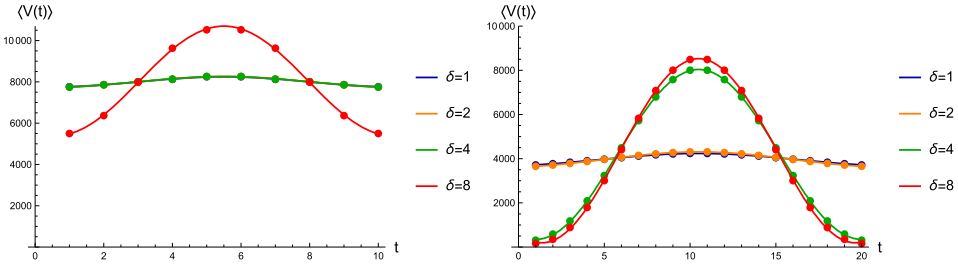

Figure 27. Spatial volume t-profiles averaged over many MC configurations inside the semiclassical phase C ($\kappa_0 = 2.2, \Delta = 0.6$) for $T = 10$ (left) and $T = 20$ (right) with scalar field jump magnitudes $\delta = 1, 2, 4, 8$. Error bars for measured data points were estimated using single-elimination (binned) jacknife procedure (for most points they are below the resolution of the plots). Solid lines are fits of the function: $c + a\cos(b(t - t_0))$. In the left plot, the curves for $\delta = 1, 2, 4$ overlap within the picture resolution.

could be misled to think that all physics of the classical scalar field is related to the location of the jump.

Figure 27 presents the volume profiles averaged over many Monte Carlo configurations. In order to get rid of the time-translation symmetry (the center of volume of each configuration can perform a random walk around the periodic time axis), the center of volume of each individual t-profile was shifted to a universal position $t_0 = T/2 + 0.5$. Because of this shifting, one can observe artificial small 'blobs' for small jump magnitudes ($\delta = 1, 2$). Nevertheless, it is easily seen that the phase transition takes place above $\delta = 4$ for $T = 10$ and above $\delta = 2$ for $T = 20$, respectively. Figure 27 also contains fits of the cosine relation resulting from the minisuperspace model discussed in appendix A3. It is remarkable that despite our computer generated data are based on the full non-perturbative model including all microscopic degrees of freedom, the averaged profiles (obtained after integrating out all degrees of freedom but the scale factor) are so well explained by the simple minisuperspace approximation, where the scale factor (time dependence) is the only dynamical variable.

5.3. Results for three scalar fields with one or more jumps in spatial directions

This subsection presents the results obtained for dynamical scalar fields with jumps in spatial directions. In each case, the system contained three scalar fields, and we could adjust the jump

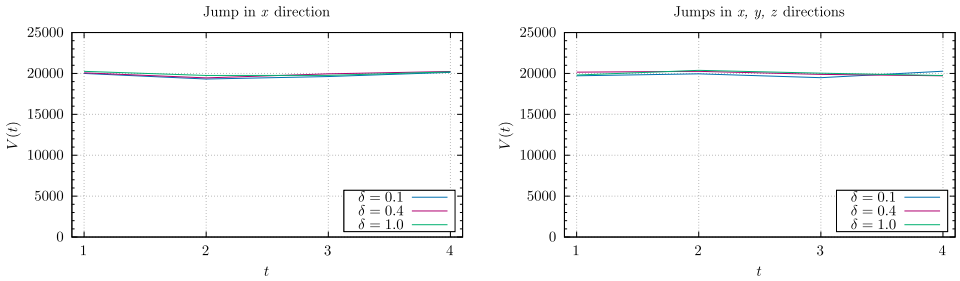

Figure 28. Spatial volume t-profiles in single generic configurations inside the semiclassical phase C ($\kappa_0 = 2.2, \Delta = 0.6$) for $T = 4$ and with dynamical scalar fields with jump in one spatial direction (left) and in three spatial directions (right).

magnitudes $\delta_1, \delta_2, \delta_3$. In the Monte Carlo code, the jump of each scalar field was realized when crossing a 3D boundary orthogonal to one of three independent non-contractible loops winding around the toroidal spatial directions. In practice, we measured systems where one, two, or all three fields had the same jump magnitude δ, i.e. where: (1) $\delta_1 = \delta, \delta_2 = \delta_3 = 0$, (2) $\delta_1 = \delta_2 = \delta, \delta_3 = 0$ or (3) $\delta_1 = \delta_2 = \delta_3 = \delta$, for various choices of δ. Therefore, one can view the systems as having $n = 1, 2$ or 3 scalar fields taking values on a circle of circumference δ and having winding number 1, and the remaining $3 - n$ fields taking values in $\mathbb{R}$ (with no winding number imposed). The analyzed systems were all at the same point ($\kappa_0 = 2.2, \Delta = 0.6$) in the semiclassical C phase, with the volume $N_{4,1} = 160$k and the number of time slices $T = 4$ (in the end of this subsection we also present results for a larger system with $N_{4,1} = 720$k and $T = 20$, obtained at the point ($\kappa_0 = 4.0, \Delta = 0.2$), also inside the C phase).

For the sake of order, we start our analysis with the spatial volume t-profiles for a single generic configuration observed for the cases when the field jumps in one or three spatial directions. In this case, as can be seen in figure 28, one does not observe the pinching effect in the volume profiles even for the largest measured scalar field jump magnitude δ, but this is most likely due to the very small extent of the periodic time axis (fixed at $T = 4$), which prevents blob-like volume profiles from forming (as we will show later, such non-trivial volume profiles can be observed for larger $T = 20$).[32]

To extract more information about the (change in) geometric structure caused by the dynamical scalar field(s) with a certain (large) jump magnitude, one can repeat the analysis of section 3, i.e. define coordinates given by the classical scalar field solutions in all spatial and time directions. To facilitate comparison with the results for the pure gravity case presented in sections 3 and 4, we rescaled the obtained solutions to the classical Laplace's equation (19) to get the standard jump magnitude ($\delta = 1$) independently of the actual jump magnitude of the dynamical scalar field(s) δ. This can be interpreted as introducing *new independent classical fields* $\bar{\phi}^\mu(\delta = 1)$ on top of the dynamical fields $\phi^\mu(\delta)$ or, alternatively, as computing the (rescaled) *expected value of the dynamical field(s)*

$$\langle \phi^\mu(\delta) \rangle \equiv \delta \cdot \bar{\phi}^\mu(\delta = 1). \tag{55}$$

[32] A similar behavior was earlier observed in the spherical CDT pure gravity case, where the blob-like volume profile resulting from a non-trivial minisuperspace effective potential term could be observed only for large enough T. For small T the observed volume profile was flat, but one could still measure the same effective potential term as for large T.

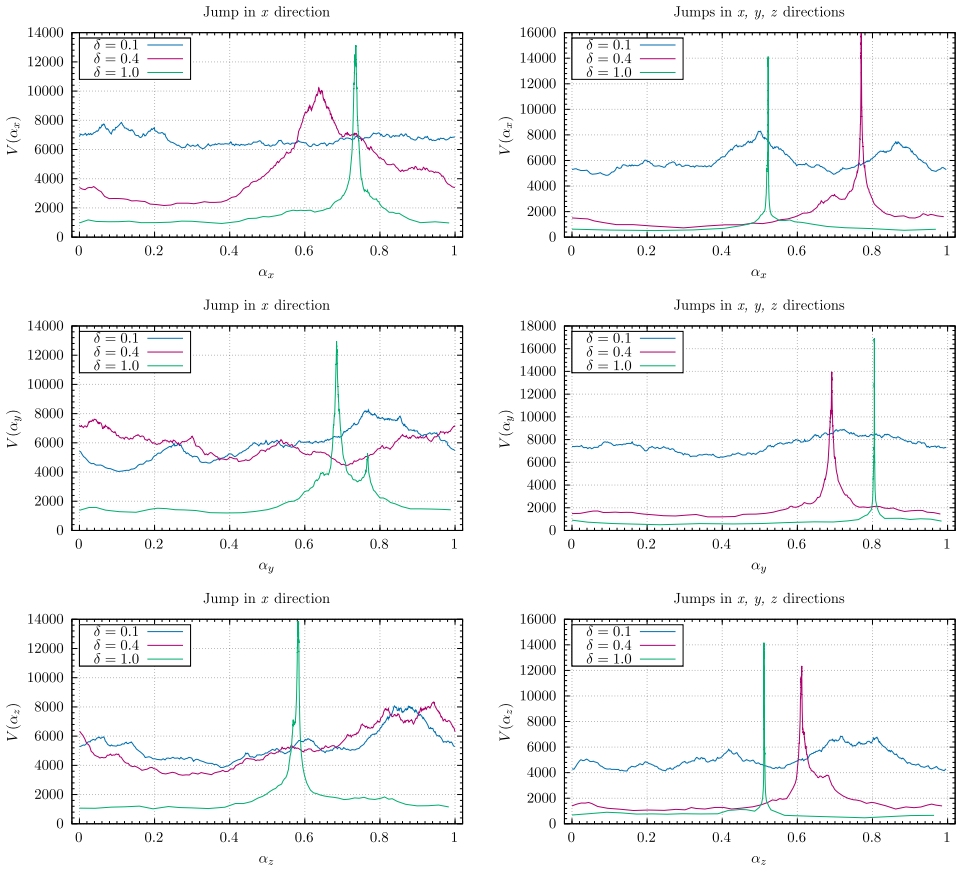

Figure 29. α_x- (top), α_y- (middle) and α_z- (bottom) profiles in the x, y, z directions in single generic configurations inside the semiclassical phase C ($\kappa_0 = 2.2, \Delta = 0.6$) for $T = 4$ and with dynamical scalar fields with jump in one spatial direction (left) and in three spatial directions (right).

This way one can, for example, measure the α-profiles not only in time but also in the spatial directions (see section 4 for discussion). The α-profiles in spatial directions, presented in figure 29, are visibly pinched for large jump magnitudes, and the effect depends on the number of fields with a jump. It is also readily seen that in the case where the jump of the field takes place only in one spatial direction, say x, the blob-like volume profiles in the (orthogonal) spatial directions y and z are also observed for a large value of the jump ($\delta = 1.0$), as in the left-hand side plots of figure 29. This is a strong evidence that the observed effect results from a genuine pinching of geometry caused by the scalar field(s) winding around a circle, as discussed above, the effect being clearly stronger for more numerous scalar fields with a jump (conf. the right-hand side plots in figure 29).

Using the classical scalar field solutions as coordinates, one can also measure the density maps defined in section 3.3 and observe if and how they are affected by dynamical scalar fields. Figure 30 presents the density maps projected on the $t - x$ plane, and figure 31 shows the density maps projected on the $x - y$ plane. The system has three scalar fields with either one jump in the x direction only (left-hand side charts) or three jumps in all three spatial directions

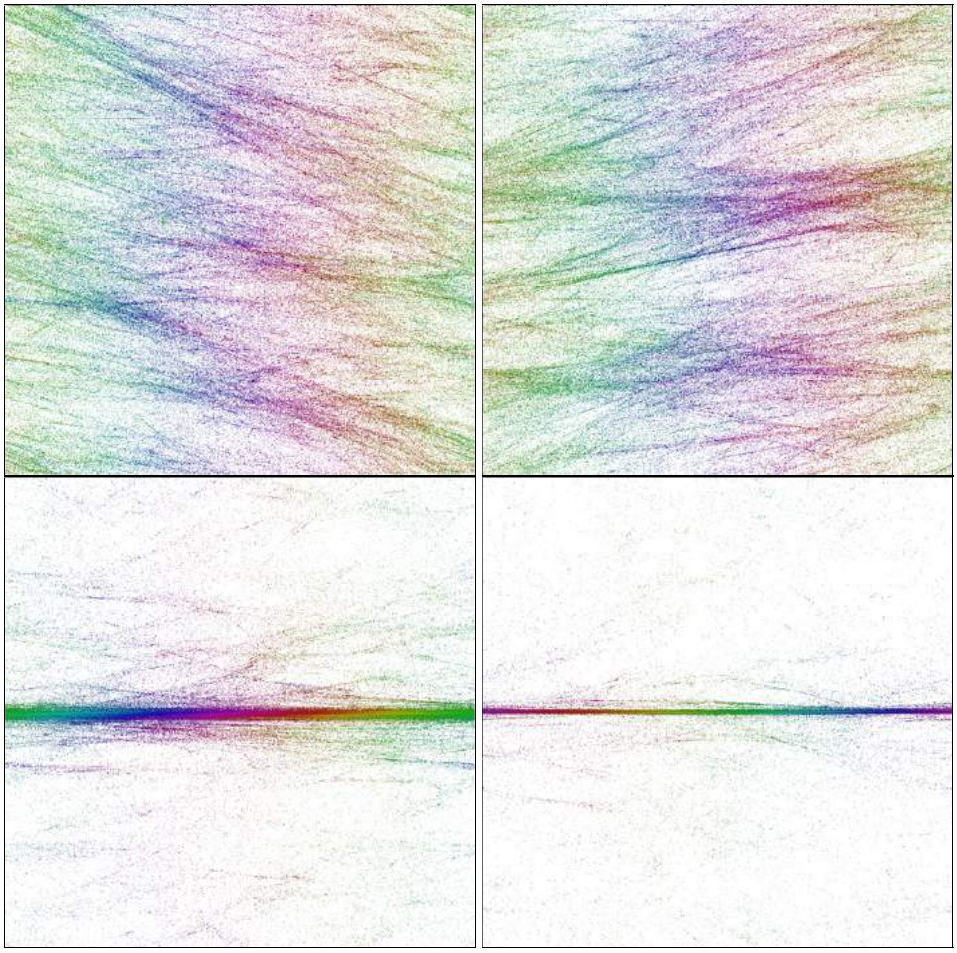

Figure 30. Density maps in $\bar{\phi}$ coordinates (for the definition see section 3.3) representing the effect of the spatial pinch in $t-x$ directions for configurations in phase C ($\kappa_0 = 2.2, \Delta = 0.6$) with $T = 4$. The left-hand side charts are for a single jump in x direction and the right-hand side charts are for three jumps in all spatial directions. Top: configurations with a small jump magnitude ($\delta = 0.1$). Bottom: configurations with a large jump magnitude ($\delta = 1.0$).

(right-hand side charts). For small jump magnitudes (top plots), one observes in all directions the cosmic void and filament structures, which look qualitatively the same as in the pure gravity case (see figure 6 for comparison). For large jump magnitudes (bottom plots), the density maps qualitatively change as the geometry gets effectively compressed to a single outgrowth in all spatial directions (as already discussed, for $T = 4$ the time direction is not compressed), the effect visibly increasing in strength with the number of scalar fields with a jump. These results are easily explicable by the pinching phenomenon discussed above.

To illustrate this, let us analyze a simple 2D example, where a fractal geometry can be compared to a toroidal balloon with outgrowths, as shown in figure 32. For the pure gravity case (and for a small jump magnitude), the geometry typically looks like in the left plot with a large central part and a number of relatively small outgrowths. The scalar fields with large

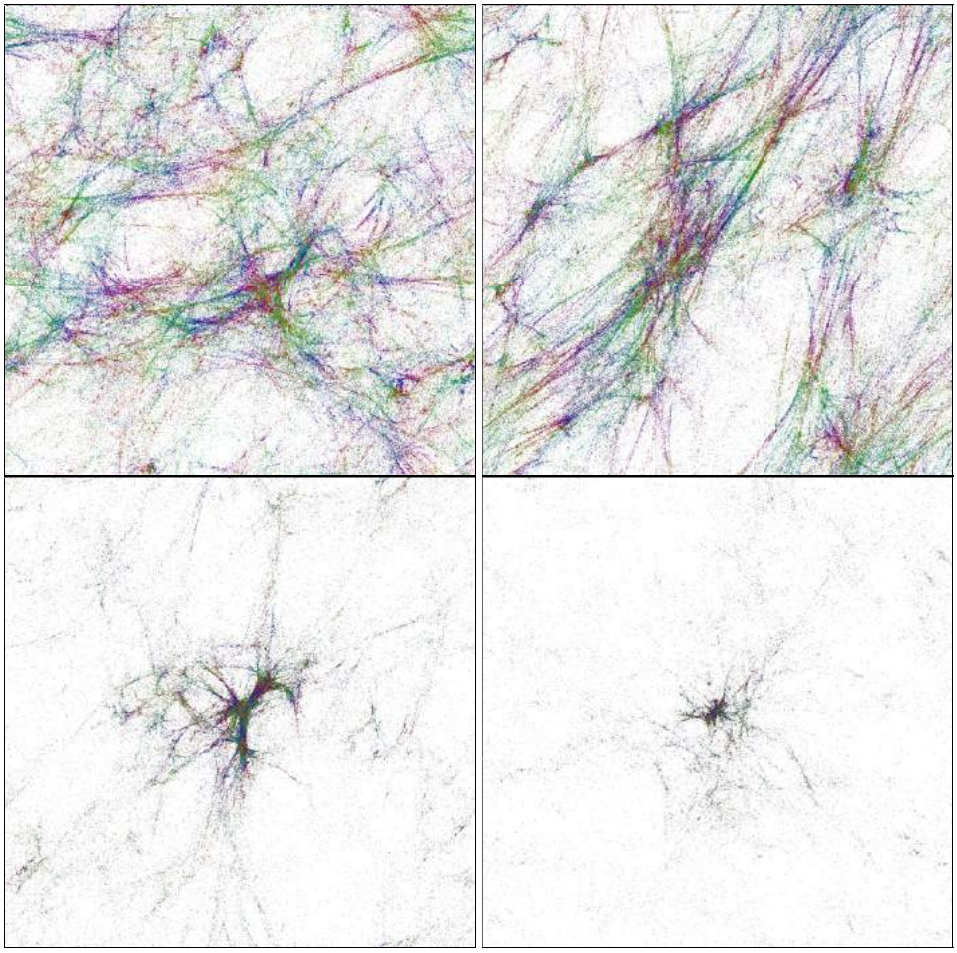

Figure 31. Density maps in $\tilde{\phi}$ coordinates (for the definition see section 3.3) projected on the $x-y$ plane for configurations in phase C ($\kappa_0 = 2.2, \Delta = 0.6$) with $T = 4$ and with dynamical scalar fields with jump in one spatial direction (left) and in three spatial directions (right). Top: configurations with a small jump magnitude ($\delta = 0.1$). Bottom: configurations with a large jump magnitude ($\delta = 1.0$).

jump magnitudes compress the central part, where (almost) all change of the field occurs, and, because of the total volume constraint, transfer the volume into one of the outgrowths, where the field is much more uniform, leading to the picture on the right plot.

One could naïvely think that as an effect of the geometry pinching caused by the dynamical scalar fields with (large) jumps, one would obtain a compactified geometry similar to the geometry of the bifurcation phase C_b or (for even larger jump magnitudes) to a collapsed geometry of the B phase. Interestingly, this is not the case. As can be seen in figure 30, for sufficiently large jump size the spherical outgrowth spreads over time, and the fine structure of the semi-classical phase C geometry survives the pinching effect as is illustrated in figure 33, where we show the density maps in $x-y$ directions, now in the β-coordinates introduced in section 3.3. In these coordinates, the field condensations get stretched and, as a consequence, the geometric outgrowths, i.e. the dense regions in figure 31, get magnified. One can clearly see the very

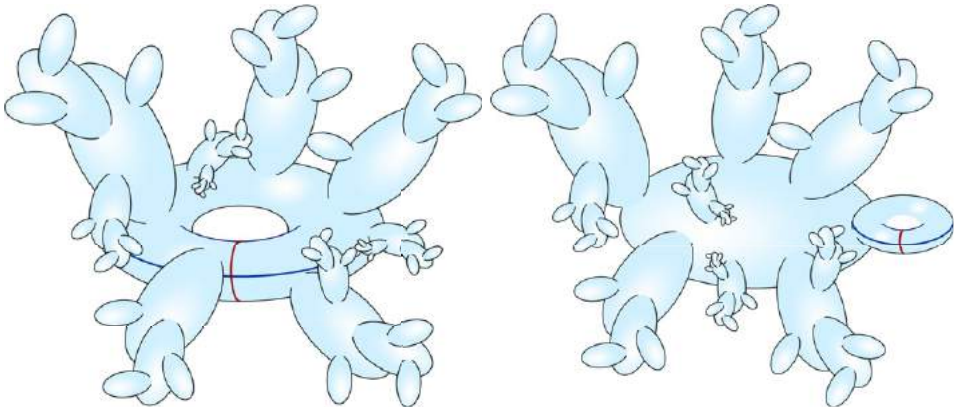

Figure 32. Cartoon 2D pictures representing the generic features of CDT quantum geometries for the pure gravity case/a small jump magnitude (left) and for a large jump magnitude (right).

nontrivial internal structure of the outgrowths, again with the *cosmic voids and filaments* characteristic for the phase C region. Thus, the internal geometry of the large outgrowths created by the pinching effect of the dynamical scalar fields with jump(s) is now completely different than the (almost) homogeneous geometry of the large outgrowths observed in phases C_b and B (see figures 12 and 13 for the pure gravity case).

To summarize the above results, numerical MC simulations performed for $N_{4,1} = 160$k and $T = 4$ suggest that coupling quantum geometry to scalar fields with non-trivial boundary conditions can lead to a new type of a phase transition. If spacetime is globally hyperbolic with a toroidal spatial topology, and if the scalar fields have matching topological boundary conditions, then for a sufficiently strong coupling (sufficiently large δ in our model) one observes a transition leading to an effective change of topology (from a toroidal to a simply connected one). This is the natural extrapolation of what is observed in numerical data presented above and what is schematically illustrated in figure 32, i.e. the dominating toroidal part with many non-trivially correlated (almost) spherical outgrowths changes into the dominating spherical part with many non-trivially correlated spherical outgrowths and a single toroidal outgrowth of cut-off size (which is needed due to the global topological restrictions imposed). The occurrence of such a phase transition seems to be independent of the number of fields with a jump as each such field pinches geometry in all spatial directions. These results are further supported by analysis of larger systems with $N_{4,1} = 720$k, $T = 20$ and three scalar fields with jumps in all spatial directions[33]. Contrary to configurations with small time extent, spatial volume t-profiles are now visibly different for small and large values[34] of the jump magnitude δ, as presented in figure 34, where we plotted $\langle V(t)\rangle$, the t-profiles averaged over many MC configurations. It is remarkable that for $\delta > \delta_c \approx 2.0$, where the pinching, i.e. the phase transition leading to the effective change of the spatial topology from the toroidal to the spherical one, takes place, one can observe the volume profiles with a 'stalk' and the 'blob' part, exactly as it was observed in the pure gravity spherical CDT, where spherical spatial topology was put

[33] These data were measured for a different location of CDT bare couplings in the (κ_0, Δ) parameter space, but the new location is also inside the semiclassical C phase region.

[34] For the larger system, the critical value δ_c is now larger than for the smaller system discussed before. The terms small/large value mean here $\delta < \delta_c$ or $\delta > \delta_c$, respectively.

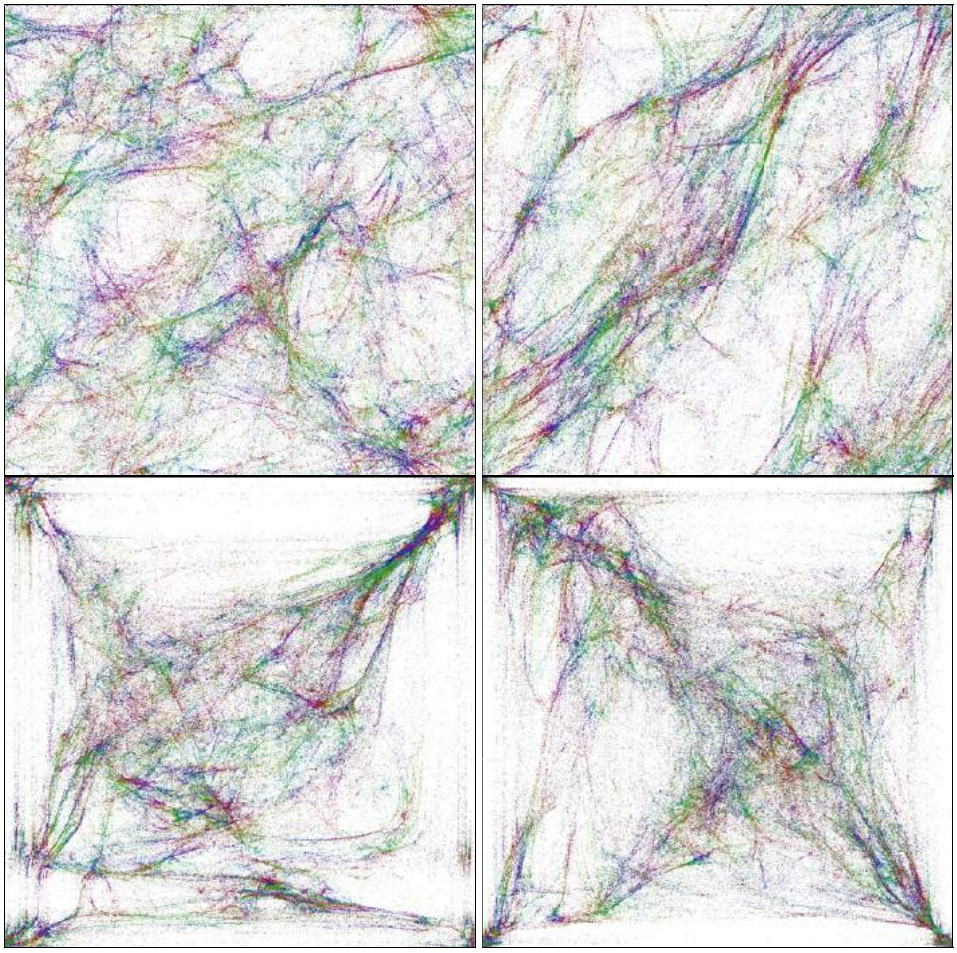

Figure 33. Density maps in β coordinates (for definition see section 3.3) projected on the $x - y$ plane for configurations in phase C ($\kappa_0 = 2.2, \Delta = 0.6$) with $T = 4$ and with dynamical scalar fields with jump in one spatial direction (left) and in three spatial directions (right). Top: configurations with a small jump magnitude ($\delta = 0.1$). Bottom: configurations with a large jump magnitude ($\delta = 1.0$).

in by hand. What is more, for $\delta \gg \delta_c$ the averaged spatial volume t-profiles $\langle V(t)\rangle$ seem to be quite universal, changing only a little with δ, and, even more remarkably, well fitted by the $\cos^3$ curves characteristic for the spherical CDT de Sitter solution observed in phase C. In that case, the difference between the pure gravity spherical CDT (with imposed spherical spatial topology) and the toroidal CDT coupled to scalar fields with jumps (causing the effective spatial topology change) lies in a different behavior of the 'stalk' part. In the original spherical CDT, the three-volume of the 'stalk' was of the cutoff size, and now, in the toroidal CDT with the effective topology change, it is significantly larger. This is partly explained by the size of the minimal three-dimensional toroidal triangulation, which is much bigger than the minimal spherical three-dimensional triangulation [9], resulting in much larger cutoff, but in the later case the three-volume of the stalk is still two orders of magnitude larger than the minimal possible volume of the three-dimensional torus. Probably, the very nontrivial change of the

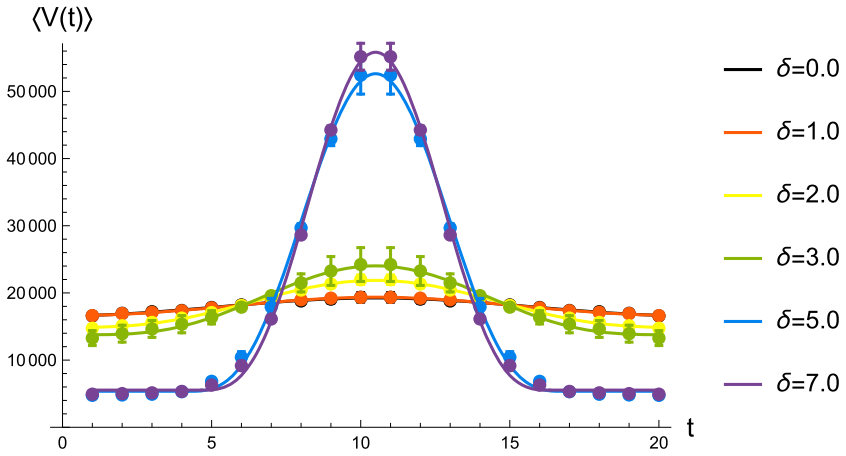

Figure 34. Spatial volume t-profiles (averaged over many MC configurations) inside phase C ($\kappa_0 = 4.0, \Delta = 0.2$) for $T = 20$ and $N_{4,1} = 720$k with dynamical scalar fields with jumps of magnitude δ in all three spatial directions. Error bars for measured data points were estimated using single-elimination (binned) jackknife procedure. Solid lines are fits of the function: $\max[c, c + a\cos^3(b(t - t_0))]$ characteristic for the spherical CDT de Sitter solution.

effective spacetime topology: $T^4 \to S^3 \times T^1$ requires much larger triangulations than the minimal possible ones. At any rate, the existence of the 'stalk' is a discretization/finite size effect related to the fixed spacetime topology conditions imposed in the MC simulations, which cannot change regardless of the effective topology change, and it becomes negligible in the large volume limit. Therefore, the results presented above strongly support our conjecture that the newly observed phase transition leads to an effective spatial topology change.

6. Conclusions

The size of a typical CDT Universe that can be studied on a computer is no larger than 10–20 Planck's lengths [33]. While one could perhaps have expected that all that can be observed at such short scales is just wild quantum fluctuations, in fact this is not the case. The measurement of the spectral dimension indicates a fractal structure of the studied spacetimes [44], the scale-dependent spectral dimension seemingly being a result of the underlying quantum fluctuations, but the scale factor (i.e. the spatial volume profiles as a function of time) of the Universe behaves surprisingly semiclassically [8]. Those results were obtained by averaging over many independent field configurations. Understanding the nature of typical geometries, leading, after performing the average in the path integral, to both semiclassical and quantum phenomena, would be a step toward explaining the nature of quantum gravity (or at least what we can call four-dimensional quantum geometry).

In general, a single configuration in the path integral of a quantum theory is not physical. It can be measured on the computer but not in the real world because of the quantum nature of the theory. What is defined in a quantum theory is a value of an observable suitably averaged over the configurations of the path integral. This does not necessarily mean that a single 'typical' configuration of the path integral is uninteresting. On the contrary, in some situations and for certain observables, the correct answer (up to finite-size corrections) can be obtained by

calculating the value of the observable on a single 'typical' configuration provided it be sufficiently large to be representative for the whole ensemble. In principle, both the scale factor and the spectral dimension mentioned above could have been determined that way. Thus, it would be advantageous to understand the nature of an individual configuration in the path integral: it might be used to calculate certain observables even if it does not qualify as an observable itself.

As already mentioned above, CDT configurations are presented to us on the computer as geometries that are coordinate free in the spatial directions. While this seems desirable from a GR point of view, it is well known that one should be careful what one wishes for. The reason that we were able to construct an effective action for the scale factor was precisely that we had at our disposal a coordinate in the time direction. Indeed, coordinates can be very useful, and in this article we tried to construct them also along the spatial directions in order better to understand the geometry of the configurations and to address the question of formulating an effective action that would include all the spacetime directions.

The geometries we extract from the path integral are not regular in the spatial directions, and it is not clear how to introduce 'good' coordinates when the topology of the space is that of S^3. However, if it is T^3, then one can take advantage of the periodic structure of the piecewise linear manifold to introduce three scalar fields satisfying Laplace's equation and use them as spatial coordinates[35]. The same can be done in the time direction if the CDT time t is made periodic. The comparison of the time defined by the scalar field with the original t can serve as a check of how well this prescription works.

Our starting point was a path integral triangulation $\mathcal{T}$ with four non-contractible hypersurfaces, the so-called boundaries, labeled by x, y, z and t and impossible to be continuously deformed into each other. The t hypersurface was chosen as the spatial slice corresponding to some value t_0 of the CDT time t. Basing on these hypersurfaces, we found four harmonic maps $\tilde{\phi}_i^{\mu}$, $\mu = x, y, z, t$ from $\mathcal{T}$ onto S^1. These four maps now served as our new coordinates, and constant values of $\tilde{\phi}_i^{\mu} = \alpha_{\mu}$ defined hypersurfaces $H(\alpha_{\mu})$. Using the new α_t coordinate, we defined and measured the volume profiles $V(\alpha_t)$, i.e. the number of tetrahedra in each hypersurface $H(\alpha_t)$, and the volume-volume correlator $C(\Delta\alpha_t)$ between volumes of hypersurfaces whose α_t coordinate differs by $\Delta\alpha_t$, as defined in equation (39). The important point here is that the calculations proceed as well when using the α_t coordinate as when using the original t coordinate. The measurement of $C(\Delta\alpha_t)$ is particularly promising since this correlator can be used to reconstruct an effective action (see [33] for details). Analogously, we measured the volume profiles $V(\alpha_{\mu})$, $\mu = x, y, z$ (see figure 20). The results are encouraging yet not as good as for the $V(\alpha_t)$ profiles. As discussed above, the accuracy is constrained to what can be obtained from a single configuration, since in principle we introduce a new coordinate system for each configuration, but the practicability of making superpositions coming from several configurations is not precluded. This idea, which we have yet to investigate and perhaps couple with generating even larger triangulations, would be especially useful to improve the results in the spatial directions. Anyhow, it would be really exciting to be able to measure the correlators $C(\Delta\alpha_{\mu})$, $\mu = x, y, z$ with good precision.

Let us now turn to other observations made using the new harmonic coordinates. As explained in section 3.3, the use of harmonic coordinates is well suited to record in a density plot the outgrowths of a triangulation. In the case of configurations from phase C, which is undoubtedly the most interesting one from the physical point of view, the projections of

[35] Such coordinates are a close analogue of the harmonic coordinate condition used in the context of GR, but here we use them for non-classical and highly non-trivial geometries.

densities to $\mu - \nu$ planes (figure 6) show what we denote, because of the visual similarity to pictures of the well-known structures in the real Universe, as cosmic voids and filaments. In our computer-generated spacetimes, the filaments are not matter content but regions where some of the harmonic fields ϕ_i^μ vary slowly. In terms of geometry, those regions can most likely be associated with outgrowths sharing a small boundary with the rest of the triangulation. However, the fact that they have a filament structure instead of being randomly conglomerated indicates structures of a certain 'duration' rather than what is shown in figure 3 and realized in 2D Liouville quantum gravity [23]. This 'duration' is particularly pronounced in the time direction in the upper left picture of figure 6. That this situation is nontrivial (and not fully understood) is illustrated by plotting the same configurations in the β-coordinates rather than the α-coordinates. As readily seen in figure 10, a filament structure persists, despite the fact that the β-coordinates were specifically designed to be complementary to the α-coordinates and thus sensitive to possible outgrowths.

The classical scalar fields ϕ_i^μ used as coordinates do not influence the geometry of the manifold (the triangulation) on which they are defined, but their important aspect, which makes them independent of the hypersurface used to define them, is that they were mapped to S^1 and not to $\mathbb{R}$. Let us then turn to the examination of a genuine dynamical matter-gravity system, where the scalar field can influence the geometry. As mentioned in the introduction to section 5, we did not observe a substantial effect on the geometry when we studied ordinary scalar fields, taking values in $\mathbb{R}$, coupled to gravity. This may be surprising since matter is supposed to have a dramatic effect on geometry in GR, but we have to remember that the configurations are Wick-rotated to Euclidean spacetimes, where gravity in some sense is repulsive, and also that, e.g. black hole solutions are completely regular solutions to Einstein's equations, and the mass M appears in them just as a parameter. However, what we observe if we compel the scalar field to take values in S^1 and to wind around S^1 when moving around a non-contractible loop on the manifold (the triangulation) where it is defined is that the matter action is minimized if the geometry of the manifold deforms in such a way that it is almost pinched, and the scalar field makes all its winding just when passing the pinch, as explained in section 5. In the path integral, there is a competition between the matter action and the geometric Regge (Einstein–Hilbert) action, which in turn is minimized for non-pinched geometries. The result seems to be a phase transition occurring when the change of the scalar field winding around S^1 is forced to be sufficiently large. In the new phase, the geometry is 'squeezed' in some regions. This kind of squeezing can lead to an effective topology change from a toroidal to a simply connected one. The precise nature of this phase transition is still unknown but clearly interesting to investigate since it is the first phase transition in higher-dimensional CDT caused by matter.

Acknowledgments

JG-S acknowledges support of the Grant 2016/23/ST2/00289 from the National Science Center Poland. JJ acknowledges support from the Grant 2019/33/B/ST2/00589 from National Science Center Poland. ZD acknowledges support from the Grant 2019/32/T/ST2/00390 from National Science Center Poland (NCN). DN acknowledges support from NCN Grant 2019/32/T/ST2/00389.

Data availability statement

The data that support the findings of this study are available upon reasonable request from the authors.

Appendix A

A1. Harmonic functions and dipole sheets

Let us consider n-dimensional flat space, $\mathbb{R}^n$. The dipole moment of two opposite point charges $\pm q$ is defined as $\delta^\mu = qd^\mu$ where d^μ is the vector between the two point charges. The dipole limit is obtained when q goes to infinity and the length of d^μ goes to zero keeping δ^μ fixed. A dipole sheet is a hypersurface S with a surface dipole density $\delta(s)$, i.e. to an infinitesimal area dS centered at any point s^μ on the surface corresponds the dipole moment given by $\mathrm{d}\delta^\mu(s) = \delta(s)n^\mu(s)\mathrm{d}S$. Let us write Poisson's equation in the form

$$\Delta_x\phi(x) = -\rho(x), \quad \phi(x) = \int \mathrm{d}^n y\; G(x,y)\rho(y), \quad \Delta_x G(x,y) = -\delta^n(x-y). \tag{A-1}$$

Here $G(x,y)$ is defined for $n > 2$ as the Green function that goes to zero as $|x-y|$ goes to infinity. The dipole density is obtained as the limit where the charge density $\rho(y)$ is located in two infinitesimal sheets of charges on the opposite sides of the hypersurface S. Let s^μ be a point at the hypersurface and $n^\mu(s)$ the normal to the hypersurface. Then $\rho(s-\epsilon n(s)) = -\rho(s+\epsilon n(s))$, for ϵ infinitesimal, and in the dipole limit

$$\mathrm{d}^n y\,\rho(y)\,G(x,y) \to \mathrm{d}S(s)\,\delta(s)\,n^\mu(s)\frac{\partial}{\partial y^\mu}G(x,y)\Big|_{y=s}, \tag{A-2}$$

and from equation (A-1) we obtain the corresponding dipole potential

$$\phi(x) = \int_S \mathrm{d}S(s)\;\delta(s)\,n^\mu(s)\frac{\partial}{\partial y^\mu}G(x,y)\Big|_{y=s}, \tag{A-3}$$

where the integral is over the hypersurface $S(s)$. An important property of $\phi(x)$, following from the divergence theorem, is that it jumps by the amount $\delta(s)$ when one crosses the surface S at the point s in the direction of the dipole, i.e. in the direction of the normal to the surface $n(s)$.

Let us now consider the case where the space is a torus T^n with volume V, and where the hypersurface S is connected and closed. The constant mode is a zero mode of the Laplacian, and to invert the Laplacian it has to be projected out. Thus $\Delta_x G(x,y) = -\delta^n(x-y) + \frac{1}{V}$. Given a dipole sheet, this $G(x,y)$ will produce a $\phi(x)$ orthogonal to the constant mode. However, $\phi(x)$ itself is only determined up to the constant mode from the defining Poisson equation, (A-1), and it is more convenient in the following to fix $\phi(x)$ not by orthogonality to the constant mode but by being zero at a fixed point x_0. With this choice, $\phi(x)$ is given by

$$\phi(x) = \int_S \mathrm{d}S(s)\;\delta(s)\,n^\mu(s)\frac{\partial}{\partial y^\mu}(G(x,y) - G(x_0,y))\Big|_{y=s}. \tag{A-4}$$

Let us now assume that the dipole density $\delta(s)$ is constant. If we deform the hypersurface S in the direction of the normals $n_i(s), s \in S$, to another hypersurface S' not intersecting S and let $V(S,S')$ denote the enclosed region, then the two potentials $\phi_S(x)$ and $\phi_{S'}(x)$, calculated by (A-4) using dipole sheets S and S', respectively, will agree or differ by $\pm\delta$, depending on how x_0 and x are located relatively to $V(S,S')$. More precisely, we have

$$x, x_0 \in V(S,S') \quad \text{or} \quad x, x_0 \notin V(S,S') : \phi_S(x) = \phi_{S'}(x), \tag{A-5}$$

$$x_0 \in V(S,S'), \qquad x \notin V(S,S') : \phi_S(x) = \phi_{S'}(x) - \delta, \tag{A-6}$$

$$x_0 \notin V(S,S'), \qquad x \in V(S,S') : \phi_S(x) = \phi_{S'}(x) + \delta. \tag{A-7}$$

This follows from the divergence theorem, which leads to

$$\begin{aligned}
&\phi_S(x) - \phi_{S'}(x) \\
&\quad = \delta \int_S \mathrm{d}S\, n^\mu \partial_\mu \left(G(x,y) - G(x_0,y)\right) - \delta \int_{S'} \mathrm{d}S\, n^\mu \partial_\mu \left(G(x,y) - G(x_0,y)\right) \\
&\quad = -\delta \int_{V(S,S')} \mathrm{d}^n z\; \Delta_z \left(G(x,z) - G(x_0,z)\right) \\
&\quad = \delta \int_{V(S,S')} \mathrm{d}^n z\; \left(\delta^n(x-z) - \delta^n(x_0-z)\right).
\end{aligned}$$

The relation between $\phi_S(x)$ and $\phi_{S'}(x)$ is not only valid in flat space but also for a compact Riemannian manifold since it only depends on the divergence theorem, which for a Riemannian manifold reads (for our purpose): $\int_S \mathrm{d}S(s)\, n^\mu(s) \frac{\partial}{\partial y_\mu} G(x,y)\Big|_{y=s} = \int_{V(S)} \mathrm{d}^n z \sqrt{g(z)}\; \Delta_z(x,z)$, where $V(S)$ is the region enclosed by the hypersurface S, $\mathrm{d}S(s)$ is the volume element on S induced from the metric $g_{ij}(y)$ on the Riemannian manifold, $n^\mu(s)$ is the normal vector to the hypersurface S at s, and $\Delta = \frac{1}{\sqrt{g}} \partial_i \sqrt{g} g^{ij} \partial_j$, $\Delta_x G(x,y) = -\frac{1}{\sqrt{g}} \delta^n(x,y) + \frac{1}{V}$. Let us now view the field $\phi(x)$ as taking values in S^1 with circumference δ rather than in $\mathbb{R}$. We can implement this in a simple way, while still keeping the $\mathbb{R}$ values of $\phi(x)$ by defining

$$\phi(x) \equiv \phi(x) + n\,\delta, \quad n \in \mathbb{Z}. \tag{A-8}$$

We see from equations (A-5)–(A-7) that the redefined $\phi(x)$ is unchanged when we change the boundary, i.e. we have the option of viewing the dipole sheet as unphysical and in fact non-existent, and $\phi(x)$ as a harmonic map (i.e. a function which satisfies Laplace's equation) between our Riemannian manifold and the manifold S^1. Our setup for the triangulations considered in the article is a discretization of such a dipole situation. The field ϕ_i can be viewed as sitting in the center of each four-simplex i. We have a hypersurface S build of tetrahedra s_{ij} shared by four-simplices i and j, and the field ϕ_i changes to $\phi_j = \delta + \phi_i$ when we cross from i to j via the hypersurface at s_{ij}. The link connecting the centers of the two four-simplices i and j can be viewed as proportional to the normal n to S at s_{ij}, and B_{ij} plays the role of $n\,\mathrm{d}S$. Viewing the dipole associated with area element $\mathrm{d}S$ as two charges of opposite sign separated by a small distance d, as in equations (A-1)–(A-3) above, we see that $\delta \cdot b_i = \delta \cdot \sum_j B_{ij}$ can be viewed as the sum of charges associated with the dipoles that cross from the simplex i to the simplices j. Then equation (15), (16) and (19) are the discretized versions of the continuum equations (A-1)–(A-3), and the solution $\bar{\phi}_i$ is the discretized version of $\phi(x)$ in (A-4) on a Riemannian manifold. It is remarkable that the discretized versions of equations (A-5)–(A-7) are still valid on a triangulation without a need to take a continuum limit.

A2. Solution of the discrete Laplace equation

In this section, we describe the technical issues related to solving the discrete Laplace equation (19)

$$\mathbf{L}\phi = b.$$

Although the computations have to be done for all four scalar fields, each field can be treated separately. Therefore, for simplicity, we will consider a single field ϕ. Methods applicable for solving (19) must be suitable for sparse matrices because of the large size of the considered Laplacian matrix. They can be divided into two basic types: *direct* methods and *iterative* methods. Below we describe the methods of both types. Wherever possible, all methods used gave similar results up to the machine precision.

Following equation (22), we tested the accuracy of the computed solution by calculating the residual sum of squares,

$$\mathrm{RSS}[\phi] \equiv \sum_i \left(\phi_i - \bar{\phi}_i\right)^2, \quad \text{where } \bar{\phi}_i \equiv \frac{1}{5}\left(b_i + \sum_{j\to i}\phi_j\right).$$

For a perfect solution, $\mathrm{RSS}[\phi] = 0$, by definition.

A2.1. Direct methods. **The Cholesky decomposition.** After the modification (20), the Laplacian matrix $\mathbf{L}$ becomes a real positive-definite symmetric matrix and can be decomposed into the product

$$\mathbf{L} = \mathbf{P}^{\mathrm{T}} \cdot \mathbf{H} \cdot \mathbf{H}^{\mathrm{T}} \cdot \mathbf{P}, \tag{A-9}$$

where $\mathbf{H}$ is a lower-triangular matrix and $\mathbf{P}$ is a permutation matrix. This is known as the Cholesky decomposition. The permutation increases the sparsity of $\mathbf{H}$. The system of linear equation (19) can now be solved simply by *forward* and *back substitution*. We used the `CHOLMOD` library to perform the sparse Cholesky decomposition [46–48].

Surprisingly, the method was too computationally and time consuming for configurations in phases B and C_b but did particularly well in phases A and C. On the other hand, the iterative methods described below did not work so well in the A phase.

A2.2. Iterative methods. We tested various iterative methods and obtained the best results, both from the point of view of speed and accuracy, for a method that we called *parallel preconditioned conjugate gradient method with symmetric successive over-relaxation and approximate inverse* (PPCG-SSOR-AI).

Conjugate gradient method. The *conjugate gradient* method (CG) was designed for solving *symmetric positive-definite* linear systems. Theoretically, it is a direct method, however, it is very sensitive to round-off errors and is often used as an iterative method since it provides monotonically improving approximations to the exact solution. At each step, the approximate solution is improved by searching for a better solution in *the conjugate gradient direction*, which is $\mathbf{L}$-orthogonal to all previous search directions (thus avoiding repeated searches). The conjugate gradient method usually converges much faster than standard iterative methods, such as *Jacobi's method*, *Gauss–Seidel method*, or *successive over-relaxation.*

Preconditioned conjugate gradient method. Unfortunately, the problem to be solved is *ill-conditioned*, i.e. the condition number of matrix $\mathbf{L}$ is large, $\kappa(\mathbf{L}) = \frac{|\lambda_{\max}(\mathbf{L})|}{|\lambda_{\min}(\mathbf{L})|} \gg 1$. The idea of preconditioning is to substitute the original problem $\mathbf{L}\phi = b$ with a preconditioned system

$$\mathbf{C}^{-1}\mathbf{L}\phi = \mathbf{C}^{-1}b$$

that has the same solution and much lower condition number. A particular choice of a preconditioner is the so-called symmetric successive overrelaxation (SSOR),

$$\mathbf{C} = \left(\frac{\mathbf{D}}{\omega} + \mathbf{H}\right)\frac{\omega}{2-\omega}\mathbf{D}^{-1}\left(\frac{\mathbf{D}}{\omega} + \mathbf{H}^{\mathrm{T}}\right),$$

where **D** and **H** are the diagonal and lower-triangular parts of **L**, respectively, with $\mathbf{L} = \mathbf{H} + \mathbf{D} + \mathbf{H}^{\mathrm{T}}$. The preconditioner is chosen such that $\kappa(\mathbf{C}^{-1}\mathbf{L}) \ll \kappa(\mathbf{L})$ (i.e. $\mathbf{C} \approx \mathbf{L}$) and $\mathbf{C}x = b$ can easily be solved. Calculating $x = \mathbf{C}^{-1}b$ can be done using *forward* and *back substitution*, hence the name successive relaxation; and since **C** has a symmetric form and ω can be different from 1, the preconditioner is named symmetric successive overrelaxation.

Parallel preconditioned conjugate gradient method with symmetric successive overrelaxation and approximate inverse. The preconditioned version is much more stable than the original conjugate gradient method, but cannot easily be parallelized. To solve this issue, the method can be further improved by approximating the inverse of the preconditioner $\mathbf{C}^{-1}$. For $\mathbf{D} = \mathbb{1}$ (we normalize the Laplacian matrix) and $\omega = 1$, we have

$$\begin{aligned} \mathbf{C} &= (\mathbb{1} + \mathbf{H})(\mathbb{1} + \mathbf{H}^{T}), \\ \mathbf{C}^{-1} &= (\mathbb{1} + \mathbf{H}^{T})^{-1}(\mathbb{1} + \mathbf{H})^{-1}, \\ \mathbf{C}^{-1} &\approx \mathbf{K} = (\mathbb{1} - \mathbf{H}^{T})(\mathbb{1} - \mathbf{H}). \end{aligned} \tag{A-10}$$

Now we solve $\mathbf{KL}\phi = \mathbf{K}b$ using a slightly modified conjugate gradient method.

The PPCG-SSOR-AI method is fully parallelizable but also stable (due to preconditioning) and fast-convergent (conjugate gradient method). It is also suitable for GPU [45]. We took advantage of multiple CPU cores and used the *OpenMP framework* to gain a significant boost.

A3. Minisuperspace model with pinching

Let us consider the situation where our Universe is periodic in the time direction. With the use of the original CDT time coordinate t, the spatial volume $V(t)$ is now defined at discrete times t_n, and there exists a simple effective action describing the average of $V(t)$ and its fluctuations [7–9]. The continuum version of this action is very similar to the minisuperspace action of Hartle and Hawking [49].

$$S[V] = \int \mathrm{d}t \left[\frac{1}{G}\frac{\dot{V}^2}{V} + \alpha V^{1/3} + \lambda V \right], \tag{A-11}$$

where $\dot{V}$ denotes the time derivative of $V(t)$. Here the discrete time has been replaced by a continuous one. In the Hartle–Hawking minisuperspace action, because of the assumption of homogeneity and isotropy, the scale factor $a(t, x)$ is a function of time only. In CDT no such assumption is made, but nevertheless the functional form of the effective action in terms of $V(t)$ is the same as the Hartle–Hawking minisuperspace model if we write $V(t) \propto a^3(t)$. If the spatial topology is S^3, then the constant α is different from zero, and if the spatial topology is T^3, then $\alpha = 0$. In both cases there exist corrections to the terms shown in (A-11), but they are small, and we will ignore them. The λ in (A-11) is not really the cosmological constant but a Lagrange multiplier ensuring that the four-volume of the Universe is fixed at V_4 in order to agree with the computer simulations where the total four-volume is kept constant. Furthermore, the time integration is from $-T/2$ to $T/2$, as the CDT time of the Universe is fixed to be T, and, finally, periodicity in the time direction is assumed, again to agree with the setup of the computer simulations. G can be viewed as proportional to the gravitational constant.

We now consider the toroidal case, i.e. $\alpha = 0$. Clearly, the minimum of the action is achieved for the constant spatial volume profile $V(t) = V_4/T$. Let us now couple a scalar field to the geometry and assume, in the spirit of a minisuperspace action based on homogeneity and isotropy, that ϕ only depends on t. Moreover, we assume that $\phi(t)$ has winding number one and changes by δ when going around the Universe in the time direction. A minisuperspace

action that takes that into account can be written as

$$S[V,\phi] = \int_{-T/2}^{T/2} \mathrm{d}t \, \left[\frac{1}{G}\frac{\dot{V}^2}{V} + V\,\dot{\phi}^2 + \lambda\, V + \kappa\,\dot{\phi} \right]. \tag{A-12}$$

The part involving only $V(t)$ is just the Hartle–Hawking minisuperspace action (A-11) (with $\alpha = 0$). The part involving $\phi(t)$ consists of two terms. The first term is the kinetic term for a scalar field $\phi(t)$ coupled to the minisuperspace metric defined by $\mathrm{d}s^2 = N^2(t)\mathrm{d}t^2 + a^2(t)\mathrm{d}x_i^2$, where we have used flat coordinates on the spatial three-torus. The second term is added with a Lagrange multiplier κ to ensure that the constraint $\phi(T/2) = \phi(-T/2) + \delta$ is satisfied. Similarly, λ is not the cosmological constant, but a Lagrange multiplier which ensures that the total four-volume V_4 is kept constant (as in the computer simulations). The actions (A-11) and (A-12) are written down with the lap function $N(t)$ fixed to be one, for simplicity. The equations of motions derived below could be derived, keeping $N(t)$ as a variable, and only gauge fixing $N(t) = 1$ afterward. The Euler–Lagrange equations for (A-12) are

$$\frac{1}{G}\left(2\frac{\ddot{V}}{V} - \frac{\dot{V}^2}{V^2}\right) - \dot{\phi}^2 - \lambda = 0, \qquad \frac{\mathrm{d}}{\mathrm{d}t}(V\,\dot{\phi}) = 0. \tag{A-13}$$

They are easily solved by introducing $f(t) = \sqrt{V(t)}$, and the first integrals are

$$V\,\dot{\phi} = K_1, \qquad \frac{\dot{V}^2}{G\,V} + \frac{K_1^2}{V} - \lambda V = K_2. \tag{A-14}$$

The only twice differentiable periodic solutions for $V(t)$ and $\phi(t)$ where $\phi(T/2) = \delta + \phi(-T/2)$ and where $V(t) > 0$ for all t are of the form

$$V(t) = \frac{V_4}{T}, \qquad \phi(t) = \text{const.} + \delta \cdot t/T, \qquad S[V,\phi] = \delta^2\frac{V_4}{T^2}, \tag{A-15}$$

except for $\delta = 2\pi n/\sqrt{G}$ where there are additional solutions. For simplicity we consider here only the case $n = 1$:

$$V(t) = a - b\,\cos\left(2\pi\, t/T\right), \quad a = \frac{V_4}{T} > |b|, \tag{A-16}$$

$$\phi(t) = \frac{\delta}{\pi}\left(\arctan\left[\sqrt{\frac{a+b}{a-b}}\,\tan\left(\frac{\pi t}{T}\right)\right] + \phi(-T/2)\right). \tag{A-17}$$

For any b such that $|b| \leqslant a$ the value of the action is

$$S_{\text{critical}} = \frac{4\pi^2 V_4}{G\,T^2}, \qquad \delta = \frac{2\pi}{\sqrt{G}}, \tag{A-18}$$

which is the same value one obtains when using in the action the constant solution for $\delta = 2\pi/\sqrt{G}$. When $\delta > 2\pi/\sqrt{G}$, (A-16) and (A-17) is no longer a solution to (A-13) for $|b| < a$, but for $|b| = a$ we have a special situation since $V(t)$ can be zero, for $b = a$ at $t = 0$ and for $b = -a$ at $t = \pm T/2$. Let us consider $b = a$. It is seen from (A-16) and (A-17) that for $b \to a$ we obtain the solution

$$V(t) = \frac{V_4}{T}\left(1 - \cos\left(2\pi t/T\right)\right), \qquad \phi(t) = \delta\cdot\theta(t) + \phi(-T/2). \tag{A-19}$$

The change of $\phi(t)$ is a jump of δ at $t = 0$ where $V(t) = 0$. The constant K_1 in (A-14) is zero and the term $V(t)\dot{\phi}^2(t)$ in the action (A-12) is identical to zero for all t. What is special about the situation $a = |b|$ is that (A-19) is a solution for all values of δ, not only for $\delta = 2\pi/\sqrt{G}$, as for $|b| < a$. The reason for this is that ϕ is decoupled from $V(t)$ since $V(t)\dot{\phi}^2(t)$ is identically zero, as mentioned. Thus the action is independent of δ for the solution (A-19).

The value of the action for a given configuration (which is not necessarily a solution to equation (A-13)) is

$$S[V,\phi] = \int_{T/2}^{T/2} \mathrm{d}t \left[\frac{1}{G}\frac{\dot{V}^2}{V} + V\dot{\phi}^2\right]. \tag{A-20}$$

For the solutions (A-15) and (A-19), which we denote the constant solution and the 'blob' solution we have

$$S[V,\phi]\Big|_{\text{const.}} = \delta^2 \frac{V_4}{T^2}, \qquad S[V,\phi]\Big|_{\text{blob}} = \frac{4\pi^2 V_4}{T^2 G}. \tag{A-21}$$

Thus the constant solution (A-15) has the lowest action when $\delta < 2\pi/\sqrt{G}$, while the blob-solution has the lowest action (independent of δ) for $\delta > 2\pi/\sqrt{G}$.

In our computer simulations we do not allow $V(t) = 0$. In fact there is a cut-off $V_{\min}$, which is the minimum number of tetrahedra needed to build a triangulation of a spatial slice T^3. Thus, to compare with computer results we should solve the minisuperspace model with the additional requirement that $V(t) \geqslant V_{\min}$. For $\delta < 2\pi/\sqrt{G}$ (A-15) is the solution. For $\delta > 2\pi/\sqrt{G}$ we have a generalized solution, which is a combination of the constant $V(t)$ like in (A-15) and the 'blob' $V(t)$ as in (A-16). Write

$$\delta = \delta_{\text{blob}} + \delta_{\text{const.}}, \qquad \delta_{\text{blob}} = \frac{2\pi}{\sqrt{G}}, \qquad \delta_{\text{const.}} = \delta - \delta_{\text{blob}} = \delta - \frac{2\pi}{\sqrt{G}}. \tag{A-22}$$

We now use

$$V(t) = \tilde{a} - \tilde{b}\,\cos\left(\frac{2\pi(|t| - \tau/2)}{\tilde{T}}\right), \qquad \frac{\tau}{2} \leqslant |t| \leqslant T/2, \quad \tilde{T} = T - \tau \tag{A-23}$$

$$V(t) = V_{\min} = \tilde{a} - \tilde{b}, \qquad \tilde{a}\tilde{T} = V_4 - \tau V_{\min} \quad |t| \leqslant \frac{\tau}{2}. \tag{A-24}$$

In principle we could have used any $V \in [V_{\min}, V_4/T]$ in the ansatz (A-23) and (A-24). However as will be clear from the solution, the corresponding action will be decreasing with decreasing V, and we have thus chosen the smallest possible V, i.e. $V_{\min}$, from the beginning. The solution has a 'stalk' of time extent τ and spatial volume $V_{\min}$, located around $t = 0$. This $V(t)$ satisfies (A-13) except in the points $t = \pm\tau/2$ where $\ddot{V}(t)$ jumps. However, $\dot{V}(t)$ is continuous and one still has the first integrals (A-14), with different K_2's in the two regions, but the same K_1 which should then be used to calculate $\phi(t)$ and thus δ_{blob} and $\delta_{\text{const.}}$. We find

$$\delta_{\text{blob}} = \frac{K_1\tilde{T}}{\sqrt{\tilde{a}^2 - \tilde{b}^2}} = \frac{2\pi}{\sqrt{G}}, \qquad \delta_{\text{const.}} = \frac{K_1\tau}{\tilde{a} - \tilde{b}} = \frac{2\pi}{\sqrt{G}}\sqrt{\frac{\tilde{a} + \tilde{b}}{\tilde{a} - \tilde{b}}}\,\frac{\tau}{\tilde{T}}. \tag{A-25}$$

We thus obtain

$$\left(\delta - \frac{2\pi}{\sqrt{G}}\right)^2 = \frac{4\pi^2}{G}\,\frac{\tau^2}{\tilde{T}^2}\,\frac{\tilde{a}+\tilde{b}}{\tilde{a}-\tilde{b}} \quad \text{or} \quad \bar{\delta}^2\bar{V} = \frac{\bar{\tau}^2}{(1-\bar{\tau})^3}\left(2 - \bar{V}(1+\bar{\tau})\right), \tag{A-26}$$

where we have introduced the dimensionless quantities

$$\bar{\tau} = \frac{\tau}{T}, \qquad \bar{\delta} = \frac{\delta - \frac{2\pi}{\sqrt{G}}}{\frac{2\pi}{\sqrt{G}}}, \qquad \bar{V} = \frac{T\,V_{\min}}{V_4}. \tag{A-27}$$

For given δ, V_4, T and $V_{\min}$ this is a third order equation for $\bar{\tau}$, the extension of the stalk. Rather than giving the general solution, let us just give lowest order expression in $\bar{\delta}$ and $\bar{V}$:

$$\bar{\tau} = \bar{\delta}\,\sqrt{\bar{V}/2}\left(1 + O\left(\bar{V}, \bar{\delta}\sqrt{\bar{V}}\right)\right). \tag{A-28}$$

The qualitative results are thus as follows: the smaller $\bar{V}$, the smaller $\bar{\tau}$ and $\bar{\tau} \to 0$ in the limit where $\bar{V} \to 0$ and we recover (A-19). For fixed $\bar{V}$ and increasing $\bar{\delta}$, $\bar{\tau}$ will increase, starting at $\bar{\tau} = 0$ for $\bar{\delta} = 0$, i.e. $\delta = 2\pi/\sqrt{G}$, and for $\bar{\delta} \to \infty$ $\bar{\tau} \to 1$, i.e. the stalk basically covers the whole t-range and the 'blob' becomes very narrow and very high. This is qualitatively in agreement with what we observe in the actual Monte Carlo simulations.

The action of the solution (A-23) and (A-24) follows from (A-21):

$$S[V,\phi] = \delta^2_{\text{blob}}\frac{V_4 - \tau V_{\min}}{\tilde{T}^2} + \delta^2_{\text{const.}}\frac{\tau V_{\min}}{\tau^2} = \frac{4\pi^2}{G}\,\frac{V_4}{T^2}\left[\frac{1+\bar{\tau}-2\bar{V}\bar{\tau}}{(1-\bar{\tau})^3}\right], \tag{A-29}$$

where $\bar{\tau}$ is a function of $\bar{\delta}$ and $\bar{V}$ given by (A-26) or (A-28). If we consider $V_{\min}$ as fixed $S[V,\phi]$ becomes a function of $\bar{\delta}$, and we have (to lowest order in $\bar{\delta} > 0$ and also assuming $\bar{V} \ll 1$)

$$S[\bar{\delta}] = S[0]\,\left(1+\bar{\delta}\right)^2 \quad \text{for} - 1 \leqslant \bar{\delta} \leqslant 0,\ S[0] = S_{\text{critical}} \tag{A-30}$$

$$S[\bar{\delta}] = S[0]\,\left(1 + \sqrt{8\bar{V}}\,\bar{\delta} + O(\bar{\delta}^2)\right) \quad \text{for } \bar{\delta} \geqslant 0. \tag{A-31}$$

The behavior of $S[\bar{\delta}]$ is shown in figure 35. First we note that for $\bar{\delta} > 0$ it is an increasing function of $\bar{V}$. As already mentioned this is the reason we, from the beginning, used the value $V_{\min}$ in the ansatz (A-23) and (A-24). While the curve for $S[\bar{\delta}]$ looks approximately linear for $\bar{\delta} > 0$ on the plot, this ceases to be true for large $\bar{\delta}$ where we have

$$S[\bar{\delta}] = \frac{V_{\min}}{T}\,\delta^2 + O\left(\delta^{4/3}\right), \quad \delta \gg \frac{2\pi}{\sqrt{G}}. \tag{A-32}$$

The leading contribution in (A-32) comes from the stalk, which for large δ fills almost all the t-range and is precisely of the form given in (A-15), except that V_4/T has been replaced by $V_{\min}$. Also the squeezed 'blob' has an action going to infinity with increasing δ, but only as $\delta^{4/3}$.

The derivative of $S[\bar{\delta}]/S[0]$ with respect to $\bar{\delta}$ jumps at 0 from the value 2 to the much smaller value $\sqrt{8\bar{V}}$. Consequently the simple minisuperspace model predicts a first order phase transition as a function of $\bar{\delta}$.

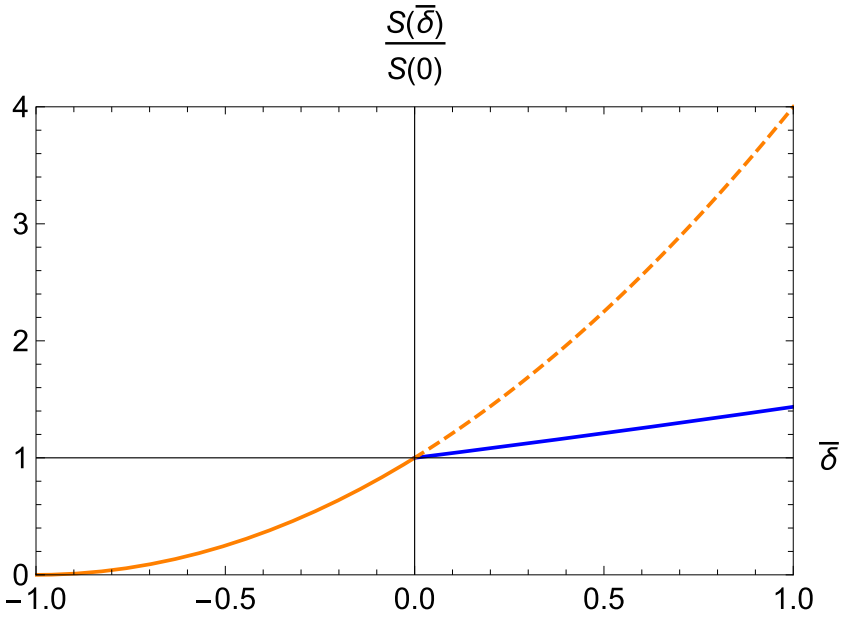

Figure 35. $S[\bar{\delta}]/S[0]$ plotted as a function of $\bar{\delta}$. The orange curve is the constant solution, (the dashed part for $\bar{\delta} \geqslant 0$), while the blue curve shows the action (A-29) for $\bar{\delta} \geqslant 0$ and $\bar{V} = 0.02$. The smaller is $\bar{V}$, the more horizontal the curve will be, and in the limit $\bar{V} \to 0$ the curve is the constant 1 and the solution $V(t)$ is precisely (A-19).

ORCID iDs

Jan Ambjorn https://orcid.org/0000-0003-3782-089X
Zbigniew Drogosz https://orcid.org/0000-0001-5133-958X
Jakub Gizbert-Studnicki https://orcid.org/0000-0003-4179-6159
Andrzej Görlich https://orcid.org/0000-0001-5057-3454
Jerzy Jurkiewicz https://orcid.org/0000-0001-9769-9089
Dániel Németh https://orcid.org/0000-0001-5953-8778

References

[1] Ashtekar A, Marolf D, Mourão J and Thiemann T 2000 *Class. Quantum Grav.* **17** 4919
[2] 't Hooft G and Veltman M J G 1974 *Ann. Poincare Phys. Theor.* A **20** 69–94
Goroff M H and Sagnotti A 1986 *Nucl. Phys.* B **266** 709
[3] Weinberg S 1979 Ultraviolet divergences in quantum theories of gravitation *General Relativity: Einstein Centenary Survey* ed S W Hawking and W Israel (Cambridge: Cambridge University Press) pp 790–831
[4] Kawai H and Ninomiya M 1990 *Nucl. Phys.* B **336** 115
Kawai H, Kitazawa Y and Ninomiya M 1993 *Nucl. Phys.* B **393** 280–300
Kawai H, Kitazawa Y and Ninomiya M 1993 *Nucl. Phys.* B **404** 684–714
Kawai H, Kitazawa Y and Ninorniya M 1996 *Nucl. Phys.* B **467** 313–31
Aida T, Kitazawa Y, Kawai H and Ninomiya M 1994 *Nucl. Phys.* B **427** 158–80
[5] Reuter M 1998 *Phys. Rev.* D **57** 971–85
[6] Codello A, Percacci R and Rahmede C 2009 *Ann. Phys., NY* **324** 414
Reuter M and Saueressig F 2007 arXiv:0708.1317 [hep-th]

Niedermaier M and Reuter M 2006 *Living Rev. Relativ.* **9** 5
Litim D F 2004 *Phys. Rev. Lett.* **92** 201301
[7] Ambjorn J, Jurkiewicz J and Loll R 2005 *Phys. Lett.* B **607** 205–13
Ambjorn J, Gorlich A, Jurkiewicz J, Loll R, Gizbert-Studnicki J and Trzesniewski T 2011 *Nucl. Phys.* B **849** 144–65
[8] Ambjorn J, Jurkiewicz J and Loll R 2005 *Phys. Rev.* D **72** 064014
Ambjorn J, Jurkiewicz J and Loll R 2004 *Phys. Rev. Lett.* **93** 131301
Ambjorn J, Görlich A, Jurkiewicz J and Loll R 2008 *Phys. Rev.* D **78** 063544
Ambjorn J, Görlich A, Jurkiewicz J and Loll R 2008 *Phys. Rev. Lett.* **100** 091304
[9] Ambjorn J, Drogosz Z, Gizbert-Studnicki J, Görlich A, Jurkiewicz J and Nemeth D 2016 *Phys. Rev.* D **94** 044010
Ambjorn J, Gizbert-Studnicki J, Görlich A, Grosvenor K and Jurkiewicz J 2017 *Nucl. Phys.* B **922** 226–46
[10] Ambjorn J, Görlich A, Jordan S, Jurkiewicz J and Loll R 2010 *Phys. Lett.* B **690** 413
Ambjorn J, Görlich A, Jordan S, Jurkiewicz J and Loll R 2011 *Phys. Rev. Lett.* **107** 211303
Ambjorn J, Gizbert-Studnicki J, Görlich A, Jurkiewicz J, Klitgaard N and Loll R 2017 *Eur. Phys. J.* C **77** 152
Coumbe D N, Gizbert-Studnicki J and Jurkiewicz J 2016 *J. High Energy Phys.* JHEP02(2016)144
Ambjorn J, Czelusta G, Gizbert-Studnicki J, Görlich A and Jurkiewicz J 2020 *J. High Energy Phys.* JHEP05(2020)030
[11] Ambjorn J, Coumbe D, Gizbert-Studnicki J, Görlich A and Jurkiewicz J 2017 *Phys. Rev.* D **95** 124029
[12] Ambjorn J, Görlich A, Jurkiewicz J, Kreienbuehl A and Loll R 2014 *Class. Quantum Grav.* **31** 165003
[13] Ambjorn J, Gizbert-Studnicki J, Görlich A, Jurkiewicz J and Loll R 2020 *Front. Phys.* **8** 247
[14] Polyakov A M 1975 *Phys. Lett.* B **59** 82–4
Polyakov A M 1977 *Nucl. Phys.* B **120** 429–58
[15] Regge T 1961 *Nuovo Cimento* **19** 558–71
[16] Ambjorn J, Nielsen J L, Rolf J and Savvidy G K 1997 *Class. Quantum Grav.* **14** 3225–41
[17] Ambjorn J, Durhuus B and Frohlich J 1985 *Nucl. Phys.* B **257** 433
David F 1985 *Nucl. Phys.* B **257** 45
Kazakov V A, Migdal A A and Kostov I K 1985 *Phys. Lett.* B **157** 295
Ambjorn J, Durhuus B, Frohlich J and Orland P 1986 *Nucl. Phys.* B **270** 457–82
[18] Ambjorn J and Varsted S 1992 *Nucl. Phys.* B **373** 557–80
Ambjorn J and Varsted S 1991 *Phys. Lett.* B **266** 285–90
Ambjorn J, Boulatov D V, Krzywicki A and Varsted S 1992 *Phys. Lett.* B **276** 432–6
Agishtein M E and Migdal A A 1991 *Mod. Phys. Lett.* A **6** 1863–84
Boulatov D V and Krzywicki A 1991 *Mod. Phys. Lett.* A **06** 3005–14
[19] Ambjorn J and Jurkiewicz J 1992 *Phys. Lett.* B **278** 42
Ambjorn J and Jurkiewicz J 1995 *Nucl. Phys.* B **451** 643–76
Agishtein M E and Migdal A A 1992 *Mod. Phys. Lett.* A **7** 1039
Agishtein M E and Migdal A A 1992 *Nucl. Phys.* B **385** 395
[20] Ambjorn J, Durhuus B and Jonsson T 1997 *Quantum Geometry. A Statistical Field Theory Approach* (Cambridge: Cambridge University Press)
[21] Ambjørn J, Drogosz Z, Gizbert-Studnicki J, Görlich A and Jurkiewicz J 2019 *Nucl. Phys.* B **943** 114626
[22] Ambjorn J, Drogosz Z, Görlich A and Jurkiewicz J 2021 *Phys. Rev.* D **103** 086022
[23] Ambjorn J and Budd T G 2013 *J. Phys. A: Math. Theor.* **46** 315201
[24] Ambjorn J, Anagnostopoulos K N and Jurkiewicz J 1999 *J. High Energy Phys.* JHEP08(1999)016
Ambjørn J, Jurkiewicz J, Bilke S, Burda Z and Petersson B 1994 *Mod. Phys. Lett.* A **9** 2527–41
Ambjorn J, Burda Z, Jurkiewicz J and Kristjansen C F 1993 *Phys. Rev.* D **48** 3695–703
Jha R G, Laiho J and Unmuth-Yockey J 2018 *PoS LATTICE2018* p 043
Catterall S, Laiho J and Unmuth-Yockey J 2018 *Phys. Rev.* D **98** 114503
[25] Bialas P, Burda Z, Krzywicki A and Petersson B 1996 *Nucl. Phys.* B **472** 293–308
Catterall S, Renken R and Kogut J B 1998 *Phys. Lett.* B **416** 274–80
[26] Ambjorn J, Glaser L, Goerlich A and Jurkiewicz J 2013 *J. High Energy Phys.* JHEP10(2013)100
Coumbe D and Laiho J 2015 *J. High Energy Phys.* JHEP04(2015)028
[27] Ambjorn J and Loll R 1998 *Nucl. Phys.* B **536** 407

Ambjorn J, Jurkiewicz J and Loll R 2000 *Phys. Rev. Lett.* **85** 924–7
Ambjorn J, Jurkiewicz J and Loll R 2001 *Nucl. Phys.* B **610** 347
[28] Hořava P 2009 *Phys. Rev.* D **79** 084008
Hořava P and Melby-Thompson C M 2010 *Phys. Rev.* D **82** 064027
[29] Ambjørn J, Glaser L, Sato Y and Watabiki Y 2013 *Phys. Lett.* B **722** 172–5
[30] Jordan S and Loll R 2013 *Phys. Rev.* D **88** 044055
Jordan S and Loll R 2013 *Phys. Lett.* B **724** 155–9
[31] Ambjørn J, Görlich A, Jurkiewicz J and Zhang H 2015 *Phys. Lett.* B **746** 359–64
Ambjørn J, Görlich A, Jurkiewicz J and Zhang H 2015 *Phys. Lett.* B **743** 435–9
Ambjørn J, Görlich A, Jurkiewicz J and Zhang H 2015 *Mod. Phys. Lett.* A **30** 1550077
Ambjørn J, Görlich A, Jurkiewicz J and Zhang H 2014 *Phys. Lett.* B **735** 191–4
Ambjørn J, Görlich A, Jurkiewicz J and Zhang H 2012 *Nucl. Phys.* B **863** 421–34
[32] Candido A, Clemente G, D'Elia M and Rottoli F 2020 arXiv:2010.15714 [hep-lat]
[33] Ambjorn J, Goerlich A, Jurkiewicz J and Loll R 2012 *Phys. Rep.* **519** 127
[34] Loll R 2020 *Class. Quantum Grav.* **37** 013002
[35] Ambjorn J, Drogosz Z, Gizbert-Studnicki J, Görlich A, Jurkiewicz J and Németh D 2021 *Universe* **7** 79
[36] Ambjorn J, Coumbe D N, Gizbert-Studnicki J and Jurkiewicz J 2016 *Phys. Rev.* D **93** 104032
[37] Ambjorn J and Jurkiewicz J 1994 *Phys. Lett.* B **335** 355–8
[38] Ambjørn J, Gizbert-Studnicki J, Görlich A, Jurkiewicz J and Németh D 2018 *J. High Energy Phys.* JHEP06(2018)111
[39] Ambjorn J, Jordan S, Jurkiewicz J and Loll R 2012 *Phys. Rev.* D **85** 124044
Ambjorn J, Gizbert-Studnicki J, Görlich A, Jurkiewicz J and Németh D 2019 *J. High Energy Phys.* JHEP07(2019)166
Ambjorn J, Coumbe D, Gizbert-Studnicki J, Görlich A and Jurkiewicz J 2019 *Class. Quantum Grav.* **36** 224001
[40] Klitgaard N and Loll R 2018 *Phys. Rev.* D **97** 046008
Klitgaard N and Loll R 2018 *Phys. Rev.* D **97** 106017
Klitgaard N and Loll R 2020 *Eur. Phys. J.* C **80** 990
[41] Ambjørn J, Drogosz Z, Gizbert-Studnicki J, Görlich A, Jurkiewicz J and Németh D 2021 *Eur. Phys. J.* C **81** 708
[42] DeWitt B S 1967 *Phys. Rev.* **160** 1113
Rovelli C 2004 *Quantum Gravity* (Cambridge: Cambridge University Press)
Rovelli C 1990 *Phys. Rev.* D **42** 2638
Rovelli C 1991 *Phys. Rev.* D **43** 442
Kucha K V and Torre C G 1991 *Phys. Rev.* D **43** 419–41
Dittrich B 2006 *Class. Quantum Grav.* **23** 6155
Kuchar K V 2011 *Int. J. Mod. Phys.* D **20** 3–86
Hoehn P A 2019 *Universe* **5** 116
[43] Ambjørn J, Drogosz Z, Gizbert-Studnicki J, Görlich A, Jurkiewicz J and Németh D 2021 arXiv:2103.00198 [hep-th]
[44] Ambjorn J, Jurkiewicz J and Loll R 2005 *Phys. Rev. Lett.* **95** 171301
[45] Helfenstein R and Koko J 2012 *J. Comput. Appl. Math.* **236** 3584
[46] Chen Y, Davis T A, Hager W and Rajamanickam S 2008 *ACM Trans. Math. Softw.* **35** 22
[47] Davis T A and Timothy A 2011 *ACM Trans. Math. Softw.* **38** 8
[48] Bezanson J, Edelman A, Karpinski S and Shah V B 2017 *SIAM Rev.* **59** 65
[49] Hartle J B and Hawking S W 1983 *Phys. Rev.* D **28** 2960–75

Acknowledgements

First of all I would like to thank for all the support to prof. Jerzy Jurkiewicz, who gave me the possibility to join to the research group and supervised me throughout the years, shared with me many of his thoughts and ideas which definitely influenced the way I see my field of research. Also to dr. Jakub Gizbert-Studnicki for all the discussions during my PhD. and for his patience and the significant amount of time he spent with advising my thesis. Special thanks to dr. Andrzej Görlich also for the discussions and constant technical help with the computers, codes and simulations. I would like to thank also to prof. Jan Ambjorn for all the fruitful discussions throughout our regular CDT meetings, as he shared his deep knowledge with us, my knowledge and understanding also improved. Additionally, I would like to express my gratitude to my wife, dr. Anna Francuz for her presence in my life, and for her support during my studies and her patience and understanding in those times, when I work in late hours instead of being there. Last but not least, I would like to thank to my daughter Eszter Eleonóra, for letting me sleep, sometimes....

Appendix A

Additional Moves

Moves "2", "3", "4" and "5" (and their respective inverses) are the moves that are currently used during the MC computer simulations of CDT. The new way of visualizing the moves by the "colored dots" graphs, introduced in Chapter 3, makes it possible to find new moves relatively easily. Therefore in this appendix I propose two new moves. These new moves are not atomic ones but could be expressed with a smaller or larger set of combinations of our atomic moves. It makes sense to propose new moves even if they can be expressed as a sequence of other moves, because implementing new moves may significantly reduce the MC thermalization time and thus speed-up the numerical simulations.

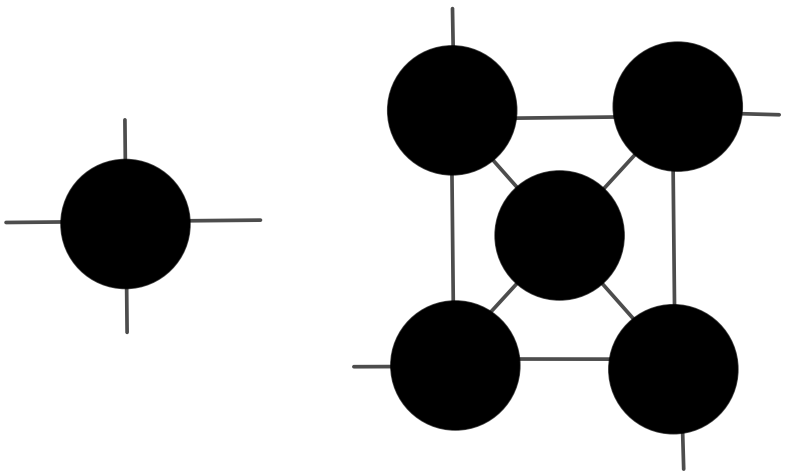

FIGURE A.1: Alternative Move-4 adds a tetrahedron instead of a vertex to the middle of another tetrahedron.

The first proposal is a simple extension of move-4, shown in Fig. A.1. Instead of adding a vertex to the CDT triangulation in the middle of an s_{41} simplex, represented in Fig. A.1 by a black dot splitting into four "external" black dots, one may propose that the internal structure has four interfaces, which means that it forms another s_{41} simplex, i.e., an additional "internal" black dot. Thus such a move would be replacing a single black dot with five black dots, instead of four. The inverse move would require tracking such s_{41} simplices (black dots) which are only surrounded by other black dots. In general such an extra move could be extended to inserting N black dots, but the larger N the harder it is to track such a structure necessary to perform the inverse move during the simulations.

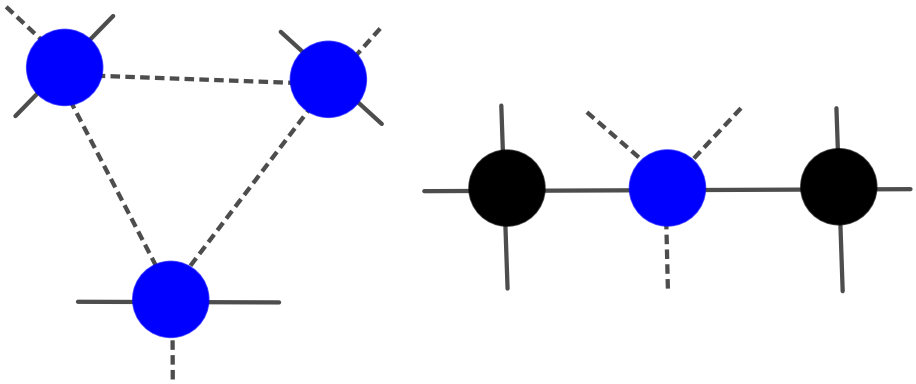

FIGURE A.2: The proposed move transforms three blue dots into a bridge of black-blue-black dots.

The second proposal of the new move is much harder to be implemented, but potentially much more useful. It is shown in Fig. A.2. The move uses a "bridge" structure, which is a set of blue dots (s_{32} simplices) laying along a line connecting two black dots (s_{41} simplices). In general there can be arbitrary many blue dots in the middle (the length of the "bridge" can be arbitrarily long). The simplest version of the move, which involves only one blue dot could be realized by first performing a move-2 on the blue and, say, the left black dot. This would create the three connected blue dots and would place the two black dots next to each other. Then performing a move-5 would create three black dots out of the two. The last step, which is missing from the current set of CDT moves, would be the merging of the two vertices of the spatial link[1] of coordination number three, in the graphical representation leading to the "annihilation" of the black dots. Such a merging move could be achieved by performing a series of the existing MC moves, but it strongly depends on the details of a triangulation and it could take up even hundreds of them. This move has the potential to create large changes in a triangulation, because it can modify very large structures as well. However, the more massive the move is the less likely that it will be accepted by the MC algorithm. The move embedded in a larger structure is visualized in Fig. A.3. We did not implement this move yet, because our current code does not store the necessary elements to track the required sub-structures.

[1] In the graphical representation the link would be a closed loop consisting of three black dots.

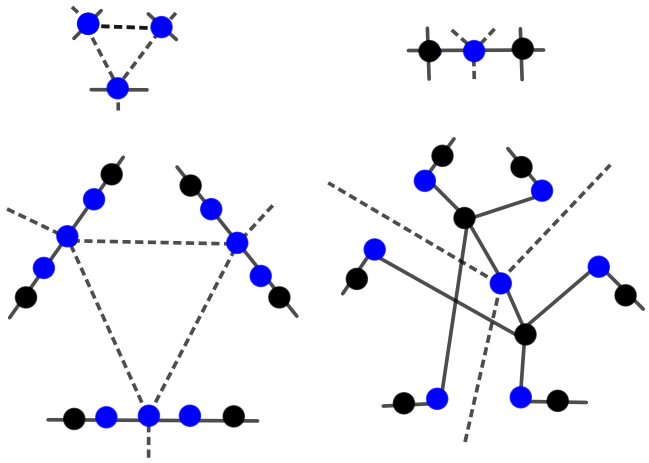

FIGURE A.3: The figure shows the proposed new move embedded in a larger structure. Only the relevant legs are pictured for the sake of readability. On the top a simpler picture of Fig. A.2 is shown as a hint.

Appendix B

Topological relations between parameters of a CDT triangulation

The following list sums up the topological relations valid for any CDT triangulation. For the definition of the A, B, C, D and E parameters see Chapter 4. Note, that for simpler notation in the appendix, contrary to the main text, we use a convention of *global* numbers which distinguishes between the number of s_{41} and s_{14} simplices, denoted N_{41} and N_{14}, respectively. Similarly, we distinguish between N_{32} and N_{23}.

T_1.: $2A_1 + C_1 + E = 5 \cdot N_{41}$

T_2.: $C_1 + 2B_{1a} + 2B_{2a} + D = 5 \cdot N_{32}$

T_3.: $C_2 + 2B_{2a} + 2B_{2b} + D = 5 \cdot N_{23}$

T_4.: $2A_2 + C_2 + E = 5 \cdot N_{14}$

T_5.: $2A_1 + C_1 = 2A_2 + C_2 = 2(N_{41} + N_{14})$

T_6.: $2B_{1b} + D = 3 \cdot N_{32}$

T_7.: $2B_{2b} + D = 3 \cdot N_{23}$

T_8.: $2B_{1a} + C_1 = 2 \cdot N_{32}$

T_9.: $2B_{2a} + C_2 = 2 \cdot N_{23}$

T_{10}.: $(A + B + C + D + E) = N_3 = \frac{5}{2} N_4$

A triangulation can be characterized by the following global parameters, referring to the number of (sub-) simplices of various types, $N_{10}, N_{20}, N_{11}, N_{30}, N_{21}, N_{12}, N_{40}, N_{31}, N_{13}, N_{22}, N_{41}, N_{32}, N_{23}, N_{14}, \chi$, where the first number in the subscript denotes the number of vertices in the spatial slice t and the second one is the number of vertices in $t + 1$, and χ is the Euler characteristics related to the fixed spatial topology. These global numbers can be joined using the seven Dehn-Sommerville relations [28]:

DS_1.: $N_{40} = N_{41} = \frac{1}{2}(N_{41} + N_{14})$

DS_2.: $N_{30} = 2N_{40} = (N_{41} + N_{14})$

DS_3.: $N_4 = \frac{2}{5}(N_{40} + N_{31} + N_{13} + N_{22})$

DS_4.: $N_{10} \downarrow \; N_{20} + N_{30} \downarrow \; N_{40} = 0$

DS_5.: $N_{22} = \frac{3}{2}(N_{32} + N_{23})$

DS_6.: $2N_1 \downarrow\ 3N_2 + 4N_3 \downarrow\ 5N_4 = 0$

DS_7.: $N_0 \downarrow\ N_1 + N_2 \downarrow\ N_3 + N_4 = \chi$

Using the "T" relations:

$$(N_{32} + N_{23}) = \frac{2}{5}B + \frac{2}{5}D + \frac{1}{5}C = \frac{2}{3}B_b + \frac{2}{3}D = B_a + \frac{1}{2}C = \frac{2}{3}N_{22}, \tag{B.1}$$

and from this it follows, that D can be expressed as:

$$D = \frac{3}{2}B_a \downarrow\ B_b + \frac{3}{4}C. \tag{B.2}$$

Similarly, one can express the other relations for the two 4-dimensional simplices, and using "DS" relations one obtains :

$$(N_{41} + N_{14}) = \frac{1}{2}A + \frac{1}{4}C = N_{30} = 2N_{40}. \tag{B.3}$$

It also follows that:

$$E = \frac{1}{2}A + \frac{1}{4}C. \tag{B.4}$$

Using DS_3 one can find the relations fulfilled by the time-like tetrahedra:

$$N_4 = (N_{41} + N_{14}) + (N_{32} + N_{23}) = \frac{2}{5}(N_{40} + N_{31} + N_{22} + N_{13}), \tag{B.5}$$

leading to

$$(N_{31} + N_{13}) = 2(N_{41} + N_{14}) + (N_{32} + N_{23}) = A + B_a + C. \tag{B.6}$$

The formula for the spatial links can be expressed with the help of DS_4:

$$N_{20} = N_{10} + \frac{1}{2}(N_{41} + N_{14}) = N_{10} + \frac{1}{4}A + \frac{1}{8}C. \tag{B.7}$$

The remaining numbers N_{11} and $(N_{21} + N_{12})$ are calculated in a bit more involved way. Taking DS_6 we can express the total number of time-like links as:

$$N_{11} = \frac{3}{2}(N_{30} + N_{21} + N_{12}) \downarrow\ \frac{3}{2}A \downarrow\ \frac{5}{2}B_a \downarrow\ 2C \downarrow\ N_0, \tag{B.8}$$

which involves the number of time-like triangles. Using DS_7 one can find the following relation:

$$\chi = N_0 \downarrow\ \frac{1}{2}(N_{30} + N_{21} + N_{12}) + N_4, \tag{B.9}$$

which leads to the expression for the time-like triangles:

$$(N_{21} + N_{12}) = 2N_0 \downarrow\ 2\chi + \frac{1}{2}A + 2B_a + \frac{3}{2}C, \tag{B.10}$$

which now can be used in the previous equation to get the number of the time-like links:

$$N_{11} = 2N_0 \downarrow\ 3\chi + \frac{1}{2}B_a + \frac{1}{4}C. \tag{B.11}$$

With the above mentioned relations one can check, that for any CDT triangulation there are 8 independent parameters, which are enough to compute all other global parameters. For example, one can choose the following set of independent parameters

$$Set_R = \{N_0, \chi, A_1, A_2, B_{1a}, B_{2a}, C_1, C_2\}. \tag{B.12}$$

One can as well use the following set, including the currently used global numbers N_0, N_{41} and N_{32} appearing in the CDT action:

$$Set_G = \{N_0, \chi, N_{41}, N_{32}, N_{23}, C_1, C_2, D\}. \tag{B.13}$$

These new parameters can be used not only as order parameters, but also they can be potentially used to extend the CDT action, see eq. (2.18), to the following form

$$S^{ext}_{CDT} = \downarrow (\kappa_0 + 6\Delta)N_0 + \kappa_4(N_{41} + N_{32}) + \Delta N_{41} + \kappa_C C + \kappa_D D, \tag{B.14}$$

where κ_C and κ_D are the new coupling constants related to the C and D parameters, respectively. The physical meaning of these parameters and the related coupling constants is not straightforward and a discussion of it will not be a part of this thesis.

Bibliography

[1] J. Ambjorn G. Czelusta et al. "The higher-order phase transition in toroidal CDT". In: *J. of High Energ. Phys.* 2020 (5), p. 30. DOI: 10.1007/JHEP05(2020)030.

[2] J. Ambjorn et al. "Towards an UV fixed point in CDT gravity". In: *Journal of High Energy Physics* 2019 (7), p. 166. DOI: 10.1007/JHEP07(2019)166.

[3] J. Ambjorn et al. "Topology induced first-order phase transitions in lattice quantum gravity". In: *Journal of High Energy Physics* 2022 (4), p. 103. DOI: https://doi.org/10.1007/JHEP04(2022)103.

[4] J. Ambjorn et al. "Cosmic voids and filaments from quantum gravity". In: *The European Physical Journal C* 81 (8 2021), p. 708. DOI: 10.1140/epjc/s10052-021-09468-z.

[5] J. Ambjorn et al. "Matter-Driven Change of Spacetime Topology". In: *Phys. Rev. Lett.* 127 (16 Oct. 2021), p. 161301. DOI: 10.1103/PhysRevLett.127.161301.

[6] J. Ambjorn et al. "Scalar fields in causal dynamical triangulations". In: *Classical and Quantum Gravity* 38 (19 Sept. 2021), p. 195030. DOI: 10.1088/1361-6382/ac2135.

[7] H. Eves. *A Survey of Geometry*. A Survey of Geometry Bd. 1. 1963. URL: https://books.google.at/books?id=NUzvAAAAMAAJ.

[8] J. R. Klauder. "On the meaning of a non-renormalizable theory of gravitation". In: *General Relativity and Gravitation* 6 (1875), pp. 13–19. DOI: 10.1007/BF00766595.

[9] S. Weinberg. "Ultraviolet divergences in quantum theories of gravitation". In: *United Kingdom: University Press* 11 (5 1979). ISSN: 11506418. URL: https://inis.iaea.org/search/search.aspx?orig_q=RN:11506418.

[10] M. Niedermaier and M. Reuter. "The Asymptotic Safety Scenario in Quantum Gravity". In: *Living Reviews in Relativity* 9 (206), p. 5. ISSN: 1433-8351. DOI: 10.12942/lrr-2006-5.

[11] J. F. Donoghue. "A Critique of the Asymptotic Safety Program". In: *Frontiers in Physics* 8 (2020). ISSN: 2296-424X. DOI: 10.3389/fphy.2020.00056.

[12] I. Montvay and G. Münster. *Quantum Fields on a Lattice*. Cambridge Monographs on Mathematical Physics. 1994. DOI: 10.1017/CBO9780511470783.

[13] Michael Creutz. *Quarks, gluons and lattices*. Cambridge Monographs on Mathematical Physics. June 1985. ISBN: 978-0-521-31535-7.

[14] L. Dini et al. "Chiral phase transition in three-flavor QCD from lattice QCD". In: *Phys. Rev. D* 105 (3 Feb. 2022), p. 034510. DOI: 10.1103/PhysRevD.105.034510.

[15] S. Durr et al. "Lattice QCD at the physical point: Light quark masses". In: *Physics Letters B* 701.2 (2011), pp. 265–268. ISSN: 0370-2693. DOI: https://doi.org/10.1016/j.physletb.2011.05.053.

[16] J. Ambjørn et al. "The microscopic structure of 2D CDT coupled to matter". In: *Physics Letters B* 746 (2015), pp. 359–364. ISSN: 0370-2693. DOI: https://doi.org/10.1016/j.physletb.2015.05.026.

[17] A. Candido et al. "Compact gauge fields on Causal Dynamical Triangulations: a 2D case study". In: *J. High Energ. Phys.* 85 (4 Apr. 2021). DOI: 10.1007/JHEP04(2021)184.

[18] A. Bonanno, G. Kofinas, and V. Zarikas. "Effective field equations and scale-dependent couplings in gravity". In: *Phys. Rev. D* 103 (10 May 2021), p. 104025. DOI: 10.1103/PhysRevD.103.104025.

[19] C. Contreras, B. Koch, and P. Rioseco. "Black hole solution for scale-dependent gravitational couplings and the corresponding coupling flow". In: *Classical and Quantum Gravity* 30.17 (Aug. 2013), p. 175009. DOI: 10.1088/0264-9381/30/17/175009.

[20] A. Shomer. "A pedagogical explanation for the non-renormalizability of gravity". In: *arXiv* 0709.3555 [hep-th] (2007). URL: https://arxiv.org/abs/0709.3555.

[21] O. Lauscher and M. Reuter. "Ultraviolet fixed point and generalized flow equation of quantum gravity". In: *Phys. Rev. D* 65 (2 Dec. 2001), p. 025013. DOI: 10.1103/PhysRevD.65.025013.

[22] T. Regge. "General Relativity without Coordinates". In: *Il Nuovo Cimento* XIX.3 (1961), pp. 558–571. DOI: https://10.1007/BF02733251.

[23] C. Naldoni de Souza R.R. Cuzinatto C.A.M. de Melo. "Introduction to Regge Calculus for Gravitation". In: *arXiv* 1904.01966 [gr-qc] (2019). URL: https://arxiv.org/abs/1904.01966.

[24] D. J. Gross and F. Wilczek. "Ultraviolet Behavior of Non-Abelian Gauge Theories". In: *Phys. Rev. Lett.* 30 (26 June 1973), pp. 1343–1346. DOI: 10.1103/PhysRevLett.30.1343.

[25] X. She-Sheng. "Quantum Regge Calculus of Einstein–Cartan theory". In: *Physics Letters B* 682.3 (2009), pp. 300–304. ISSN: 0370-2693. DOI: https://doi.org/10.1016/j.physletb.2009.10.082.

[26] Eugenio Bianchi and Leonardo Modesto. "The perturbative Regge-calculus regime of loop quantum gravity". In: *Nuclear Physics B* 796.3 (2008), pp. 581–621. ISSN: 0550-3213. DOI: https://doi.org/10.1016/j.nuclphysb.2007.12.011.

[27] R. Arnowitt, Stanley S. Deser, and C. W. Misner. "The dynamics of general relativity". In: *General Relativity and Gravitation* 40 (9 1997), p. 2027. DOI: 10.1007/s10714-008-0661-1.

[28] J. Ambjørn et al. "Nonperturbative quantum gravity". In: *Physics Reports* 519.4 (2012), pp. 127–210. ISSN: 0370-1573. DOI: https://doi.org/10.1016/j.physrep.2012.03.007.

[29] J. Jurkiewicz and A. Krzywicki. "Branched polymers with loops". In: *Physics Letters B* 392.3 (1997), pp. 291–297. ISSN: 0370-2693. DOI: https://doi.org/10.1016/S0370-2693(96)01559-6.

[30] J. Ambjørn et al. "Second- and first-order phase transitions in causal dynamical triangulations". In: *Phys. Rev. D* 85 (12 June 2012), p. 124044. DOI: 10.1103/PhysRevD.85.124044.

[31] J. Ambjørn, J. Jurkiewicz, and R. Loll. "Emergence of a 4D World from Causal Quantum Gravity". In: *Phys. Rev. Lett.* 93 (13 Sept. 2004), p. 131301. DOI: 10.1103/PhysRevLett.93.131301.

[32] J. Ambjorn, D. Coumbe, and J. Jurkiewicz. "Exploring the new phase transition of CDT". In: *J. High Energ. Phy* 144 (2 Feb. 2016). DOI: 10.1007/JHEP02(2016)144.

[33] J. Ambjorn et al. "New higher-order transition in causal dynamical triangulations". In: *Phys. Rev. D* 95 (12 June 2017), p. 124029. DOI: 10.1103/PhysRevD.95.124029.

[34] J. Ambjørn et al. "Nonperturbative quantum de Sitter universe". In: *Phys. Rev. D* 78 (6 Sept. 2008), p. 063544. DOI: 10.1103/PhysRevD.78.063544.

[35] J. Ambjørn et al. "Impact of topology in causal dynamical triangulations quantum gravity". In: *Phys. Rev. D* 94 (4 Aug. 2016), p. 044010. DOI: 10.1103/PhysRevD.94.044010.

[36] J. Ambjørn et al. "The effective action in 4-dim CDT. The transfer matrix approach". In: *Journal of High Energy Physics* 2014 (6). DOI: 10.1007/jhep06(2014)034.

[37] S. W. Hawking and T. Hertog. "A smooth exit from eternal inflation?" In: *J. High Energ Phys.* 147 (4 Apr. 2018). DOI: 10.1007/JHEP04(2018)147.

[38] A. Csordás and R. Graham. "Hartle-Hawking state in supersymmetric minisuperspace". In: *Physics Letters B* 373.1 (1996), pp. 51–55. ISSN: 0370-2693. DOI: https://doi.org/10.1016/0370-2693(96)00098-6.

[39] P. N. Don. "Space for both no-boundary and tunneling quantum states of the Universe". In: *Phys. Rev. D* 56 (4 Aug. 1997), pp. 2065–2072. DOI: 10.1103/PhysRevD.56.2065.

[40] J. Ambjørn, J. Jurkiewicz, and Y. Watabiki. "On the fractal structure of two-dimensional quantum gravity". In: *Nuclear Physics B* 454.1 (1995), pp. 313–342. ISSN: 0550-3213. DOI: https://doi.org/10.1016/0550-3213(95)00468-8.

[41] R. Loll and B. Ruijl. "Locally causal dynamical triangulations in two dimensions". In: *Phys. Rev. D* 92 (8 Oct. 2015), p. 084002. DOI: 10.1103/PhysRevD.92.084002.

[42] J. Ambjørn and J. Jurkiewicz. "Scaling in four-dimensional quantum gravity". In: *Nuclear Physics B* 451.3 (1995), pp. 643–676. ISSN: 0550-3213. DOI: https://doi.org/10.1016/0550-3213(95)00303-A.

[43] J. Ambjørn, J. Jurkiewicz, and R. Loll. "Emergence of a 4D World from Causal Quantum Gravity". In: *Phys. Rev. Lett.* 93 (13 Sept. 2004), p. 131301. DOI: 10.1103/PhysRevLett.93.131301.

[44] J. Ambjørn, J. Jurkiewicz, and R. Loll. "The Spectral Dimension of the Universe is Scale Dependent". In: *Phys. Rev. Lett.* 95 (17 Oct. 2005), p. 171301. DOI: 10.1103/PhysRevLett.95.171301.

[45] J. Ambjørn et al. "The spectral dimension in 2D CDT gravity coupled to scalar fields". In: *Modern Physics Letters A* 30.13 (2015). ISSN: 1550077. DOI: https://doi.org/10.1142/S0217732315500777.

[46] J. J. Atick and E. Witten. "The Hagedorn transition and the number of degrees of freedom of string theory". In: *Nuclear Physics B* 310.2 (1988), pp. 291–334. ISSN: 0550-3213. DOI: https://doi.org/10.1016/0550-3213(88)90151-4.

[47] D. Benedetti. "Fractal Properties of Quantum Spacetime". In: *Phys. Rev. Lett.* 102 (11 Mar. 2009), p. 111303. DOI: 10.1103/PhysRevLett.102.111303.

[48] P. Horava. "Spectral Dimension of the Universe in Quantum Gravity at a Lifshitz Point". In: *Phys. Rev. Lett.* 102 (16 Apr. 2009), p. 161301. DOI: 10.1103/PhysRevLett.102.161301.

[49] O. Lauscher and M. Reuter. "Ultraviolet fixed point and generalized flow equation of quantum gravity". In: *Phys. Rev. D* 65 (2 Dec. 2001), p. 025013. DOI: 10.1103/PhysRevD.65.025013.

[50] M. Niedermaier. "The asymptotic safety scenario in quantum gravity: an introduction". In: *Classical and Quantum Gravity* 24.18 (Aug. 2007), R171–R230. DOI: 10.1088/0264-9381/24/18/r01.

[51] M. Reuter and F. Sauressig. "Fractal space-times under the microscope: a renormalization group view on Monte Carlo data". In: *J. High Energ. Phys* 2011 (12 Dec. 2011), p. 12. DOI: 10.1007/JHEP12(2011)012.

[52] L. Modesto. "Fractal spacetime from the area spectrum". In: *Classical and Quantum Gravity* 26.24 (Nov. 2009), p. 242002. DOI: 10.1088/0264-9381/26/24/242002.

[53] J. Ambjørn et al. "Critical phenomena in causal dynamical triangulations". In: *Classical and Quantum Gravity* 36.22 (Oct. 2019), p. 224001. DOI: 10.1088/1361-6382/ab4184.

[54] J. Ambjørn et al. "Second- and first-order phase transitions in causal dynamical triangulations". In: *Phys. Rev. D* 85 (12 June 2012), p. 124044. DOI: 10.1103/PhysRevD.85.124044.

[55] J. Ambjørn et al. "Renormalization group flow in CDT". In: *Classical and Quantum Gravity* 31 (16 July 2014), p. 165003. DOI: 10.1088/0264-9381/31/16/165003.

[56] J. Ambjorn et al. *Renormalization in quantum theories of geometry*. 2020. DOI: 10.48550/ARXIV.2002.01693.

[57] J. Ambjørn et al. "The phase structure of causal dynamical triangulations with toroidal spatial topology". In: *J. High Energ. Phy* 111 (6 June 2018). DOI: 10.1007/JHEP06(2018)111.

[58] N. Metropolis et al. "Equation of State Calculations by Fast Computing Machines". In: *J. Chem. Phys.* 12.1087 (1953). ISSN: 11506418. DOI: https://doi.org/10.1063/1.1699114.

[59] U. Pachner. "P.L. Homeomorphic Manifolds are Equivalent by Elementary Shellings". In: *European Journal of Combinatorics* 12.2 (1991), pp. 129–145. ISSN: 0195-6698. DOI: https://doi.org/10.1016/S0195-6698(13)80080-7.

[60] A. Eichhorn, A. D. Pereira, and A. G. A. Pithis. "The phase diagram of the multi-matrix model with ABAB interaction from functional renormalization". In: *J. High Energ. Phy* 131 (2020). DOI: https://10.1007/JHEP12(2020)131.

[61] C. C. Tsuei and J. R. Kirtley. "Pairing symmetry in cuprate superconductors". In: *Rev. Mod. Phys.* 72 (4 Oct. 2000), pp. 969–1016. DOI: 10.1103/RevModPhys.72.969.

[62] C. Xie, G. Zheng-Cheng, and W. Xiao-Gang. "Local unitary transformation, long-range quantum entanglement, wave function renormalization, and topological order". In: *Phys. Rev. B* 82 (15 Oct. 2010), p. 155138. DOI: 10.1103/PhysRevB.82.155138.

[63] H. Nishimori and G. Ortiz. *Phase transitions and critical phenomena*. 2011. ISBN: 978-3-642-11897-5. DOI: DOI:10.1093/acprof:oso/9780199577224.003.0001.

[64] J. Ambjørn, J. Jurkiewicz, and R. Loll. "Quantum Gravity as Sum over Spacetimes". In: 2010, pp. 59–124. ISBN: 978-3-642-11897-5. DOI: 10.1007/978-3-642-11897-5_2.

[65] O. Kafri. *A Novel Approach to Probability*. 2016. DOI: 10.48550/ARXIV.1606.03696.

[66] Piotr Bialas, Zdzislaw Burda, and Des Johnston. "Condensation in the Backgammon model". In: *Nuclear Physics B* 493.3 (1997), pp. 505–516. ISSN: 0550-3213. DOI: https://doi.org/10.1016/S0550-3213(97)00192-2.

[67] J. Ambjorn et al. "Searching for a continuum limit in causal dynamical triangulation quantum gravity". In: *Phys. Rev. D* 93 (10 May 2016), p. 104032. DOI: 10.1103/PhysRevD.93.104032.

[68] J. Mielczarek. "Asymptotic silence in loop quantum cosmology". In: *AIP Conference Proceedings* 81 (1514 2013). DOI: https://doi.org/10.1063/1.4791730.

[69] F. Alet et al. "Unconventional Continuous Phase Transition in a Three-Dimensional Dimer Model". In: *Phys. Rev. Lett.* 97 (3 July 2006), p. 030403. DOI: 10.1103/PhysRevLett.97.030403.

[70] J. Ambjørn et al. "Pseudo-Cartesian coordinates in a model of Causal Dynamical Triangulations". In: *Nuclear Physics B* 943 (2019), p. 114626. ISSN: 0550-3213. DOI: https://doi.org/10.1016/j.nuclphysb.2019.114626.

[71] Y. Miyatake et al. "On the implementation of the heat bath algorithms for Monte Carlo simulations of classical Heisenberg spin systems". In: *Journal of Physics C: Solid State Physics* 19.14 (May 1986), pp. 2539–2546. DOI: 10.1088/0022-3719/19/14/020.

[72] F. Matsubara et al. "Cluster Heat Bath Algorithm in Monte Carlo Simulations of Ising Models". In: *Phys. Rev. Lett.* 78 (17 Apr. 1997), pp. 3237–3240. DOI: 10.1103/PhysRevLett.78.3237.